Dissertation

Zur

Erlangung der Doktorwürde (Dr. rer. nat.)

der

Gesamtfakultät für Mathematik, Ingenieur- und Naturwissenschaften

der

Ruprecht-Karls-Universität

Heidelberg

vorgelegt von

Steffen Ott

geboren in Hanau

Tag der mündlichen Prüfung

13. Juni 2022

Preparation of 2D Material Thin Films
for
Optical Applications

Gutachter

Prof. Dr. Claudia Backes

Prof. Dr. Petra Tegeder

Eidesstattliche Versicherung gemäß § 8 der Promotionsordnung für die Gesamtfakultät für Mathematik, Ingenieur- und Naturwissenschaften der Universität Heidelberg / *Sworn Affidavit according to § 8 of the doctoral degree regulations of the Combined Faculty of Mathematics, Engineering and Natural Sciences at Heidelberg University*

1. Bei der eingereichten Dissertation zu dem Thema / *The thesis I have submitted entitled*

Preparation of 2D Material Thin Films for Optical Applications

handelt es sich um meine eigenständig erbrachte Leistung / *is my own work.*

2. Ich habe nur die angegebenen Quellen und Hilfsmittel benutzt und mich keiner unzulässigen Hilfe Dritter bedient. Insbesondere habe ich wörtlich oder sinngemäß aus anderen Werken übernommene Inhalte als solche kenntlich gemacht. */ I have only used the sources indicated and have not made unauthorised use of services of a third party. Where the work of others has been quoted or reproduced, the source is always given.*

3. Die Arbeit oder Teile davon habe ich bislang nicht an einer Hochschule des In- oder Auslands als Bestandteil einer Prüfungs- oder Qualifikationsleistung vorgelegt. / *I have not yet presented this thesis or parts thereof to a university as part of an examination or degree.*

4. Die Richtigkeit der vorstehenden Erklärungen bestätige ich. / I confirm that the declarations made above are correct.

5. Die Bedeutung der eidesstattlichen Versicherung und die strafrechtlichen Folgen einer unrichtigen oder unvollständigen eidesstattlichen Versicherung sind mir bekannt. / *I am aware of the importance of a sworn affidavit and the criminal prosecution in case of a false or incomplete affidavit.*

Ich versichere an Eides statt, dass ich nach bestem Wissen die reine Wahrheit erklärt und nichts verschwiegen habe. / *I affirm that the above is the absolute truth to the best of my knowledge and that I have not concealed anything.*

....	....
Ort und Datum / Place and date	Unterschrift / Signature

Table of Content

Abbreviations

0D	zero-dimensional
1D	one-dimensional
2D	two-dimensional
a. u.	arbitrary unit
ac	armchair
AFM	atomic force microscopy
ALD	atomic layer deposition
BuLi	butyllithium
CB	conduction band
CBM	conduction band minimum
CHP	1-cyclohexyl-2-pyrrolidone
CNT	carbon nanotube
CPS	counts per second
CVD	chemical vapor deposition
DFT	density functional theory
DGU	density gradient ultracentrifugation
DLS	dynamic light scattering
DLVO	Derjaguin-Landau-Verwey-Overbeek
DMF	*N,N*-dimethylformamide
EDX	energy dispersive X-ray
FL	few layer
FTIR	Fourier transform infrared
funct	functionalized
FWHM	full-width-at-half-maximum
HATCN	hexaazatriphenylenehexacarbonitrile
L. film	Langmuir film
LCC	liquid-cascade centrifugation
LED	light-emitting diode
LEFET	light-emitting field effect transistor
LP	lower polariton

LPE	liquid phase exfoliation
ML	monolayer
NA	numerical aperture
NMP	*N*-methyl-2-pyrrolidone
PCA	1-pyrenecarboxylic acid
PL	photoluminescence
PLE	photoluminescence excitation
PLQY	photoluminescence quantum yield
PMMA	poly(methyl methacrylate)
PVK	polyvinylcarbazole
Q factor	quality factor
RCF	relative centrifugal force
RMS	root mean square
RPM	revolutions per minute
SAW	surface acoustic wave
SC	sodium cholate
SEM	scanning electron microscopy
TEM	transmission electron microscopy
TFSI	trifluoromethanesulfonimide
TGMS	thermal gravimetric mass spectrometry
THF	tetrahydrofuran
TMD	transition metal dichalcogenide
UP	upper polariton
UV	ultraviolet
VB	valence band
VBM	valence band maximum
VdW	Van der Waals
Vis	visible
XRD	X-ray diffraction
zz	zig-zag

Abstract

Two-dimensional materials have gained tremendous interest over the last decade due to their unique properties and their potential to be employed in future electronic or optoelectronic devices. One class of materials that are subject of ongoing research are transition metal dichalcogenides (TMDs) such as MoS_2 or WS_2. In their 2H-phase, these layered Van der Waals (VdW) crystals are semiconducting and undergo a transition from an indirect to a direct band gap, when the layer number is decreased to the monolayer (ML) limit, giving rise to emerging photoluminescence. One of the research areas where ML TMDs are promising materials due to their high oscillator strength and large exciton binding energies is strong light-matter coupling, where the energy exchange between photons and matter (for example excitons) in optical microcavities results in the formation of hybrid light-matter quasi particles, so-called polaritons. These polaritons exhibit properties of both light and matter, making them interesting for their own sake but also for future polaritonic devices, such as polariton lasers.

One of the most commonly applied techniques for the production of two-dimensional nanoobjects is exfoliation of bulk crystals, for example in the liquid phase by sonication assisted liquid phase exfoliation (LPE), where the interlayer binding energies of the bulk crystals are overcome by sonication. However, this process is still not fully understood, and exfoliated nanosheets are relatively small in their lateral dimensions due to scission events within the layers. Additionally, the deposition of the nanosheets from dispersion into homogeneous thin films with preservation of the ML properties remains a major challenge. Therefore, most demonstrations of TMD based applications are designed with single flakes of TMDs, which restricts the scale-up. For example, the formation of polaritons in homogeneous films of TMDs has not been demonstrated yet.

The first part of this thesis focuses on the optimization and understanding of the LPE process. It was demonstrated that purity, particle size, and defectiveness do not impact the yield or dimensions of LPE produced nanosheets. However, differences in the PL properties were observed, which might be related to the defectiveness of the starting material. The exfoliation efficiency and the dimensions of the nanosheets can be altered by pretreatment of the starting material, leading to intercalation of the pretreatment agents and reduction of the interlayer binding strength, but the effect is small when high power sonication conditions are chosen.

In the next part of the thesis, thin films of TMDs were produced by different strategies, including spin coating of WS_2-polymer composite films and deposition of WS_2 in Langmuir-type films, that were formed at liquid-liquid phase interfaces. The films were characterized and assessed regarding their usability for the implementation in optical microcavities. Here, the Langmuir films were superior to the composite films due to stronger PL, better homogeneity, and lower thickness for a given optical density. The production of high-quality composite films was only possible with

low WS_2 concentrations, resulting in insufficient optical density or high film thickness. Both composite and Langmuir films were implemented in microcavities, but strong light-matter interaction was only observed in the cavities based on the Langmuir films. While this is the first time that strong coupling is demonstrated based on angle-dependent reflectivity in homogeneous and large-scale thin films of TMDs, it was not possible to measure the PL emission of the cavities, due to low signal intensity.

In the last part of this thesis, hydrogen and methyl derivatized germanene (Ge-H and Ge-Me) were subjected to LPE, since these materials are known for higher PL intensities and are also fluorescent in the bulk structure. The fluorescence properties of Ge-H were not preserved after sonication, but the more stable Ge-Me nanosheet dispersions showed promising properties, including strong PL. However, Ge-Me is susceptible to basal plane degradation under ambient conditions and film preparation was only possible with relatively large nanosheets. In these films, the fluorescence properties were preserved, but no working light-emitting devices could be built, which was attributed to inhomogeneities that are related to the large nanosheets with broad size distribution.

Kurzzusammenfassung

Das Interesse an zwei-dimensionalen Materialien erfuhr die letzten Jahre über einen gewaltigen Aufschwung, was auf deren einzigartigen Eigenschaften und die mögliche Verwendung in elektronischen oder optoelektronischen Bauelementen zurückzuführen ist. Eine Klasse an zwei-dimensionalen Materialen, an denen aktiv und fortlaufend geforscht wird, sind einlagige Übergangsmetalldichalkogenide (TMDs), wie MoS_2 oder WS_2. Diese Van der Waals (VdW) Schichtkristalle sind in ihrer 2H-Phase halbleitend und vollziehen einen Übergang von einer indirekten zu einer direkten Bandlücke, wenn die Lagenanzahl auf eine Monolage (ML) reduziert wird, wodurch die TMDs fluoreszent werden. Wegen hoher Oszillatorstärke und Exziton-Bindungsenergie werden ML TMDs im Forschungsgebiet der starken Licht-Materie Kopplung verwendet, in dem der Energieaustausch zwischen Licht und Materie (z. B. Exzitonen) in optischen Mikrokavitäten zu der Bildung von neuen Hybrid-Quasipartikeln aus Licht und Materie führt, den sogenannten Polaritonen. Diese haben sowohl Eigenschaften von Licht als auch von Materie. Dieser Fakt allein macht sie einzigartig, aber das Interesse an Polaritonen begründet sich auch in der Möglichkeit sie zukünftig in polaritonischen Bauelementen zu verwenden, z. B. in Polaritonlasern.

Einer der gängigsten Methoden für die Exfolierung von Schichtkristallen ist die Flüssigphasenexfolierung (LPE), bei der die Bindungsenergie zwischen den Schichten, z. B. mittels Ultraschall, überwunden wird. Dieser Prozess ist zwar weltweit etabliert, jedoch noch nicht vollständig verstanden und exfolierte Schichten sind verhältnismäßig klein in der lateralen Ausdehnung. Hinzu kommt, dass die Abscheidung der exfolierten Materialien zu Dünnschichtfilmen schwierig ist, ohne dass dabei die Eigenschaften der Monolagen verloren gehen. Dies führte dazu, dass die meisten bisher gezeigten Anwendungen auf einzelnen Kristallen von TMDs basieren, was eine Skalierbarkeit erschwert. So konnte z. B. noch keine Bildung von Polaritonen in homogenen Filmen von TMDs demonstriert werden.

Der erste Teil dieser Arbeit ist auf die Optimierung und dem Verständnis der LPE fokussiert. So wurde gezeigt, dass die Reinheit, die Partikelgröße oder die Defektdichte der Startmaterialien keinen Einfluss auf die Ausbeute oder die Dimensionen der Nanokristalle hat, die mittels LPE hergestellt wurden. Nichtsdestotrotz wurden Unterschiede in der Photolumineszenz (PL) nachgewiesen, die womöglich auf unterschiedliche Defektdichten zurückzuführen sind. Des Weiteren wurde gezeigt, dass die Exfolierungseffizienz und damit die Dimensionen der exfolierten Nanokristalle durch Vorbehandlung der Startmaterialien beeinflusst werden kann, was auf Interkalation von Vorbehandlungsstoffen und eine Veränderung der Bindungsenergie zwischen den Lagen zurückzuführen ist. Dieser Effekt ist jedoch vernachlässigbar, wenn effiziente Ultraschallbedingungen gewählt werden.

Im nächsten Teil wurden WS_2 Dünnschichtfilme hergestellt, was sowohl rotationsbeschichtete WS_2-Polymer-Kompositfilme als auch Langmuir-Filme beinhaltete, die an flüssig-flüssig Phasengrenzen gebildet wurden. Die Filme wurden charakterisiert und bezüglich ihrer Eignung für die Verwendung in optischen Mikrokavitäten beurteilt. Dabei stellten sich die Langmuir-Filme gegenüber den Kompositfilmen als überlegen heraus, was sich in stärkerer PL, besserer Homogenität und besserem Verhältnis von optischer Dichte zu Filmdicke zeigte. Kompositfilme konnten nur mit geringem WS_2-Anteil in hoher Qualität produziert werden, was eine zu geringe optische Dichte oder zu hohe Filmdicke zur Folge hat. Sowohl die Komposit- als auch die Langmuir-Filme wurden in Mikrokavitäten implementiert, aber starke Licht-Materie Wechselwirkung konnte nur in den Kavitäten nachgewiesen werden, die auf den Langmuir-Filmen basierten. Obwohl zum ersten Mal die Bildung von Polaritonen in homogenen TMD-Filmen anhand winkelaufgelöster Reflektivität gezeigt wurde, konnte die PL-Emission der Kavitäten aufgrund von zu geringer Intensität nicht gemessen werden.

Im letzten Teil dieser Arbeit wurden Wasserstoff und Methyl derivatisierte Germane (Ge-H und Ge-Me) exfoliert, da diese eher unbekannten Materialien eine starke Fluoreszenz besitzen und diese auch im mehrlagigen Kristall behalten. Die Fluoreszenzeigenschaften von Ge-H konnten während der Exfolierung nicht erhalten werden, aber das stabilere Ge-Me zeigte vielversprechende Eigenschaften, insbesondere eine intensive PL. Allerdings wurde eine Zersetzung der exfolierten Nanokristalle beobachtet, sodass die Herstellung von Langmuir-Filmen nur mit relativ großen exfolierten Schichten möglich war. In diesen Filmen blieb die PL erhalten, aber es konnten keine funktionierenden, Licht-emittierende Bauelemente hergestellt werden. Dies ist auf die Inhomogenität der Filme zurückzuführen, welche von der relativ breiten Größenverteilung stammt, die bei größeren exfolierten Nanoschichten vorzufinden ist.

Acknowledgements

This work would not have been possible without the tremendous support I received from several people.

First of all, I have to thank my supervisor Dr. Claudia Backes, who was always there for me with good advice, and who accepted and welcomed me warmly in her newly founded research group.

I really appreciated all my colleagues of the PC2D and NMOE group, who guaranteed that my time at the university was not only work, but also fun. I explicitly want to mention Jan, Felix, Merve, and Yuri – my office mates – and Daniel, who sweetened the lunch breaks with chess matches and who was up for mountaineering trips during vacation.

I would like to thank everyone, who contributed to my work in one or another way and I have to mention Dr. Jan Lüttgens, Dr. Felix Berger, Tim Nowack, Dr. Kevin Synnatschke, Dr. Farnia Rashvand, Daniel Heimfarth, Dr. Vaishnavi Rao, Dr. Sebastian Grieger, Dr. Andreas Mischok, Jiří Šturala, Prof. Dr. Zdeněk Sofer, Prof. Dr Zaumseil, and of course all my students, Nadja Wolff, Tjark Harders, Anne Sehnal, Melanie Lakmann, Johanna Stemmer, Tamara Skarke, who provided great experimental support. Big thanks for the proofreading to Fabian Ebner, Tim Nowack, Felix Berger, Daniel Heimfarth, Lukas Nowotka, and Rica Kaufmann.

Next, I want to mention the APC staff Peter Jeschka, Günter Meinusch, Reinhold Jehle, Karin Jordan, Swetlana Duchnay, Isabella Haffelder, and Benjamin Scherke, as well as Klaus Schmitt and his team, since they were always helpful when IT-, technical, or administrative issues needed to be fixed.

Last but not least I need to thank my family, which supported me during my whole time at the university not only mentally but also financially. Rica, thank you for being there for me. Without you, the intense writing time would have been a lot harder.

1 Introduction

When descending a steep mountain on solid rock or on a flank covered by gravel of the same natural stone, it becomes obvious that the properties of materials change with the particle size. While the solid rock provides good friction and a secure step, the gravel is slippery and potentially dangerous. On a smaller scale, everyone has observed the change in color of oil or soap when it forms thin films with thicknesses in the range of the wavelength of visible light, which is due to interference patterns.[1]

Although the intrinsic properties of the materials in the examples mentioned above are retained, they can indeed drastically change, when one or more dimensions of materials are reduced to the nanometer scale, giving rise to tremendous interest in low dimensional materials, which developed to a new research field over the last decades. Low dimensional materials are categorized into two-dimensional (2D), one-dimensional (1D), or zero-dimensional (0D) materials, with an extended structure of the materials in two, one, or zero directions, whereas the remaining dimensions are on the nanometer scale. These materials can be further classified by their geometry, for example into nanocrystals, -wires, -rods, -spheres, -prisms, -rings, -films, or -sheets.

Examples of low dimensional materials are 0D quantum dots or nanoparticles such as fullerenes or gold nanoparticles, 1D nanowires, nanorods, or nanotubes such as carbon-nanotubes (CNTs) or ZnO nanorods, and 2D thin films or nanosheets of layered materials such as graphene or 2D transition metal dichalcogenides.[2] The one atom thick graphene consists of a single layer of graphite and is the earliest and most prominent 2D material, first investigated as single layer in 2004.[3, 4] As a consequence of the reduced layer number, graphene exhibits excellent tensile mechanical strength[5] with values higher than graphite or even steel, and features high charge carrier mobility and thermal conductivity.[6] Additionally, the reduction in thickness results in an increased surface area per volume unit, increasing the surface related reactivity.

The unique properties of graphene and the fact that mechanical but also electronic or optical properties can be altered due to confinement of electrons gave birth to the exploration of many other 2D materials. One class of these newly explored materials are transition metal dichalcogenides, which are semiconducting (in the 2H-phase) and undergo a transition from an indirect to a direct band gap, when the number of layers is decreased to the ML limit, resulting in emerging photoluminescence. ML TMDs are known for large exciton binding energies about a couple of hundred meV[7-9] or high oscillator strength[10] and found application in transistors,[11-14] photodetectors,[15-17] batteries,[18-20] or light-emitting diodes (LEDs).[21, 22] Another research field where ML TMDs are considered as promising materials is strong light-matter coupling, where so-called polaritons are formed in optical microcavities. Polaritons are hybrid quasi particles which consist of both light and matter and exhibit unique properties which cannot be found in pure light or pure matter. Researchers are interested in fundamental physics of polaritons as well as in the development of polariton based devices,[23] such as polariton lasers,[24] polariton LEDs,[25] or polariton transistors.[26, 27]

Within the context of TMDs, many devices are based on single flakes which have been grown by chemical vapor deposition (CVD) or have been mechanically-exfoliated from bulk crystals. With the aim in mind to pave the path towards real world applications in an industrial environment, other methods need to be developed to cover large areas with TMDs on arbitrary substrates in a reproducible fashion. In recent years this has been addressed by the exfoliation of layered bulk crystals in the liquid phase and deposition of the nanosheets into films. In liquid phase exfoliation (LPE), the attractive forces between the layers can be overcome by chemical/electrochemical intercalation, or more commonly by sonication.

Exfoliated stock dispersions are polydisperse and need to be subjected to size-selection methods which are mostly centrifugation-based. The isolated few layer (FL) or ML nanosheets are typically small in their lateral size in comparison to CVD-grown or mechanically-exfoliated flakes. However, a major obstacle is the deposition of the nanosheets, since it is extremely challenging to deposit the nanosheets into high quality networks or thin films. Previous attempts include spray coating,[13] spin coating of polymer/nanosheet composite films,[28] or more recently the deposition of self-assembled Langmuir films formed at liquid-liquid phase interfaces.[15, 29-31] Despite the progress that has been accomplished, devices based on nanosheet networks are still rare, especially in the area of optoelectronics. This is because it is extremely difficult to preserve the photoluminescence and prevent aggregation during deposition.

These issues mentioned above will be one of the main points addressed in this thesis: The deposition of nanosheets as thin films using WS_2 as prototype and the implementation of homogenous thin films into optical microcavities.

2 State of the Art

2.1 Transition Metal Dichalcogenides

Beside graphene, ML transition metal dichalcogenides in the form of MX_2, where M is a metal (such as W, Mo, or Nb) and X is the chalcogenide (such as S, Se, or Te), are probably the most prominent 2D materials due to their interesting properties and their potential to be used for future applications.

While most metals of group 8 to 10 form non-layered structures, many metals of group 4 to 7 with the molecular formula MX_2 form layered crystals and are therefore susceptible for the exfoliation to two-dimensionality.[32] Even though many TMDs are subject of ongoing research, this discussion will mostly focus on group VI TMDs, such as MoS_2 and WS_2, since these materials are most relevant for this thesis.

In the bulk structure, these TMDs exist in nature and form layered crystals with hexagonally packed planes, hold together by weak Van der Waals (VdW) forces between the layers. The crystals can exist in different phases, most commonly the trigonal prismatic 2H-phase with an ABA stacking of the crystal layers or the octahedral 1T-phase with layers arranged in an ABC stacking (see Figure 2.1 A). For most group VI TMDs, the (semiconducting) 2H-phase is thermodynamically favored but the (metallic) 1T-phase can exist in a metastable state. The point group of 2H-MoS_2 or -WS_2 is D_{6h} for the bulk material, and D_{3h} for an odd number of layers or D_{3d} for an even number of layers, in case of few layer TMDs.[33] The M-X bonding length is between 3.15 and 4.03 Å and the layer thickness about 6–7.[32]

Historically, TMDs found application as dry lubricants[34-37] similar to graphite,[38] but in recent years, attention shifted towards optoelectronic applications. This is because TMDs in their 2H-phase are semiconducting with an indirect band gap in the bulk structure, which undergoes a transition to a direct band gap when the number of layers is decreased to the ML limit, giving rise to emerging photoluminescence (PL). The relation between layer number and band structure will be explained based on a summary by WANG *et al.*[7]

The band gap of the bulk materials goes from the maximum of the valence band (VB) to the minimum of the conduction band (CB), which are located at the Γ-point (VB) or between the Γ-and the K-point (CB) of the Brillouin zone, respectively (Figure 2.1 B). Atomic orbitals associated with this indirect band gap are strongly influenced by adjacent layers in the crystal, since they contain contributions from the p_z orbital of the chalcogen atom and the d_{z2} orbital of the metal atom (at the Γ-point), which point in a direction perpendicular to the plane of the layers.

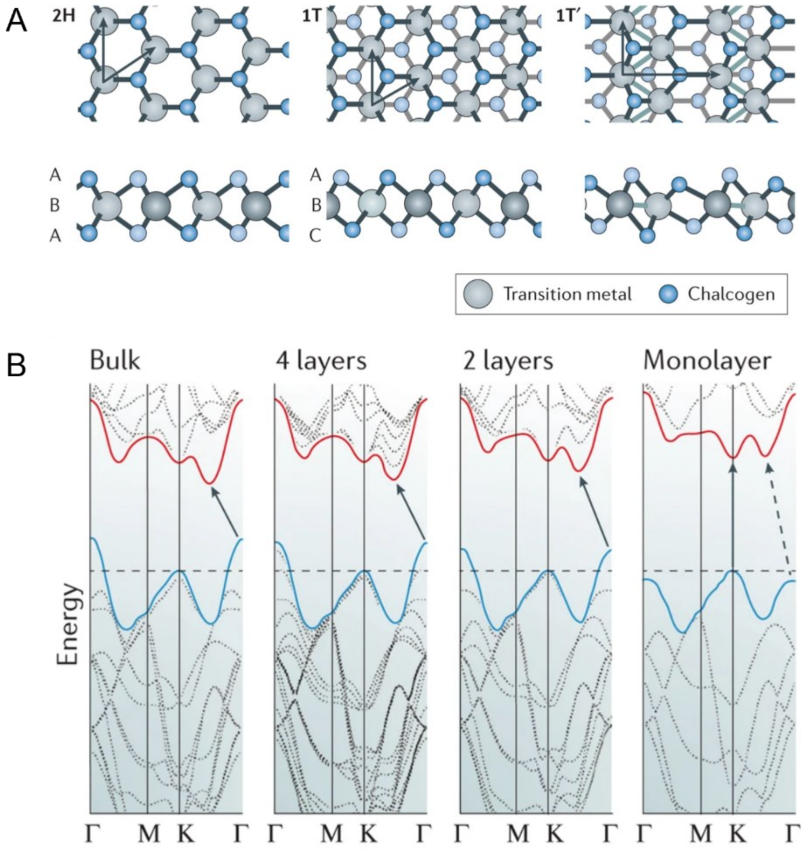

Figure 2.1: A: Structure of different phases of TMDs, including the semiconducting 2H-phase and the metallic 1T/1T'-phases. The illustration only involves a single layer of the crystals. B: Band structure of 2H-MoS_2 for different numbers of layers, showing the transition from an indirect to a direct band gap, when the ML limit is reached. The band gap is indicated by the solid arrow. Adapted by permission from *Nature Reviews Materials* **2017,** *2* (8), 17033.[39] © 2017 Macmillan Publishers Limited, part of Springer Nature.

This implies that the energies of the VB maximum (VBM) or the conduction band minimum (CBM) are altered when the number of layers in the crystal is reduced, resulting in an increase of the band gap. For obvious reasons, this alteration is most pronounced when the overall number of layers is small. When the ML limit is reached, a new and direct band gap forms at the *K*-point of the Brillouin zone, where the energy states are associated with the metal orbitals $d_{x2-y2} \pm id_{xy}$ states (VB) and d_{z2} states (CB), mixed with chalcogen $p_x \mp ip_y$ orbitals. These are localized in the plane of the metal and thus less affected by the layer number.

As mentioned above, the newly formed direct band gap is origin of photoluminescence, as visible in the photoluminescence-excitation (PLE) contour plots of MoS_2 and WS_2, presented in Figure 2.2. The PL is associated with the A-exciton, which itself is associated with an optical transition from the CBM to the VBM at the *K*-point of the Brillouin zone and is the (bright) exciton of lowest energy. Relatively strong spin-orbit coupling in TMDs results in a spin splitting of the VBM and hence to the presence of the B-exciton – a second (bright) exciton related to the *K*-point. Strictly speaking, also the CBM is split by spin-orbit coupling, but the splitting is smaller and results in only one bright exciton.

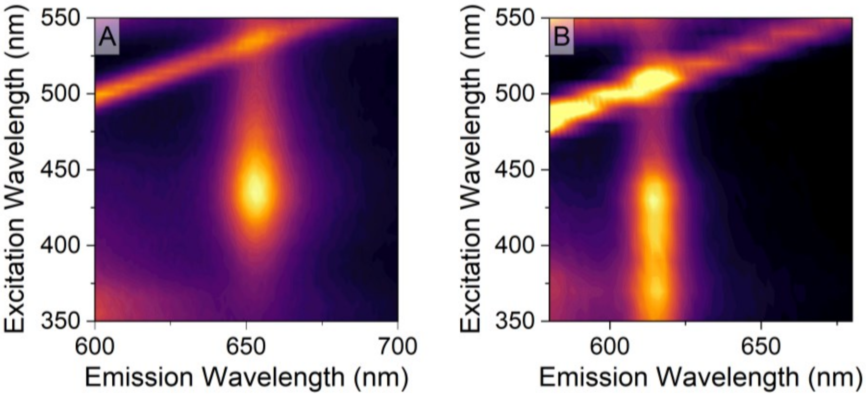

Figure 2.2: Photoluminescence excitation (PLE) contour plot of MoS_2 (A) and WS_2 (B) nanosheet dispersions. The diagonal line visible in both PLE maps originates from Raman scattering of H_2O.

The excitons in ML TMDs have characteristics of both Wannier-Mott excitons that are commonly found in inorganic crystals, and Frenkel excitons which are typical for organic molecules. Properties attributed to Wannier-Mott excitons are delocalization of the excitons or low binding energies and oscillator strength, whereas Frenkel excitons are typically localized and exhibit high binding energies and oscillator strength. In ML TMDs, the excitons can move freely in plane of the material, have relatively small radii of a few nanometers, and relatively large binding energies up to ~ 0.5 eV[7] (~ 0.37 eV for WSe_2,[8] ~ 0.32 eV for WS_2[9]). However, despite small radii and large binding energies, a description as Wannier-Mott excitons is sufficient for the explanation of most experimental observations.

The strong oscillator strength ($\geq 10^3$) gives rise to strong absorption of the materials and a single layer of TMDs can absorb 20 % of the light for resonant excitation of the A-exciton.[10] The versatile and unique properties of TMDs have resulted in the demonstration of several applications,[40] for example in transistors,[11-14, 41] in photodetectors,[15-17] in light-emitting devices,[25, 42, 43] in batteries,[18-20] or as catalysts in the hydrogen evolution reaction.[44, 45]

Defects in TMDs

No real crystal exhibits a perfect crystal structure. Instead, defects such as grain boundaries or point defects exist in the lattice, which impact the mechanical, electrical, and optical properties of the material.[46]

In TMDs, possible point defects are illustrated in Figure 2.3 on the example of MoS_2, including sulfur vacancies (V_S), disulfur vacancies (V_{S2}), antisite defects where a Mo atom is substituting S_2

columns (Mo_{S2}), Mo vacancies nearby three sulfur atoms (V_{MoS3}), Mo vacancies nearby three disulfur pairs (V_{MoS6}), and S_2 columns substituting Mo atoms ($S2_{Mo}$).[47] The most common point defect in TMDs are chalcogen vacancies, such as V_S, since these have the lowest formation energies, followed by dichalcogen vacancies.[47] However, the formation energy of V_{S2} defects is still twice as high as the formation energy of V_S defects, making V_{S2} defects less common. On the opposite side, Mo_{S2} and $S2_{Mo}$ have the highest formation energies and are rare.

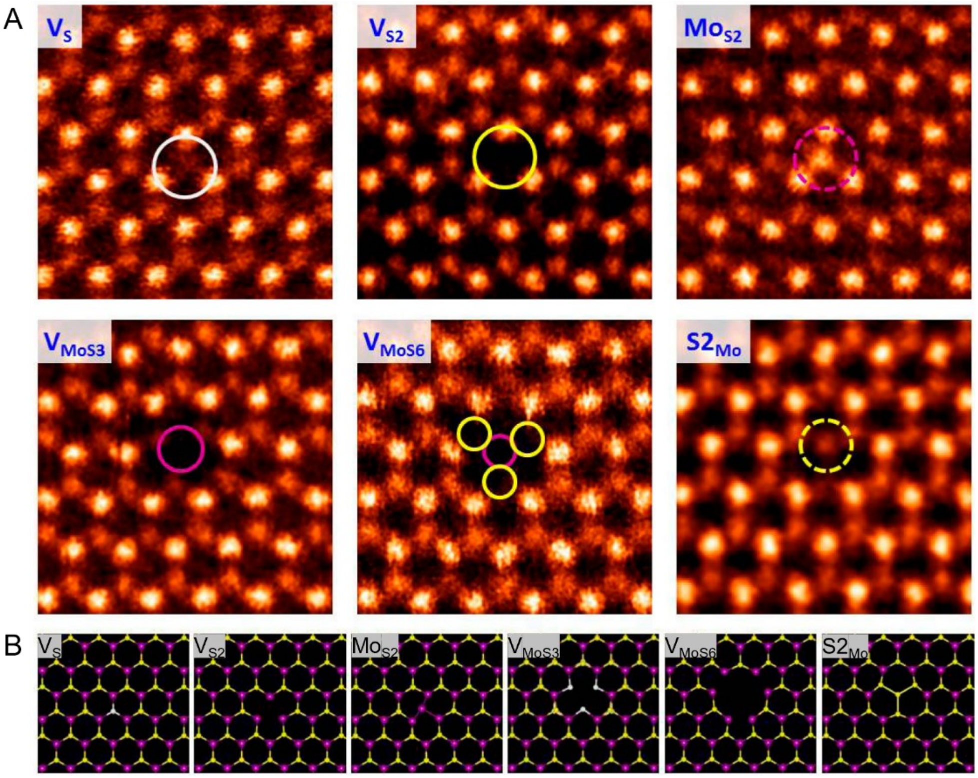

Figure 2.3: Intrinsic point defects in MoS_2. A: Atomic resolution annular dark field images of intrinsic point defects in ML MoS_2, including sulfur vacancy (V_S), disulfur vacancy (V_{S2}), antisite defect where a Mo atom is substituting a S_2 column (Mo_{S2}), Mo vacancy nearby three sulfur atoms (V_{MoS3}), Mo vacancy nearby three disulfur pairs (V_{MoS6}), and a S_2 column substituting a Mo atom ($S2_{Mo}$). B: Structural model of the point defects shown in A. The figure was adapted by permission from *Nano Lett.* **2013**, 13, 2615–2622.[47] © 2013 American Chemical Society.

The impact of defects on optical properties such as PL is complex and both defect-induced enhancement and suppression of PL has been reported. The PL of intrinsic and defect free TMDs is dominated by radiative decay of neutral excitons. However, unsaturated electrons in the most frequently found V_S defects act as electron donor, resulting in n-doping of natural TMDs[46] and PL contributions from negatively charged trions. While this defect-related trion emission can result in an enhancement of the total PL intensity,[48] it is generally excepted that excitons are more likely to decay radiatively and hence with higher quantum efficiency. For example, it was demonstrated that trions in MoS_2 or WS_2 can be suppressed by electrostatic doping, resulting in a strong increase of the overall emission which was dominated by neutral excitons.[49] Counterintuitively, this concept is also applicable to experimental observations, where defect induced PL enhancement was reported. For example, TONGAY *et al.* introduced defects to mechanically-exfoliated TMDs by irradiation of MeV α particles or thermal annealing and observed an increase in the overall PL intensity with the defect density.[50] It was proposed that gas molecules such as N_2 interact with the TMDs at the defect site, resulting in depletion of electrons and hence vanishing of negative trions and stabilization of neutral excitons bound to the defects. Similar observations were made in related studies.[51] Comparable principles were applied when TMDs were subjected to chemical modifications with the aim of withdrawing electron density from the TMD surface to reduce the trion density and to enhance the PL, for example by treatment with hexaazatriphenylene-hexacarbonitrile (HATCN)[52] or trifluoromethanesulfonimide (TFSI).[53]

It should be mentioned that the mechanisms described above have restrictions. While they are feasible for relatively low exciton densities, exciton-exciton annihilation is accelerated at high exciton densities, forming a dominant non-radiative decay path.[54, 55] This implies that at high exciton densities, suppression of trions has limited influence on the PL intensity, which might explain the power dependency of the PL quantum yield (PLQY) in TFSI treated MoS_2, where the PLQY decreases with increasing excitation power.[53] Nevertheless, exciton trapping by defects hinders the movement of excitons and can thus reduce the exciton-exciton annihilation, resulting in improved PL, as demonstrated by LEE *at al.*[56] However, it should further be mentioned that these PL enhancements are accompanied by a newly arising redshifted PL signal, whenever the PL emission of excitons occurs from defect related trap states, which are lower in energy.

While the section above leaves the impression that defects are mostly positive, defects are also well known for PL quenching. A possible mechanism that explains how defects decrease the quantum efficiency of PL is the so-called Auger scattering. In short, Auger scattering is a non-radiative decay path for excitons, where an electron or hole releases its energy by scattering another electron or hole to a higher energy level. In defective TMDs, this process takes place after electrons or holes are captured by defects. Auger scattering is theoretically slow in defect free semiconductors, but becomes more efficient due to strong Coulomb interactions and small exciton radii in TMDs, and is significantly accelerated by defects[57, 58] and might be the major path of energy dissipation in 2D TMDs.[46]

2.2 Liquid phase Exfoliation

A common problem in the field of 2D materials is related to production methods. While bottom-up synthesis such as chemical vapor deposition (CVD) is capable of growing ML TMD crystals in high quality, the substrate cannot be chosen freely and needs to be tailored to the material. Further a certain lack of scalability hinders application in an industrial environment. The latter issue also applies to top-down methods, such as mechanical exfoliation with scotch tape.

A methodology which addresses this issue is LPE, where bulk crystals are exfoliated to small nanosheets in a liquid medium, driven by chemical/electrochemical intercalation or sonication (see Figure 2.4). In the following part of this chapter, the basic principle and mechanism of LPE will be elaborated. The focus will be kept on sonication-assisted LPE, since chemical or electrochemical exfoliation of TMDs is typically accompanied with a phase transition to the metallic 1T-phase and has limited relevance for this thesis.

Long before LPE became a commonly used exfoliation technique for the preparation of nanosheet dispersions, the preparation of colloidal MoS_2 and WSe_2 dispersions by sonication was reported in 1989.[59] Later, the partial exfoliation of graphite was reported in 2005,[60] but only three years later in 2008, COLEMAN *et al.* successfully demonstrated that graphite can be thinned down to ML graphene by sonication,[61] which is considered as the starting point of sonication-assisted LPE. In the following years, it was revealed that this methodology is universally applicable, as has been demonstrated on a wide range of materials, including *h*-BN,[62-64] 2H-TMDs[62, 63, 65] (WS_2, MoS_2, WSe_2, $MoSe_2$), 1T-TMDs (TiS_2,[66, 67] TaS_2,[68] ReS_2[69]), group III-IV semiconductors (GaS,[70] InSe[71]), group IV-VI semiconductors (SnS[72], GeTe[73]), transition metal oxides (MoO_3,[74] MoO_2,[75]), pnictogens (black phosphorus,[76-78] Sb[79, 80]), transition metal phosphorus trisulphides (e.g. $NiPS_3$[81, 82]), layered silicates (e.g. talc[83]), hydroxides (e.g. $Ni(OH)_2$,[84] $Co(OH)_2$[85]), graphitic carbon nitride,[86] organic 2D polymers,[87] or natural minerals such as franckeite[88] and cylindrite.[89]

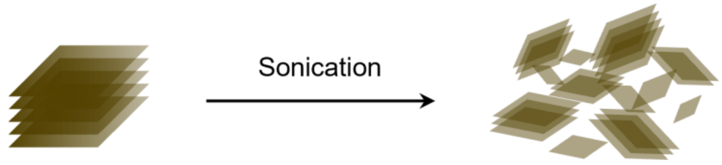

Figure 2.4: Illustration of sonication-assisted liquid phase exfoliation. A layered crystal is subjected to sonication, resulting in both exfoliation of the layers and scission within the layers.

A drawback of LPE is that exfoliated monolayered nanosheets are relatively small in their lateral dimensions, for example ~ 100–200 nm for graphene or < 50 nm for TMDs, despite many attempts to optimize the LPE process.[90-93] A theoretical model predicts that the lateral dimension of LPE produced nanosheets is intrinsically limited by the materials structure and binding situation.[94] This is because the exfoliation is typically governed by equipartition of energy between delamination and scission events, as described by equation (2.1), where $\langle A_{\mathrm{S}} \rangle$ and $\langle A_{\mathrm{E}} \rangle$ are the created edge and surface areas, and E_{S} and E_{E} are the energies required to create surfaces or edges.

$$\langle A_{\mathrm{S}} \rangle E_{\mathrm{S}} = \langle A_{\mathrm{E}} \rangle E_{\mathrm{E}} \tag{2.1}$$

It was concluded that the length of a ML nanosheet is defined by equation (2.2), with the characteristic ML length D_{ML} and the ML height h_0, which implies that the lateral length of LPE produced ML nanosheets is defined by the ratio of intra- and interlayer binding energy.

$$\frac{D_{\mathrm{ML}}}{h_0} = 2\frac{E_{\mathrm{E}}}{E_{\mathrm{S}}} \tag{2.2}$$

In the simplified ideal case, the aspect ratio from lateral size to thickness k is independent of the nanosheet size as described by equation (2.3), where L and w are the length and the width of a nanosheet, and where N is the layer number.

$$k = \frac{\sqrt{\langle Lw \rangle}}{\langle N \rangle h_0} = 2\frac{E_{\mathrm{E}}}{E_{\mathrm{S}}} \tag{2.3}$$

Mechanism of sonication-assisted LPE

It is generally accepted that sonication-assisted exfoliation is driven by acoustic cavitation[95] – the formation and collapse of microbubbles, causing micro implosions and thus shock waves and micro jets. While the exfoliation process is complex and not fully understood, one can imagine the delamination of the layers according to the following scheme (Figure 2.5): Cavitation induced shock waves create compressive and tensile stress in the bulk crystal, which results in a separation of the layers.[96] Secondary ways of delamination, such as wedging effects by micro jets or shearing by lateral compressive stress are imaginable.[96] Simulations on the example of MoS_2 predict that the collapse of bubbles can lead to surface temperatures about ~ 3000° K and pressures up to 20 GPa.[97] Since sonication is a high energy process, delamination is accompanied by fragmentation, similar to scission in CNTs.[61]

As mentioned above, the exfoliation process is not fully understood and even the cavitation itself is a complex process that is subject of investigation. For example, TURNER *et al.* suggested that tuning of the cavitation can be used to control the flake size of exfoliated nanosheets.[98] In this study, the authors distinguished between stable and inertial cavitation. Stable cavitation is characterized by a relatively long lifetime of the bubbles and dominantly causes short range vortices (micro-streams), whereas the bubble's lifetime of inertial cavitation is comparably short and results in spherical shock waves. The contribution of the preferred inertial cavitation was improved by tuning the acoustic frequency and amplitude, which impacted the yield and nanosheet size. However, most research institutions have limited possibilities to determine and improve the type of cavitation, since solvent (and hence density, viscosity, or boiling point) or vessel geometry are given by other requirements. Nevertheless, other studies suggested that cavitation can be improved by simple changes such as the filling height of the liquid in the vial.[99]

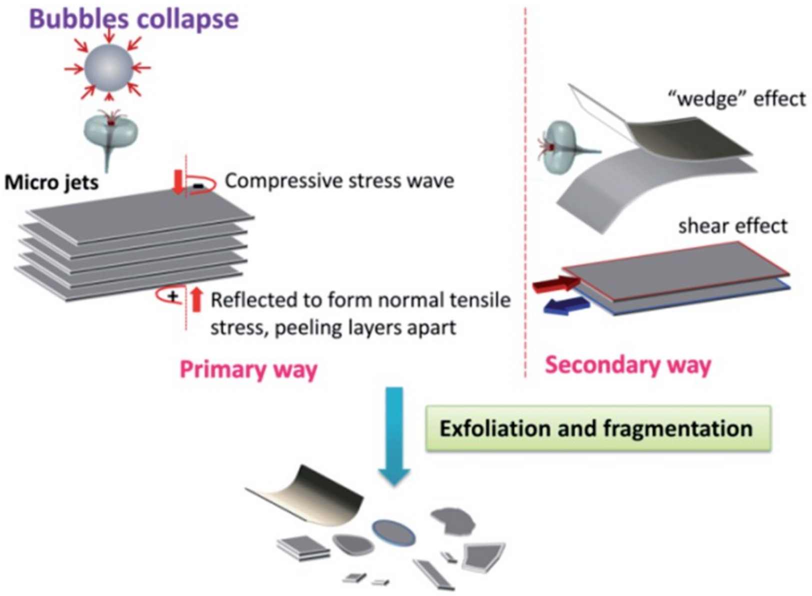

Figure 2.5: Illustration of cavitation-induced exfoliation. The implosion of bubbles causes shock waves, inducing compressive and tensile stress in bulk crystals, which results in delamination of the layers (left side). Secondary exfoliation pathways are possible, based on wedging effects by micro jets or shearing effects caused by lateral compressive stress. Reprinted by permission from *Journal of Materials Chemistry A* **2015,** *3* (22), 11700–11715.[96] © 2015 The Royal Society of Chemistry.

LI *et al*. investigated the mechanism of sonication assisted LPE on the example of graphene[100] and subdivided the exfoliation mechanism into three distinct stages (Figure 2.6). Stage I is related to the first seconds or minutes of the sonication and leads to fragmentation of the graphite flakes into smaller pieces. It was emphasized that this fragmentation mainly occurs along existing defect lines. In addition, the formation of kink bands was observed. Generally spoken, kink bands are formed by a dislocation movement of the basal plane when the material is exposed to thermal or mechanical stress. The kink bands in graphite predominantly evolve parallel to the low energy armchair (ac) and zig-zag (zz) edges.[101] The dislocation of the layers was explained by cavitation induced shock waves, which are converted into surface acoustic waves (SAWs). In contrast to bulk waves of elastic materials, where the longitudinal and transverse modes are independent, the modes of SAWs are coupled,[102] resulting in an elliptical vibration of the carbon atoms. The amplitude of this movement decreases exponentially with depth and causes the surface layers of graphite to kink. The carbon ridges of the kink bands are prone to oxidative attack, due to an increased chemical activity, which was revealed by density functional theory (DFT) calculation.[100] Elemental mapping by scanning electron microscopy combined with energy dispersive X-ray (SEM-EDX) showed that the ridges are indeed rich in oxygen and depleted in carbon. The oxygen was still present after removal of adsorbents and impurities, indicating that it is covalently bonded to the carbon.

This leads to stage II of the overall exfoliation process, where thin graphite stripes are peeled off from the parent flake. This peeling process takes place between the kink bands, since the oxidative attack together with a higher probability of stacking faults along the carbon ridges triggers efficient crack formation. This is analogous to longitudinal unzipping of carbon nanotubes[103] or the strain induced cutting of graphene.[104] The graphite stripes can undergo further kink band induced fragmentation, implying a fast decrease of the lateral nanosheet size with less exfoliation.

In stage III, the graphite stripes are further thinned down. However, the fragmentation mechanism described above becomes unlikely for graphite with $N < 30$ layers, since nanotube-like bending becomes favorable over kinking/twinning.[101] The further exfoliation process is slow and guided by the in-plane and out-of-plane binding energies, according to the equipartition model.[101]

While this mechanism was explicitly formulated and experimentally supported for the exfoliation of graphite, similarities to the exfoliation of other materials may exist. For example, it was demonstrated that moisture and oxygen plays an important role during the exfoliation of MoS_2, resulting in a decreased yield when the sonication is carried out in dried solvents under inert gas atmosphere.[105]

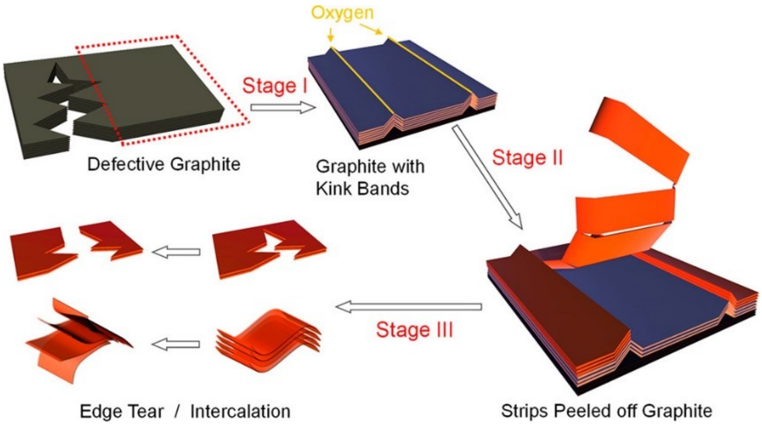

Figure 2.6: Mechanism of the exfoliation and fragmentation of graphite, divided into three distinct stages. In stage I, graphite is rapidly fractured into smaller pieces and kink bands form on the surface. During stage two, thin stripes of graphite are peeled off from the parent flakes, which are further thinned down and fragmented in stage III. Reprinted by permission from *ACS Nano* **2020**, 14, 10976–10985.[100] © 2020 American Chemical Society.

Stabilization of the Nanosheets

After exfoliation and fragmentation of bulk crystals, the newly formed nanosheets need to be stabilized in the dispersion to prevent reaggregation. This stabilization can either be accomplished by suitable solvents or requires additives, as will be discussed below.

A simple theoretical approach to describe this stabilization is given by the Gibbs energy of the mixing process ΔE_{mix}, expressed by equation (2.4) with the mixing enthalpy H_{mix}, the temperature T, and the mixing entropy S_{mix}, as summarized by BACKES[106] or COLEMAN.[107] The mixing entropy is always positive, but it is small in dispersions of large nanoparticles compared to solutions of small molecules, which implies that the mixing only takes place when the mixing enthalpy is small enough to obtain negative values for ΔG_{mix}.

$$\Delta G_{\mathrm{mix}} = \Delta H_{\mathrm{mix}} - T\Delta S_{\mathrm{mix}} \tag{2.4}$$

A traditional and most basic way to estimate the mixing enthalpy is expressed by equation (2.5), where $\Delta H_{\text{mix}}/V_{\text{mix}}$ is the mixing enthalpy per volume of the mixture, ϕ the volume fraction of the solute, and $\delta_{\text{T,S}}$ and $\delta_{\text{T,N}}$ are the so-called Hildebrand solubility parameters of the solvent (S) and solute (N), respectively, which are a measure for the cohesive energy density (the energy that is required to remove particles from the bulk to infinity). The meaning of the equation is that $\Delta H_{\text{mix}}/V_{\text{mix}}$ becomes small, when the Hildebrand parameters of the solvent and the solute have similar values.

$$\frac{\Delta H_{\mathrm{mix}}}{V_{\mathrm{mix}}} = \phi(1-\phi)\left(\delta_{\mathrm{T,S}} - \delta_{\mathrm{T,N}}\right)^2 \tag{2.5}$$

It is possible to extend equation (2.5) and to introduce the Hansen solubility parameters, δ_{D}, δ_{P}, and δ_{H}, which represent the dispersive (D), polar (P) and hydrogen bonding (H) interaction between the solute and the solvent. The Hansen parameters are linked to the Hildebrand parameters by equation (2.6), resulting in an empirical expression of $\Delta H_{\text{mix}}/V_{\text{mix}}$ as shown in equation (2.7). This equation shows that all three interaction parameters of the solute and the solvent need to match, to minimize the mixing enthalpy. Even though these equations are not formulated for dispersions of nanosheets, they can be a helpful guide for the solvent choice.

$$\delta_{\mathrm{T}}^2 = \delta_{\mathrm{D}}^2 + \delta_{\mathrm{P}}^2 + \delta_{\mathrm{H}}^2 \tag{2.6}$$

$$\frac{\Delta H_{\mathrm{mix}}}{V_{\mathrm{mix}}} \approx \phi(1-\phi)\left[\left(\delta_{\mathrm{D,S}} - \delta_{\mathrm{D,N}}\right)^2 + \frac{1}{4}\left(\delta_{\mathrm{P,S}} - \delta_{\mathrm{P,N}}\right)^2 + \frac{1}{4}\left(\delta_{\mathrm{H,S}} - \delta_{\mathrm{H,N}}\right)^2\right] \tag{2.7}$$

Solvents which are commonly used for LPE of graphene, TMDs, and other materials are *N*-methyl-2-pyrrolidone (NMP), 1-cyclohexyl-2-pyrrolidone (CHP) or *N,N*-dimethylformamide (DMF). These solvents are toxic, hard to remove due to high boiling points and can degrade during sonication, introducing impurities in the dispersion. For these reasons it is often favorable to work in environmentally friendly and non-hazardous aqueous dispersions. In this case, additives such as polymers or surfactants are required to stabilize the dispersion, since water itself is a relatively poor solvent for most nanomaterials. Commonly used surfactant candidates are sodium dodecyl sulfate (SDS) or sodium cholate (SC, Figure 2.7), which have a non-polar tail and a polar, anionic head.

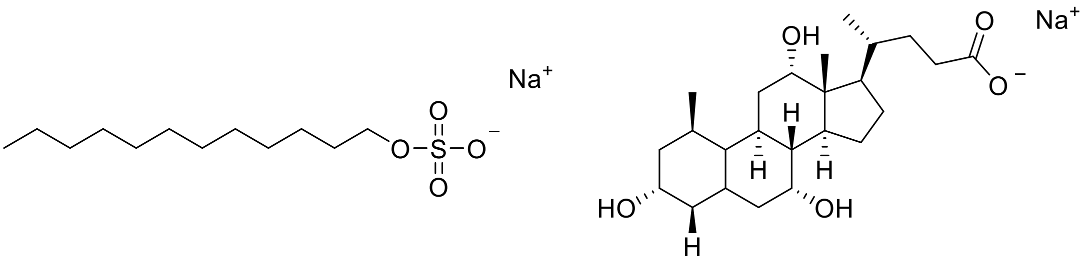

Sodium dodecyl sulfate (SDS) Sodium cholate (SC)

Figure 2.7: Molecular structure of sodium dodecyl sulfate (left) and sodium cholate (right).

According to the current understanding, the stabilization of nanoparticles occurs by the following mechanism: The non-polar and hydrophobic tail is adsorbed to the basal plane of the nanosheets and the surfactant's heads are pointing into the solution. The surfactant-loaded nanosheets are surrounded by a diffuse cloud of positively charged counterions, due to the anionic character of the surfactant's head (see Figure 2.8 A). The negative and positive charges are spatially separated and are considered as an electric double layer.

Different forces act on the nanosheets due to the electric double layer, which are attractive VdW forces, pulling the nanosheets together, and repulsive Coulomb forces, acting as antagonist of the VdW forces. The VdW forces are given by equation (2.8), where d is the distance to the particle, B is a constant and κ is related to the thickness of the double layer (κ^{-1} is the so-called Debye screening length).

The constant B depends on κ, on the geometry of the cloud of counterions, and on the zeta-potential ζ, which is the electric potential at the slipping plane of the diffuse cloud of counterions and of great importance to predict colloidal stability.

$$V_{\mathrm{VdW}}(d) = Be^{-\kappa d} \tag{2.8}$$

The repulsive Coulomb forces can be described according to Derjaguin, Landau, Verwey, and Overbeek (DLVO) by equation (2.9), where A is the so-called Hamaker constant, and r the radius of the particle.

$$V_{\mathrm{DLVO}}(d) = -\frac{Ar}{6d} \tag{2.9}$$

The combined, total interaction potential V_{T}, is given by equation (2.10) and the curve progression is illustrated in Figure 2.8 B for three different zeta-potentials.

$$V_{\mathrm{T}} = -\frac{Ar}{6d} + Be^{-\kappa d} \tag{2.10}$$

The attractive VdW forces dominate at low distance but are overcome by the repulsive Coulomb forces at intermediate distance when the zeta-potential is large enough, creating a potential barrier that stabilizes the nanosheets. If the zeta-potential is small, no potential barrier arises, and the colloidal stability of a dispersion is predicted to be low.

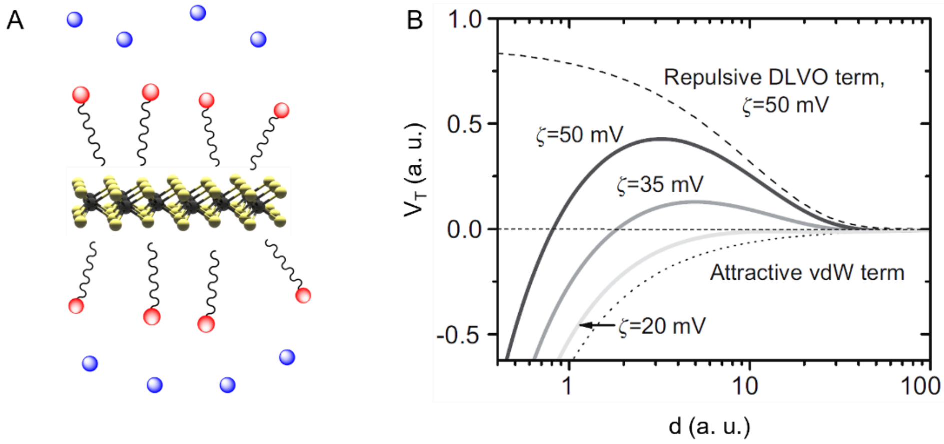

Figure 2.8: A: Illustration of a ML WS_2 nanosheet with adsorbed surfactant. The anionic heads of the surfactants (red spheres) are causing a diffuse cloud of counterions (blue spheres), surrounding the nanosheet. B: Total interaction potential as a function of the distance. At small distances, the attractive VdW forces dominate and create a negative potential but are overcome by the repulsive Coulomb forces at intermediate distance and for sufficiently high zeta-potential, creating a potential barrier that stabilizes the dispersion. Figure 2.8 B was adapted by permission from *Adv. Funct. Mater*. **2009**, 19, 3680–3695.[107] © 2009 WILEY-VCH Verlag GmbH & Co. KGaA, Weinheim.

2.3 Liquid-Cascade Centrifugation

As mentioned above, stock dispersions of LPE produced nanosheets are highly polydisperse and require size-selection techniques. Most size-selection techniques are centrifugation based, for example liquid-cascade centrifugation (LCC),[108] which is probably the most applied size-selection technique in this research area. When dispersions of nanosheets are subjected to centrifugation, the centrifugal Force F_C acts on the nanosheets and drives them towards the bottom of the tube, as given by equation (2.11), where m is the mass of the nanosheet, ω the angular velocity, and r the radius of the rotor.

$$F_{\mathrm{C}} = m\omega^2 r \tag{2.11}$$

The movement of the nanosheets is origin of additional forces, namely the buoyant force F_B and the frictional force F_F, pointing towards the opposite direction of movement and slowing down the nanosheets. As expressed by equation (2.12) and (2.13), these forces depend on the volume of the particle V, the density of the centrifugation medium ρ, the frictional coefficient f (and thus on the viscosity and the particle shape), and the velocity of the nanosheet v.

$$F_{\mathrm{B}} = m\omega^2 rV\rho \tag{2.12}$$

$$F_{\mathrm{F}} = f\nu \tag{2.13}$$

In LCC, a polydisperse stock dispersion of exfoliated nanosheets is successively centrifuged with increasing relative centrifugal force (RCF), allowing to collect sediments of different nanosheet sizes, where the size decreases with proceeding centrifugation cascade, as illustrated in Figure 2.9 with example centrifugation speeds (expressed in multiples of the earth gravitational acceleration g).

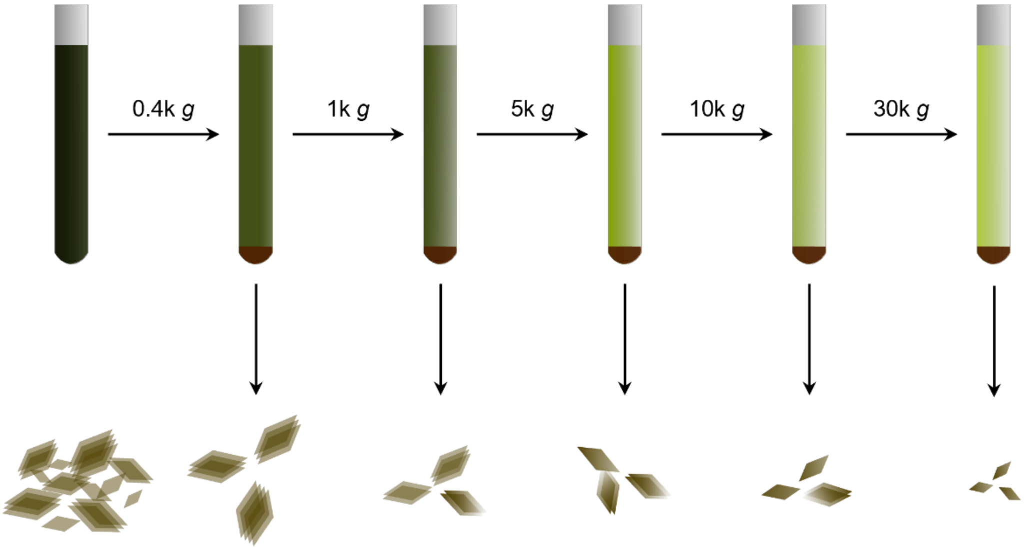

Figure 2.9: Illustration of liquid-cascade centrifugation. A stock dispersion of nanosheets is successively centrifuged with increasing centrifugation speed. The sediments are collected after each centrifugation step, resulting in nanosheet dispersions, where the nanosheet size decreases with proceeding centrifugation cascade.

A drawback of LCC is the necessity of multiple centrifugations, making the size-selection time consuming. However, this simple technique is universally applicable with inexpensive tabletop centrifuges and can efficiently separate large and thick from small and thin nanosheets.

Additionally, the individual centrifugation runs are carried out with relatively short times (~ 1–2 h) compared to other methodologies (as will be detailed below). The required centrifugation time depends on the mass of the material and the solvent, as implied in equation (2.11)–(2.13). While large nanosheets are easily isolated, it can be tedious to spin down the smallest nanosheets if heavy solvents with high viscosity are chosen. A recent model[109] of the size selection predicts that the product of time and centrifugal force is constant for a given centrifugation result, which means that for example centrifugation at 10k *g* (10,000 *g*) for 1 h is identical to centrifugation at 5k *g* for 2 h. Practically, the reduction of time by increasing the centrifugation speed is limited due to the performance of the centrifuge or (solvent) stability of the centrifugation tubes.

The size selection of nanosheets by LCC is demonstrated in Figure 2.10 with WS_2. Figure 2.10 A–C show atomic force microscopy (AFM) images of WS_2 nanosheets deposited from a stock dispersion (A), and two fractions of the size selection (B and C), isolated at relatively low and high RCF, respectively. The nanosheets deposited from the stock dispersion (A) are polydisperse with a broad distribution in the nanosheet size but are efficiently separated into large (B, early fraction of the centrifugation cascade) and small (C, late fraction of the centrifugation cascade) nanosheets after LCC. This separation is further highlighted on the example of the distribution of the nanosheet length (referring to the longest dimension of a nanosheet), as displayed in Figure 2.10 D and E. Figure 2.10 F shows the lateral dimensions of WS_2 nanosheets (expressed as the square root of the product of length L and width w of the nanosheets) as a function of the nanosheet height H. The different colors of the data points refer to different fractions after LCC. The separation of the nanosheets occurs along the dashed lines, which visualizes a second drawback of LCC: Nanosheets are predominantly separated by mass, but it is not possible to separate the nanosheets purely by the layer number.

The drawbacks of LCC are addressed by alternatives such as band sedimentation[110] or density gradient ultracentrifugation (DGU).[111, 112] In band sedimentation, the polydisperse sample is layered on top of a liquid medium with higher density. During centrifugation, the nanosheets travel towards the bottom of the tube with different velocities, depending on the nanosheet mass. The process is stopped before the nanosheets travelled the entire distance to the bottom of the vial. This allows to collect several fractions from the top, resulting in dispersions containing different nanosheet sizes after a single centrifugation run.

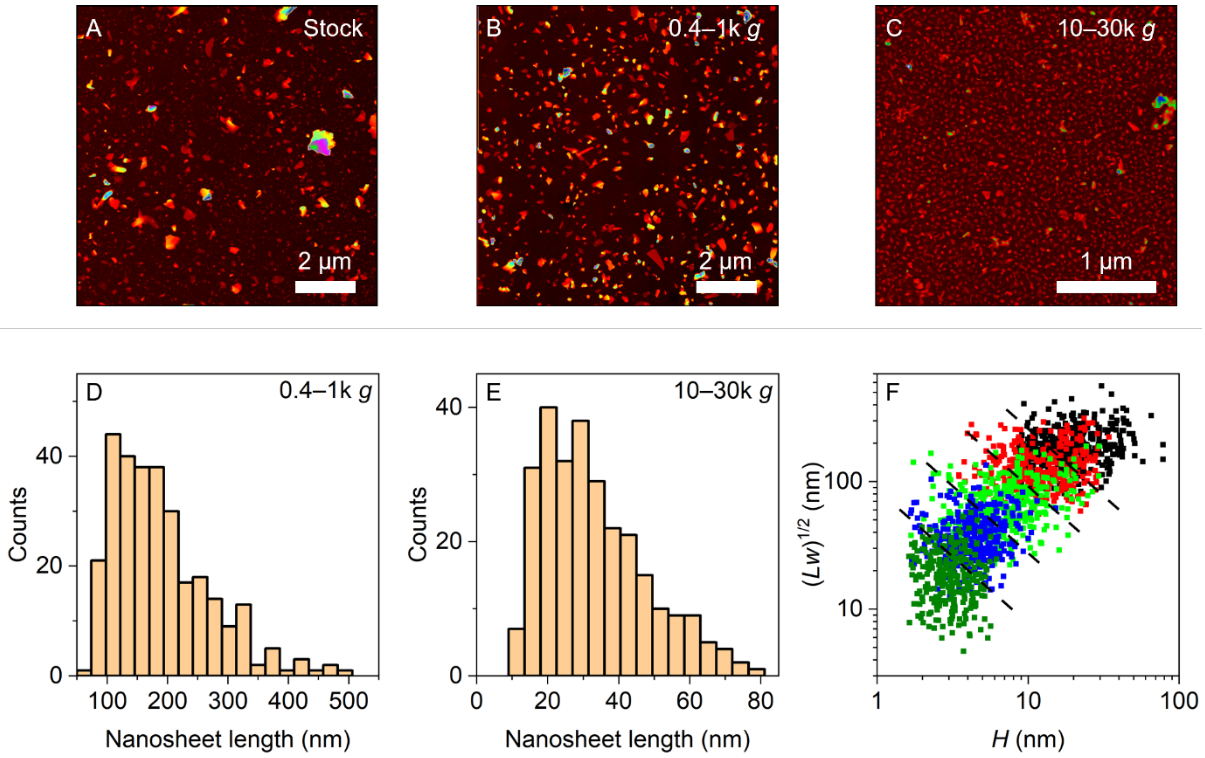

Figure 2.10: A–C: AFM images of liquid phase exfoliated WS_2 nanosheets deposited from different stages of the size selection cascade. A: As-exfoliated stock dispersion, containing nanosheets with a broad size distribution. B: Early fraction of the size selection cascade, containing large nanosheets isolated as supernatant after centrifugation at 100 *g* and sediment at 400 *g*. C: Late fraction of the size selection, containing mostly small nanosheets, isolated as supernatant after centrifugation at 10,000 *g* and sediment at 30,000 *g*. D, E: Nanosheet length distribution histogramm of the nanosheets shown in B and C. F: Lateral dimensions of the nanosheets as a function of the nanosheet height. The different colors of the data points indicate the different fractions of LCC. The dashed lines illustrate the separation of LCC.

A separation of nanosheets by layer number is possible by DGU, which separates the nanosheets according to the (layer number dependent) buoyant density. Note that – opposed to the material density – the buoyant density is dependent on the nanosheet thickness since it includes contributions from adsorbed surfactant and solvent. The polydisperse nanosheet sample is added to a centrifugation tube containing a density gradient medium and ultracentrifuged until an equilibrium state is reached. At this equilibrium point, the nanosheets do not travel further anymore since their buoyant density matches the buoyant density of the medium (isopycnic point).

However, both techniques are barely applied, since they require special equipment (centrifuge or ultracentrifuge with swinging buckets), can only process small volumes, and can suffer from aggregation problems due to the solvents e.g., chloroform in band sedimentation or aqueous solutions of salts in density gradient ultracentrifugation. Additionally, the initial sample is diluted, in the case of DGU with high concentration of an additive and the techniques can be complicated, especially when the material of interest is of high density or has a pronounced polydispersity.

2.4 Characterization of Nanosheet Dispersions

Within the course of time, different methodologies were established to characterize nanosheets of layered materials. The most reliable methods for the determination of nanosheet dimensions are based on microscopy such as transmission electron microscopy (TEM) or AFM. TEM delivers the most accurate values of the lateral nanosheet dimensions, but cannot easily provide information about the nanosheet height, which is an advantage of AFM. The measurement of lateral dimensions and differentiation between different layer numbers was also suggested by optical microscopy,[113] but all of these techniques require the deposition of nanosheets and the assessment of large numbers of sheets for a statistical evaluation of the dispersions and the extraction of mean values. Since both measurement and data evaluation of microscopic characterization is time consuming, other methods were developed, for example based on dynamic light scattering (DLS). DLS is commonly applied to determine the particle size in colloidal dispersions but cannot be directly applied to nanosheet dispersions due to the non-spherical geometry of the sheets. COLEMAN *et al*. observed a correlation between values obtained from DLS and true nanosheet dimensions,[114] allowing an estimation of the nanosheet length. In principle, also the intensity of non-resonant light scattering can be linked to the nanosheet length,[115] but this is only possible for specific materials and both methods could not establish in the field of 2D materials.

More promising and reliable characterization is based on optical extinction spectroscopy. The rich electronic properties of many materials, such as graphene,[116] TMDs,[110, 117] or *h*-BN,[64] allow the *in-situ* determination of both nanosheet length and thickness due to edge and confinement effects as well as the concentration of the dispersion. The electronic structure of nanosheets is altered in the edge region compared to the basal plane, giving rise to different absorption coefficients. This implies that the spectral shape depends on the area of the nanosheet, since the contributions of the absorption coefficients related to the edge and basal plane change with the sheet size. It was demonstrated by BACKES *et al.* that an intensity ratio of the absorbance at different wavelengths, $Abs(\lambda_1)/Abs(\lambda_2)$, is linked to the nanosheet size by equation (2.14), where α_{center} and α_{edge} are the absorption coefficients in the center and at the edge of the sheets, L is the length of the nanosheet (referred to the longest dimension), x the width of the edge region, and k the length to width aspect ratio.[110]

$$\frac{Abs(\lambda_1)}{Abs(\lambda_2)} = \frac{\alpha_{\text{center}}(\lambda_1)L + 2x(k+1)(\alpha_{\text{edge}}(\lambda_1) - \alpha_{\text{center}}(\lambda_1))}{\alpha_{\text{center}}(\lambda_2)L + 2x(k+1)(\alpha_{\text{edge}}(\lambda_2) - \alpha_{\text{center}}(\lambda_2))} \tag{2.14}$$

In solutions of small molecules, differences between extinction and absorbance are negligible but extinction spectra of nanosheet dispersions can contain a significant scattering background. However, it was demonstrated that the size dependency of intensity ratios is still encoded in the extinction despite the scattering background, allowing the calculation of the mean nanosheet length directly from extinction spectra. For example, the mean nanosheet length ⟨*L*⟩ of WS_2 can be calculated from the ratio of the extinctions at 235 nm, Ext_{235}, and 290 nm, Ext_{290}, by equation (2.15).[108] In case of MoS_2, the ratio of the extinction at 270 nm, Ext_{270}, and 345 nm, Ext_{345}, provides the information about ⟨*L*⟩ by equation (2.16).[110]

$$\langle L\rangle(\mathrm{WS_2}) = \frac{2.30 - Ext_{235}/Ext_{290}}{0.02Ext_{235}/Ext_{290} - 0.0185} \tag{2.15}$$

$$\langle L\rangle(\mathrm{MoS_2}) = \frac{2.30 - Ext_{270}/Ext_{345}}{0.02Ext_{270}/Ext_{345} - 0.0185} \tag{2.16}$$

As described in section 2.1, the band gap of TMDs exhibits a strong dependence on the nanosheet thickness. If the thickness of the nanosheet is reasonably low, the position of the A-exciton in the absorbance or extinction spectra, λ_A, can be linked to the layer number. The mean layer number ⟨*N*⟩ of the nanosheets in a dispersion is given by equation (2.17) or (2.18) in case of WS_2 or MoS_2, respectively.[108, 110, 118] The determination of nanosheet dimensions from optical extinction spectra stands out due to its simplicity and reasonable reliability, enabling studies which where otherwise not feasible due to the workload associated with microscopy statistics.[90, 119, 120]

$$\langle N\rangle(\mathrm{WS_2}) = 6.35 \cdot 10^{-32} \cdot \exp\,(\lambda_\mathrm{A}(\mathrm{nm})/8.51) \tag{2.17}$$

$$\langle N\rangle(\mathrm{MoS_2}) = 2.3 \cdot 10^{36} \cdot \exp(-54888/\lambda_\mathrm{A}) \tag{2.18}$$

For dispersions of TMDs, it was suggested that the ML content of the dispersion can be derived from other spectroscopic techniques, such as Raman spectroscopy. The Raman modes of TMDs depend on the layer number and allow identification of ML nanosheets.[121-125] While this method is suitable to prove the ML character of CVD grown, mechanically-exfoliated, or even liquid exfoliated single TMD flakes, it is quite challenging to analyze nanosheets in an ensemble.

Therefore, it was proposed to take advantage of the emerging photoluminescence, when TMDs reach the ML limit, as has been explained before. Under excitation with an appropriate laser wavelength, the ML PL becomes visible in the Raman spectrum, allowing to record Raman scattering and PL simultaneously.[126] Since all nanosheets contribute to the Raman scattering but only ML sheets have significant PL emission, it was suggested that the intensity ratio of PL to the Raman modes correlates with the ML content of a dispersion.[108, 117] However, this concept only holds if the intrinsic PL of the ML nanosheets is identical and should be applied carefully. Nevertheless, the PL/Raman ratio allows a fast assessment of the relative PL intensity of a dispersion and can be used to compare dispersions regarding their optical quality.

2.5 Strong Light-Matter Coupling

If light travels through a medium of matter, it will interact with it. In the simplest case, only the speed of light is changed. However, if the frequency of a photon is resonant to an optical transition, the photon can get absorbed and excite the matter, e.g., when the absorption of a photon leads to the formation of an exciton in a semiconducting material. The excited matter (i.e., the exciton) can decay radiatively and emit a photon that propagates away from the matter. Under most circumstances, the system is in the weak coupling regime – a regime, where these processes are irreversible and where the photon or exciton preserve their individual properties. The situation can change when matter is placed into an optical resonator, such as an optical microcavity, which is in resonance with the absorber/emitter. Even without a photon in the resonator, the presence of the vacuum field can interact with the emitter, for example by increasing the rate of spontaneous emission (Purcell effect). If an exciton in a resonator decays radiatively, the emitted photon gets reflected by the mirrors and multiple reabsorption by the emitter is possible, until the exciton decays non-radiatively or the photon escapes the resonator. However, if the energy exchange between emitter and photon is faster than the loss rates, the system undergoes a transition to the strong coupling regime, where differentiation between excitons and photons becomes impossible and where new quasi particles form: The (exciton-) polaritons. Polaritons are hybrid quasi particles with Bosonic nature, consisting of light and matter and giving rise to unique properties such as superfluidity or Bose-Einstein condensation. The following part will provide a detailed description of the building blocks and formation of polaritons, with orientation on books written by Kalt and Klingshirn[127] and Iman.[128]

Photons in a Microcavity

In the simplest case, an optical microcavity can be pictured as two planar, opposite mirrors which are separated by the distance L_{cav}. Light fulfilling the resonance condition $L_{\mathrm{cav}} = m \cdot \lambda_{\mathrm{C}}/2$ can form a standing wave between the mirrors, where m is an integer number and λ_{C} the effective wavelength inside the cavity (see Figure 2.11 A for illustration). For simplicity reasons, m is considered as 1 in the following section, referring to the ground mode of the cavity.

In vacuum, photons follow a linear dispersion relation with $E = \left(\frac{\mathrm{hc_0}}{\lambda_0} = \mathrm{h}\nu\ =\right) \hbar\omega = \hbar \mathrm{c_0}|\mathbf{k}|$, where h is the Planck constant, $\mathrm{c_0}$ the speed of light in vacuum, λ_0 the vacuum wavelength of the light, ν the frequency of the light, ħ the reduced Planck constant, ω the angular frequency of the photon, and $\mathbf{k}$ the wavevector. The situation changes inside the cavity, where photons can propagate freely within the plane parallel to the mirrors but are confined in the perpendicular direction, resulting in an angular dependency of the energy. This is commonly described by a separation of the wavevector **k** into a transversal (parallel to the mirrors) and a longitudinal (perpendicular) component of the wavevector, $\mathbf{k}_{\parallel}$ and $\mathbf{k}_{\perp}$ (see Figure 2.11 B).

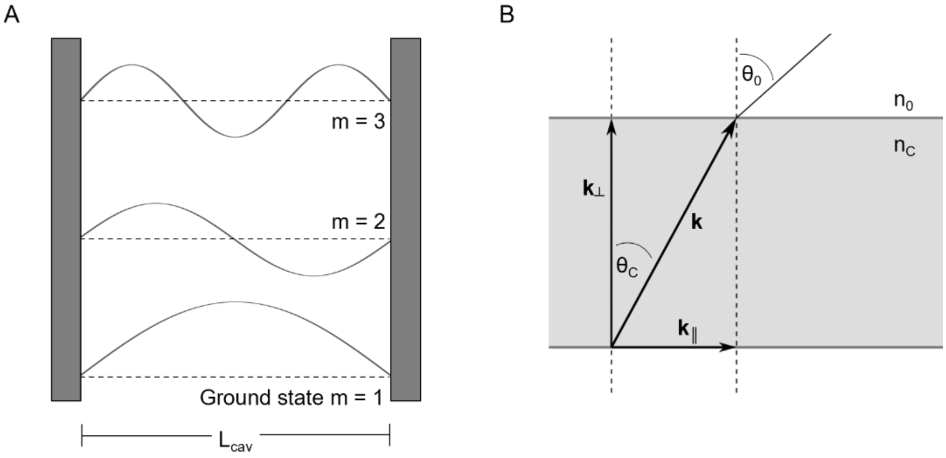

Figure 2.11: A: Light confined between two planar mirrors, forming standing waves fulfilling the condition $L_{\text{cav}} = 2m\lambda_{\text{C}}$. The different resonance modes are vertically offset for clarity. B: Illustration of the wavevector **k**, confined in an optical microcavity with the refractive indices n_{C} and n_0 inside and outside the cavity, which is split into transversal and longitudinal components $\mathbf{k}_{\parallel}$ and $\mathbf{k}_{\perp}$.

At an angle of zero-degree, **k** is $\mathbf{k}_{\perp}$ and defined by the distance of the mirrors with $|\mathbf{k}_{\perp}| = k_{\perp} = \frac{\pi}{L_{\text{cav}}} = \frac{2\pi}{\lambda_{\text{C}}} = \frac{2\pi n_{\text{c}}}{\lambda_0}$, where n_{c} is the effective refractive index of the cavity and λ_0 the vacuum wavelength of the photon. Under non-zero angles of observation, the transversal component of the wavevector sets in and can be expressed as a function of $\mathbf{k}_{\perp}$ and the angle θ_{C} (see Figure 2.11 B) by equation (2.19).

$$k_{||} = k_{\perp}\tan\left(\theta_{\text{C}}\right) \tag{2.19}$$

Please note that θ_{C} is different from the experimentally accessible angle of observation θ_0 due to refraction that occurs when photons escape the mirror. θ_{C} and θ_0 are linked by Snell's law, $n_0\sin(\theta_0) = n_{\text{C}}\sin(\theta_{\text{C}})$, resulting in equation (2.20).

$$k_{||} = k_{\perp}\tan\left(\arcsin\left(\frac{n_0\sin(\theta_0)}{n_{\text{c}}}\right)\right) = \frac{2\pi n_{\text{C}}}{\lambda_0}\tan\left(\arcsin\left(\frac{n_0\sin(\theta_0)}{n_{\text{c}}}\right)\right) \tag{2.20}$$

The final energy dispersion of the cavity photon is given by equation (2.21) and exhibits an approximately parabolic shape if $\mathbf{k}_{\parallel}$ is small.

$$E_{\text{C}}(\mathbf{k}) = \frac{\hbar c_0}{n_{\text{C}}}|\mathbf{k}| = \frac{\hbar c_0}{n_{\text{C}}}\sqrt{k_{\perp}^2 + k_{||}^2} \tag{2.21}$$

For practical reasons, it is convenient to express the energy E_{C} as a function of $\mathbf{k}_{\perp}$ or E_0 (energy at zero degree) since these values are accessible from experimental data. The relation

k = $\mathbf{k}_\perp$ $*$ 1/cos(θ_C) leads to equation (2.22), or equation (2.23) if the internal angle is correlated with the external angle of view.

$$E_\mathrm{C} = \frac{\mathrm{hc}_0}{2\pi} * k = \frac{\mathrm{hc}_0}{2\pi} * k_\perp * \frac{1}{\cos(\theta_\mathrm{C})} = E_0 * \frac{1}{\cos(\theta_\mathrm{C})} \tag{2.22}$$

$$E_\mathrm{C} = E_0 * \frac{1}{\cos(\theta_\mathrm{C})} = 1/\cos(\arcsin\left(\frac{n_0 \sin(\theta_0)}{n_\mathrm{c}}\right)) \tag{2.23}$$

Since the mirrors of optical microcavities have a finite reflectivity R, photons will escape and have a limited lifetime τ_C in the cavity. The lifetime of the photons is related to the reflectivity of the mirrors by equation (2.24) and has a direct impact on the linewidth of the cavity mode, γ_C (equation (2.25)), due to the Heisenberg's uncertainty principle.

$$\frac{1}{\tau_\mathrm{C}} \propto \frac{1-R}{\sqrt{R}} \tag{2.24}$$

$$\frac{1}{\tau_\mathrm{C}} \leq \frac{\gamma_\mathrm{C}}{\hbar} \tag{2.25}$$

In literature, the quality factor Q of microcavities is commonly determined. It is derived from the photon's lifetime and calculated from the energy of the cavity mode and its linewidth by equation (2.26). Concretely, the quality factor describes how many round trips a photon makes inside a cavity before it escapes.

$$Q = \frac{E_\mathrm{C}}{\gamma_\mathrm{C}} = \frac{E_\mathrm{C}\tau_\mathrm{C}}{\hbar} \tag{2.26}$$

Excitons

Excitons typically form when light is absorbed by semiconductors. A negatively charged electron is excited from the valence band into the conduction band, leaving a positive hole behind. If the momenta of the electron and hole are small enough, Coulomb interactions can lead to a bound state of the electron and hole pair, named exciton, which can often be described analogously to a hydrogen atom. The energies of the electron or the hole, $E_\mathrm{e}(k)$ and $E_\mathrm{h}(k)$, can be described by equation (2.27) and (2.28), respectively, where E_g is the energy band gap of the lattice material, $m_\mathrm{e,eff}$ and $m_\mathrm{h,eff}$ are the effective masses of the excited electron and the hole, and k is the wave vector of the particle.

$$E_\mathrm{e}(k) = E_\mathrm{g} + \frac{\hbar^2 k^2}{2m_\mathrm{e,eff}} \tag{2.27}$$

$$E_\mathrm{h}(k) = \frac{\hbar^2 k^2}{2m_\mathrm{h,eff}} \tag{2.28}$$

The total energy of the exciton in three-dimensional space is given by equation (2.29), with the binding energy of the exciton $E_{\text{bind,i}}$, the wave vector of the center-of-mass motion **K**, and the effective mass of the exciton $m_{\text{X,eff}} = m_{\text{e,eff}} + m_{\text{h,eff}}$.

$$E_{\mathrm{X}}(k, i) = E_{\mathrm{g}} - E_{\text{bind,i}} + \frac{\hbar^2 \mathbf{K}^2}{2m_{\text{X,eff}}} \tag{2.29}$$

The binding energy of the exciton can be expressed by equation (2.30), using Bohr's model of the hydrogen atom, where m_{r} is the reduced mass of the exciton ($m_{\mathrm{r}} = m_{\text{e,eff}}*m_{\text{h,eff}}/m_{\text{X,eff}}$), i the quantum number of the hydrogenic system, and $a_{\mathrm{B,X}}$ the Bohr radius, given by equation (2.31) with the relative dielectric constants in the crystal and in vacuum, ε_{r} and ε_0, and the elementary charge e.

$$E_{\text{bind,i}} = \frac{\hbar^2}{2m_{\mathrm{r}} i^2 a_{\mathrm{B,X}}^2} \tag{2.30}$$

$$a_{\mathrm{B,X}} = \frac{4\pi\hbar^2 \varepsilon_{\mathrm{r}} \varepsilon_0}{m_{\mathrm{r}} \mathrm{e}^2} \tag{2.31}$$

If excitons become restricted in their motion of freedom, for example in a quantum well where a semiconductor is sandwiched between two insulating materials, the eigen-energies and wavefunctions are altered by the confinement. This results in increased binding energies and oscillator strength, which is a measure of the likelihood that an absorbed photon will form an exciton. Restricted in one dimension, the wavevector of the exciton can be split into two components, $\mathbf{k} = \mathbf{k}_{||} + \mathbf{k}_{\perp}$, with $\mathbf{k}_{||} = k_{\mathrm{x}}\mathbf{e}_{\mathrm{x}} + k_{\mathrm{y}}\mathbf{e}_{\mathrm{y}}$ (with the unit vectors $\mathbf{e}_{\mathrm{x/y/z}}$), analogously to the wavevector of a photon in an optical microcavity. The energy of the 2D exciton is approximated by equation (2.32), where $\Delta E_{\mathrm{e,h}}(d)$ is the difference in the energy level of the 2D electron and hole, and $E_{\text{bind,i}}^{(\text{3D})}$ the binding energy in the 3D space, which gets increased by a factor of 4 times by the confinement.

$$E_{\mathrm{X}}(\mathbf{k}, i) = \Delta E_{\mathrm{e,h}}(d) - 4E_{\text{bind,i}}^{(\text{3D})} + \frac{\hbar^2 \mathbf{k}_{||}^2}{2m_{\text{X,eff}}} \tag{2.32}$$

Strong Light-Matter Coupling

A relatively simple approach to describe the interaction between photons and excitons is the semi-classical coupled oscillator model, where both the photon and the exciton resonance are pictured as harmonic oscillator with orthogonal degrees of freedom, exchanging energy. The fundamental vectors of the exciton and the photon, $|X\rangle$ and $|C\rangle$, are $|X\rangle = \begin{pmatrix} 0 \\ 1 \end{pmatrix}$ and $|C\rangle = \begin{pmatrix} 1 \\ 0 \end{pmatrix}$.

For a mathematical description of a polaritonic system, the polaritonic Hamiltonian $\widehat{H}_{\mathrm{xp}}$ can be considered as the sum of the photonic and excitonic Hamiltonian, $\widehat{H}_{\mathrm{P}}$ and $\widehat{H}_{\mathrm{X}}$, and an interaction Hamiltonian $\widehat{H}_{\mathrm{i}}$ (equation (2.33)), which are given by equation (2.34) to (2.36), with the interaction energy ħΩ, the creation operators of the resonator field and emitter, $\hat{f}^{\dagger}$ and $\hat{e}^{\dagger}$, and the corresponding annihilation operators, $\hat{f}$ and $\hat{e}$. The interaction energy involves the so-called Rabi frequency Ω, which is the dipole interaction frequency, and is commonly named coupling strength or coupling constant g (with g = ħΩ).

$$\hat{H}_{\mathrm{xp}} = \hat{H}_{\mathrm{P}} + \hat{H}_{\mathrm{X}} + \hat{H}_{\mathrm{i}} \tag{2.33}$$

$$\hat{H}_{\mathrm{P}} = E_{\mathrm{C}}\hat{f}^{\dagger}\hat{f} \tag{2.34}$$

$$\hat{H}_{\mathrm{X}} = E_{\mathrm{X}}\hat{e}^{\dagger}\hat{e} \tag{2.35}$$

$$\hat{H}_{\mathrm{i}} = \hbar\Omega(\hat{f}^{\dagger}\hat{e} + \hat{f}\hat{e}^{\dagger}) \tag{2.36}$$

Since strong light-matter coupling comes with the formation of new quasi particles, new Hamiltonians with new creating and annihilation operators, $\hat{l}^{\dagger}_{k_{\parallel}}$ or $\hat{u}^{\dagger}_{k_{\parallel}}$, and $\hat{l}_{k\parallel}$ or $\hat{u}_{k\parallel}$, are defined by equation (2.37) and (2.38), referring to the lower (l) or upper polariton (u). In these equations, X and C are coefficients describing the contributions from the excitons or photons.

$$\hat{l}_{\mathrm{k}_{\parallel}} = X_{k_{\parallel}}\hat{e}_{\mathrm{k}_{\parallel}} + C_{k_{\parallel}}\hat{f}_{k_{\parallel}} \tag{2.37}$$

$$\hat{u}_{k_{\parallel}} = C_{k_{\parallel}}\hat{e}_{k_{\parallel}} + X_{k_{\parallel}}\hat{f}_{k_{\parallel}} \tag{2.38}$$

These equations allow for the description of the polaritons by the linear Hamiltonian shown in equation (2.39).

$$\hat{H}_{\mathrm{xp}} = \sum_{\mathrm{N},k_{\parallel}} E_{\mathrm{LP}}\left(k_{\parallel}\right)\hat{l}^{\dagger}_{k_{\parallel}}\hat{l}_{k_{\parallel}} + \sum_{\mathrm{N},k_{\parallel}} E_{\mathrm{UP}}(k_{\parallel})\hat{u}^{\dagger}_{k_{\parallel}}\hat{u}_{k_{\parallel}} \tag{2.39}$$

In matrix representation, the Hamiltonian can be approximated by:

$$\hat{H}_{\mathrm{xp}} = \begin{pmatrix} E_{\mathrm{C}} & \hbar\Omega \\ \hbar\Omega & E_{\mathrm{X}} \end{pmatrix} \tag{2.40}$$

Diagonalization of the matrix results in new eigen-vectors associated with the polaritons, given by equation (2.41).

$$\begin{pmatrix} E_{\mathrm{C}} & \hbar\Omega \\ \hbar\Omega & E_{\mathrm{X}} \end{pmatrix}\begin{pmatrix} C_{\mathrm{i}} \\ X_{\mathrm{i}} \end{pmatrix} = E_{\mathrm{xp}}\begin{pmatrix} C_{\mathrm{i}} \\ X_{\mathrm{i}} \end{pmatrix} \tag{2.41}$$

As mentioned above, X_{i} and C_{i} describe the contributions from the excitons or photons. The squares of their absolute value, $|C_{\mathrm{i}}|^2$ and $|X_{\mathrm{i}}|^2$, are the so-called Hopfield coefficients, and fulfill the condition $|C_{\mathrm{i}}|^2 + |X_{\mathrm{i}}|^2 = 1$. The Hopfield coefficients depend on the detuning of the photonic and excitonic resonances, defined by equation (2.42), and the angle of observation, reflected in $k_{\parallel}$.

$$\Delta\left(k_{\parallel}\right) = E_{\mathrm{C}}\left(k_{\parallel}\right) - E_{\mathrm{X}}(k_{\parallel}) \tag{2.42}$$

Figure 2.12 A pictures these dependencies: At zero detuning and zero transversal component of **k**, the Hopfield coefficients are $|C_{\mathrm{i}}|^2 = |X_{\mathrm{i}}|^2 = 0.5$, and the contribution of the photon and exciton to the polariton is equal. With increasing $k_\parallel$, the lower polariton (LP) becomes excitonic and the upper polariton (UP) photonic. At negative detuning, an inversion of the polaritonic character is observed with changing angle of observation. The LP is mostly of photonic nature for $k_\parallel = 0$ but becomes excitonic with rising $k_\parallel$, whereas the UP shows the opposite trend. At positive detuning, the lower and upper polariton remain mostly excitonic or photonic over all angles, respectively.

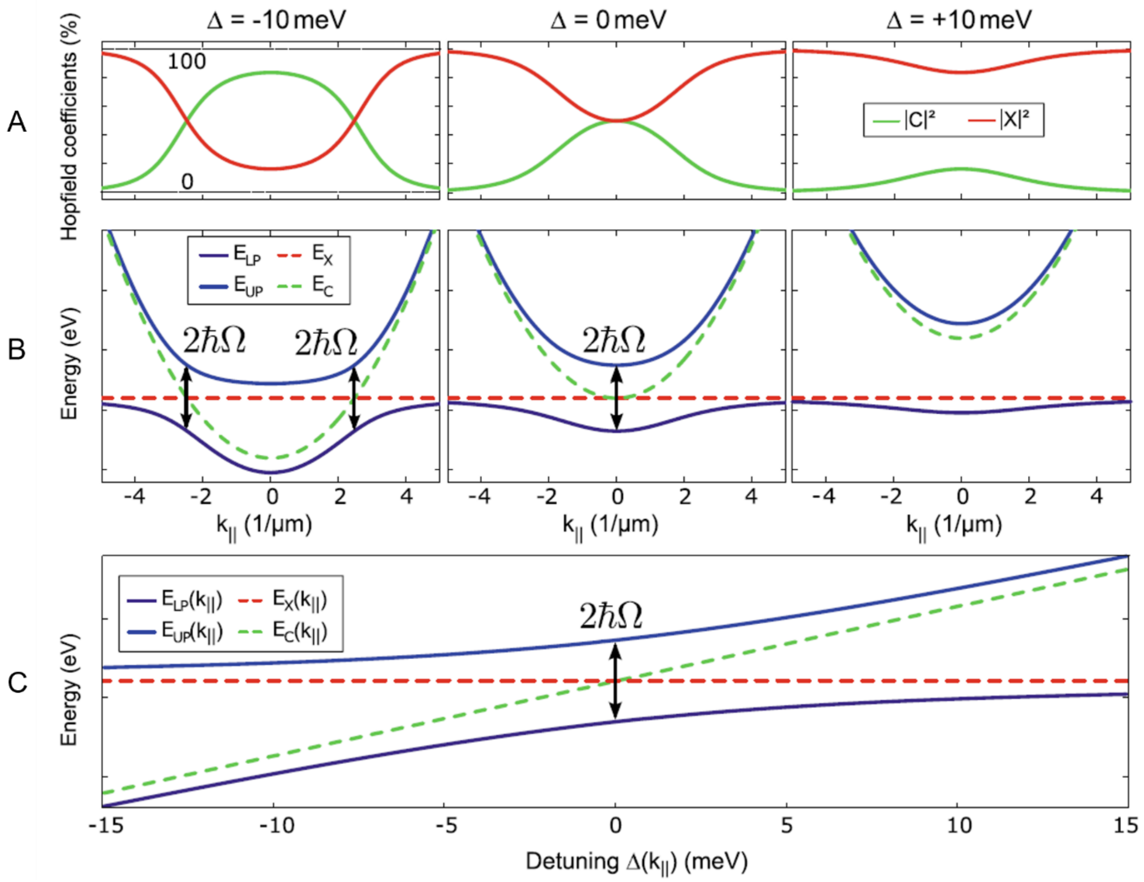

Figure 2.12: A, B: Hopfield coefficients (A) and polariton dispersions (B) at negative, zero, and positive detuning of the photon and exciton resonance. C: Rabi splitting as a function of the detuning, featuring an anti-crossing of the polariton modes, characteristic for the strong coupling regime. Reprinted by permission from *Fundamentals of Polariton Physics, in Polariton Physics: From Dynamic Bose–Einstein Condensates in Strongly-Coupled Light–Matter Systems to Polariton Lasers, Springer International Publishing: Cham,* **2020**; pp 33-64.[128] © 2020 Springer Nature Switzerland AG.

This behavior is further highlighted by the dispersions of the polaritons, as illustrated in Figure 2.12 B. Characteristic for the polaritonic dispersions is the observed anti-crossing or avoided crossing of the polaritonic modes, which separates the modes by the so-called Rabi splitting $2\hbar\Omega$ (at $k_\parallel = 0$). The relation between Rabi splitting and detuning is illustrated in Figure 2.12 C, highlighting the beforementioned anti-crossing.

The eigen-energies of the polaritons, E_{LP} and E_{UP}, correspond to the eigen-values of the diagonalized matrix $\widehat{H}_{\mathrm{xp}}$ and are given by equation (2.43). However, this equation is simplified and factors such as the lifetime of the photons or excitons, reflected in their linewidth, are not taken into account, despite having an impact on the eigen-energies of polaritons. Nevertheless, equation (2.43) can be considered as reasonable approximation, if $\hbar\Omega \gg \gamma_\mathrm{C} \gg \gamma_\mathrm{X}$, where γ_C and γ_X are the linewidths of the photon and exciton modes. If this condition is not fulfilled, equation (2.43) can be extended to equation (2.44). This equation implies another important condition that must be fulfilled, to observe strong coupling. The term inside the square root only becomes positive and hence real, if $2\hbar\Omega > |(\gamma_\mathrm{C} - \gamma_\mathrm{X})|$. In simple words this means that strong coupling can be observed, when the splitting of the modes is larger than their linewidth, or that the interaction between the photon and exciton oscillator is faster than their decoherence. In practical work, this condition is simplified to $2\hbar\Omega > \gamma_\mathrm{C}$, since the loss rates of photons are commonly dominant.

$$E_\mathrm{LP,UP}\left(k_\parallel\right) = \frac{1}{2}\left[E_\mathrm{C}\left(k_\parallel\right) + E_\mathrm{X}\left(k_\parallel\right) \mp \sqrt{(2\hbar\Omega)^2 + \left(E_\mathrm{C}\left(k_\parallel\right) - E_\mathrm{X}\left(k_\parallel\right)\right)^2}\right] \tag{2.43}$$

$$E_\mathrm{LP,UP}\left(k_\parallel\right) = \frac{1}{2}\left[E_\mathrm{C}\left(k_\parallel\right) + E_\mathrm{X}\left(k_\parallel\right) + i(\gamma_\mathrm{C} + \gamma_\mathrm{X}) \mp \sqrt{(2\hbar\Omega)^2 + \left(\Delta\left(k_\parallel\right) + i(\gamma_\mathrm{C} - \gamma_\mathrm{X})\right)^2}\right] \tag{2.44}$$

3 Objectives

As elucidated in the introduction of this thesis, the chemistry and physics of two-dimensional materials gained tremendous interest over the last decade. One class of materials that are focus of ongoing research due to their rich electronic properties are ML TMDs, which show light emission when the crystals are thinned down to the ML limit. One of the research areas where TMDs have been employed and that has recently evolved to a new field within chemistry is strong light-matter coupling, where new hybrid light-matter quasi particles are formed. However, most applications of TMDs have been restricted to single flakes of TMDs. For example, to the author's best knowledge, no strong coupling has been demonstrated with homogenous thin films of WS_2 nanosheets.

This leads to the goal of this thesis: To prepare thin films of two-dimensional materials for optical applications with the ultimate goal to prove strong light-matter coupling and the formation of exciton-polaritons in homogenous thin films of WS_2. To accomplish this goal, several steps are required: First, the investigation and optimization of the liquid phase exfoliation to start the film preparation with the best conditions possible. Second, the preparation and characterization of high-quality WS_2 thin films. Here, films with high optical density are required, where the preservation of the PL and the morphology of the film surface are of great importance. Various thin film preparation methods such as spin coating of TMD/polymer composite films or the deposition of Langmuir films need to be tested and assessed regarding their usability for optical microcavities. The last step is the preparation of optical microcavities with optimized WS_2 films as semiconductor, where several cavity designs are possible. The formation of exciton polaritons needs to be proven by the dispersion of the polaritonic modes.

Additionally, it should be kept an eye out for other materials, that are less explored than TMDs but might be suitable for optoelectronic applications. This involves the exfoliation and characterization of the materials and design of potential devices.

4 Results and Discussion

4.1 Optimization of Liquid phase Exfoliation

4.1.1 Introduction

A common saying states that every journey begins with a single step. In the field of 2D materials this step is often the production and in this case the exfoliation of layered materials in the liquid phase, which becomes the foundation for further processing and potential applications. This means that the outcome of LPE naturally restricts the outcome of all consecutive steps. For example, the quality of nanosheet thin films will never exceed the quality of the nanosheets in dispersion, and a poor nanosheet thin film will never be turned into a good device. This implies that the LPE process is of great importance and that one should always aim for improvements to begin the journey with the best conditions possible.

One of the major drawbacks of sonication-assisted LPE which has not been overcome yet is that nanosheets are comparatively small in their lateral dimensions (~ 100–200 nm for graphene and < 50 nm for TMDs). A recent exfoliation model[94] suggests that the aspect ratio of LPE produced nanosheets is a result of the intra- and interlayer binding strength of the bulk crystal. This implies that the dimensions of the exfoliated sheets are characteristic for the material and that the lateral dimensions of the nanosheets are intrinsically limited by the material's crystal structure. However, the exfoliation is a complex process, and the relatively simple exfoliation model neither considers potential influences of defects nor predicts optical properties of the nanosheets. Especially the role of defects and imperfections of the bulk crystal is currently still unclear. While LPE produced nanosheets are considered as widely free of basal plane defects,[129, 130] defects on exfoliated nanosheets have been observed for graphite/graphene.[131-133]

In the past, many attempts have been made to optimize the LPE process and the influence of surfactant choice and concentration,[90] tip sonication parameters,[91, 92] vessel diameter and filling height,[99] and cavitation type[98] have been subject of investigation. Despite the large variety of studies, a full understanding of the LPE process is still not yet accomplished. For example, the impact of the starting material on the outcome of LPE has not been sufficiently assessed. Some studies on graphite[134, 135] indicate that the graphite source impacts the dispersibility[134] of the bulk material as well as the stability and size distribution of exfoliated nanosheet dispersions.[135] Similar observations were made for the exfoliation of graphene oxide[136] and molybdenum minerals,[137] where variations in yield, nanosheet size and exfoliation rate have been observed. These findings are partly in contrast to the exfoliation model mentioned above.[94] However, the methodology of these studies has not been ideal, which limits the significance of the results. For example, the exfoliation was conducted under low energy conditions and no size selection was executed after exfoliation which complicates the characterization of the dispersion. Additionally, some questions remain untouched and neither the important nanosheet aspect ratio nor interesting optical properties such as the PL of ML MoS_2 were subject of the investigations.

While knowledge about the natural impact of the starting material would help to purchase the most suitable bulk materials available, the question arises whether artificial improvements of the LPE process are possible. For example, one could imagine to decrease the out-of-plane binding strength of the bulk material, which should lead to nanosheets with increased relative lateral dimensions according to theoretical predictions.[94] This approach was proposed in the context of surfactant-assisted LPE, where the intercalation or molecular wedging of 1-pyrenecarboxylic acid (PCA) into graphite in combination with bath sonication was suggested as efficient exfoliation strategy.[138] Even though a recent study[139] questions this mechanism, intercalation of Li-ions or electrolytes is applied in chemical or electrochemical exfoliation, resulting in nanosheets which are significantly larger in their lateral dimensions than nanosheets exfoliated by sonication-assisted LPE.[140-142] However, the downside of these exfoliation methods are aggressive chemicals (*n*-BuLi, H_2SO_4), introduction of defects and alteration of properties. For example, the Li-intercalation of TMDs is accompanied by a phase transition to the metallic 1T phase and thus by loss of the photoluminescence and requires annealing to restore the semiconducting properties.[142]

This chapter aims for further optimization of LPE and addresses both the question in which way the starting material impacts the quality and quantity of LPE produced nanosheet dispersions and whether the LPE process can be improved by intercalation agents. First, the impact of the starting material is investigated on the example of MoS_2 due to the wide range of commercially available MoS_2 materials. Six MoS_2 bulk materials containing different crystallite sizes, impurities and defects have been exfoliated and the nanosheet dimensions as well as optical properties of the dispersions were characterized. In contrast to other studies, the bulk material is first purified and the exfoliated stock dispersions subjected to centrifugation-based size selection, facilitating the characterization and providing a more comprehensive and detailed picture. In a second study, it was investigated whether aspect ratios and optical properties of LPE produced nanosheets can be altered by simple pretreatment methods applied to bulk materials prior to exfoliation. These experiments aim towards intercalation of the pretreatment agents, lowering the interlayer binding strength. The study was executed on WS_2, since its optical properties allow a straightforward assessment of both nanosheet dimensions and optical properties such as relative PLQY.

4.1.2 Preparation of TMD Nanosheet Dispersions

This subchapter explains the preparation of the TMD nanosheet dispersions used in this and following chapters and will provide all relevant information to understand the experimental procedures.

The nanosheet dispersions were prepared by sonication-assisted LPE, where sonication is used to overcome the interlayer binding energies of layered crystals and to exfoliate the crystals. The exfoliation was carried out in aqueous surfactant media and the exfoliation protocol is illustrated in Scheme 4.1 A. Bulk powders of TMDs were dispersed in aqueous SC-solution (8 g/L) and tip sonicated for 1 h. This relatively short sonication does not lead to complete exfoliation of the bulk materials but breaks up crystallites and releases impurities into the SC-solution. The dispersions were centrifuged at a relative centrifugal force (RCF) between ~ 4k and ~ 8k *g* (4,000 and 8,000 *g*, where *g* is the earth gravitational acceleration), leading to sedimentation of the relatively heavy TMD particles. The impurities mostly remain in the supernatant which is discarded after the centrifugation. The TMD sediments were redispersed in fresh SC-solution and subsequently sonicated again for ~ 5–7 h to complete the exfoliation process. The dispersions were not continuously exposed to sonication since this would lead to overheating of the dispersion, which should be avoided. Instead, pulsed sonication was applied with on and off times about 8s/2s for the first, short sonication and 6s/4s for the second, long sonication. As will be demonstrated later, the sonication amplitude should be kept at 60 %, since exfoliation at lower energies decreases the dispersion quality.

As explained in chapter 2.3, stock dispersions of liquid exfoliated nanosheets are polydisperse with a broad distribution in nanosheet size and thickness, and size selection techniques are required before characterization or further processing of the dispersion. In this thesis, liquid-cascade centrifugation (Scheme 4.1 B) was applied. In a first step, the stock dispersions were centrifuged at low speeds such as 0.4k *g* (400 *g*). The resulting sediments were discarded since they mostly contain unexfoliated material. The supernatants were successively centrifuged again with increasing centrifugal acceleration. A typical centrifugation cascade applied in this work involves steps at 0.4k, 1k, 5k, 10k, and 30k *g*, but deviations from this cascade are possible and depend on the purpose of the experiment. The sediments of these centrifugation steps were collected and dispersed in a defined volume of fresh SC-solution (0.1 g/L). The supernatants of the last centrifugation step at 30k *g* were discarded, since they only contain the undesired, smallest nanosheets of the exfoliation with altered photoluminescence.

The sediments were labelled according to the centrifugation boundaries, as will be explained on the example cascade mentioned above: The first collected sediment (collected after centrifugation at 1k *g*) is labelled as 0.4–1k *g*, the second sediment collected at 5k *g* is labelled as 1–5k *g*, and so forth. To visualize the results of the characterization, the samples are often referred to the midpoint of the centrifugation boundaries (central RCF), which is 0.7k *g* in case of the sample 1–5k *g*, and 3k *g* in case of the sample 1–5k *g*. With proceeding size selection cascade, both the lateral nanosheet size and the nanosheet thickness decreases, as described in chapter 2.3. While the fractions isolated at high centrifugal force are commonly most relevant, since they contain a larger population of monolayers, fractions isolated at the beginning of the cascade can be important as well depending on the purpose.

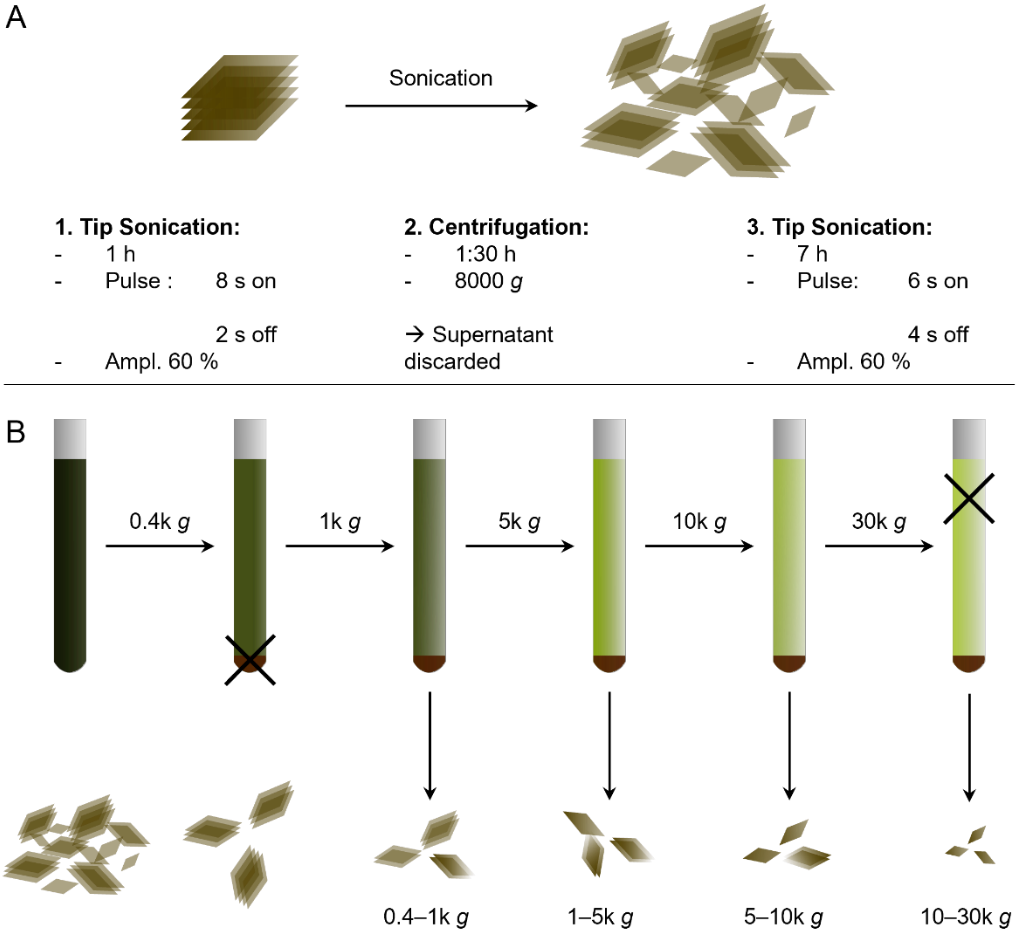

Scheme 4.1: Exfoliation and size selection protocol applied in this thesis. A: Sonication-assisted LPE, executed in three steps including relatively short tip sonication to break up crystallites and release impurities, a centrifugation to spin down the TMD nanosheets, and a long tip sonication to conduct the exfoliation. B: LCC including centrifugation steps of 0.4k, 1k, 5k, 10k, and 30k *g*. The sediment of the first centrifugation and the supernatant of the last centrifugation step were discarded, since they only contain unexfoliated material or the undesired smallest nanosheets of the exfoliation, respectively.

4.1.3 Impact of the MoS_2 Starting Material on the Dispersion Quality and Quantity after Liquid phase Exfoliation

As elucidated in the introduction, this subchapter aims to resolve the question whether the choice of starting material has an impact on the yield, nanosheet dimensions or optical properties of nanosheet dispersions produced by sonication-assisted LPE. The study was executed on six different commercially available MoS_2 bulk materials, including powders from Sigma Aldrich with specified particle size of 6 µm (SA6), 2 µm (SA2) and 90 nm (SAnp), powders from Tribotecc (Tribo) and Alfa Aesar (AA), and a MoS_2 single crystal from SPI supplies (Crystal) which was pestled before use. The data of this study have been published before[119] and were acquired with experimental support from Dr. Farnia Rashvand (SEM), Dr. Vaishnavi J. Rao (XRD), and Nadja Wolff (sample preparation and characterization).

Characterization of the Bulk Materials

The bulk materials were analyzed by scanning electron microscopy (SEM, Figure 4.1), energy dispersive X-ray spectroscopy (EDX, Table A 1–Table A 6) and powder X-ray diffraction (XRD, Figure 4.2) before any further processing.

Figure 4.1 shows SEM images of the different starting materials, highlighting the layered structure of MoS_2. The lateral dimensions of the particles were measured from these images and are summarized in Figure A 1 (Appendix). While this method does not result in a reliable or precise statistic, it allows a qualitative comparison of the particle size. The largest particles were found in the pestled crystal (up to ~ 350 µm), followed by AA, Tribo and SA6. In agreement with the supplier's information SA2 and SAnp contain the smallest particles. The lateral dimensions of SAnp partly appear transparent in the SEM images (Figure 4.1 E), indicating that the particles are relatively thin.

The results of the elemental analysis by EDX are summarized in Table A 1–Table A 6 in the Appendix. To reduce the impact of observed spot-to-spot variations, five different spots were measured and averaged. From these data the S:Mo stoichiometry was extracted and is presented in the Appendix (Table A 7). The different stoichiometries can be considered as an indicator for different amounts of point defects, such as sulfur vacancies (V_S) or molybdenum vacancies (V_{Mo}).[143, 144] The elemental analysis further revealed different amounts and kinds of impurities, including period 4 transition metals as well as Y, Pb, F, which might impact the outcome of the exfoliation. However, due to the spot-to-spot variations mentioned above, a large number of measurements would be required to draw ultimate conclusions and results should be treated carefully.

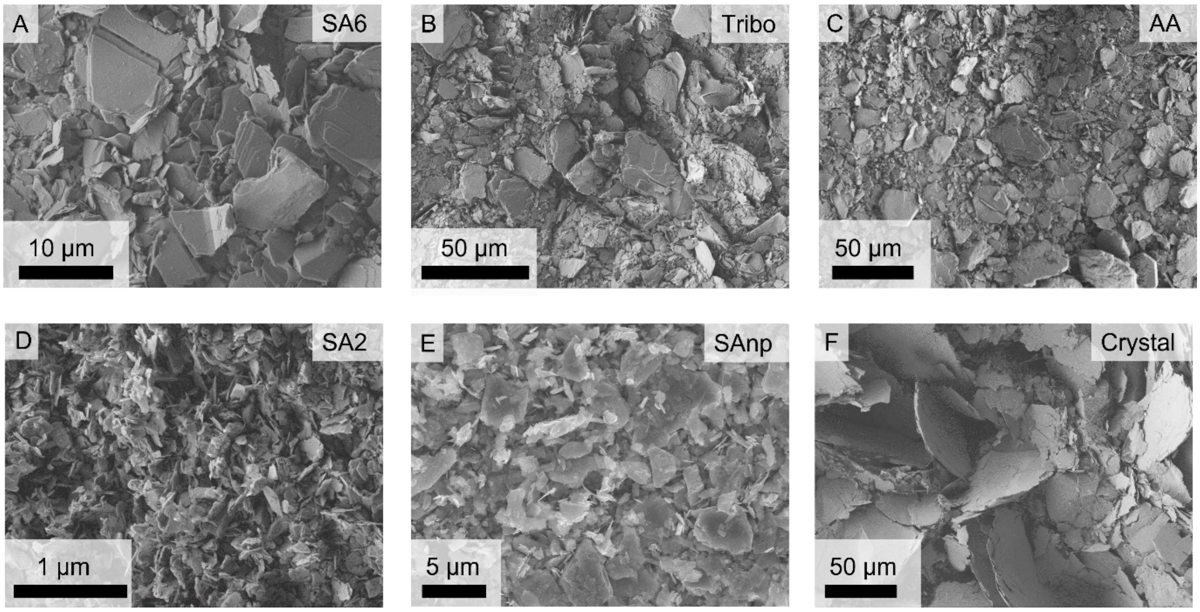

Figure 4.1: SEM images of bulk MoS_2 powders available from different suppliers. The SEM images reveal different flake sizes and size distributions in the raw materials. A: Sigma Aldrich, 6 µm particle size, B: Tribotecc, C: Alfa Aesar, D: Sigma Aldrich, 2 µm particle size, E: Sigma Aldrich, nanopowder, F: ground MoS_2 crystal from SPI Supplies.

The XRD spectra of all MoS_2 powders (Appendix, Figure 4.2 A) feature the literature known reflections of 2H-MoS_2.[145-147] Analysis of the spectra provides more information about the powders. For example, significant contributions of ML in the powders can be excluded, since this would lead to Debye scattering at low angles,[145] which is not present in any spectrum. The (002) reflection (Figure 4.2 B) primarily arises from interlayer Mo-Mo scattering with weaker contributions from S-S scattering and is only present for crystallites with number of layers $N \geq 2$. With increasing number of layers, the linewidth of the reflection decreases and the peak position moves to higher angles towards the expected Bragg position of 14.64°.[146] The reflection is affected by the number of layers and the spacing between the layers, but mostly unaffected by the lateral dimensions of the particles. The thickness of the MoS_2 starting materials D_{hkl} can be estimated from the (002) peak position by the Scherrer equation[146] (equation (4.1)), where $k = 0.76$ is a shape factor, λ is the wavelength of the X-rays, β the angular line width and θ the diffraction angle.

$$D_{hkl} = \frac{k\lambda}{\beta_{hkl}\cos(\theta)} \tag{4.1}$$

Table 4.1 summarizes the estimated thicknesses. The observed trends agree with the results acquired from the SEM images. However, according to the results obtained from the Scherrer equation, SAnp only features the second thinnest nanosheets, despite appearing transparent in the SEM images. This discrepancy highlights the limited reliability of the Scherrer equation. For example, changes in the (002) reflection can also originate from stacking faults or turbostratic disorders, which is not accounted for in equation (4.1).[145, 146]

Figure 4.2 C shows the (100) reflection, which is unaffected by the layer number but influenced by stacking faults or turbostratic disorders. These cause a broadening of the (100) reflection,[145] which is observed for SA6, Tribo, SA2 and SAnp. The (103) reflection (Figure 4.2 D) features a super Lorentzian line shape for SA6, Tribo, SA2, and most pronounced for AA, which is attributed to bimodal size distributions.[145]

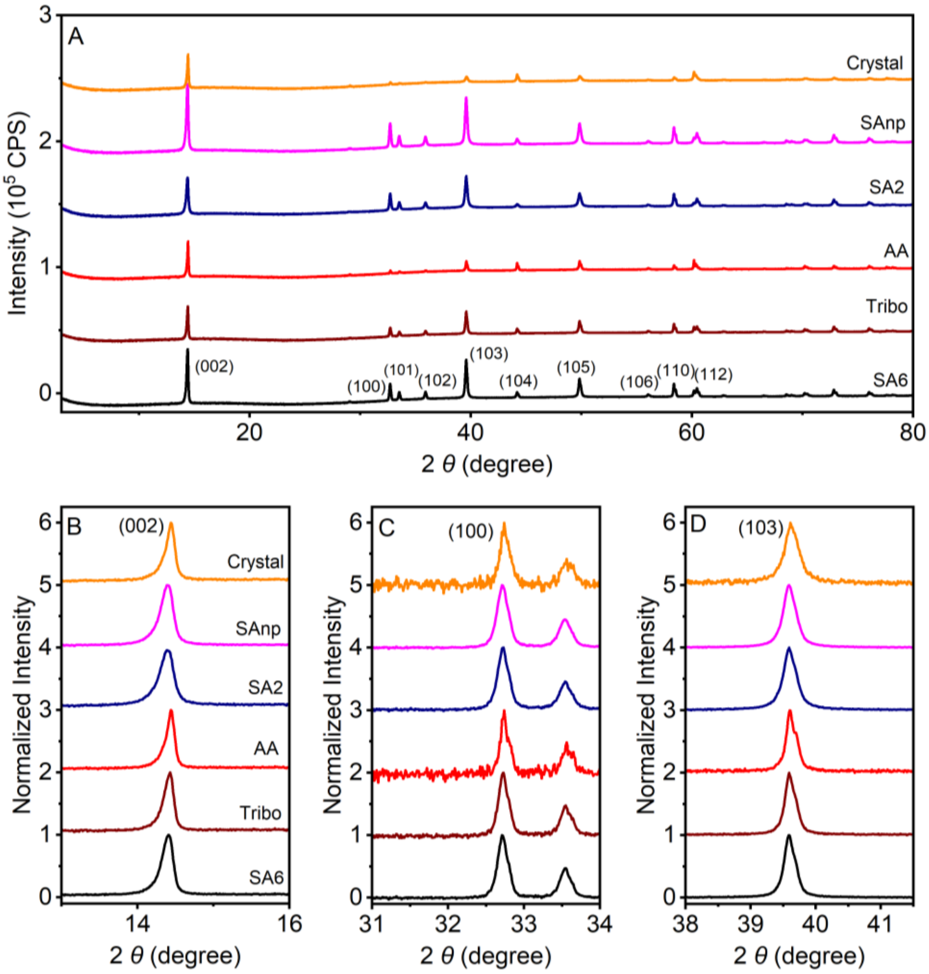

Figure 4.2: Powder XRD spectra of different bulk MoS_2 powders. The spectra are vertically offset for clarity. A: Full baseline corrected spectra, exhibiting typical features of 2H-MoS_2. B–D: Sections of the spectra shown in A. The (002) reflection shows some variations in peak position and linewidth, indicating different thicknesses of the particles (B). Broadening of the (100) reflection is observed for SA6, Tribo, SA2, and SAnp (C), indicating different degrees of stacking faults and turbostratic disorders. The (103) reflection exhibits a super Lorentzian line shape for SA6, Tribo, and SA2, and most pronounced for AA, attributed to bimodal particle size distributions.

Table 4.1: Estimated particle thicknesses of the bulk MoS_2 powders purchased from different suppliers. Thicknesses are estimated from the powder XRD (Figure 4.2) spectra using Scherrer's equation (equation (4.1)), assuming a shape factor $k = 0.76$.

Starting Material	**Thickness *D* (nm)**
SA6	39.5
Tribo	45.3
AA	69.3
SA2	31.6
SAnp	35.1
Crystal	52.4

Exfoliation and Size Selection of the MoS_2 Powders

The results presented above demonstrate that the purchased powders of bulk-MoS_2 vary in particle size, purity, defectiveness and stacking and that they are suitable candidates to investigate the impact of the starting material on the nanosheet yield, nanosheet dimensions and optical properties after LPE. The bulk materials were exfoliated by sonication-assisted LPE using a standard protocol (see chapter 4.1.2 or experimental section for details). In short, the MoS_2 powders were dispersed in aqueous SC-solution and sonicated for 1 h and centrifuged at a relative centrifugal force (RCF) of 3,820 *g*. The supernatants were discarded, and the purified MoS_2 sediments redispersed in fresh aqueous SC-solution. The MoS_2 dispersions were subjected to a longer sonication (5 h), resulting in polydisperse stock dispersions of nanosheets. The stock dispersions were subjected to LCC, including centrifugation steps at 0.1k, 0.4k, 0.8k, 2k, 5k, 10k, and 30k *g*. Six sediments of each starting material were collected, dispersed in a defined volume of fresh SC-solution and labelled as explained in chapter 4.1.2.

Characterization of the Nanosheet Dispersions

The dispersions collected during LCC were characterized by UV-Vis, Raman and fluorescence spectroscopy. First, UV-Vis extinction spectra were recorded and are presented in Figure 4.3. All spectra display the characteristic excitonic transitions of 2H-MoS_2,[148] proving that the 2H-polytype was maintained during exfoliation. Additionally, the extinction spectra show characteristic size-dependent changes, as indicated by the arrow in Figure 4.3 A. As explained in the theory section of this thesis, extinction spectra of nanosheet dispersions are composed of absorbance and a non-negligible scattering background, which both change with the nanosheet size and hence contribute to the size-dependent changes observed in the extinction spectra. The scattering background is most dominantly visible in spectra of large nanosheets and is the major contribution in the low energy regime below the absorption edge.

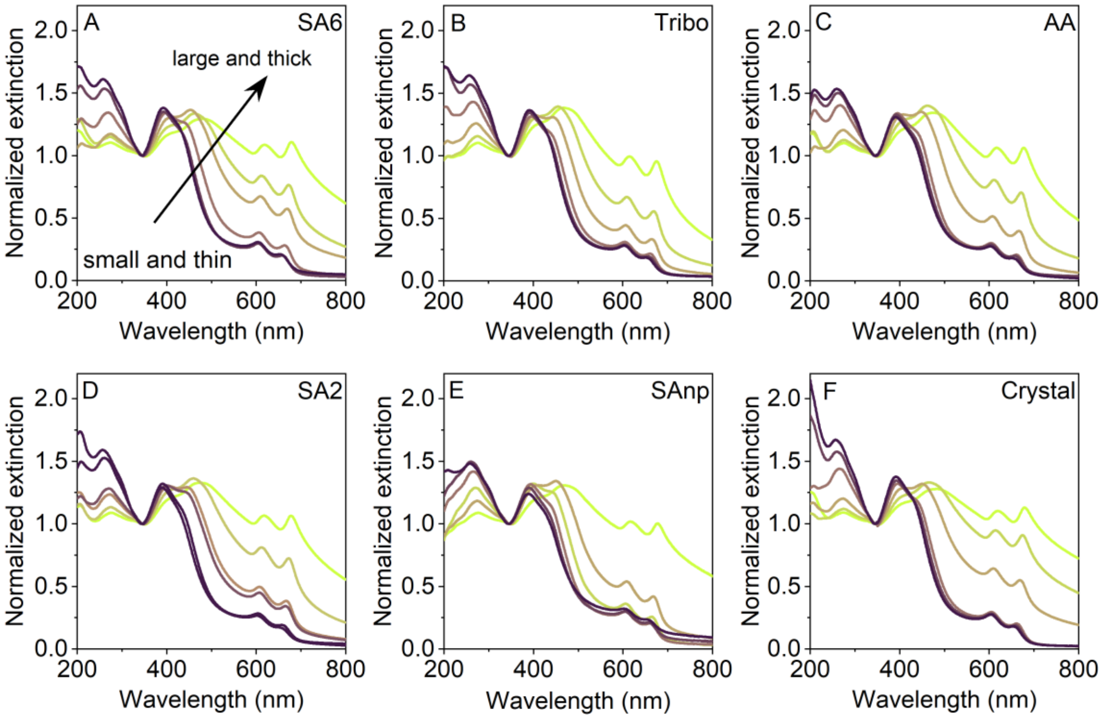

Figure 4.3: UV-Vis extinction spectra of MoS_2 nanosheet dispersions, produced by LPE and LCC. The spectra feature the transitions of 2H-MoS_2. Size-dependent changes are indicated by an arrow in A. A: Sigma Aldrich, 6 µm particle size, B: Tribotecc, C: Alfa Aesar, D: Sigma Aldrich, 2 µm particle size, E: Sigma Aldrich, nanopowder, F: ground MoS_2 crystal from SPI Supplies.

The high energy region of the spectra is dominated by the absorbance, enabling the estimation of the concentration directly from the extinction, using Lambert Beer's law (Equation (4.2)). Here, c is the concentration of the dispersion, Ext the extinction, d the path length of the light and ε the extinction coefficient. The concentration of MoS_2 can be determined from the extinction at 345 nm, Ext_{345}, with the extinction coefficient ε_{345} (MoS_2) = 69 mL mg^{-1} cm^{-1},[110] where the extinction coefficient is relatively invariant with respect to the nanosheet size.

$$c = \frac{Ext}{d * \varepsilon} \tag{4.2}$$

As elucidated in chapter 2.4, changes in the absorbance are attributed to edge or confinement effects and are specific for nanosheet length or nanosheet thickness, respectively. These changes in the absorbance are still encoded in the extinction and can be utilized to extract size information from the UV-Vis extinction spectra. The mean length, $\langle L \rangle$, of the MoS_2 nanosheets can be calculated by the ratio of the extinction at 270 nm, Ext_{270}, and 345 nm, Ext_{345} by equation (2.16).[110] The mean layer number, $\langle N \rangle$, of MoS_2 nanosheets can be determined by the position of the A-exciton by equation (2.18), since a decreasing layer number is reflected by a blue shift of the A-exciton. The position of the A-exciton was determined from the second derivative of the extinction, $d^2Ext/d\lambda^2$ (Figure A 2), since this partially compensates for an additional artificial redshift originating from the scattering background. Here, the extinction spectrum was differentiated twice and subsequently smoothed by adjacent averaging. This methodology leads to a loss of fine structure of the signal, allowing to determine the combined position of the optical transition.

$$\langle L\rangle(\mathrm{MoS_2}) = \frac{2.30 - Ext_{270}/Ext_{345}}{0.02Ext_{270}/Ext_{345} - 0.0185} \tag{2.16}$$

$$\langle N\rangle(\mathrm{MoS_2}) = 2.3 \cdot 10^{36} \cdot \exp(-54888/\lambda_\mathrm{A}) \tag{2.18}$$

Yield (*Y*), ⟨*L*⟩, and ⟨*N*⟩ were calculated from the UV-Vis spectra (Figure 4.3 and Figure A 2) according to equation (4.2), (2.16), and (2.18), and are plotted against central RCF in Figure 4.4 A–C. Yield, ⟨*L*⟩*,* and ⟨*N*⟩ decrease with central RCF and can be described by an empirical power law in form of equation (4.3), resulting in a linear curve progression on the log-log scale. In Figure 4.4 D ⟨*L*⟩ is plotted as a function of ⟨*N*⟩. The curve progression can be described as power law in form of equation (4.4) and suggests a relationship between length and the thickness of the nanosheets.

$$Y, \langle L\rangle, \langle N\rangle = 10^a \cdot RCF^n \tag{4.3}$$

$$\langle L\rangle = 10^a \cdot \langle N\rangle^n \tag{4.4}$$

The data in Figure 4.4 were fitted according to equation (4.3) and (4.4) with fixed exponents of $n_{\text{Yield-RCF}} = -1$, $n_{\langle L\rangle\text{-RCF}} = -0.46$, $n_{\langle N\rangle\text{-RCF}} = -0.54$ and $n_{\langle L\rangle\text{-}\langle N\rangle} = 0.85$.

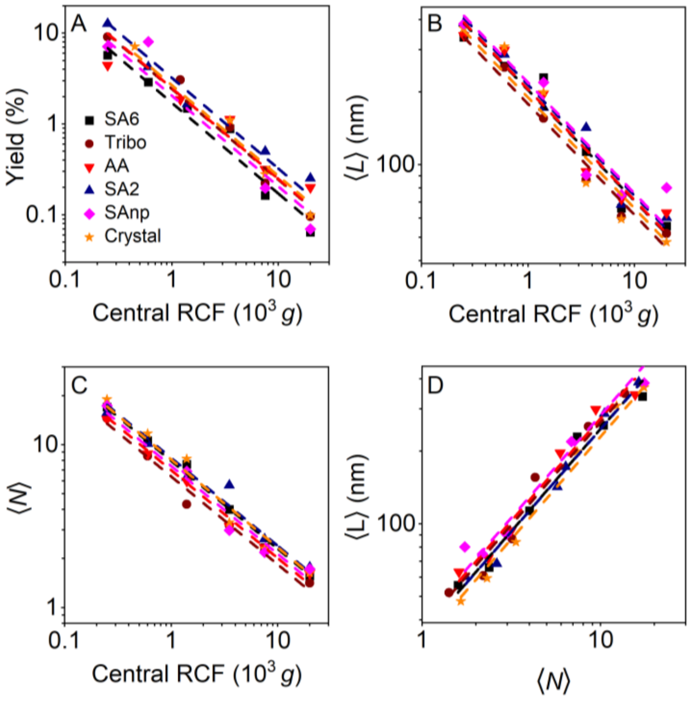

Figure 4.4: Yield and size information derived from the optical extinction spectra shown in Figure 4.3 and Figure A 2, using equation (4.2), (2.16), and (2.18). A–C: Yield (A), ⟨*L*⟩ (B) and ⟨*N*⟩ (C) as a function of central RCF, fitted by power laws in form of equation (4.3). The exponent *n* of the fits was fixed ($n_{\text{Yield-RCF}} = -1$, $n_{\langle L\rangle\text{-RCF}} = -0.46$, $n_{\langle N\rangle\text{-RCF}} = -0.54$). D: ⟨*L*⟩ as a function of ⟨*N*⟩, indicating a relation between lateral dimensions and thickness of the nanosheets. Data were fitted by a power law in form of equation (4.4) with a fixed exponent of $n_{\langle L\rangle\text{-}\langle N\rangle} = 0.85$.

These fixed exponents are based on previous power law fits shown in Figure A 6 (Appendix), where the fits have been conducted without restraints. The exponents of the unrestraint fits were extracted and compared in Figure A 7 (Appendix). No significant differences between the exponents were observed (with $n_{\text{Yield-RCF}}$ = -1 ± 0.17, $n_{\langle L\rangle\text{-RCF}}$ = -0.46 ± 0.04, $n_{\langle N\rangle\text{-RCF}}$ = -0.54 ± 0.04 and $n_{\langle L\rangle\text{-}\langle N\rangle}$ = 0.85 ± 0.06, where the standard deviation is statistical), justifying the fixing.

The prefactors *a* were extracted from the fits shown in Figure 4.4. Despite not having a relevant physical meaning in all cases, a comparison of the prefactors *a* implies a comparison of the output of the exfoliation. The extracted prefactors are displayed and compared in Figure 4.5, where the error bars represent the errors of the fits. The mean value of the different starting materials is indicated as dotted line and the range of standard deviation (1 σ) is added as solid lines. In Figure 4.5 A the prefactors of the fit of the yield vs. central RCF exhibits relatively large error bars which can be attributed to the experimental procedure, in which the yield is affected by natural variations on pipetting after LCC. However, the mean value of $a_{\text{Yield-RCF}}$ was found to be -1.62 ± 0.09, with a standard deviation between the batches of only 5 %. Considering the different particle sizes and morphologies of the starting material, this is surprisingly low. For example, one might intuitively expect that the exfoliation of starting materials containing smaller crystallites is more efficient. In contrast to this expectation, SA2 contains the second smallest particles in the bulk powder but exhibits the highest prefactor of the yield. The two lowest prefactors were found for SA6 and SAnp, with bulk crystallites of intermediate and the smallest size, respectively.

The prefactors from the fits $\langle L\rangle$ vs *RCF* and $\langle N\rangle$ vs *RCF* are presented in Figure 4.5 B and C, respectively. The mean values were determined as $a_{\langle L\rangle\text{-RCF}}$ = 2.30 ± 0.03 and $a_{\langle N\rangle\text{-RCF}}$ = 0.87 ± 0.04. This implies standard deviations of only 1.3 % and 4.6 %, respectively. The grey background in the plots indicates the standard deviation range (1 σ range) which originates from multiple exfoliations of the same starting material (in particular of the starting material SA6). Significant differences between the range of scatter in the data acquired from different starting materials and data acquired from multiple exfoliations with the same starting material are not discernible, considering the experimental deviations mentioned above.

Figure 4.5 D displays the prefactors extracted from the fits $\langle L\rangle$ vs $\langle N\rangle$. The mean value of the prefactors $a_{\langle L\rangle\text{-}\langle N\rangle}$ was found to be 1.56 ± 0.03. This is basically identical to the mean value found for multiple exfoliations of SA6, which is 1.56 ± 0.02. In contrast to the previous extracted prefactors, the prefactor of the fit $\langle L\rangle$ vs $\langle N\rangle$ has indeed a relevant physical meaning since it represents the nanosheet length of a theoretical pure ML dispersion, which is here called the characteristic ML length. In case of the extracted prefactor 1.56 ± 0.03, this characteristic ML length is 36.3 ± 1.0 nm.

The data presented above effectively reveal that the quality or crystallite size of the starting material in LPE neither have an impact on the yield, nor on the dimensions of the nanosheet. One possible explanation of the yield being independent of the bulk crystallize size can be derived from an exfoliation model developed for graphene (see chapter 2.2 for details).[100] This model describes the exfoliation as a process with three distinct stages, where large graphite crystals are fragmented and turned into graphite stripes within the first and second stage of the exfoliation. The final exfoliation towards few-layer graphite or graphene only occurs in the last step of the whole process. While the first and second stage occur on a relatively short time scale, the third stage is slow and time consuming. Even though this model is explicitly developed and experimentally supported for graphite/graphene, there might be parallels to TMDs such as MoS_2. If the crystallites in the bulk powders are quickly fragmented into smaller pieces and only slowly exfoliated any further, then all bulk materials might quickly reach the same fragment size in the dispersions, which explains why the crystallite size of the bulk powders is not reflected in the yield when using prolonged sonication times as used here. Note that the starting material might nonetheless affect the kinetics of the exfoliation for shorter sonication times. That the dimensions of the nanosheets are unaffected by the starting material supports the exfoliation model presented by BACKES *et al.*,[94] which describes the ratio of lateral dimensions and nanosheet thickness as a consequence of intra- and interlayer binding energies.

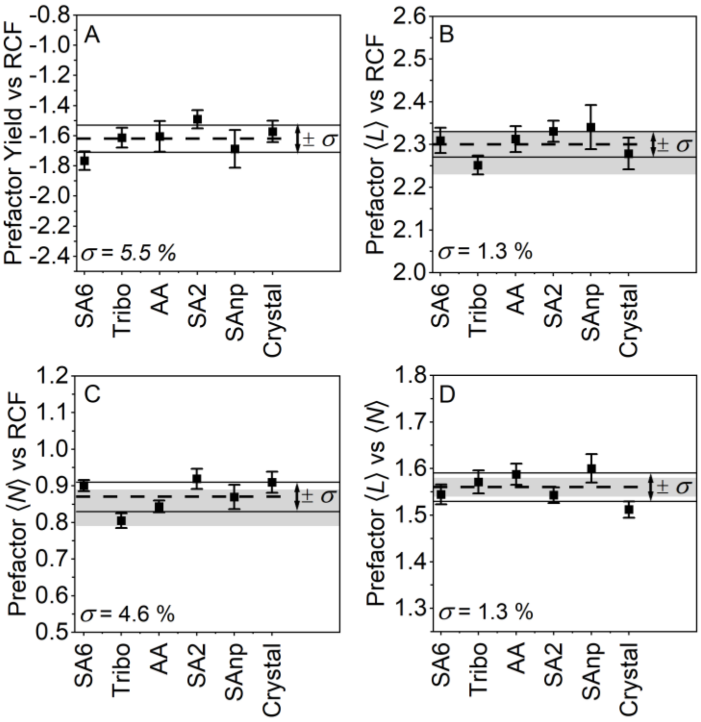

Figure 4.5: Comparison of the prefactors *a* extracted from the power law fits shown in Figure 4.4. The mean value of the prefactor across the different starting materials is indicated as a dashed line. The standard deviation range is indicated by solid lines. The standard deviation range of multiple exfoliations of the same starting material (SA6) is indicated as a grey background. A: Prefactor yield vs central RCF. B: Prefactor ⟨*L*⟩ vs central RCF. C: Prefactor ⟨*N*⟩ vs central RCF. D: Prefactor ⟨*L*⟩ vs ⟨*N*⟩.

Despite not having an impact on the yield or nanosheet dimensions, it is still unclear whether the choice of the starting material affects the fluorescence of the resulting nanosheet dispersions. A convenient method for PL investigations of TMDs is Raman spectroscopy, since Raman signals and the PL originating from the A-exciton can be measured in a single spectrum if an appropriate excitation wavelength is chosen. The PL to Raman ratio can be extracted and used for comparison of the relative PL intensity. The Raman spectra (λ_{exc} = 633 nm) of the MoS_2 dispersions are shown in Figure 4.6.

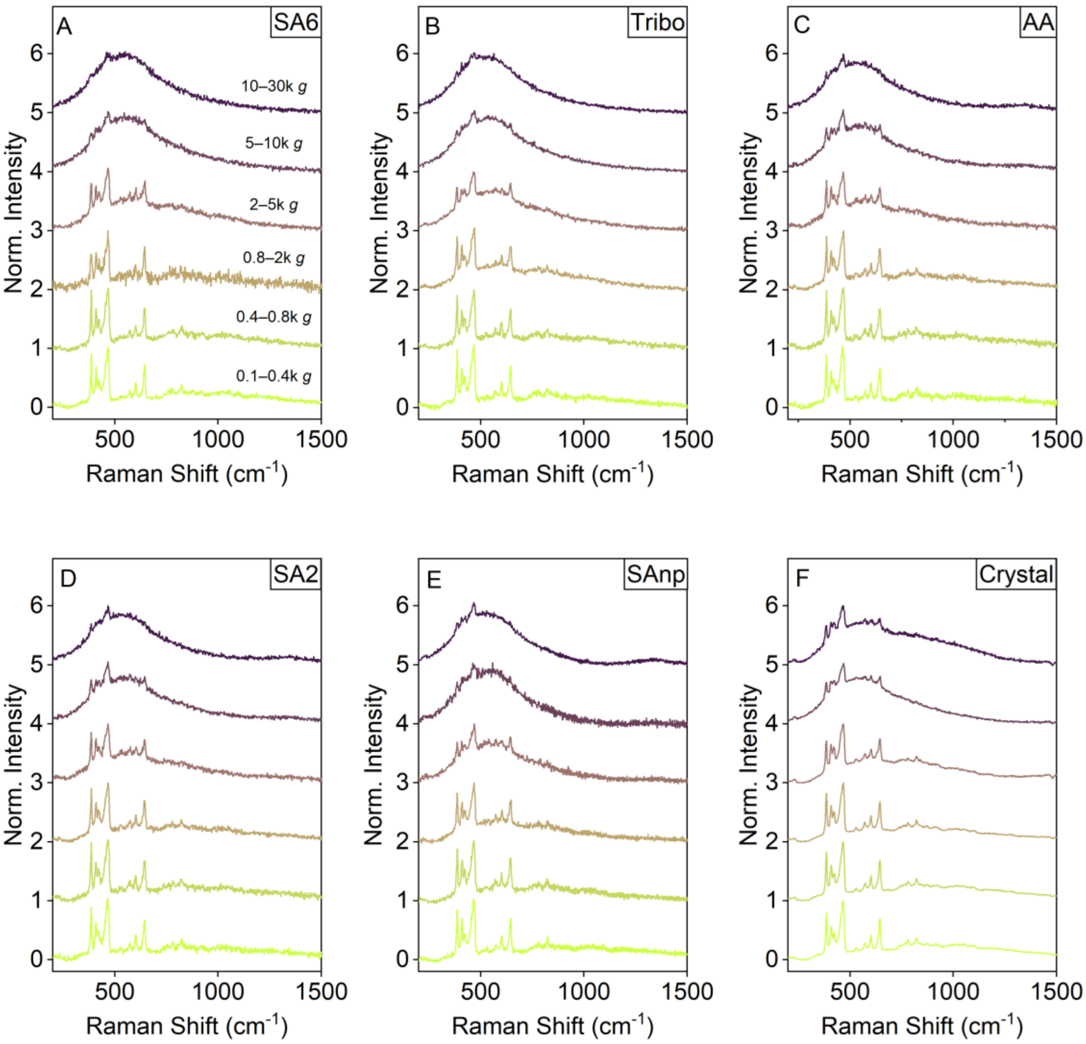

Figure 4.6: Raman spectra (λ_{exc} = 633 nm) of the MoS_2 nanosheet dispersions produced from different starting materials by LPE and LCC. The spectra are normalized to the highest Raman signal and vertically offset for clarity. With increasing ML content, a PL background becomes visible, originating from the A-exciton. Due to the overlap of the PL with the Raman signals, quantitative analysis is error prone. A: Sigma Aldrich, 6 µm particle size, B: Tribotecc, C: Alfa Aesar, D: Sigma Aldrich, 2 µm particle size, E: Sigma Aldrich, nanopowder, F: ground MoS_2 crystal from SPI Supplies.

All spectra feature the typical Raman modes for 2H-MoS_2[33, 121] without significant differences. Since only ML MoS_2 is fluorescent,[149, 150] the PL of dispersions collected at early stages of the size selection cascade is negligible and the PL intensity gradually increases with the ML content. It was previously suggested that the PL scales with the ML content,[117] but this metric is only reliable if the intrinsic ML PL of all MoS_2 sources is identical which is questionable. Additionally, the data evaluation of the MoS_2 Raman spectra is inconvenient due to overlapping PL and Raman signals. Nonetheless, the PL/Raman ratios were extracted by calculating the ratio of the PL maximum and the difference from the highest Raman signal to the next local minimum. The extracted PL/Raman ratios are plotted against central RCF (Figure 4.7 A) and ⟨*N*⟩ (Figure 4.7 B). While a rough scaling of the PL/Raman ratio with the ML content was found, no ultimate conclusion could be drawn due to overlapping signals which makes the analysis of the spectra difficult and error-prone.

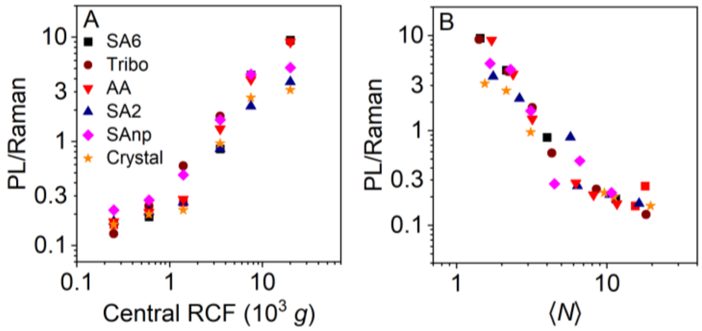

Figure 4.7: PL to Raman ratios as a function of central RCF (A) and ⟨*N*⟩ (B), extracted from the Raman spectra shown in Figure 4.6. The PL/Raman ratio increases with central RCF or decreasing layer number of the nanosheets and was calculated from the PL maximum and the difference from the highest Raman signal to the next local minimum.

To investigate the PL further, photoluminescence excitation (PLE) contour plots of the fractions 10–30k *g* were recorded (Figure 4.8), since these fractions contain the highest ML portion and are thus expected to exhibit the strongest PL. The PL intensity was corrected for the lamp spectrum and normalized to the MoS_2 concentration known from the optical extinction spectra (Figure 4.3) for better comparability. Raman modes of water are visible in the spectra as diagonal signal, as indicated by the dashed line in Figure 4.8 A. In all PLE maps, the PL related with the A-exciton is visible, but different intensities are discernible. The strongest PL signal is detected from the dispersion of crystal (Figure 4.8 F), followed by SA6 (Figure 4.8 A), Tribo (Figure 4.8 B) and AA (Figure 4.8 C). SA2 (Figure 4.8 D) and SAnp (Figure 4.8 E) show only weak PL.

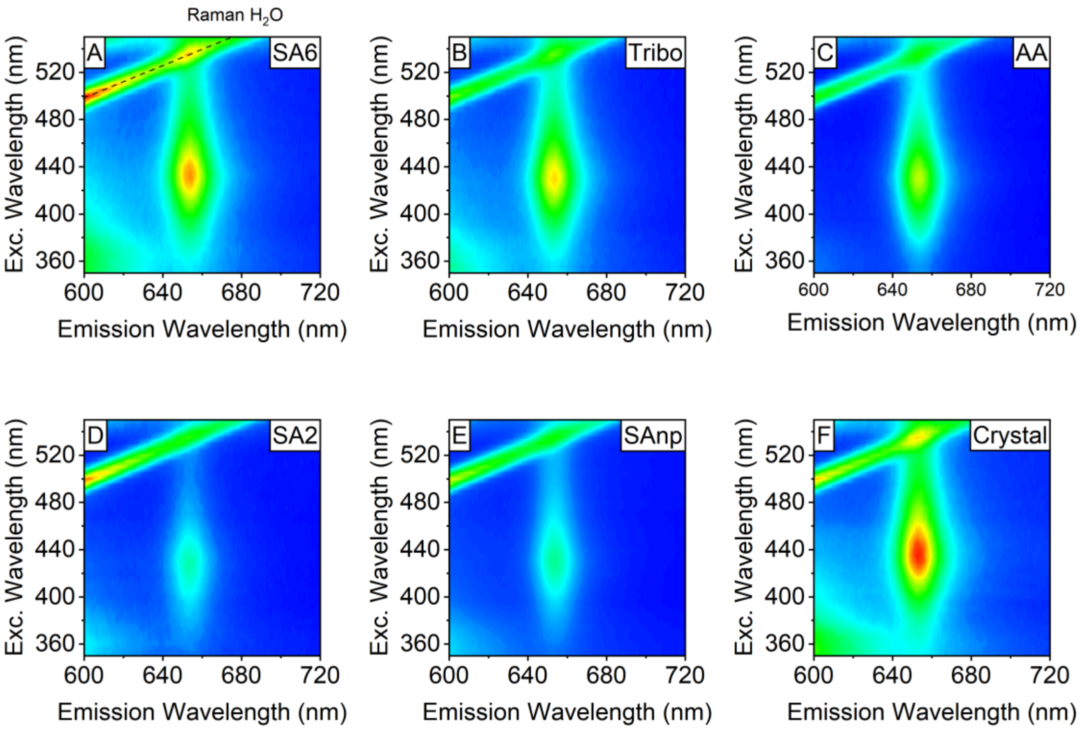

Figure 4.8: PLE contour maps of MoS_2 nanosheet dispersions, exfoliated from different bulk starting materials. The PLE maps display the PL associated with the A-exciton and Raman signals of water (indicated by a dashed line in A). The data were recorded from the size selection fractions 10–30k *g*, which contain the highest ML portion. The intensities were corrected for the lamp spectrum and normalized on the nanosheet concentration, indicating material related differences in the PL intensity. The excitation light was cut-off by a long pass filter, absorbing below 550 nm. A: Sigma Aldrich, 6 µm particle size, B: Tribotecc, C: Alfa Aesar, D: Sigma Aldrich, 2 µm particle size, E: Sigma Aldrich, nanopowder, F: ground MoS_2 crystal from SPI Supplies.

A meaningful evaluation of the PL requires a quantification of the PL intensities which need to be linked to the ML content of the dispersions. The quantification of the PL was conducted by measuring PL spectra of the size selection fractions 2–5k *g*, 5–10k *g* and 10–30k *g* at an excitation wavelength of 440 nm (Figure 4.9). Fractions containing larger and thicker nanosheets were neglected, due to their weak PL. Again, the intensities were corrected for the different nanosheet concentrations. As has already been demonstrated with the Raman experiments, the PL intensity increases with proceeding size selection cascade and increasing ML content for all starting materials. In agreement with the recorded PLE maps, the dispersions exfoliated from the ground crystal (Figure 4.9 F) exhibits the highest PL intensity, followed by the dispersions exfoliated from SA6 (Figure 4.9 A), Tribo (Figure 4.9 B) and AA (Figure 4.9 C). The dispersions exfoliated from SA2 (Figure 4.9 D) and SAnp (Figure 4.9 E) again show only weak PL. The PL signals were fitted assuming a Lorentzian line shape, and peak position, linewidth (full-width-at-half-maximum, FWHM), and intensity were extracted from the fits.

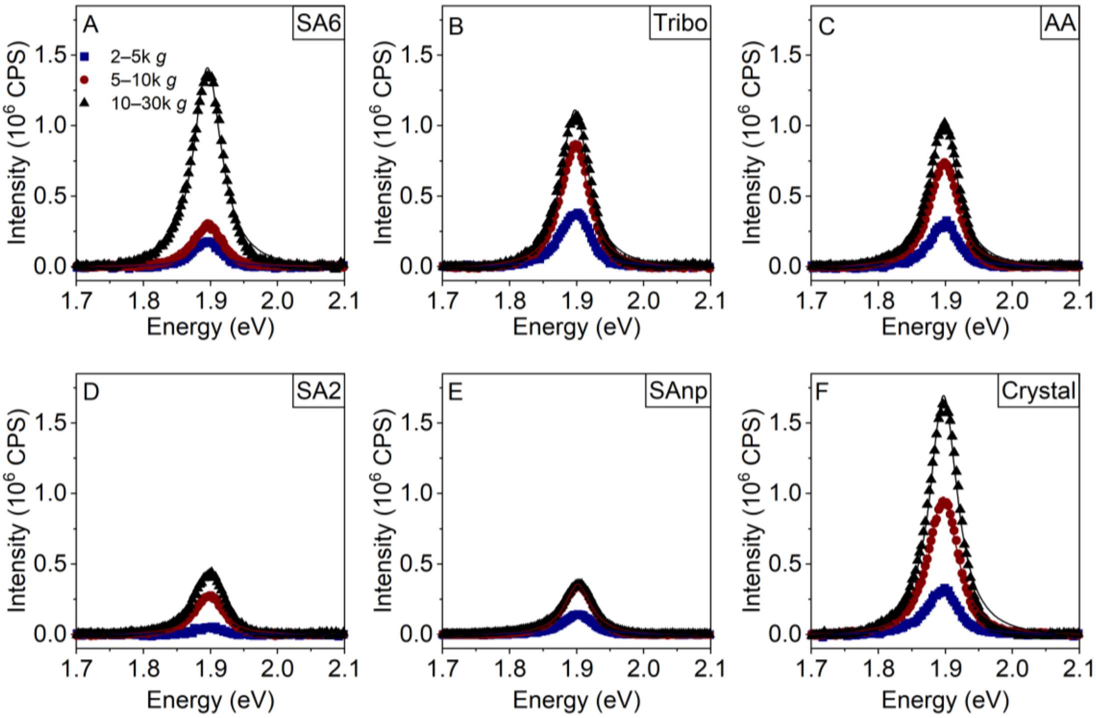

Figure 4.9: PL spectra (λ_{exc} = 440 nm) of MoS_2 nanosheet dispersions exfoliated from different starting materials. Displayed are the fractions of the size selection 2–5k *g*, 5–10k *g*, and 10–30k *g*. The PL signals were fitted by Lorentzians to obtain quantitative information. The PL intensity is normalized to the nanosheet concentration. Fractions containing larger and thicker nanosheets showed no or negligible PL. The excitation light was cut-off by a long pass filter absorbing below 495 nm. A: Sigma Aldrich, 6 µm particle size, B: Tribotecc, C: Alfa Aesar, D: Sigma Aldrich, 2 µm particle size, E: Sigma Aldrich, nanopowder, F: ground MoS_2 crystal from SPI Supplies.

Line shape, peak position, and linewidth of the PL is compared in Figure 4.10. Figure 4.10 A shows an overlay of the normalized PL signals recorded from the 10–30k *g* fractions of the size selection. No differences in the line shape are discernible between the different starting materials. Figure 4.10 B compares the PL positions extracted from the fits shown in Figure 4.9 as a function of ⟨*N*⟩. Some scatter in the data is observed, but variations between the batches can be considered as negligible, considering the overall small differences between the data points. Additionally, no trend with ⟨*N*⟩ is discernible. This is intuitively understandable considering that the PL emission only stems from the thinnest (ML) flakes, independent from the mean layer number of the dispersion. Figure 4.10 C shows the linewidth, represented as FWHM as a function of ⟨*N*⟩. While at first glance it appears that the PL slightly sharpens with increasing ⟨*N*⟩, it should be noted that this is most likely artificial and originates from the weakened PL found in dispersions with fewer ML nanosheets which worsens the quality of the fits and increases the error bars.

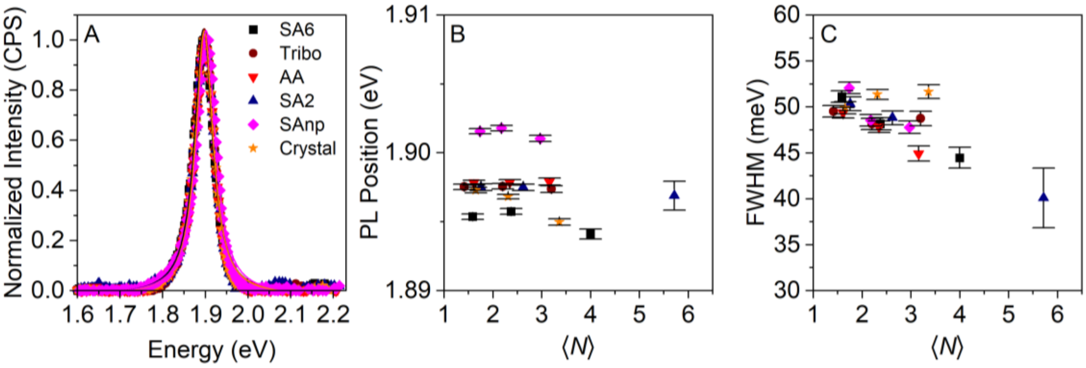

Figure 4.10: Comparison of the PL peak position and linewidth of MoS_2 nanosheet dispersions exfoliated from different bulk starting materials. A: Normalized PL signals of the 10–30k *g* fractions, showing no changes in the PL shape. B, C: PL position (B) and FWHM (C) as a function of ⟨*N*⟩, showing only negligible differences between the batches.

As mentioned above, a meaningful comparison of the PL intensity needs to take the ML content into account. Figure 4.11 shows the PL intensities derived from the fits in Figure 4.9 as a function of ⟨*N*⟩ (A) and the ML volume fraction, ML V_f (B). The ML_{Vf} was calculated from ⟨*N*⟩ by Equation (4.5) and (4.6), where $\langle N\rangle_{Vf}$ is the volume-fraction weighted mean layer number.

$$\langle N\rangle_{\mathrm{Vf}} = \frac{\langle N\rangle - 0.38}{0.65} \tag{4.5}$$

$$ML\ V_f = \left[0.9 + 0.1\langle N\rangle_{\mathrm{Vf}}^{3.4}\right]^{-1} \tag{4.6}$$

For all starting materials, the PL intensity decreases with increasing number of layers or decreasing ML_{Vf}, as observed above without quantification, but differences between the batches are significant. The highest PL for a given ML content was detected for the dispersion exfoliated from the ground crystal, followed by SA6, Tribo, and AA, even though the intensity of the 10–30k *g* fraction of Tribo is slightly weaker than the extrapolation of the fractions containing larger nanosheets. However, the 10–30k *g* fraction of Tribo also contains nanosheets with slightly smaller lateral dimensions and thus a higher contribution of nanosheet edges, which can quench the PL.[108] The dispersions of SA2 and SAnp show significantly weaker PL, despite a comparable ML content. These findings prove that there are real intrinsic differences between the PL intensities of ML nanosheets exfoliated from different starting materials. These differences could be rationalized by either different characteristic ML length of the nanosheets or different defect contents and types. The characteristic ML length can be excluded as an explanation due to the following reason: The characteristic ML length is described by the prefactors of the fits shown Figure 4.5 D and compared in Figure 4.5 D. As discussed above, only minor changes are observed and additionally, Crystal exhibits the smallest characteristic ML length, but the strongest PL, and SAnp exhibits the largest characteristic ML length, but only weak PL. Defects on the other side will have an impact on the optical properties of MoS_2 with high probability.[144, 151, 152] In the following subchapter 4.1.4, the role of defects will be discussed in greater depth and it will be experimentally shown, that defects in LPE produced samples indeed quench the PL of TMDs using WS_2 as model substance. While it is plausible that the single crystal has the lowest defect density and that the dispersions resulting from its exfoliation exhibit the strongest PL, there is no experimental evidence proving that the nanosheets of Crystal are less defective.

One might assume that the defect density is reflected in the S:Mo stoichiometry (Appendix, Table A 7) derived from EDX elemental analysis (Appendix, Table A 1–Table A 6), but no correlation between the S:Mo ratio and PL intensity was found. For example, the starting materials Tribo and AA exhibit a relatively strong PL and a S:Mo ratio of 1.78 ± 0.07 and 1.77 ± 0.30, respectively, where the standard deviation is statistical and related to spot-to-spot variations. The weakest PL was found for SA2 and SAnp with S:Mo ratios of 1.92 ± 0.00 and 2.11 ± 0.00, respectively, which is closer to the theoretical value of 2. It is further to mention that different point defects like sulfur vacancies or molybdenum vacancies will shift the S:Mo ratio to different directions, limiting its relevancy.

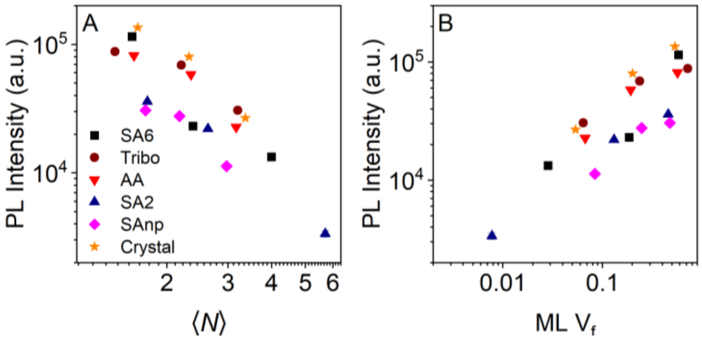

Figure 4.11: Integrated PL intensity (λ_{exc} = 440 nm) as a function of the mean layer number ⟨*N*⟩ (A) and the ML volume fraction MLV$_f$ (B). The PL intensities were derived from the Lorentzian fits shown in Figure 4.9. Error bars are errors of the fits. Most starting materials show an apparent linear scaling of the PL intensity with the ML content. The dispersions exfoliated from the bulk materials SA2 (dark blue) and SAnp (magenta) show a significantly lower PL intensity than the dispersions exfoliated from SA6, Tribo and the ground crystal.

In conclusion, the data presented above proved that crystallite size, purity, and defectiveness of the bulk material do not have an impact on the dimensions of nanosheets exfoliated by sonication-assisted LPE. Minor differences observed in the nanosheet dimensions are in the same order of magnitude as natural variations occurring in multiple exfoliations of the same starting material. However, significant differences in the PL intensity were observed, whereas PL position and linewidth remained unaffected. The highest PL intensity was observed for the dispersions exfoliated from the pestled single crystal, which is expected to have the lowest defect density. However, there is no experimental evidence, that the different PL intensities are related to defects.

4.1.4 Impact of Pretreatment of the Bulk Starting Material on the Efficiency of Liquid phase Exfoliation of WS_2

In the previous subchapter it was demonstrated that the nanosheet dimensions are widely unaffected by the choice of starting materials. The question arises whether the nanosheet dimensions, in particular the nanosheet aspect ratio, can be altered by intercalation of pretreatment agents between the layers of the bulk crystal. Intercalation could lower the interlayer binding strength and thus increase the relative lateral dimension of the nanosheets after exfoliation. Increased lateral dimensions of ML flakes should be reflected in optical properties such as an increased PL intensity of TMDs. WS_2 was chosen as a suitable model system since it allows a simple monitoring of the PL by Raman spectroscopy in contrast to MoS_2, where this is less straight forward as shown in the previous subchapter. The data of this study have been published before[120] and were partially acquired with experimental support of Melanie Lakmann.

Pretreatment, Exfoliation and Size Selection of WS_2 powders

Bulk WS_2 powder was subjected to different pretreatments according to Scheme 4.2. The pretreatments include stirring in aqueous NaCl solution (NaCl stir), stirring in NMP (NMP stir), stirring in *n*-BuLi/hexane (BuLi stir), bath sonication in water (H_2O bath), and bath sonication in aqueous LiCl solution (LiCl bath). Some of the methods such as stirring in aqueous NaCl solution or NMP and bath sonication in water were chosen due to their simplicity, and other methods such as stirring in *n*-BuLi or bath sonication in aqueous LiCl solution, since these methods are known to lead to intercalation.

After the pretreatment, the WS_2 powders were thoroughly washed to remove the excess of pretreatment agents, and subsequently filtered and dried in vacuum. The dried WS_2 powders were weighed for later yield determination and exfoliated by tip sonication. The standard protocol for the exfoliation of TMDs described in chapter 4.1.2 includes a short sonication step to remove impurities, which was excluded in this experiment to keep the exfoliation as simple as possible. Additionally, the amplitude during the tip sonication was reduced from 60 % to 30 % to avoid that potentially small impacts of the pretreatments become unnoticeable under harsh sonication conditions. However, since the results obtained from the 30 % amplitude exfoliations turned out to be promising, the pretreatment method NaCl stir was repeated with subsequent exfoliation at 60 % amplitude sonication (NaCl stir 60 %) to investigate whether changes remain when the standard protocol is used.

The exfoliated stock dispersions were subjected to LCC with centrifugation steps of 0.1k, 0.4k, 0.8k, 2k, 5k, 10k, and 30k *g*, resulting in six different dispersions of each exfoliation batch, containing nanosheets of different sizes.

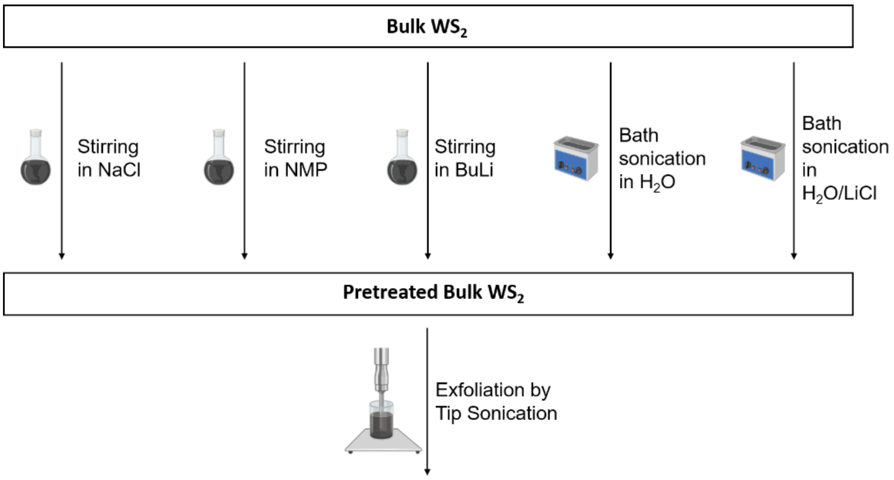

Scheme 4.2: Pretreatments of bulk WS$_2$ powders executed prior to exfoliation. Bulk WS$_2$ was treated by stirring in aqueous NaCl solution, stirring in NMP, stirring in hexane/*n*-BuLi, bath sonication in H$_2$O, and bath sonication in aqueous LiCl solution. The subsequent exfoliation was carried out by tip sonication.

Characterization of the WS$_2$ Nanosheet Dispersions

The dispersions were analyzed by UV-Vis and Raman/fluorescence spectroscopy. The UV-Vis extinction spectra are presented in Figure 4.12. All spectra feature the characteristic excitonic transitions of 2H-WS$_2$.[148] Chemical exfoliation of TMDs with *n*-BuLi is accompanied with a transition to the 1T-polytype,[142] but in this experiment the BuLi concentration was low and reaction conditions mild enough to maintain the 2H-phase. The spectra feature the typical size-dependent changes which have been observed and explained before.

The WS$_2$ concentration of the dispersions was calculated by Beer-Lambert's law, from the extinction at 235 nm, Ext_{235}, using the extinction coefficient ε_{235} = 47.7 mL mg^{-1} cm^{-1}.[108] The mean nanosheet length $\langle L \rangle$ was determined from the ratio of the extinction at 235 nm, Ext_{235}, and the extinction at 290 nm, Ext_{295}, according to equation (2.15),[108] and the mean layer number $\langle N \rangle$ of the nanosheets in dispersion was calculated from the position of the A-exciton by equation (2.17).[108]

$$\langle L \rangle = \frac{2.30 - Ext_{235}/Ext_{290}}{0.02 Ext_{235}/Ext_{290} - 0.0185} \tag{2.15}$$

$$\langle N \rangle = 6.35 \cdot 10^{-32} \cdot \exp\left(\lambda_{\mathrm{A}}(\mathrm{nm})/8.51\right) \tag{2.17}$$

Analogously to the evaluation of the UV-Vis extinction spectra of MoS_2 in chapter 4.1.3, the position of the A-exciton was determined from the second derivatives of the extinction spectra, $d^2Ext/d\lambda^2$, which are displayed in Figure A 8 (Appendix), to partially compensate for an additional artificial redshift originating from the scattering background. Again, the extinction spectrum was differentiated twice and subsequently smoothed by adjacent averaging before the position of the A-exciton was extracted. Yield, ⟨*L*⟩ and ⟨*N*⟩ have been compared and are discussed later.

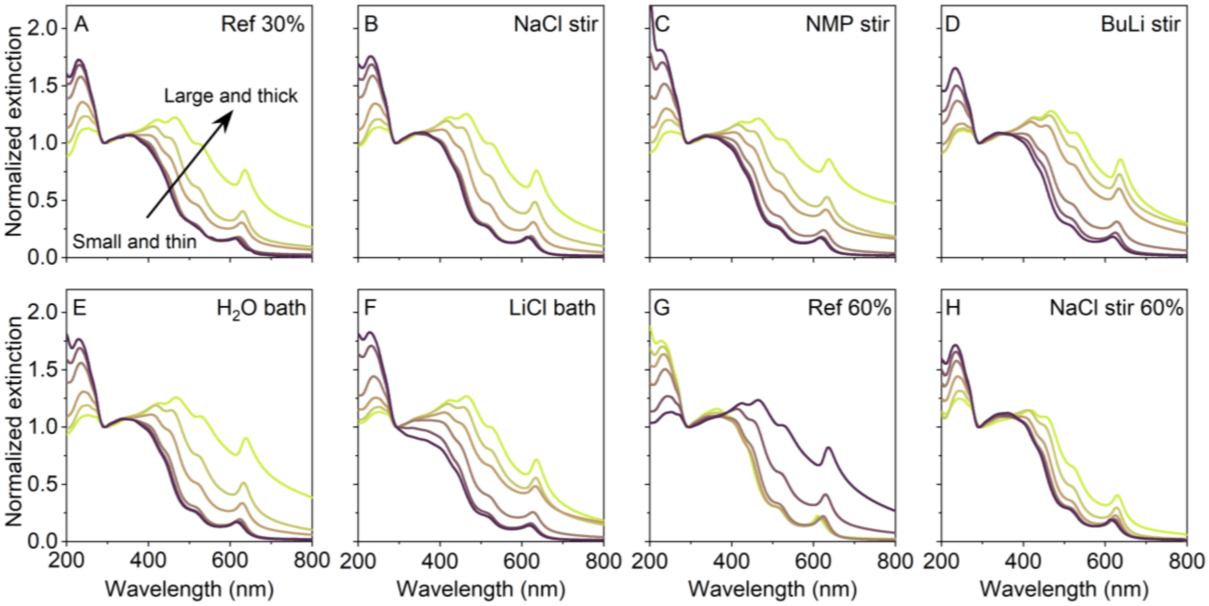

Figure 4.12: UV-Vis extinction spectra of WS_2 nanosheet dispersions, displaying characteristic transitions of 2H-WS_2. Bulk WS_2 powders were treated according to Scheme 4.2 and exfoliated by sonication-assisted LPE. The exfoliated stock dispersions were subjected to size selection via LCC. Size-dependent changes are indicated by the arrow in A. A: Ref 30 %, B: NaCl stir, C: NMP stir, D: BuLi stir, E: H_2O bath, F: LiCl bath, G: Ref 60 %, NaCl stir 60 %.

Raman spectra (λ_{exc} = 532 nm) of the dispersions were recorded to investigate the photoluminescence properties of the exfoliated WS_2 (Figure 4.13). The spectra were normalized to the highest Raman signal of WS_2 and are vertically offset for clarity. All Raman spectra feature the characteristic Raman signals of 2H-WS_2. Additionally, Raman signals of water are visible at ~ 3300 cm^{-1} in dispersions with low WS_2 concentration, as indicated in A and B. With proceeding centrifugation cascade, the ML content of the dispersions increases, and PL associated with the A-exciton of WS_2 becomes visible. Ref 30 % shows only negligible PL, but the PL intensity of the pretreated batches of the 30 % amplitude series is more intense, even though with significant differences. Ref 60 % exhibits a stronger PL which is even exceeded from the batch NaCl stir 60 %.

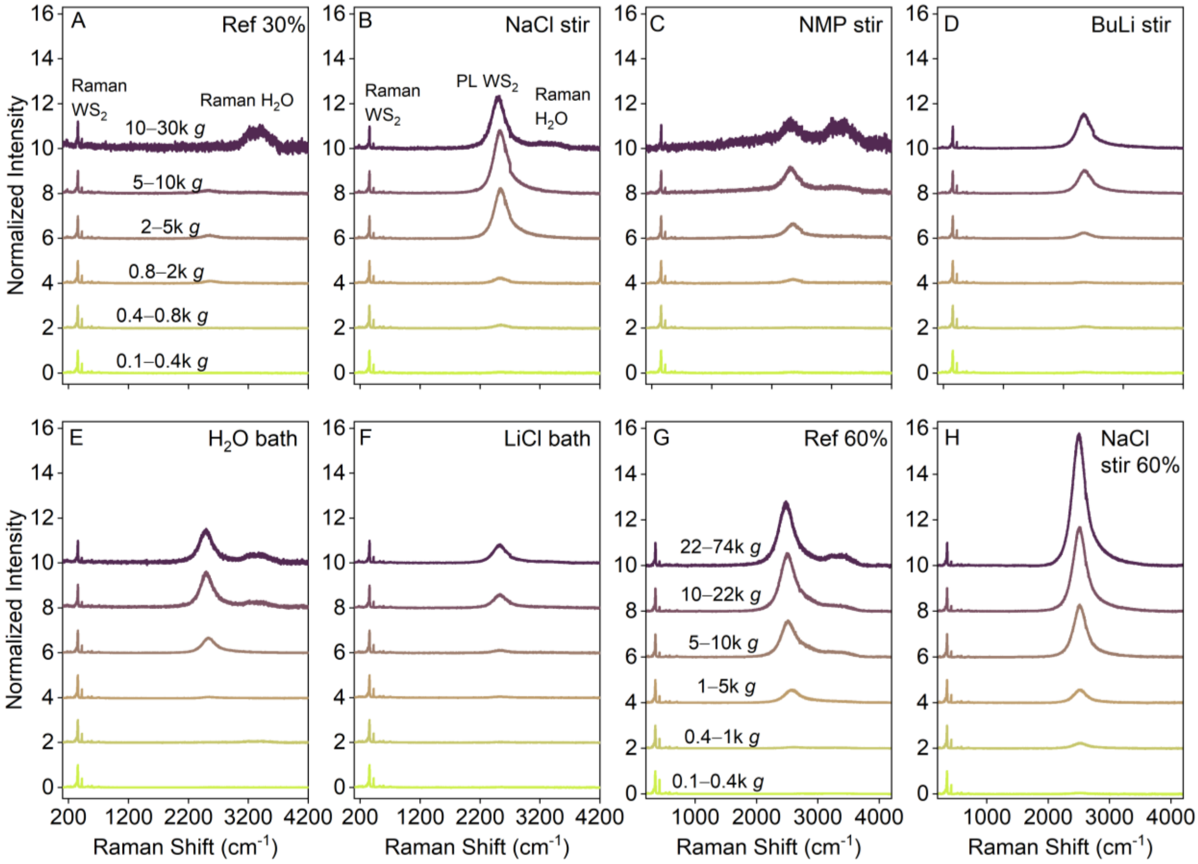

Figure 4.13: Raman spectra (532 nm excitation) of exfoliated and size-selected WS_2 nanosheet dispersions. All spectra feature characteristic Raman signals of 2H-WS_2. Additionally, PL related to the A-exciton of ML WS_2 becomes visible in dispersions with significant ML content, and Raman signals of water appear in spectra recorded from dispersions with relatively low WS_2 concentration, as indicated in A and B. Spectra are vertically offset for clarity. A: Ref 30 %, B: NaCl stir, C: NMP stir, D: BuLi stir, E: H_2O bath, F: LiCl bath, G: Ref 60 %, NaCl stir 60 %.

To quantify these observations, the Raman shift was converted to the energy scale and the PL signals were fitted by Lorentzians. Figure 4.14 exemplarily shows the fitted PL spectra of the 5–10k *g* fractions. The full data set is available in the Appendix (Figure A 9–Figure A 16). PL position, FWHM and PL/Raman ratio were extracted from the fits and are compared below.

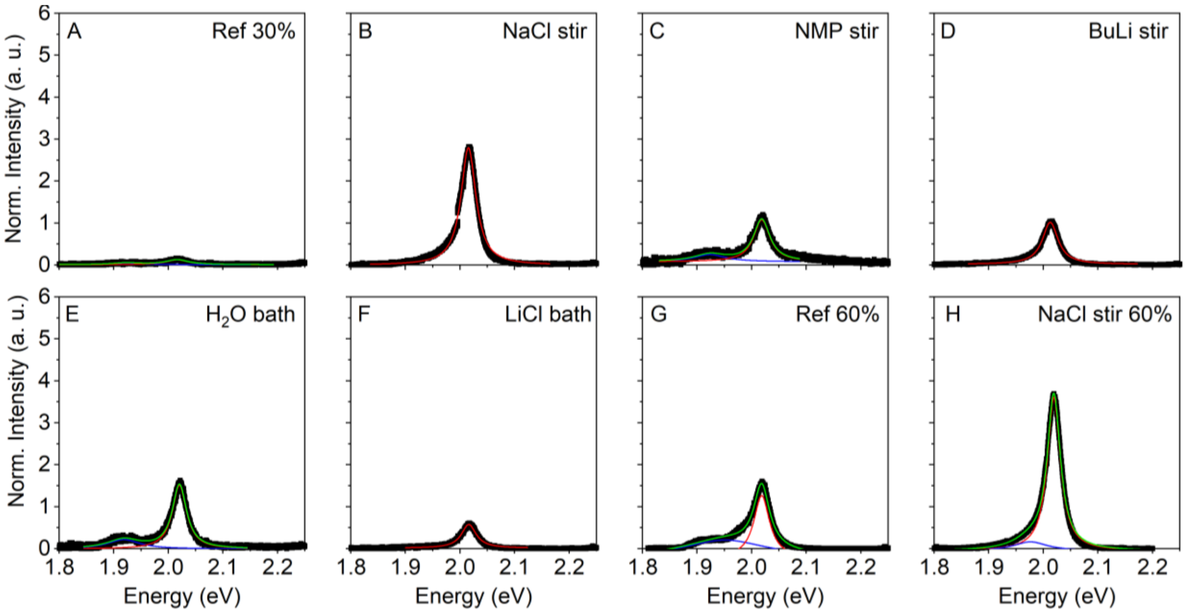

Figure 4.14: PL spectra (λ_{exc} = 532 nm) of the 5–10k *g* fractions of the size selection. The PL signals were fitted assuming a Lorentzian line shape. In some spectra, non-negligible H_2O Raman background is present and required fitting with two Lorentzians (Red line: PL of ML WS_2, blue line: Raman of water, green line: combined fit). A: Ref 30 %, B: NaCl stir, C: NMP stir, D: BuLi stir, E: H_2O bath, F: LiCl bath, G: Ref 60 %, NaCl stir 60 %.

Figure 4.15 summarizes the yield and size information extracted from the UV-Vis extinction spectra shown in Figure 4.12. The total yield of the exfoliation batches is presented in A and is the sum of the yields from the individual LCC fractions. The highest yield within the 30 % amplitude exfoliation series was found for the reference sample without any pretreatment (9 %), followed by the pretreated batches in the order BuLi stir (4 %), NaCl stir (3.5 %), LiCl stir (2.8 %), NMP stir (2.2 %), and H_2O bath (2.2 %). All yields determined from the pretreated batches are less than half of the reference yield. The same observation was made for the 60 % amplitude exfoliations. The total yield of NaCl stir 60 % is 8.7 % and comparable with the yield of Ref 30 %. For the 60 % amplitude reference sample, the total yield was found to be 20 %, which is more than twice of the yield of NaCl stir 60 %.

While it is easy to explain that the yields of the 60 % amplitude exfoliations are higher than the yields of the 30 % amplitude series due to the higher energy input, it is not intuitively rationalized why pretreatment of the starting material would reduce the yield. One potential explanation could be that residues of the pretreatment agents artificially increase the mass of the WS_2 powder and hence decrease the calculated yield. However, it is highly unlikely that this accounts for such a big difference. For example, the mass of surfactant in graphene samples was found to be less than 20 % after washing,[116] despite the lower density of graphene/graphite compared to WS_2. Unfortunately, no reasonable explanation was found.

A decreased yield seems to be an unfavorable effect of the pretreatment, but the major aim of this study was to investigate the impact of the pretreatment on the nanosheet dimensions or relative fluorescence intensity. Figure 4.15 B and C show the mean nanosheet length $\langle L \rangle$ (B) and the mean layer number $\langle N \rangle$ (C) as a function of the midpoint of the centrifugation boundaries, central RCF. These data are empirically found to follow a power law function, resulting in a linear curve progression on the log-log scale. The data points of the 60 % amplitude series fall a bit below the data points of the 30 % amplitude series, indicating that the nanosheets are generally smaller and thinner, due to higher energy input and a more proceeded exfoliation.

Figure 4.15 D shows the important correlation $\langle L \rangle$ vs $\langle N \rangle$. Without any pretreatment, a fixed ratio from the nanosheet length to thickness is expected, which would lead to data falling on a mastercurve. In contrast, in this plot, differences between the batches are discernible. For further and more quantitative evaluation, the data were fitted by power laws in the form of equation (4.4).

$$\langle L \rangle = 10^{a} \cdot \langle N \rangle^{n} \tag{4.4}$$

The prefactors a and the exponents n were extracted from the fits and are presented in Figure 4.15 E in a plot a vs n. Within the 30 % amplitude series, the data points of the pretreated batches group together, but the reference exhibits a higher prefactor and lower exponent. The sample NaCl stir 60 % groups together with the other pretreated materials, but Ref 60 % shows slightly higher values of a and n. As explained before, the prefactor a has a physical meaning and represents the characteristic ML length. The characteristic ML length is presented in Figure 4.15 F, where significant differences are observed. Within the 30 % amplitude series the characteristic ML length decreases in the order Ref 30 % (23 nm), NaCl stir (12 nm), BuLi stir (11 nm), H_2O bath (10 nm), NMP stir (8 nm), and LiCl bath (7 nm). The ML lengths of the two batches with 60 % amplitude sonication are 12 nm for NaCl stir 60 % and 14 nm for the reference.

Without any pretreatment, one would expect that only minor differences in the characteristic ML length are observed between the different batches, as has been explained and experimentally proved in chapter 4.1.3 using MoS_2 as model substance. In short, this is because the length to thickness aspect ratio is a material-dependent parameter which results from the intra- and interlayer binding energies and the equipartition of energy during the exfoliation process.[94] The fact that significant differences in the characteristic ML length are observed must be caused by altered interlayer binding energy, which is a strong indicator for successful intercalation by the pretreatment agents.

However, the aim of the pretreatment was to reduce the interlayer binding energies, which should lead to increased lateral dimensions of the nanosheets in pretreated samples and to an equal ML length for the two reference batches. The experimental data reveal an opposite trend: Within the 30 % amplitude series, the highest characteristic ML length (23 nm) was found for the reference and the largest ML length of pretreated samples (12 nm) is roughly half of the reference ML length. A similar, but less pronounced trend, was found for the two 60 % amplitude exfoliation samples, where the ML length of the reference (14 nm) slightly exceeds the ML length of NaCl stir 60 %

(12 nm). It should be highlighted that the ML length of Ref 30 % is the highest ML length across all batches and hence significantly higher than the ML length of Ref 60 % as well.

These experimental observations are in stark contrast to the expectations and indicate that the aspect ratio of the nanosheets must be influenced by additional factors, which are not considered in the relatively simple exfoliation model mentioned above. One factor which comes to mind are defects, which are always present and surely have an impact on the interlayer binding strength. Different characteristic ML lengths could thus be rationalized by different degrees of basal plane defectiveness. It is unclear, whether defects increase or decrease the interlayer binding energy, but the PL data suggest that the nanosheets of Ref 30 % are highly defective, as will be demonstrated later. This implies that the basal plane defects in the present samples lead to decreased interlayer binding energy. Consequently, the exfoliation rate of defective areas is increased and at the same time, the relative scission rate is decreased due to equipartition of energy.

With this in mind, the large characteristic ML length of Ref 30 % can be explained by the low energy input during sonication, which only allows the exfoliation of defective areas of the bulk material. As discussed above, the lateral dimensions of the resulting nanosheets are increased. This concept resolves the apparent contradiction that pretreatment reduced the characteristic ML length of the samples in the 30 % amplitude series. If successful intercalation decreased the out of plane binding strength, then exfoliation of defect free areas becomes possible despite the low energy input during sonication. The energy required for the exfoliation of these defect free areas can still be higher than the energy required to exfoliate highly defective areas, which can explain the reduced lateral dimensions of the nanosheets, reflected in the ML length. The same approach can be used for the interpretation of the differences between the reference batches Ref 30 % and Ref 60 %. The high energy sonication enables the exfoliation of defect free areas which again results in nanosheets which are laterally smaller but with lower defect density. A small impact of the pretreatment seems to remain under harsh sonication conditions, as can be seen by the reduced ML length of the batch NaCl stir 60 %. However, the difference to the reference is only small.

Interestingly the characteristic ML length of Ref 60 % is slightly larger than ML length of the pretreated materials of the 30 % amplitude series. This might indicate effective scission along basal plane defects, slightly increasing the ML length.

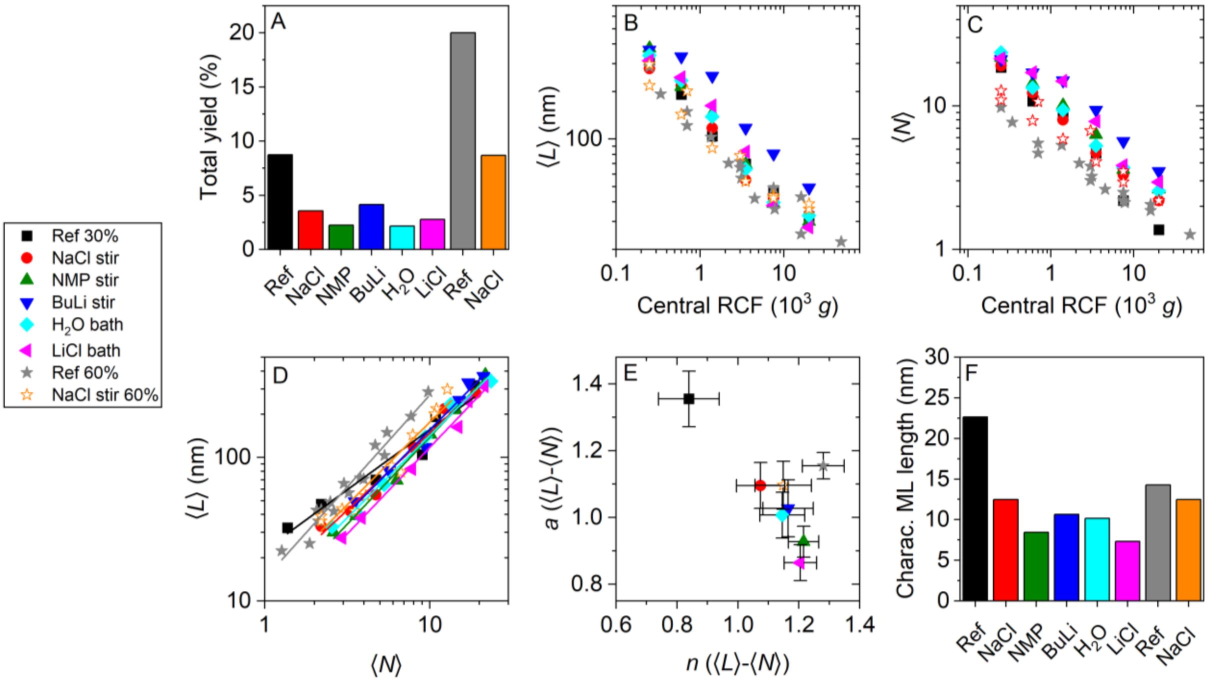

Figure 4.15: Yield and size information of exfoliated WS_2 nanosheets, derived from the optical extinction spectra shown in Figure 4.12. A: Total yield of the different exfoliation batches, where the total yield is the sum of the yields from the individual fractions obtained during LCC. B: Mean nanosheet length $\langle L \rangle$ as a function of central RCF. C: Mean layer number $\langle N \rangle$ as a function of central RCF. D: $\langle L \rangle$ as a function of $\langle N \rangle$, fitted by power laws in form of equation (4.4). E: Prefactor a as a function of the exponent n, extracted from the power law fits in D. F: Characteristic ML length of the nanosheets in the dispersions, calculated from the prefactors shown in E.

If the hypothesis made above was correct, the defect density of the nanosheets should be reflected in the PL emission. Figure 4.16 A and B show the PL position (A) and PL width (B) of the different dispersions as a function of the mean layer number. The data of the PL positions range from 2.012 eV (616 nm) to 2.024 eV (613 nm) and a slight redshift is observed for dispersions containing thicker and larger nanosheets. This is counterintuitive, considering that the PL emission only originates from the ML in the dispersion, but might be caused by variations in the defectiveness or energy transfer with few layer nanosheets, for example in incompletely exfoliated sheet stacks with protruding monolayers.

Differences in the PL position between the batches are small, considering the range of scatter in the data. Figure 4.16 C shows the PL position averaged over all dispersions obtained from each pretreatment method. The PL of the batches Ref 30 % and BuLi stir appear slightly redshifted, but no clear trend in the data is discernible. The data of the PL width (Figure 4.16 B) show FWHM values between 30 and 35 meV and no size-dependent trends. The average PL width of the batches is displayed in Figure 4.16 D. No clear trend between the batches is observed. The sharpest PL is observed for NaCl stir 60 % (31.2 meV), indicating a better quality of the ML. However, the differences to NMP stir (32.1 meV) and NaCl stir (32.4 meV) are only small. The information collected about the position or linewidth of the PL does not show any meaningful differences between the batches and thus do not provide any hints about the defectiveness of the nanosheets. However, it was already qualitatively demonstrated that there are significant differences in the PL intensity between the batches.

Figure 4.16 E and F show the PL/Raman ratios as a function of ⟨*N*⟩ and the data were fitted by power laws in form of equation (4.7). For clarity reasons, the data of the 30 % amplitude series (E) and the 60 % amplitude series (F) are plotted in two individual graphs. As already discussed earlier, the PL to Raman ratio of a TMD dispersion can be considered as a qualitative measure of the PLQY. The PLQY depends on the ML content of the dispersion on the one hand and on the intrinsic PLQY of the monolayers on the other hand. This implies that the plots in Figure 4.16 E and F, where the PL/Raman ratio is linked to ⟨*N*⟩, allow a comparison of the intrinsic PLQY of the monolayers. In all batches, the PL/Raman ratio decreases for increasing ⟨*N*⟩ or decreasing ML content, but differences are significant. Qualitatively, the data of the pretreated materials of the 30 % amplitude series (Figure 4.16 E) group together with some differences in the apparent slope (exponent *n*) and offset (prefactor *a*).

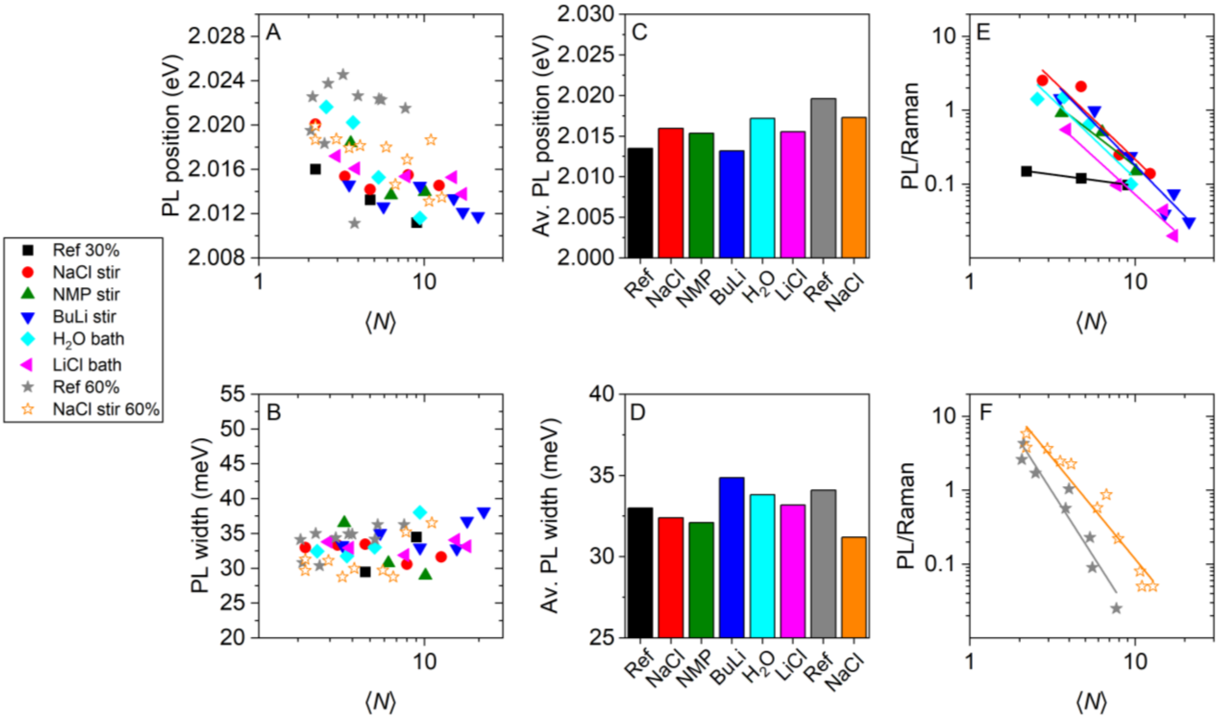

Figure 4.16: PL information derived from the PL and Raman spectra (Figure 4.13 and Figure 4.14). A: PL position as a function of ⟨*N*⟩. B: PL width as a function of ⟨*N*⟩. C: PL position averaged over all nanosheet sizes. D: PL linewidth averaged over all nanosheet sizes. E: PL/Raman ratio of the dispersions exfoliated with an amplitude of 30 % as a function of ⟨*N*⟩, fitted by power laws in form of equation (4.7). F: PL/Raman ratio of the dispersions exfoliated with an amplitude of 60 % as a function of ⟨*N*⟩.

The data points of Ref 30 % clearly fall below the data of the pretreated samples, with an apparent slope that is less steep. This leads to PL/Raman ratios of dispersions with high ML content which are much lower than their pretreated counterparts. A comparable trend is observed for the 60 % amplitude exfoliations in Figure 4.16 F, where the data points of Ref 60 % fall a bit below the data points of NaCl stir 60 %. However, this trend is less pronounced since the exfoliation conditions of Ref 60 % are already efficient.

$$\langle PL/Raman \rangle = 10^{a} \cdot \langle N \rangle^{n} \tag{4.7}$$

The prefactor *a* and the exponent *n* were extracted from the power law fits shown in Figure 4.16 E and F and are presented in Figure 4.17 A. Again, the data points of the pretreated materials of the 30 % amplitude series group together in the plot, with the reference being far off this grouping with lower prefactor *a* and larger exponent *n*. The sample NaCl stir 60 % sits close to the pretreated materials of the 30 % amplitude series, but with slightly higher prefactor *a* and lower exponent *n*. The exponent of Ref 60 % is a bit lower than the exponent of NaCl stir 60 %, but the prefactor is comparable.

The prefactors were converted to the PL/Raman ratios of a theoretical pure ML dispersion with $\langle N \rangle = 1$ (ML PL/Raman) and plotted against the characteristic ML length in Figure 4.17 B. The ML PL/Raman ratio is the qualitative measure of the intrinsic PLQY of the monolayers. Without the consideration of defects, the ML PL/Raman ratio is expected to depend on the characteristic ML length. This is because the edges of LPE produced nanosheets do not exhibit PL[108] and the edge contribution depends on the lateral dimensions of the nanosheets. Small nanosheets suffer from a higher edge contribution and are thus expected to exhibit a low ML PL/Raman ratio.

The expected relation is found within the pretreated batches of the 30 % amplitude series, where the ML PL/Raman ratio indeed increases with the characteristic ML length with only small deviations from this trend. The batches LiCl bath and NMP stir exhibit the smallest ML lengths and the lowest ML PL/Raman ratios (7 and 8, respectively). The ML PL/Raman ratio further increases in the order H_2O bath (17), NaCl stir (31), and BuLi stir (35). This trend continues with Ref 60 % which exhibits a slightly higher ML length and higher ML PL/Raman ratio (53). However, Ref 30 % exhibits the weakest ML PL/Raman ratio (0.2) despite the highest characteristic ML length. This contradiction must originate from the defectiveness. The effects of defects on the PL properties of TMDs are complex and can both weaken or enhance PL, as has been explained in the theory section of this thesis. For example, PL brightening was demonstrated on mechanically-exfoliated TMDs and explained by a mechanism based on exciton trapping.[46, 50, 51] In short, the excitons radiatively decay from a lower lying trap state which is related to the defects. However, since the PL emission occurs from a lower lying trap state, these PL enhancements should be accompanied with a redshift of the PL. This concept is not only known for TMDs but also for other materials such as carbon nanotubes.[153, 154] At the other end of the story, defects can induce non-radiative recombination of the exciton which leads to PL quenching.[46, 155] In the data sets recorded for this study, neither significant redshifts nor newly arising PL signals are observed, which hints toward the conclusion that defects in the present sets of samples lead to PL quenching and that the nanosheets in Ref 30 % are highly defective. This conclusion is further supported by the results of chapter 4.1.3, where the impact of the starting material on the dispersion quality in LPE was investigated using MoS_2 as model system. The strongest fluorescence was observed for the dispersions exfoliated from a single crystal of MoS_2. This is the bulk material of the highest quality, where the lowest defect density is expected.

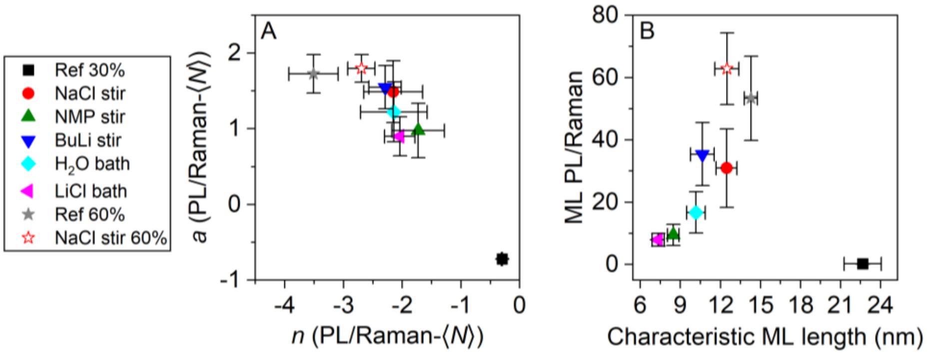

Figure 4.17: A: Prefactor *a* as a function of the exponent *n*, derived from the power law fits shown in Figure 4.16 E and F. B: PL/Raman ratio of a theoretical pure ML dispersion as a function of the characteristic ML length, calculated from the prefactors shown in A and Figure 4.15 E.

The combined size information and PL data support the hypothesis made above and deliver a comprehensive picture: The low energy input during the exfoliation of Ref 30 % only allowed the exfoliation of defective areas of the bulk material, where the interlayer binding strength is reduced. The resulting nanosheets are highly defective, which leads to PL quenching and a low PLQY. The pretreatments led to successful intercalation, which reduced the interlayer binding strength and enabled the exfoliation of defect free areas. The exfoliated nanosheets have a lower defect density and the PLQY values are improved. The pretreatments improved the exfoliation efficiency in the order LiCl bath < NMP stir < H_2O bath < NaCl stir < BuLi stir. However, tip sonication with a 30 % amplitude is not ideal for LPE and the dispersions of Ref 60 % are qualitatively better than the pretreated samples of the 30 % amplitude series. The high energy input allows the exfoliation of defect free areas without any additional pretreatment. Nevertheless, NaCl 60 % exhibits a (extrapolated) ML PL/Raman ratio of 63 and even exceeds the ML PL/Raman ratio of the reference, despite a slightly smaller characteristic ML length. This demonstrates that a small impact of the pretreatment remains even under harsh sonication conditions. While the study has limited relevance for practical lab work, it shines light on the exfoliation mechanism and the role of defects and contributes to important understanding of the LPE process as a whole.

4.1.5 Summary and Conclusion

In this chapter, both the impact of the choice of starting material and the impact of pretreatments of the bulk material on the dispersion quality, quantity and on nanosheet dimensions in sonication-assisted LPE were investigated on the example of MoS_2 and WS_2, respectively.

To address the first question, six different starting materials with variations in the crystallite size, purity, and defectiveness were exfoliated by tip sonication using a standard protocol, and the resulting stock dispersions were subjected to liquid-cascade centrifugation for size selection. Six different nanosheet fractions were collected from each starting material and characterized by UV-Vis, Raman, and photoluminescence spectroscopy. Yield and nanosheet dimensions were extracted from the UV-Vis spectra and it was demonstrated that these metrics remain unaffected by the choice of starting material, supporting a recently developed model which describes the area to thickness aspect ratio as a material dependent parameter, which is a result from the inter- and intralayer binding strength.

The PL of the MoS_2 dispersions was investigated by Raman and fluorescence spectroscopy. No changes in the PL position or linewidth were observed, but significant differences in the PL intensity were discernible. It was observed that the dispersions with the weakest PL were exfoliated from the bulk materials with the smallest crystallites, but it is possible that this is based on coincidence. A more likely explanation for the different PL intensities is based on different defect densities. The highest PL intensity was observed for the dispersions exfoliated from the pestled single crystal. Despite no experimental evidence for different levels of defectiveness, it is plausible that a single crystal has fewer defects and thus a higher relative PLQY.

To address the second question, bulk WS_2 powders were subjected to five different pretreatments prior to exfoliation with the aim to lower the interlayer binding strength through intercalation, and to increase the length to thickness aspect ratio of exfoliated nanosheets. Pretreatments included stirring in aqueous NaCl solution (NaCl stir), stirring in NMP (NMP stir), stirring in *n*-BuLi/hexane (BuLi stir), bath sonication in water (H_2O bath) and bath sonication in aqueous LiCl solution (LiCl bath). The pretreated bulk materials were exfoliated, and six different dispersions of each material were prepared by LPE and LCC and the dispersions were analyzed by UV-Vis and Raman spectroscopy. LPE was first conducted under relatively mild conditions with a sonication amplitude of 30 %, but the sample NaCl stir was repeated with 60 % sonication amplitude (NaCl stir 60 %).

Yield and nanosheet dimensions were extracted from the UV-Vis extinction spectra, and the relative PLQY of the nanosheets was compared through the PL/Raman ratios derived from the Raman spectra. The determined yield of the pretreated materials was decreased in comparison to the reference yields, but no reasonable explanation was found. Significant differences in aspect ratios and characteristic ML length of the nanosheets were observed, which hints towards successful intercalation of the pretreatment agents. However, in a counterintuitive manner, Ref 30 % exhibits the largest ML length, with smaller ML length for the pretreated batches. The Raman/PL spectra show that the PL of Ref 30 % is almost completely quenched, which suggests that the nanosheets are highly defective. The laterally smaller nanosheets of the pretreated starting materials exhibit stronger PL and thus lower defect density. The data strongly suggest that defects decrease the interlayer binding strength and that, in the case of Ref 30 %, the low sonication amplitude only allowed the exfoliation of defective areas of the bulk material, which explains the weak PL. The relative exfoliation and scission rates are in- or decreased, respectively, resulting in laterally larger nanosheets. The pretreatment enabled the exfoliation of defect free areas and the nanosheets are laterally smaller compared to the reference dispersion, but the relative PLQY of the nanosheets is increased. The exfoliation efficiency was improved by the pretreatment in the order LiCl bath < NMP stir < H_2O bath < NaCl stir < BuLi stir. However, the quality of the dispersions obtained from pretreated batches of the 30 % amplitude series was still worse than the quality of untreated samples exfoliated under the conditions of our standard protocol with 60 % amplitude sonication. High energy input during sonication allows the exfoliation of defect free areas without the necessity of pretreatment. Interestingly, both the characteristic ML length and the ML PL/Raman ratio of Ref 60 % are slightly higher than the values determined from the pretreated batches of the 30 % amplitude series, which might hint towards effective scission along defect sides. A small impact of the pretreatment agents remains with 60 % amplitude, even though the effect is small.

In conclusion, the knowledge that the choice of starting material can have an impact on the PL intensity of the exfoliated material is important for the preparation of fluorescent nanosheet thin films and hence to produce potential light-emitting devices. Single crystals of TMDs are expensive and no suitable starting materials for mass production of nanosheet dispersions, but it is worth to test different bulk powders to start with the most promising conditions possible.

Pretreatment of the starting materials has a negligible impact on the dispersion quality, when the established exfoliation conditions are chosen. Despite not having a relevance for practical lab work, the results of the pretreatment series are of academic interest and provide more information about the exfoliation mechanism or the role of defects and hence contribute to the understanding of the LPE process.

4.2 WS_2 Thin Films and Optical Microcavities

4.2.1 Introduction

Over the last years, strong light-matter coupling has gained tremendous interest and developed to a new field within chemistry. The research aims for both fundamental understanding of polariton physics and for paving the path for new, polariton based future applications, for example polariton lasers.[24]

Beside other materials, also TMDs are subject of ongoing research related to strong light-matter coupling. Excitons in TMDs are often described as so-called Wannier-Mott excitons which are commonly found in inorganic materials, but exhibit higher binding energies compared to traditional 3D semiconductors.[7] The relatively large binding energies in combination with high oscillator strength turn TMDs into promising candidates for strong light-matter coupling and polariton based devices.[10] The first evidence for exciton-polaritons in TMDs was found in MoS_2,[156] embedded in a dielectric microcavity. Later, more experimental[157] and theoretical[158] studies were published and research was driven towards applications, resulting in polaritonic devices such as a polariton LED based on ML WS_2.[25] Despite the progress that has been accomplished in the field, all demonstrations mentioned above have been based on CVD grown[156, 157] or mechanically-exfoliated[159-161] TMD flakes, restricting the experimental work with TMDs to non-scalable methods. Looking into the future, devices should be based on homogenous thin films allowing to cover large areas on arbitrary substrates in a reproducible fashion and enabling the production of potential devices on an industrial scale.

However, film preparation with nanosheets from dispersion is challenging. In a previous attempt, WS_2 was embedded in a PMMA matrix and deposited by spin coating.[28] While decent quality of the films was accomplished, no strong light-matter coupling was observed after implementing the films into optical microcavities. Another film preparation technique that recently gained attention in the field of two-dimensional materials is based on nanosheet self-assembly at phase interfaces. For example, Langmuir films of graphene oxide were formed at a water-air interface and deposited in a way comparable to Langmuir Blodgett or Langmuir Schaeffer deposition.[162] Self-assembly of TMD nanosheet films is slightly more complicated and needs to be carried out at liquid-liquid interfaces, such as ethylene glycol and *n*-hexane,[29] water and *n*-heptane,[163] or water and *n*-hexane,[30] as has been demonstrated for WSe_2 or MoS_2.

In this chapter, both WS_2-polymer composite films and WS_2-Langmuir films are produced and characterized with the aim to assess their suitability for the implementation in optical microcavities. Eventually, metal based optical microcavities were produced to investigate whether the obtained quality is sufficient to accomplish strong light-matter coupling with homogenous films of WS_2. Parts of the chapter were carried out in collaboration with Dr. Farnia Rashvand, Tim Nowack, and Dr. Andreas Mischok, as stated in the corresponding section.

4.2.2 WS_2-Polymer Composite Films

In this subchapter, composite films of WS_2 and PVK were prepared by spin coating with the purpose of eventually implementing the films in optical microcavities for the demonstration of strong light-matter coupling in homogenous TMD thin films. For this purpose, a high quality of the films is required, including a smooth surface of the film, good homogeneity, and spatial separation of the nanosheets in the film to preserve the optical properties of ML WS_2.

The relevant key parameters governing a potential Rabi splitting in an optical microcavity are the number of absorbers/emitters, the photonic mode volume, and the orientation of the transition dipole moment of the TMD nanosheets relative to the electric field. These parameters can be tuned by the optical density of the film, the film thickness, or the orientation of the nanosheets. Practically spoken, the number of absorbers can be tuned by the WS_2 content in the composite films, and the absorbance at the position of the A-exciton should be > 0.1. A maximum mode volume is accomplished by matching the exciton resonance with the ground mode of the cavity, which requires a relatively thin diameter of the cavity and hence a low thickness of the film. Lastly, the WS_2 nanosheets should have a parallel orientation with respect to the substrate, since the dipoles of spin-allowed bright excitons lie in the plane of the material and are more efficiently excited in a direction perpendicular to the nanosheet[7] (the excitation occurs perpendicular to the substrate in optical microcavities).

Preparation of WS_2-PVK Composite Films

The first challenge was to find a suitable polymer and solvent system. Ideally, the polymer should act as a matrix that spatially separates the nanosheets without any additional interaction with WS_2. Polymers such as PVK or PMMA are transparent in the visible range and thus suitable candidates. PMMA has already been reported as polymer matrix for WS_2 nanosheets, resulting in high quality films, efficiently preventing aggregation, and preserving the PL of WS_2.[28] Here, PVK was chosen, since it showed better stability in highly concentrated polymer/WS_2 solutions which were required to achieve sufficient optical densities of the films (as will be discussed later).

TMDs like WS_2 show good stability in environmentally friendly and non-toxic solvents like water or IPA, but these solvents are neither compatible with PVK nor PMMA. Another solvent which is commonly used in LPE without the necessity of additional surfactants is NMP. The downsides of NMP are toxicity, a high boiling point which makes the removal of solvent residues more difficult, and impurities which partially stem from solvent degradation and which are often present in the solvent.[164] PVK on the other side is commonly spin-coated from organic solvents such as toluene,[165] which is not compatible with TMDs. Due to the opposite solvent compatibilities, it was required to work in solvent mixtures. A promising solvent mixture which has been used before[28] and was adapted in this work is NMP and THF in a ratio 1:2.

The preparation of the WS_2/PVK films is illustrated in Scheme 4.3. In a first step the WS_2 nanosheets prepared by LPE and LCC (as described in chapter 4.1.2) were transferred from the aqueous SC-solution to NMP (A). The 5–10k *g* or 10–30k *g* fractions of the size selection were centrifuged at 30k *g* for 3 h to spin down the nanosheets. The sediment was redispersed in fresh H_2O and centrifuged again under identical conditions. These centrifugations serve as washing steps to remove the sodium cholate of the dispersion, and the supernatants of both centrifugation steps were discarded. The sediment of the second centrifugation was dispersed in NMP. Please note that it is important to distill the NMP before usage, since this purifies the solvent and removes impurities such as degradation products. The WS_2/NMP dispersion was centrifuged again to spin down the WS_2 nanosheets and to obtain a highly concentrated dispersion. The high density (1.03 g/cm^{-3}) and viscosity (1.65 cP) of NMP make the sedimentation process very slow which partially results in a loss of the ML nanosheets in the dispersion. While a loss of ML nanosheets is unavoidable, it can be reduced by long overnight centrifugations at centrifugation speeds such as 23k *g* (the reduction in ML content will be discussed in greater depth later). The sediment of this final centrifugation step was labelled as WS_2 concentrate and the supernatant discarded. While the expression sediment suggests a paste or solid state of WS_2 nanosheets, it is better described as a highly concentrated dispersion and can be handled with Eppendorf pipettes without any additional solvent. In fact, additional solvent decreases the WS_2 concentration of the final spin coating solution and should be avoided.

In a second step, it was required to mix the WS_2 concentrate with a prepared PVK solution. For the preparation of the PVK solution, PVK was dissolved in THF (30 g/L) and filtered, using a polytetrafluorethylene (PTFE) syringe filter with 45 µm pore size. For the mixing, the PVK/THF solution was slowly and successively added to the WS_2 concentrate (Scheme 4.3 B). Fast mixing can result in heavy aggregation of the highly concentrated WS_2 which is transferred to an unfavorable solvent system which prevents successful production of homogeneous thin films. In this step, polymer solutions containing PMMA tended to be more susceptible for this aggregation and PVK became the polymer of choice. The WS_2/PVK dispersion was centrifuged again for 30 minutes at 100 *g* to remove any potentially formed aggregates. The supernatant of this final centrifugation step was used for spin coating within 30 min after centrifugation.

In a third step, the films were prepared by spin coating, which was executed in a glovebox under inert gas atmosphere to reach higher reproducibility due to constant low humidity. In a classical spin coating process, the solution is dropped on a rotating or still standing substrate, called dynamic or static dispensing, respectively, where the dynamic dispensing is often considered to be superior to the static dispensing. Fast rotation of the substrate (~ 1000–8000 rpm) causes an equal distribution of the solution on the substrate and excess of solvent splatters away. Flattening of the solution takes place during the spinning and a thin polymer film forms. The spinning process is commonly continued until most of the solvent is evaporated and the thinning of the film is completed.

For the given purpose, classical spin coating was not successful, since the resulting films were thin with optical densities below the requirements (see Figure A 17 in the Appendix). The thickness of the films is typically increased by lower spin coating speeds or higher polymer concentrations. In this case, the spin coating speed was already at the lower limit of practicability and a higher polymer concentration would only increase the thickness of the film, but not the optical density associated with WS_2. Increasing the WS_2 concentration was not possible, since the NMP concentrate was already used without any further dilution. A last possibility would be to change the ratio from the WS_2 dispersion in NMP to the PVK solution in THF. However, significant deviations from the ratio used in this work failed due to reduced dispersion stability or bad film quality, if an insufficient amount of polymer was used. To achieve higher optical densities of the films for the cost of increasing film thickness, a rather uncommon and inventive spin coating protocol was applied, as illustrated in Scheme 4.3 C. 200 µl of the spin coating solution was dynamically dispensed on a cleaned glass substrate (20×25 mm) and spun at low speeds such as 100 rpm for ~ 10 minutes. After 10 minutes, the spinning speed was increased to ~ 1000 rpm for additional 60 s. After finished spin coating, the substrate was left at 80 °C for 1 h, allowing the WS_2/PVK film to dry.

The low spinning speed after dispensing allows the solution to spread on the substrate, but no solvent splatters away from it. As the substrate is spun at low speed, the volatile THF component of the solution evaporates, increasing the viscosity of the solution. The NMP component of the solution exhibits a low vapor pressure and high boiling point and prevents the solution from drying out. Acceleration to higher spin coating speed removes the excess of solvent and the actual thinning process takes place. The WS_2/PVK films obtained after finished spinning and baking show increased thickness and optical density compared to classical spin coating (as will be demonstrated later).

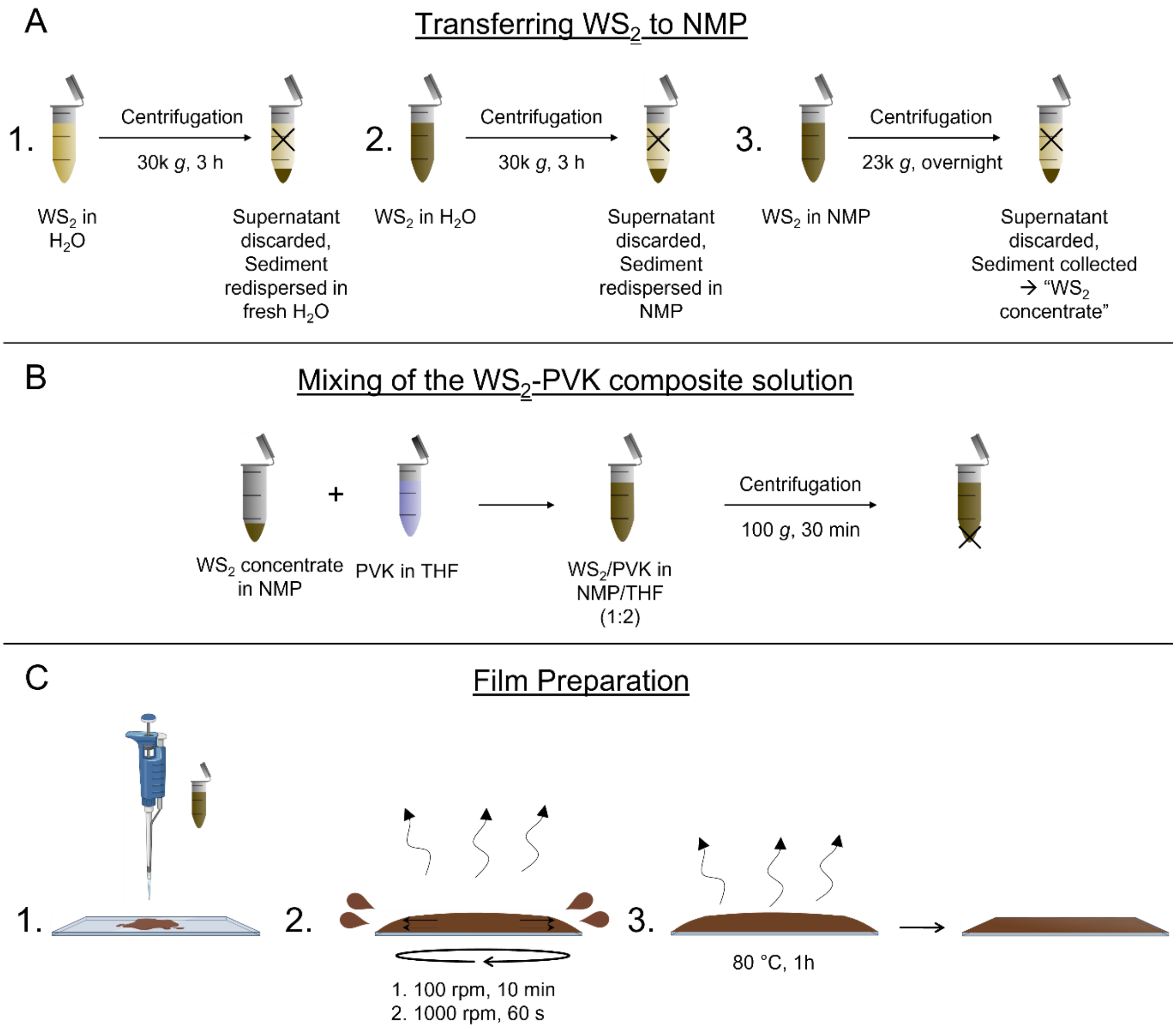

Scheme 4.3: Preparation of WS_2-PVK composite films. A: As-exfoliated WS_2 in H_2O/SC is transferred to NMP in a three-step process. First, the WS_2 nanosheets are spun down and the supernatant containing sodium cholate is discarded. The sediment is redispersed in fresh H_2O and the washing step is repeated. The sediment of the second centrifugation is redispersed in NMP and centrifuged overnight at 23k *g*. The supernatant is discarded again, and the dense sediment collected and labelled as WS_2 concentrate. B: The WS_2 concentrate in NMP was mixed with a PVK solution in THF in a ratio 1:2. C: The WS_2/PVK solution in NMP/THF is deposited on a substrate and spun at 100 rpm for 10 minutes. This allows the dispersion to spread on the substrate and the THF component to evaporate, increasing the viscosity of the solution. Subsequently the spin coating speed is increased to 1000 rpm for 60 s, where the actual thinning process takes place and where the excess of solvent flies off the substrate. After finished spin coating, the substrate is heated to 80 °C for 1 h to evaporate the solvent residues.

However, some drawbacks of the methodology remain. First, centrifugation in NMP for the preparation of the WS_2 concentrate leads to several difficulties. For example, the concentration of the WS_2 concentrate is not controllable in practical lab work, assuming that further dilution of the concentrate should be avoided. Significant differences in the concentration of the concentrate were observed between different batches, which impacts the WS_2 content in the resulting films and limits the reproducibility of the whole process. Additionally, the centrifugation in NMP leads to a loss of ML nanosheets, and long and time-consuming centrifugation is required to minimize this loss.

Figure 4.18 A and B show UV-Vis extinction spectra of aqueous WS_2 dispersions after size selection (10–30k *g*) and WS_2 concentrates in NMP after centrifugation for 4 h at 40k *g* (A) and for 15 h at 23k *g* (B). The second derivative of the A-exciton region of these spectra, d^2Ext/dE^2, are presented in Figure 4.18 C and D, respectively, and fitted by the second derivative of Lorentzians. In previous chapters of this thesis, the extinction at the region of the A-exciton was differentiated twice and subsequently smoothed by adjacent averaging, resulting in a combined signal of the A-exciton originating from FL and ML TMD nanosheets. Here, the extinction spectra were first smoothed by the Lowess method and differentiated twice in a second step, which preserves the fine structure of the signal. The difference between both methods is highlighted in Figure A 18 (Appendix). In the latter case, the optical transitions from both ML and FL flakes are distinguishable in the second derivative spectra, if the linewidth of the optical transitions is small enough (as it is in case of WS_2). Lorentz fits can be applied to determine the volume fraction of the monolayers, ML V_f, defined by equation (4.8).[108]

$$ML\ V_{\mathrm{f}} = \frac{\sum_{\mathrm{ML}} LWt}{\sum_{\mathrm{All}} LWt} \tag{4.8}$$

In the spectra of the initial aqueous WS_2 dispersions, the optical transitions of the A-exciton related to ML flakes are the major contribution of the spectra, observed at 2.03 eV. In the spectrum of the NMP concentrate which was obtained by short centrifugation of the NMP dispersion, the contribution of the ML flakes is drastically decreased (Figure 4.18 C). After long overnight centrifugation, the ML contribution is still reduced, but the decrease is less pronounced (Figure 4.18 D). The ML volume fractions of the dispersions were extracted and are compared in Figure 4.18 E. Additionally, the mean nanosheet length was calculated from the UV-Vis spectra and is compared in Figure 4.18 F. The aqueous dispersions exhibited a ML volume fraction of 0.57 and 0.59, respectively. In the WS_2 concentrate in NMP it is reduced to 0.08 after short centrifugation and 0.39 after long centrifugation. Similar observations were made for the mean nanosheet length, which is increased in the NMP dispersions in both cases, but where $\langle L \rangle$ is larger after short centrifugation (Figure 4.18 F). One would intuitively increase the centrifugation speed to accelerate the sedimentation process, but this was not possible due to leakage of the centrifuge tubes, which are not fully compatible with NMP.

Lastly, classical models for the prediction of film thickness, such as equation (4.9), where d_f is the film thickness and ω is the angular frequency, may not be applicable to the films. However, this is not relevant since the reproducibility of films produced in different batches is poor anyway.

$$d_{\mathrm{f}} \propto \frac{1}{\sqrt{\omega}} \tag{4.9}$$

Several batches of WS_2-PVK films were spin-coated with minor differences in the spin coating speed. The resulting films were characterized by AFM, profilometry, UV-Vis-, and Raman spectroscopy.

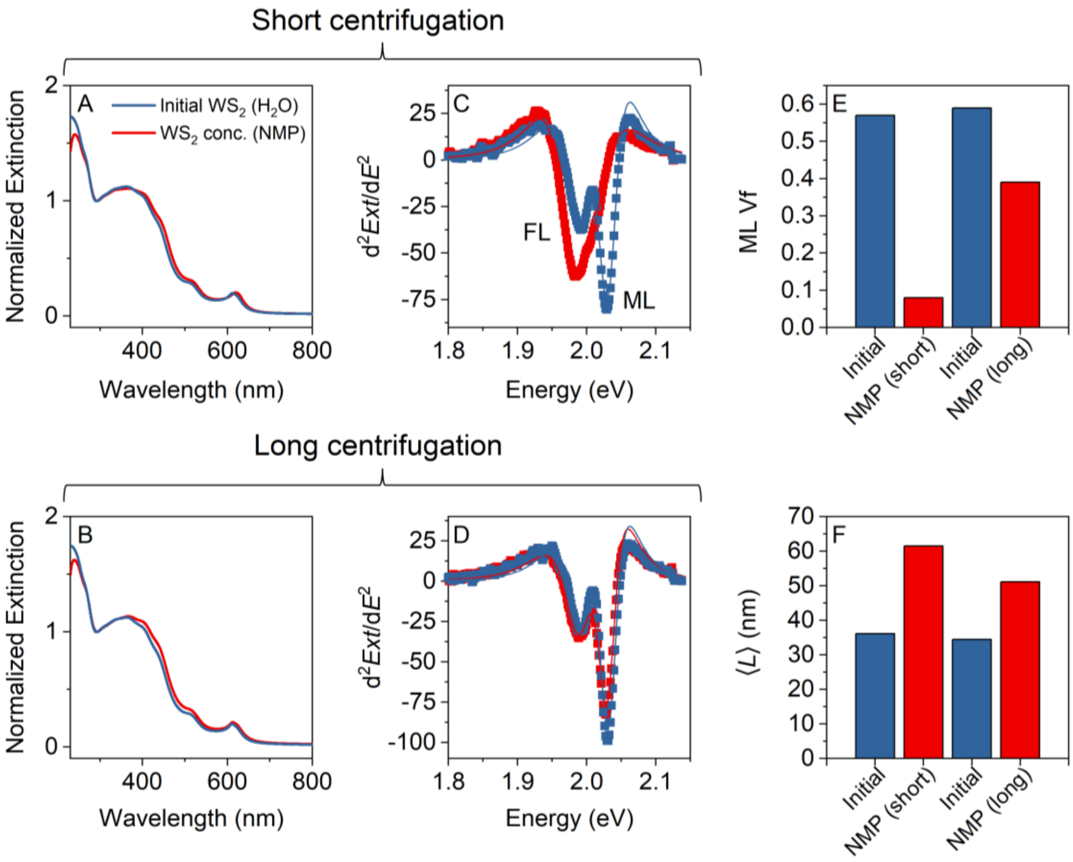

Figure 4.18: Characterization of WS$_2$ nanosheet dispersions before and after transfer to NMP. A, B: UV-Vis extinction spectra of the initial aqueous WS$_2$ dispersion and the WS$_2$ concentrate in NMP after short centrifugation (A) and long centrifugation (B). C, D: Second derivative of the A-exciton region of the UV-Vis extinction spectra shown in A and B. C refers to the short centrifugation and D refers to the long centrifugation. E: Monolayer volume fraction of the WS$_2$ dispersions extracted from the spectra shown in C and D. After short centrifugation most of the ML sheets remain in the supernatant. After longer centrifugation, the ML volume fraction is significantly increased compared to the shorter centrifugation. F: Mean nanosheet length ⟨*L*⟩ of the WS$_2$ dispersions, extracted from the UV-Vis extinction spectra shown in A and B. After both short and long centrifugation ⟨*L*⟩ is significantly increased, but the flakes are slightly smaller after long centrifugation.

Characterization of the WS$_2$-PVK Composite Films

Figure 4.19 shows AFM images of selected WS$_2$-PVK composite films (more images available in the Appendix, Figure A 19). In all cases, WS$_2$ nanosheets are visible under the polymer surface. Ideally, the nanosheets in the polymer matrix would be embedded in parallel orientation with respect to the polymer surface, but in all images a random orientation of the nanosheets is observed, and sharp lines under the surface indicate an undesired orientation of the nanosheet basal plane perpendicular to the polymer surface. Despite comparable film preparation, the morphologies of the films show significant differences. Some films exhibit a relatively smooth surface with most nanosheets being spatially separated below the surface (A), whereas others exhibit a relatively rough surface (B) where nanosheets are densely packed and aggregation is observed. In Figure 4.19 C, a third type of morphology is presented. Patches of aggregated nanosheets are visible below the surface and the polymer forms elevations and valleys between these patches. The difference between the films presented in Figure 4.19 A and B could be easily rationalized by different contents of WS_2 nanosheets in the films as a result of different concentrations in the WS_2 concentrate, but the differences between the films presented in Figure 4.19 B and C is not intuitively understandable. Within this work, it could not be resolved which factors or conditions lead to rather homogenous distribution (B) of the nanosheets or to the formation of nanosheet patches (C).

The nanosheet films were further characterized by profilometry, UV-Vis spectroscopy, and Raman spectroscopy. The films were scratched before the profilometry measurements to determine the film thickness.

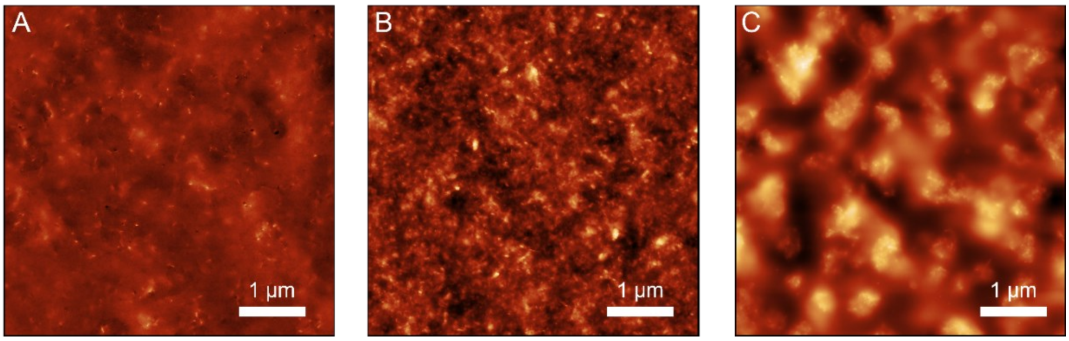

Figure 4.19: AFM Images of WS_2-PVK composite films, revealing different morphologies of the surface despite comparable preparation. While some films exhibit a smooth surface (A), others show a significantly higher roughness with more aggregation (B). In some films, patches of aggregated WS_2 nanosheets are visible below the surface and the polymer forms elevations and valleys between the nanosheet patches (C). In all cases a random orientation of the nanosheets is observed and sharp lines indicate an undesired perpendicular orientation of the nanosheet basal plane with respect to the polymer surface.

Figure 4.20 shows an example UV-Vis (A) and Raman (B) spectrum, and cross comparison between the properties of the WS_2-PVK composite films (C–F). Figure 4.20 A displays an exemplary UV-Vis spectrum, featuring the optical transitions of WS_2 as well as signals originating from PVK in the high energy region of the spectrum < 370 nm. The Raman spectra (B) of the films are comparable to spectra recorded from dispersion, although the WS_2-PL is weaker and a broad PL background of PVK is visible in the case of low WS_2 concentrations. Full data sets of UV-Vis and Raman spectra are available in the Appendix (Figure A 20–Figure A 29).

Optical densities and PL/Raman ratios were extracted from the UV-Vis and Raman spectra and are compared below. In Figure 4.20 C, the optical density of the films at the position of the A-exciton is plotted as a function of the film thickness. Ideally one would like to plot the optical density at 235 nm, where the extinction coefficient of WS_2 is relatively invariant with respect to the nanosheet size and where the optical density is proportional to the WS_2 concentration. However, this region is not accessible in the given sets of samples due to the absorption of PVK. The optical density at the position of the A-exciton was chosen since it is an important parameter for the evaluation whether the films are suitable for implementation in optical microcavities. The plot includes data from films produced in different batches, as indicated by different colors. Within one exfoliation and film preparation batch, the optical density can be considered as proportional to the film thickness. Between the batches, significant differences are observed despite comparable film preparation methods. This is attributed to different concentrations of the WS_2 concentrate in NMP, which is an uncontrollable factor and impacts the WS_2 content of the composite films, as has been discussed before.

For a comparison of the WS_2 contents, the optical density (of the WS_2 A-exciton) per 100 nm film thickness, OD/d, was defined and extracted from this plot. The unit (100 nm)$^{-1}$ was chosen for OD/d since it delivers intuitively understandable values in relevant orders of magnitude. OD/d was linked to the PL/Raman ratio and film roughness to find correlations between the film properties. Figure 4.20 D shows the PL/Raman ratios as a function of OD/d. The graph shows PL/Raman ratios of ~ 1 for low values of OD/d. At OD/d = 0.024 (100 nm)$^{-1}$, the PL/Raman ratio drastically decreases and falls to values below 0.1. This implies that WS_2-PVK composite films should be produced with OD/d values below 0.024 (100 nm)$^{-1}$ to preserve the PL.

The given purpose of implementing the films in optical microcavities requires optical densities of the A-exciton > 0.1, which results in film thicknesses > 400 nm. 400 nm should be understood as a theoretical, lower limit and neglects the scattering background which is present in this kind of nanosheet films and contributes to the extinction. The real absorbance at the position of the A-exciton is lower, which means that the optical density measured as extinction should be higher than 0.1, resulting in films thicker than 400 nm. This is not ideal, since thicker microcavities exhibit a lower mode volume of the cavity mode, decreasing a potential mode splitting.[166] It should be further noted that a PL/Raman ratio of 1 is still relatively low compared to values obtained from dispersions.

The root mean square (RMS) roughness (R_q) of the films, given by equation (4.10) or (4.11) with the profile height function $z(x)$ and the evaluation length l_r, was extracted from the AFM images and is plotted as a function of OD/d in Figure 4.20 E.

$$R_{\mathrm{q}} = \sqrt{\frac{1}{l_{\mathrm{r}}}\int_0^{l_{\mathrm{r}}} z(x)^2 \mathrm{d}x} \tag{4.10}$$

$$R_{\mathrm{q}} = \sqrt{(z_1^2 + z_2^2 + \ldots + z_3^2} \tag{4.11}$$

The lowest roughness is observed for the lowest OD/d values, but apart from this, no real trend is discernible. Intuitively one would expect increasing roughness with increasing OD/d, but the absence of this relationship indicates that additional factors impact the morphology of the film. High nanosheet concentrations lead to more aggregation and thus to larger particles which increases the roughness of the films (compare Figure 4.19 A and B), but the highest roughness

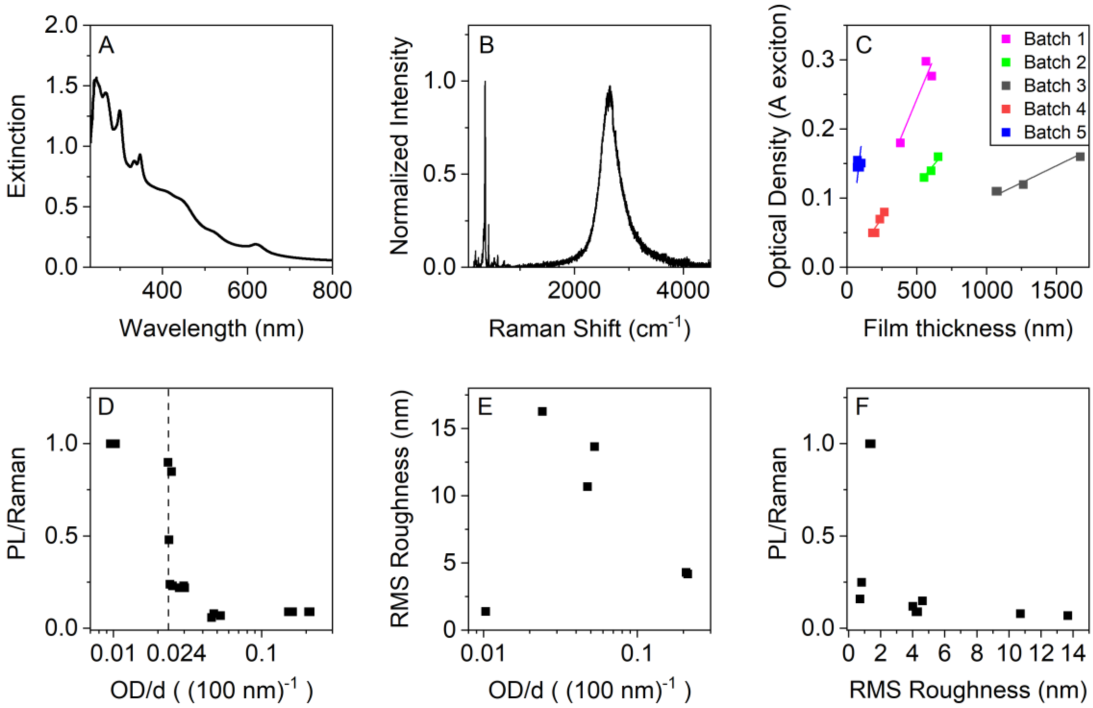

Figure 4.20: Characterization of WS$_2$-PVK composite films. A: Example UV-Vis extinction spectrum of a WS$_2$-PVK film. The spectrum features characteristic transitions of 2H-WS$_2$ and absorption bands from PVK (below 370 nm). B: Example Raman spectrum (λ_{exc} = 532 nm) of a WS$_2$-PVK film. C: Optical density (extinction) of the composite films at the position of the A-exciton as a function of film thickness. The films were produced in different batches, as indicated by different colors. Within one film preparation batch, the optical density can be considered as proportional to the film thickness. Significant differences are observed between different batches despite comparable film preparation conditions. D: PL/Raman ratio of the films as a function of the optical density per 100 nm film thickness (OD/d). At OD/d ~ 0.024 (100 nm)$^{-1}$ the PL/Raman ratio significantly drops. E: RMS roughness as a function of OD/d. Smooth films were only obtained when OD/d is low, but no real trend is discernible, indicating that additional factors impact the roughness. F: PL/Raman ratio as a function of the RMS roughness. The films with the lowest roughness exhibit the highest PL/Raman ratios.

values were found for films in which the nanosheets formed patches, and the polymer formed hills and valleys on the surface (see Figure 4.19 C). In the latter case, the local roughness might be small, but is high if calculated over large areas. Figure 4.20 F shows the PL/Raman ratios as a function of the RMS roughness. PL/Raman ratios above 0.2 were only recorded for films with low roughness (≤ 1 nm). Above this value, the PL/Raman ratios drop, and the PL intensities become negligible.

As demonstrated above, a correlation between the PL/Raman ratios and the optical densities of the films was found. Intuitively one would expect that the PL/Raman ratio of the film does not only depend on the WS$_2$ concentration in the film, but also on the PL/Raman ratio of the dispersion that was chosen for the film preparation. To test this hypothesis, the PL/Raman ratio of the film was plotted as a function of the PL/Raman ratio of the dispersion (Figure 4.21 A). The films with the highest PL/Raman ratios were indeed spin-coated from the dispersions with the highest PL/Raman ratios. However, there is no clear curve progression and the scatter of the data points is pronounced, since the PL/Raman ratio also depends on the optical density of the film. Figure

4.21 B shows the PL/Raman ratio of the films in dependence of both the PL/Raman ratio of the dispersion and the optical density of the film. The graph clearly shows that an acceptable PL/Raman ratio in the film is only obtained when two requirements are fulfilled: First, the PL/Raman ratio of the dispersion needs to be high. Second, the WS_2 content in the film needs to be low. It should be mentioned that the statement that WS_2-PVK composite films should be produced with OD/d values below 0.024 (100 nm)$^{-1}$ still holds, since this boundary was already found for the best WS_2 dispersions, as visible in Figure 4.21 B.

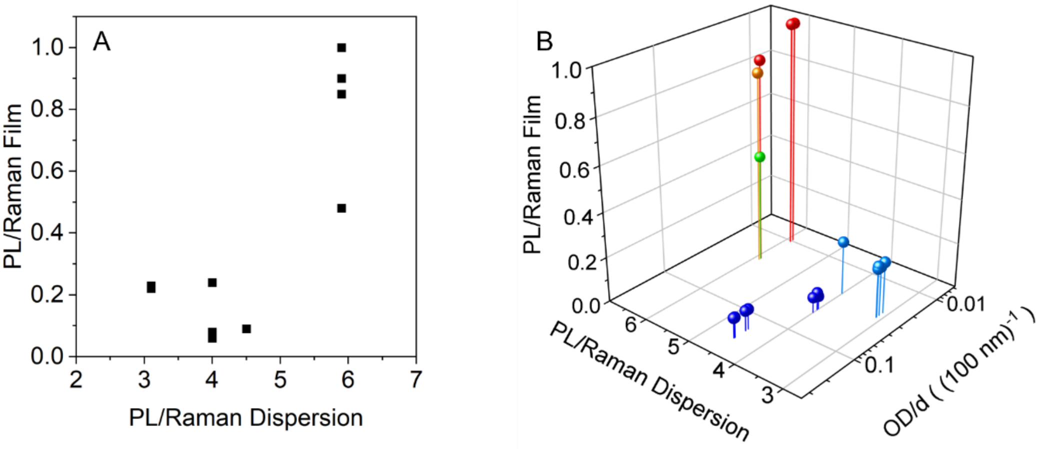

Figure 4.21: Comparison between the PL/Raman ratios of the WS_2-PVK composite films and the dispersions. A: PL/Raman ratio of the films as a function of the PL/Raman ratio of the dispersions. B: PL/Raman ratio of the films in relation to the PL/Raman ratio of the dispersions and the optical density of the films.

In conclusion, the WS_2-PVK films show limited suitability for the implementation in optical microcavities. This is because the film quality suffers from high WS_2 content which leads to heavy aggregation, resulting in vanished PL and high film roughness. Acceptable film quality was only achieved for low WS_2 content of the film, which implies that high thicknesses of the films are required to achieve sufficient optical densities. This is undesired since it decreases the mode volume of the cavity photon and thus a potential mode splitting. Additionally, the reproducibility of this film preparation technique is low, making it difficult to plan experiments and to predict film thickness. Nevertheless, the films were later implemented in microcavities to test whether strong light-matter coupling is possible despite the restrictions mentioned above.

4.2.3 Langmuir Films of WS_2 Nanosheets

In this subchapter, WS_2 nanosheet films were prepared by nanosheet self-assembly at liquid-liquid interfaces, as has been demonstrated in a couple of publications.[29, 30, 163] In literature, these films are often called Langmuir-Blodgett or Langmuir Schaeffer films. However, these expressions refer to specific deposition methods which are strictly spoken not applied. For correctness and simplicity, the films in this chapter will just be denoted as Langmuir films. In principle, the requirements on the films are identical to the requirements described in the beginning of chapter 4.2.2. However, the thickness of the films and the orientation of the nanosheets are intrinsically within the requirements due to the nature of the preparation methodology. This simplifies the optimization process and allows to keep a focus on other properties, such as maximizing PL.

The preparation of the Langmuir films in this chapter partially includes experimental contribution from Dr. Farnia Rashvand (LPE and LCC) and Tim Nowack (functionalization of WS_2).

Preparation of Langmuir Films through Self-Assembly at Liquid-Liquid phase Interfaces

The film preparation methodology of this subchapter is illustrated in Scheme 4.4. WS_2 in IPA was injected to a water/hexane phase-interface (A), leading to self-assembly of the nanosheets and film formation at the phase interface. For the solvent transfer to IPA, the aqueous WS_2/SC dispersion collected during the size selection was first washed by centrifugation at 31k *g*, where the sediment was subsequently redispersed in fresh H_2O. In a second step, the centrifugation was repeated, but the sediment was redispersed in IPA. In principle, other solvent systems such as water/toluene and deposition from NMP were successfully tested, but eventually neglected due to the unfavorable properties of NMP and concerns about WS_2/NMP dispersions that have been discussed before (see chapter 4.2.2).

After completed nanosheet assembly, the hexane layer was removed from the top (B) without destroying the WS_2 film. Residues of hexane were allowed to evaporate, before the substrate was vertically lifted, keeping an orientation parallel to the surface and nanosheet film (C). Rather large amounts of water remain on the substrate due to its horizontal orientation and long drying times (~ 15 h) under ambient conditions were required. The drying was finished by heating the nanosheet film to 50 °C for 1 h under vacuum. Shortening the drying time by applying heat or vacuum from the beginning was not possible, since it led to undesired cracks in the film. In principle it is possible to lift the substrate in a vertical or diagonal orientation to avoid large amounts of water on the substrate, but this increases the risk to tear the nanosheet films, limiting the reproducibility of the method. Without good reproducibility, stacking of multiple nanosheet films to achieve a desired thickness becomes very challenging – if not impossible.

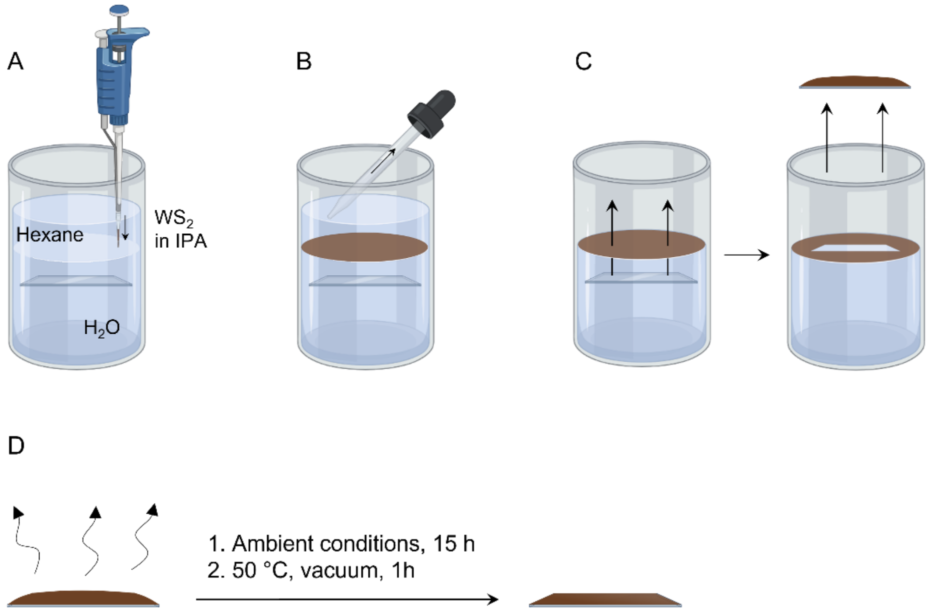

Scheme 4.4: Film preparation by nanosheet self-assembly at a liquid-liquid phase interface. WS_2 in IPA is injected to a water/hexane phase interface (A), leading to self-assembly of a nanosheet film at the interface. The hexane layer was removed from the top (B) without destroying the nanosheet film. A substrate placed in the water phase was vertically lifted (C). The substrate was left under ambient conditions, allowing the substrate to dry (D). The drying was finished by heating the nanosheet film to 50 °C for 1 h under vacuum.

As will be presented and discussed below, the fluorescence properties of these self-assembled nanosheet films can be improved by covalent functionalization of the nanosheets with diazonium salts. Functionalization of TMDs with diazonium salts under mild conditions was first demonstrated with MoS_2.[167] With other materials such as carbon nanotubes, this kind of functionalization can lead to brightening of the PL, attributed to exciton trapping at the introduced sp^3 defects.[153, 154] While brightening of the PL is not observed in case of TMDs, the functionalization can help to preserve the PL during film formation, as the monolayers are electronically decoupled. The functionalization with 3,5-dichlorobenzenediazonium tetrafluoroborate is presented in Scheme 4.5 A and was carried out according to Scheme 4.5 B by Tim Nowack.[168] WS_2 is first transferred to MeCN, where the reaction with the diazonium salt takes place, and is subsequently washed, and transferred to IPA. The functionalized nanosheets feature increased stability in IPA which is another advantage of the functionalization.

Several WS_2 nanosheet films were produced from the size selection fractions 1–5k *g*, 5–10k *g*, and 10–30k *g*, including both pristine and functionalized WS_2. Fractions containing larger nanosheets were neglected due to the low ML content and typically broader nanosheet size distribution. Up to five layers of nanosheet films were successively deposited on top of each other until an optical density was achieved that is sufficient for strong coupling experiments. The films were characterized by AFM, UV-Vis, and Raman spectroscopy after each step of deposition.

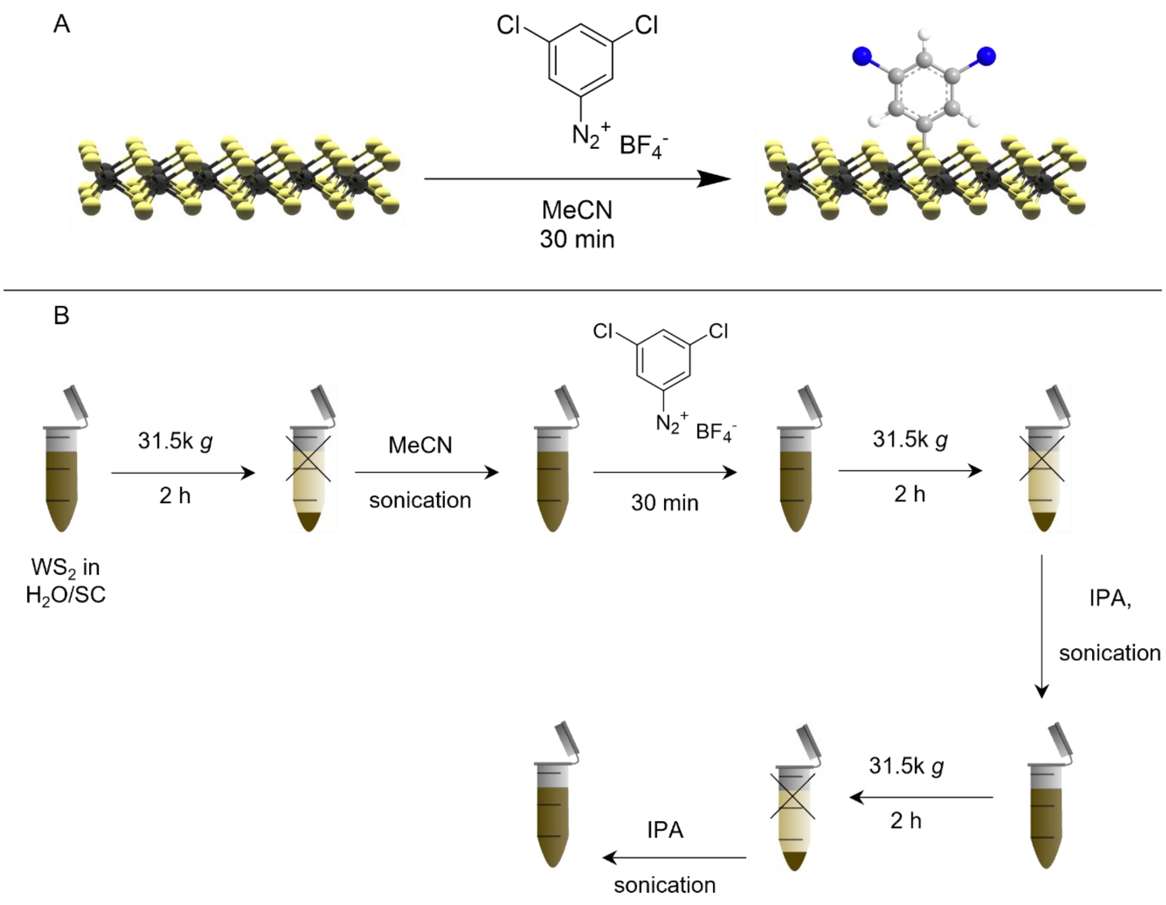

Scheme 4.5: Functionalization of WS_2 with 3,5-dichlorobenzenediazonium tetrafluoroborate. A: Functionalization scheme. B: Experimental procedure of functionalization. WS_2 is first transferred to MeCN, where the reaction with the diazonium salt takes place. The functionalized WS_2 is washed and transferred to IPA.

Characterization of WS_2 Langmuir Films

Figure 4.22 A and B show selected AFM images of the nanosheet films deposited from the 5–10k *g* fraction after one deposition (A) and 5 depositions (B) (full data set is available in the Appendix, Figure A 30–Figure A 32). In contrast to the WS_2-PVK composite films, the nanosheets lie mostly flat on the substrate. After 5 depositions, the morphology of the films appears slightly rougher, but no heavy aggregation is observed. The RMS roughness of the nanosheet films was extracted from the AFM images and is compared in Figure 4.22 C. For all fractions of the size selection, the roughness increases with the number of depositions. The highest roughness is observed for the 1–5k *g* fraction, containing the largest nanosheets. The roughness of the films deposited from the fractions 5–10k *g* and 10–30k *g* are in a comparable range with values of ~ 3.5 nm for a single deposition, rising to ~ 6 or ~ 7 nm after the fifth deposition. These values are higher than values measured for some of the WS_2-PVK composite films, but only if the OD/d of the composite films was low, which resulted in films with high thickness if required optical densities were accomplished. The thickness of the Langmuir films is 25 nm after 3 depositions in case of the fraction 1–5k *g*, and 19 nm or 13 nm after 5 depositions in case of the fractions 5–10k *g* or

10–30k *g*, respectively (Figure 4.22 D). This allows the design of optical microcavities with diameters of $L_{cav} = \lambda_C/2$ and the placement of the self-assembled nanosheet films at defined positions in the cavities (typically at the maximum of the electric field amplitude related to the cavity photon), using optical spacers such as Al_2O_3 or PMMA. Higher volumes of the photonic modes are consequently possible, compared to cavities with WS_2-PVK composite films, which needed to be thicker to obtain sufficient optical densities and where the film would be distributed over the whole length of the cavity.

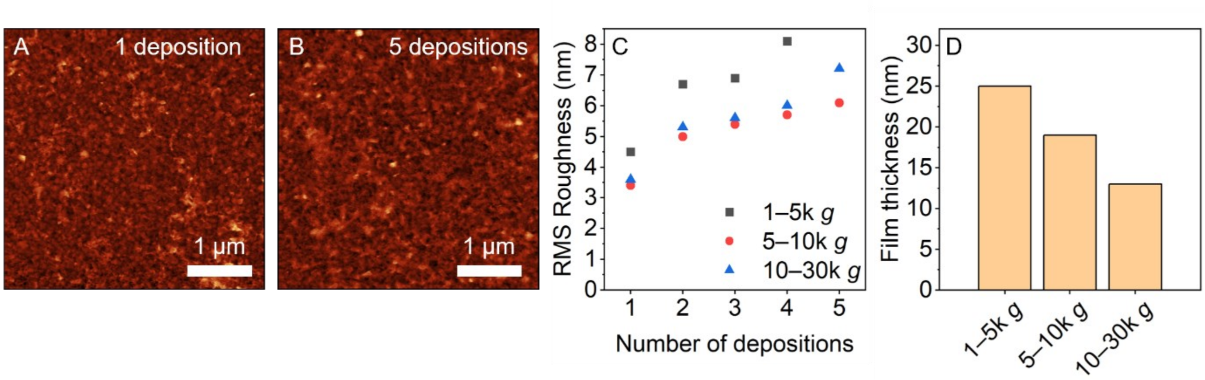

Figure 4.22: AFM investigation of WS_2 films prepared by nanosheet self-assembly at a water/hexane phase interface. A, B: Example AFM images of WS_2 films deposited from the 5–10k *g* fraction of the size selection, including an image that was recorded after a single deposition (A) and an image that was recorded after 5 depositions (B). C: RMS roughness of the WS_2 films as a function of the number of depositions, including films deposited from the size-selected fractions 1–5k *g*, 5–10k *g*, and 10–30k *g*. D: Thickness of different nanosheet films. The thickness of the 1–5k *g* film was measured after 3 depositions, and the thickness of the nanosheet films 5–10k *g* and 10–30k *g* after 5 depositions.

Figure 4.23 A–C presents the UV-Vis extinction spectra of the nanosheet films. The optical density increases with the number of layers, but no spectral changes are observed, except for a slightly increasing scattering background in the low energy region (700–800 nm). An increasing scattering background is undesired but remains in an acceptable range, and the absorption band of the A-exciton is still pronounced. The extinction at 235 nm, Ext_{235}, where the extinction coefficient is relatively invariant with respect to the nanosheet size, was extracted from the UV-Vis spectra and is compared in Figure 4.23 D. Within one nanosheet fraction, Ext_{235} rises linearly with the number of depositions. Linear fits with fixed intercepts (fixed to 0) were applied and the slope of these fits was extracted. The slope of the fits represents the optical density at 235 nm of a single deposition and decreases with the nanosheet size from 0.16 for the 1–5k *g* fraction over 0.10 for the 1–5k *g* fraction to 0.07 for the 10–30k *g* fraction. The extinction at the position of the A-exciton, $Ext_{A\text{-}exc}$, is 0.25 after 3 depositions of the 1–5k *g* fraction, 0.23 after 5 depositions of the 5–10k *g* fraction, and 0.15 after 5 depositions of the 10–30k *g* fraction. This means that the optical densities of the deposited films are sufficient for the implementation in optical microcavities for strong light-matter coupling.

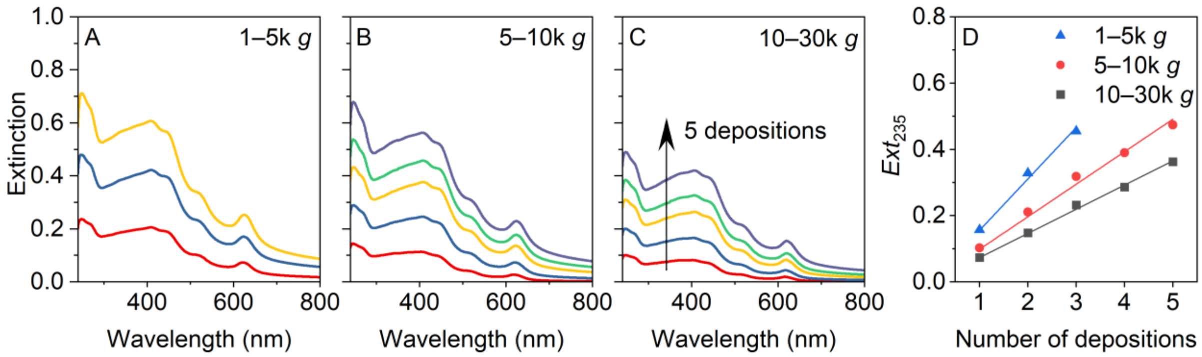

Figure 4.23: UV-Vis spectroscopy on WS_2 films prepared by nanosheet self-assembly at a water/hexane phase interface. A–C: UV-Vis extinction spectra of WS_2 films deposited from the LCC fractions 1–5k *g* (A), 5–10k *g* (B), and 10–30k *g* (C). Up to 5 depositions were stacked on top of each other. D: Extinction of the nanosheet films at 235 nm as a function of the number of depositions, including linear fits. The intercept of the fits was fixed to 0.

The Raman spectra of the nanosheet films are presented in Figure 4.24, with the spectra of pristine WS_2 being displayed in the top row of the figure. Films produced from the 1–5k *g* fraction show only negligible PL (A) due to the low ML content of the dispersions and restacking of the few ML flakes during film preparation, quenching the already weak PL. The PL remains partially preserved in films deposited from the 5–10k *g* and 10–30k *g* fraction but decreases with increasing number of depositions. Additionally, a broadening of the PL signal is observed. The bottom row shows the Raman spectra recorded from the nanosheet films of functionalized WS_2. In all cases, the PL decreases with increasing number of depositions. However, the drop in PL is significantly lower than observed for the pristine WS_2. The films of the fraction 1–5k *g* funct show weak, yet clearly discernible PL. The PL/Raman ratio of films produced from the fractions 5–10k *g* funct and 10–30k *g* funct is substantially higher than the pristine counterparts. Additionally, no broadening of the PL is observed.

To quantify these observations, the PL was fitted by Lorentzians (Appendix, Figure A 33–Figure A 38) and PL position, linewidth, and PL/Raman ratio were extracted from the fits and are compared in Figure 4.25. The PL position of the pristine WS_2 samples shows some scatter in the data with values ranging from ~ 1.96 to ~ 1.98 eV (A). The PL is slightly redshifted in comparison to the dispersion, and the fractions 5–10k *g* and 10–30k *g* show a slight blue shift with increasing number of layers. However, considering the scatter in the data, this blue shift is only small. The linewidth of the PL is specified as FWHM and shows pronounced scatter in the data as well. Values between ~ 80 and ~ 175 meV were found, which is substantially broadened compared to the dispersion (B). This scatter in the data observed for PL position and FWHM might be induced by asymmetrical broadening of the peaks. As a result, the PL is not well described by a single Lorentzian, resulting in poor fit quality. The fit quality is further influenced by the signal to noise ratio which is low due to the weak PL of the nanosheet films.

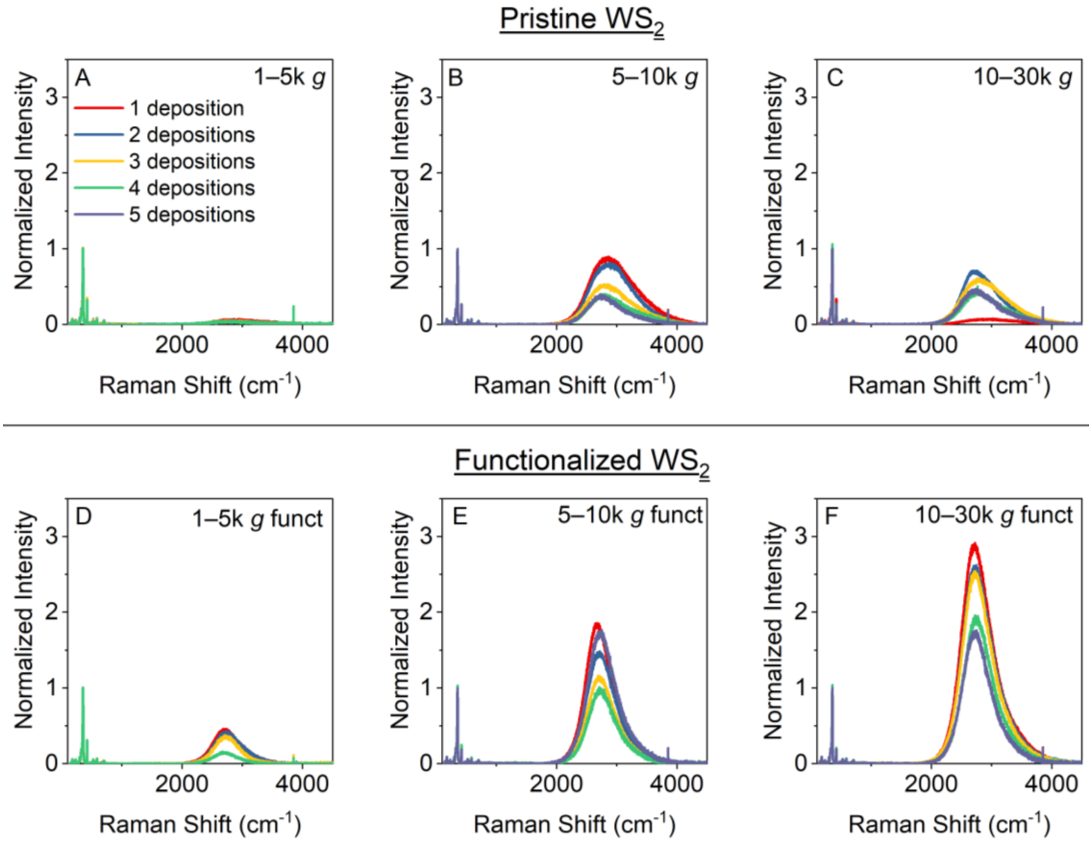

Figure 4.24: Raman spectra (λ_{exc} = 532 nm) of WS_2 films prepared by nanosheet self-assembly at a water/hexane phase interface. The WS_2 films were deposited from the size-selected fractions 1–5k *g*, 5–10k *g*, and 10–30k *g,* and up to 5 depositions were stacked on top of each other. A–C: Spectra of nanosheet films deposited from pristine WS_2. D–F: Spectra of nanosheet films deposited from WS_2, functionalized with 3,5-dichlorobenzenediazonium tetrafluoroborate. In all cases, the Raman spectra show characteristic Raman signals of 2H-WS_2 and photoluminescence associated with the A-exciton, which decreases with increasing number of depositions. The PL intensity and PL shape significantly varies between the batches, and the PL of the nanosheet films deposited from functionalized WS_2 exhibit stronger PL with less broadening of the signal.

The PL/Raman ratios decrease with the number of depositions in all cases. For the 5–10k *g* and 10–30k *g* fraction the PL/Raman ratio remains below 1, even after a single deposition. In case of the 1–5k *g* fraction, the PL is negligible and PL/Raman ratios below 0.05 were determined. Figure 4.25 D–F show the PL data recorded from the nanosheet films deposited from functionalized WS_2. With PL positions between 1.98 and 1.99 eV no redshift of the PL and no pronounced scatter in the data is observed (D). Significant differences between the nanosheet sizes are not observed. No broadening of the PL is observed and values of the FWHM are between 55 and 72 meV (E). However, most data points fall between 65 and 72 meV. 55 meV was only determined for the fraction 1–5k *g* funct after 3 and 4 depositions, respectively, where the PL is weaker and the reliability of the fit worse. The PL/Raman ratios of the functionalized WS_2 films again decrease with the number of depositions, but the values remain much higher in comparison to the films deposited from pristine WS_2. The fraction 10–30k *g* funct exhibits a PL/Raman ratio of ~ 3 after a single deposition which remains 1.8 after 5 depositions, indicating successful electronic decoupling through the functional group. PL/Raman ratios of the fractions 5–10k *g* funct or 1–5k *g* funct range from 1.9 to 1, or 0.5 to 0.2, respectively.

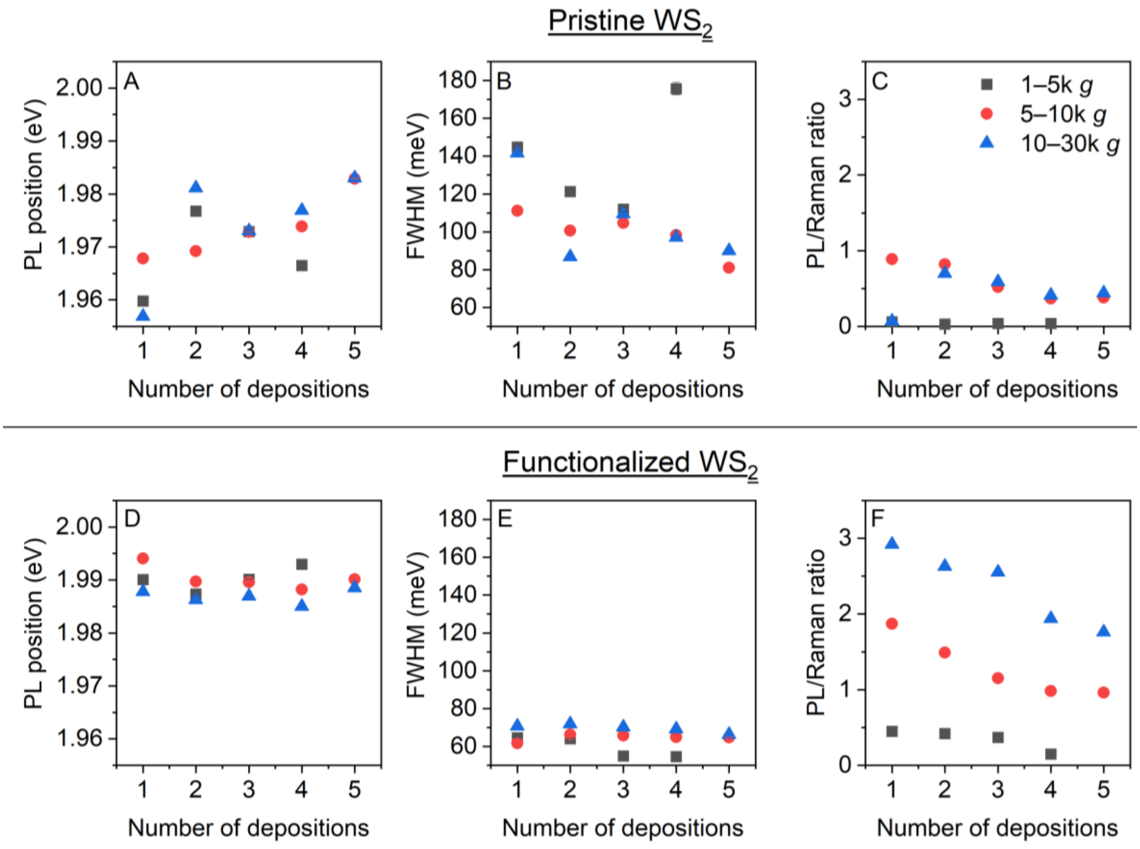

Figure 4.25: PL information about WS$_2$ nanosheet films derived from the Raman and PL spectra presented in Figure 4.24 and Figure A 32–Figure A 38 (Appendix). Top row: PL position (A), FWHM (B) and PL/Raman ratio (C) acquired from WS$_2$ films without functionalization of the nanosheets. Bottom row: PL position (D), FWHM (E) and PL/Raman ratio (F) acquired from WS$_2$ films functionalized with 3,5-dichlorobenzenediazonium tetrafluoroborate. Error bars are errors of the fits.

In conclusion, the deposited Langmuir films are superior in direct comparison to the WS$_2$-PVK composite films and are promising for the implementation in optical microcavities and for strong light-matter coupling experiments. Self-assembly of WS$_2$ nanosheets at a liquid-liquid phase interface with subsequent deposition results in relatively homogenous nanosheet films. Multiple depositions of the nanosheets allow the achievement of optical densities required for the implementation in optical microcavities. While the intensity of the photoluminescence decreases with increasing number of depositions, it remains in an acceptable order of magnitude if the nanosheets are functionalized with 3,5-dichlorobenzenediazonium tetrafluoroborate. The functionalization further prevents broadening or shifts of the PL.

4.2.4 Optical Microcavities with Thin Films of WS_2

In this subchapter, the WS_2 films were implemented in optical microcavities with the aim to observe strong light-matter coupling in large scale thin films of WS_2 nanosheets. As elucidated in the introduction of this paper, an important parameter of cavities is the quality factor (*Q* factor), since it is linked to the lifetime of a photon inside the cavity, which commonly dominates the losses in a cavity. To observe a Rabi splitting and hence strong coupling, the coupling between excitons and photons must be greater than the loss rates. The quality factor of a cavity is experimentally accessible by the linewidth of the cavity, which allows to rephrase the last statement: To observe strong coupling, a potential splitting at the resonances must be larger than the transmission linewidth of the cavity (equation (4.12)).[169]

$$\Omega > \frac{\Delta\omega_c \Delta\omega_X}{2} \tag{4.12}$$

This implies that the linewidth or the Q factor should be as low or as high as possible, respectively. However, for practical purposes there is no reason that the cavity linewidth needs to be significantly lower than the linewidth of the excitonic transition, and a comparable linewidth between those is commonly a good compromise between *Q* factor of a cavity and its transparency (since a higher *Q* factor is associated with higher reflectivity of the mirrors).[169] In previous publications, Rabi splittings in TMD based microcavities were reported to lie between ~ 40 and ~ 70 meV, when CVD grown ML TMDs were used.[156, 157, 170, 171] However, a splitting up to 270 meV was observed when mechanically-exfoliated few layer WS_2 was employed, due to the higher numbers of emitters.[160] Therefore, a potential splitting in thin films is expected in the order of hundreds of meV.

Design and Preparation of WS_2-based Microcavities

Both the WS_2-PVK composite films and the WS_2 Langmuir films were implemented in optical microcavities, including a closed (Scheme 4.6 A) and open (Scheme 4.6 B) cavity design with WS_2-PVK composite films, and closed cavities with the WS_2 Langmuir films (Scheme 4.6 C). For the closed cavities of the composite films, WS_2/PVK was embedded between two silver mirrors (Scheme 4.6 A). In principle, distribute Bragg reflectors (DBR) would be an alternative to metal-based mirrors and feature higher reflectivity, but Ag mirrors were chosen for both simplicity and higher mode volumes. Mode volumes in DBRs are reduced, since the penetration depth of the light into the mirrors is much higher compared to metal-based cavities. The bottom Ag mirror (100 nm) was deposited on a glass substrate by electron-beam evaporation (E-beam evaporation) and the WS_2-PVK film was spin-coated on the mirror. To smoothen the surface of the film, a thin layer of Al_2O_3 and PMMA was deposited on top of the WS_2-PVK film prior to deposition of 30 nm Ag by thermal evaporation, serving as top mirror. Intuitively, one would expect that spin coating a layer of pure PVK on top of the composite film would decrease the surface roughness of the film. However, no significant change in the surface roughness was observed (see Appendix, Figure A 39), which is most likely because the solvent quickly begins to dissolve the polymer component of the composite film on the surface. Introducing the deposition of Al_2O_3 prior to the spin coating of a second polymer layer reduced the RMS roughness of the test samples from 5.8 to 4.6 nm (see Appendix, Figure A 40).

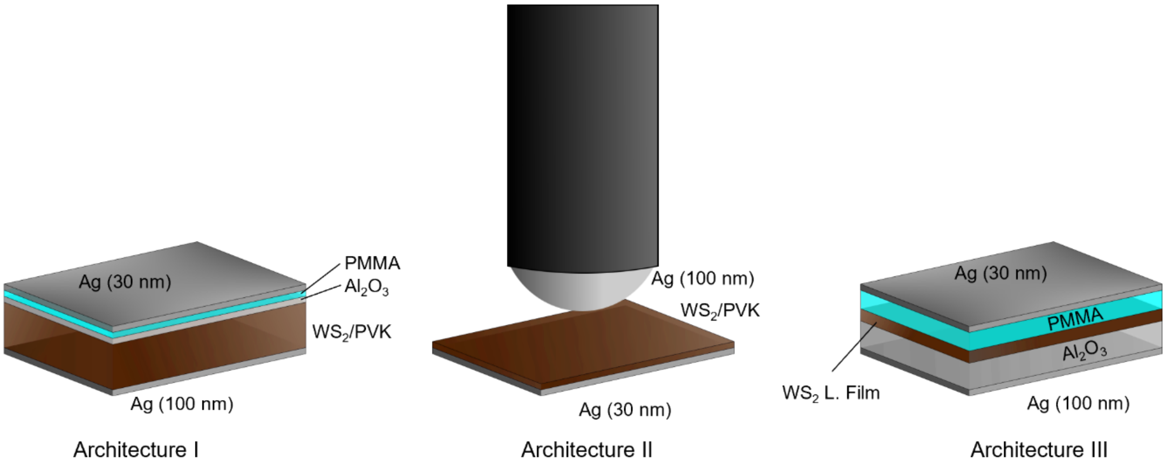

Scheme 4.6: Designs of optical microcavities. A: Closed cavity design with WS_2-PVK composite films. The WS_2-PVK film was spin-coated on a silver (100 nm) bottom mirror. To achieve a smoother surface, a thin layer of Al_2O_3 was grown on the WS_2-PVK film and another thin layer of PMMA was spin-coated on top of the Al_2O_3 layer. Deposition of 30 nm Ag finished the cavity. B: Open cavity design with WS_2-PVK composite films. The WS_2-PVK film was spin-coated on Ag (30 nm). A silver coated (100 nm) lens was approached from the top, forming the cavity. C: Closed cavity design with Langmuir films of WS_2 nanosheets. Al_2O_3 (75 nm) was grown on Ag (100 nm) and Langmuir films of WS_2 were deposited on the Al_2O_3 layer. PMMA was spin-coated on top of WS_2, and the device was finished with deposition of 30 nm Ag.

The thickness of the composite film defines the energy of the photonic mode, which should match the energy of the exciton. In a first approximation, the required thickness of the cavity can be estimated by $L_{cav} = m(\lambda_{exc}/2n_{eff})$, where L_{cav} is the thickness of the cavity, m an integer number, λ_{exc} the absorption wavelength of the exciton, and n_{eff} the effective refractive index in the cavity. Assuming λ_{exc} = 615 nm, n(PVK) = 1.68, and neglecting the contribution of WS_2 to the refractive index, this results in a calculated cavity thickness of $L_{cav} = m$*180 nm. It should be noted that this calculation cannot provide an exact prediction but can serve as starting point. As has been elucidated before, a WS_2-PVK composite film with a thickness of 180 nm cannot be realized in sufficient film quality. This means that films need to be spin-coated in thicknesses with m = 1, 2, …, which will lower the volume of the photonic mode and reduce a potential Rabi splitting.

However, a prediction of the resulting film thickness after spin coating is difficult, as has been discussed in subchapter 4.2.2. Multiple substrates were coated from different WS_2-PVK dispersions and slight changes of the spin coating parameters were applied within one preparation batch, to find a suitable thickness by trial and error. This resulted in cavities with different but unknown thicknesses and optical densities. Note that thickness and optical density cannot be measured after spin coating on the Ag mirror. For comparison reasons, reference cavities with pure PVK were prepared under identical conditions.

For the open cavities (Scheme 4.6 B), the bottom Ag mirror was deposited with a thickness of 30 nm. Again, the WS_2-PVK layer was spin-coated on top of the mirror. As top mirror, a glass lens was coated with Ag (100 nm) and mounted on a holder that is movable in all directions. The lens was approached to the substrate from the top until it touched the composite film, forming the cavity.

To design a closed cavity with the WS_2 Langmuir films (Scheme 4.6 C), optical spacers were required, since the thickness of these WS_2 nanosheet films ranges from only 13–25 nm. 75 nm of Al_2O_3 was grown on the bottom Ag mirror (100 nm) and up to 5 layers of WS_2 nanosheets were deposited on the Al_2O_3 spacer. The dispersions of functionalized WS_2 were prepared by Dr. Farnia Rashvand (LPE and LCC) and Tim Nowack (functionalization). PMMA was spin-coated on the WS_2 nanosheet film as second spacer before the deposition of the top mirror (30 nm Ag). The PMMA layer was first spin-coated with 75 nm thickness and subsequently adjusted by trial and error. The initial combined thickness of WS_2 nanosheet film and PMMA layer was determined as 100 nm. Interestingly, 100 nm combined film thickness was measured for all nanosheet sizes despite different thicknesses of the pure nanosheet film. Neglecting the WS_2 and assuming refractive indices of 1.76 for Al_2O_3 and 1.49 for PMMA, 75 nm PMMA results in a calculated position of the photonic mode at ~ 490 nm (at 0° incidence). However, measurements revealed that the cavity mode is significantly redshifted to this position due to the penetration of the electric field into the mirrors, and the thickness of the PMMA layer was successively decreased. Additionally, a reference cavity without WS_2 was prepared for comparison.

All cavities were characterized by angle dependent reflectivity, as will be discussed below.

Characterization of the Microcavities based on WS_2-PVK Composite Films

Figure 4.26 shows angle resolved reflectivity spectra of microcavities based on WS_2-PVK composite films, including a PVK reference cavity without WS_2 (A), two closed cavities with low (B) and high (C) WS_2 content, and an open cavity (D). The reference cavity features a sharp cavity mode with 56 meV linewidth, resulting in a Q factor of $Q = 34.5$. Please note that not only the polymer film has an impact on the quality of the cavity but also the silver mirrors. For example, the bottom mirror of the cavity was initially deposited by thermal evaporation, which leads to a larger grain size of the deposited silver and an increased surface roughness of $R_q = 2.3$ nm (1.2 nm for

Ag mirrors deposited by E-beam evaporation, see Figure A 41 in the Appendix). Corresponding reference cavities exhibited a linewidth of 137 meV and a *Q* factor of only 14.0.

The WS_2 filled closed cavities in Figure 4.26 B and C exhibit substantially different reflectivity spectra. The cavity presented in B exhibits a relatively large diameter and has a low WS_2 content. As discussed before, the prediction or measurement of film thickness or WS_2 content is not possible after spin coating on a silver mirror. However, multiple photonic modes are visible and at the same time no pronounced excitonic mode is discernible. The linewidth of the cavity mode with E_0 = 1.89 eV was determined as 64 meV, which is only slightly broadened in comparison to the reference and results in a quality factor of Q = 29.5. No splitting of the photonic mode is observed, indicating that the cavity remains in the weak coupling regime. Even though the optical density of the polymer film cannot be measured in the cavity, they generally have been in a sufficient range which suggests that other factors than WS_2 content or quality factor of the cavity play a role. A possible explanation is the lower volume of cavity modes in higher orders or the random orientation of the nanosheets in the film.

The cavity presented in Figure 4.26 C has a higher WS_2 content. Vertical stripes are visible in the spectrum which are attributed to heavy aggregation of WS_2 in the composite film. These aggregates lead to inhomogeneities which are visible as reduced reflectivity under certain angles. The linewidth is relatively broad but has not been determined due to an anomalous line shape (see discussion below) which makes reliable fitting impossible. Cavities without surface smoothening by thin layers of Al_2O_3 and PMMA showed even worse data quality, as presented in Figure A 42 (Appendix). Attempts to fit the linewidth of the cavity modes resulted in physically non-meaningful values up to 1.76 eV, demonstrating the requirement of the additional deposition steps of the deposition of Al_2O_3 and PMMA.

The photonic mode shows a profile with a double line at the position of the A-exciton. One possible explanation of this line profile is a mode splitting which would indicate successful strong light-matter coupling. Spectra with variations of the detuning were recorded and are presented in Figure A 43 (Appendix). Different detuning was achieved by measuring different spots on the cavity and taking advantage of natural thickness variations in the polymer composite film developing during the spin coating process. The data suggest that the double line profile is indeed more pronounced when the photonic mode is tuned to match the excitonic mode. However, the data quality is extremely poor, the cavity modes are mostly asymmetrical, and splitting of cavity modes can also occur in the weak coupling regime by effects such as inhomogeneous broadening[172] or cavity induced transparency.[173]

Similar observations were made with the open cavity design, as presented in Figure 4.26 D. Again, vertical stripes attributed to aggregation or inhomogeneities are visible in the reflectivity contour plot and the cavity mode appears split at the position of the A-exciton. One would intuitively expect that the cavity modes can easily be tuned to create different detunings, but with the home build setup used for these measurements, cavity modes only appeared after the Ag coated lens was in contact with the polymer film and was gently pressed against it, which allows the finetuning of the cavity mode only in a limited range. Another disadvantage of this setup is that the thin Ag layer can easily get scratched by the contact with the substrate and that the lens needs to be replaced after a few measurements. The linewidth of the cavity modes is improved compared to the closed cavity (120 meV for the mode around 2 eV) that has been observed in Figure 4.26 C. However, also cavity modes of higher orders show a double linewidth (Appendix, Figure A 44).

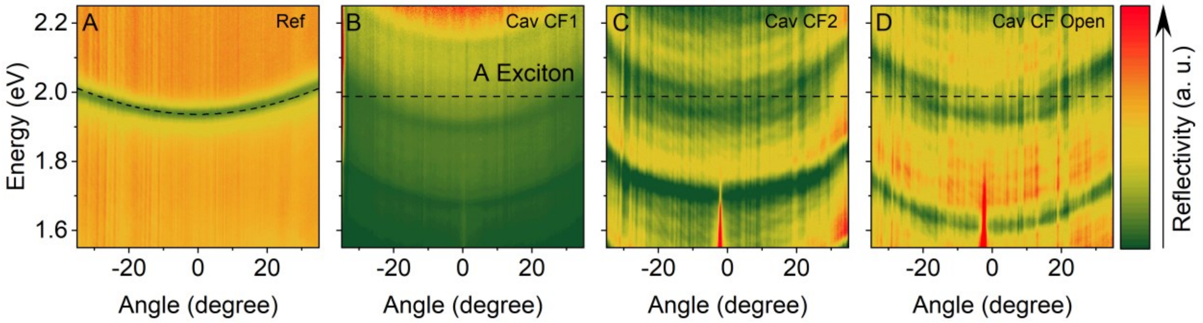

Figure 4.26: Angle resolved reflectivity of optical microcavities based on WS_2-PVK composite films. A: Closed PVK based reference cavity. B, C: WS_2-PVK in closed cavity design with relatively low (B) or high (C) WS_2 content. D: Open cavity design.

As has been mentioned before, a double line profile of the cavity mode is not necessarily related to strong light-matter coupling. In the spectra presented above, a split cavity mode could be easily rationalized by the surface of the polymer films that causes inhomogeneous broadening (see Figure 4.19 C). The measurement of the angle resolved reflectivity is conducted on a local spot (~ 50 µm diameter), which is still much larger than the hills and valleys observed at the polymer surface. In closed cavities, the cavity diameter is defined by the thickness of the WS_2-PVK composite film, which implies that different cavity diameters lie within the measurement spot, potentially explaining the double line profile of the cavity mode. At first glance this explanation appears to be in contradiction to the fact that the double line profile is also observed in the open cavities, where the cavity diameter is defined by the distance of the mirrors and independent of the polymer film. However, little air pockets might also impact the effective refractive index inside the cavity, which would have the same effect.

The hypothesis that the cavity modes are only artificially split is supported by the line shape of higher order cavity modes, (Appendix, Figure A 44) which also show a double line profile, despite the absence of pronounced excitonic modes. Additionally, more modes with lower intensity are visible in the background of the contour plots in both Figure 4.26 C and D. In conclusion, the

WS_2-polymer composites were not suitable to observe strong light matter coupling in spite of a number of optimization steps in preparation and design.

Characterization of the Microcavities based on WS_2 Langmuir Films

Figure 4.27 shows the reflectivity spectra obtained from the cavities based on Langmuir films of WS_2 nanosheets. Figure 4.27 A shows the angle resolved reflectivity of a reference cavity without WS_2, fitted by equation (2.23). The linewidth of the cavity mode (Figure 4.27 E) is relatively broad and was determined as 142 ± 3 meV, corresponding to a *Q* factor of ~ 13, which is surprisingly low compared to the PVK reference cavities. Nevertheless, the photonic mode of the WS_2 filled cavities (Figure 4.27 B–D) is split into two polaritonic modes, proving strong light-matter coupling. In contrast to previously observed double line shapes of the WS_2-PVK composite film cavities, the modes are split over the complete range of observed angles. However, the splitting is not very pronounced in the contour plots, due to the relatively broad modes. To visualize it more clearly, Figure 4.27 F–H shows line profiles of the reflectivity at different angles, highlighting the splitting. The most pronounced splitting was found for the cavity produced from the WS_2 fraction 10–30*k* g without any functionalization. While this hints toward an unfavorable effect of the functionalization, it should be mentioned that this correlation is not necessarily a causality and that the larger splitting could be caused by natural variations of the WS_2 amount in the cavity. Due to the broad linewidth, fitting of the polaritonic modes is extremely difficult.

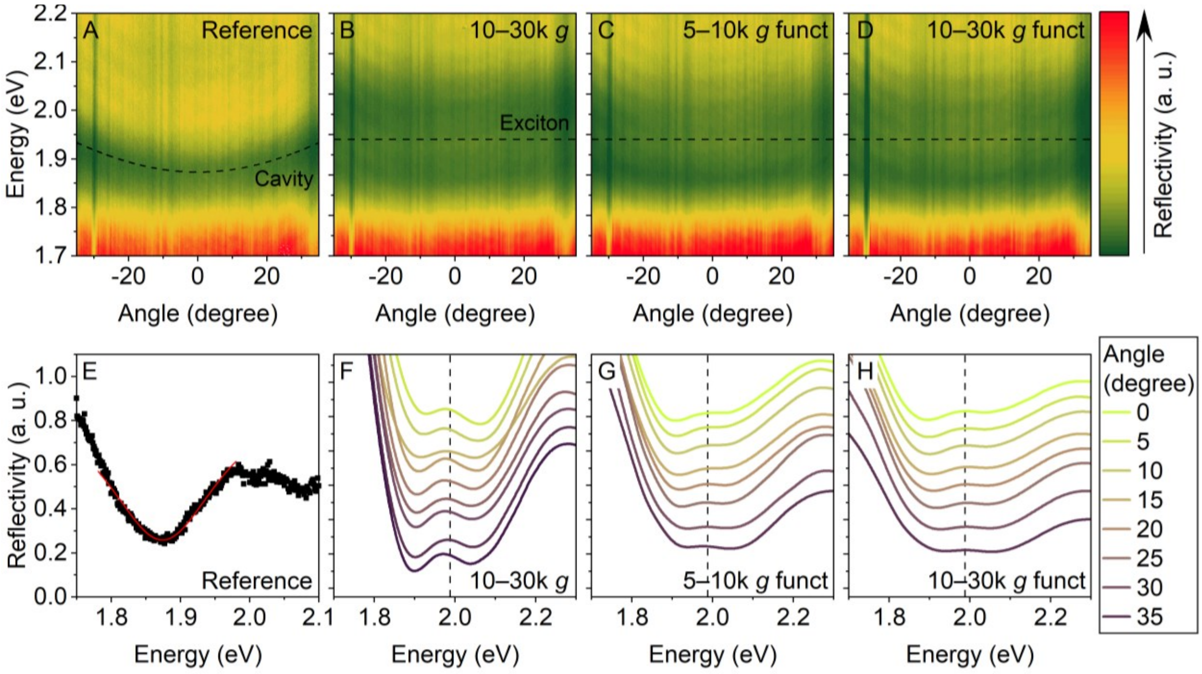

Figure 4.27: Reflectivity of optical microcavities based on Langmuir films of WS_2 nanosheets (see Scheme 4.6). A–D: Contour plots of angle resolved reflectivity of a reference cavity (A) and cavities with WS_2 fractions 10–30k *g* (B), 5–10k *g* funct (C) and 10–30k *g* funct (D), showing strong light-matter coupling. The dashed lines are fits of the photonic mode or the position of the A-exciton, respectively. E: Line profile of the cavity mode shown in A. F–H: Line profiles of the polaritonic modes shown in B–D at different angles with vertical offset.

For further characterization, the samples were sent to collaborators (Dr. Andreas Mischok, group of Prof. Dr. Gather, University of Cologne), where the reflectivity was measured at higher angles (Figure 4.28). At higher angles, the energy separation of the polaritons is larger and the polaritonic modes were fitted by a coupled oscillator model.[166, 174] Since these spectra were acquired from a larger spot, minor differences to the data measured in Heidelberg are possible, for example broader linewidth or slightly shifted energy positions. The data clearly show an avoided crossing of the polaritonic modes at the resonance of the exciton, which is indicated by the black dotted line. The white dotted line displays the dispersion of the pure photonic mode. The fitted dispersions of the polaritonic modes are presented by the blue solid lines and reveal an effective refractive index of 1.85 and a Rabi splitting of 120 meV. The exciton and photon fraction of the lower polariton were extracted from the fits and are displayed in Figure 4.28 D–F. At low angles, the lower polariton is dominated by the exciton, turning into a domination of the photon at high angles, as is the case at negative detuning of the cavity mode (see chapter 2.5).

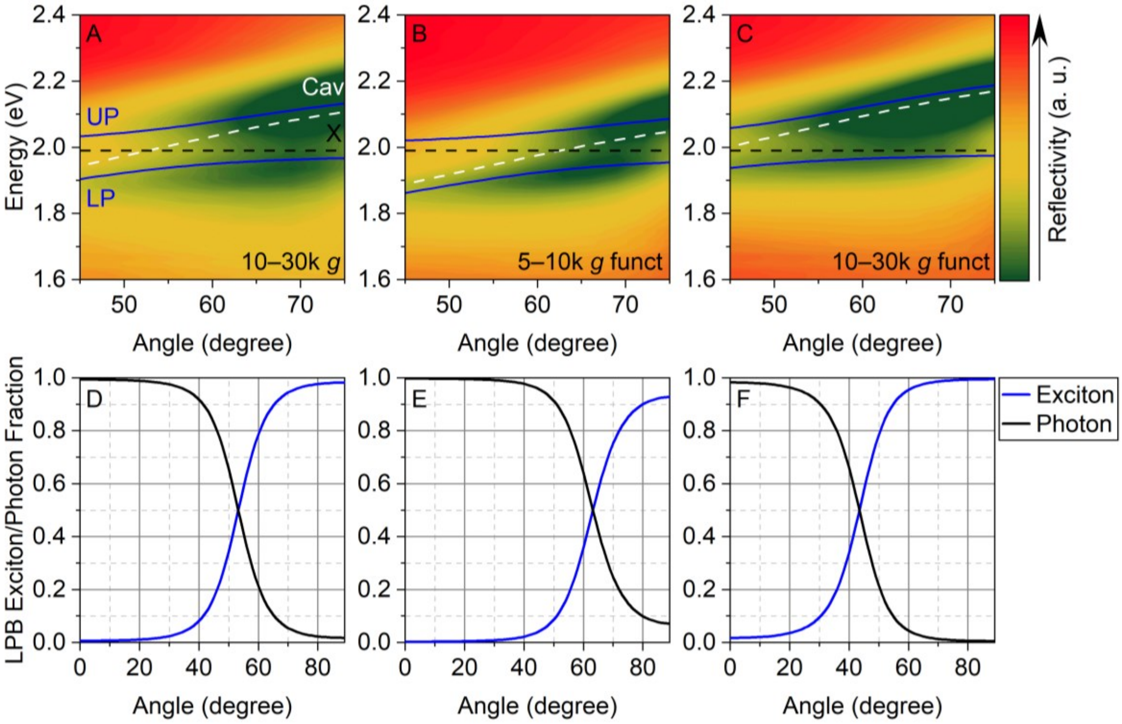

Figure 4.28: A–C: Angle resolved reflectivity of the cavities 10–30k *g* (A), 5–10k *g* funct (B), and 10–30k *g* funct (C), showing an avoided crossing of the polaritonic modes at the resonance of the A-exciton and proving strong light-matter coupling and the formation of exciton-polaritons. D–F: Exciton and photon fractions of the lower polaritons shown in A–C. At low angles, the lower polariton is dominated by the exciton. At high angles, the nature of the polariton becomes mostly photonic.

While the reflectivity data clearly prove strong light-matter coupling and the formation of polaritons, no angle resolved PL emission could be acquired from the cavities due to the low PL intensity and limited sensitivity of the employed setups. However, with sensitive instruments like the Raman microscope, a detection of the PL is still possible (Figure 4.29) and reveals that the PL mostly remains preserved during the spin coating and evaporation processes which are required to finish the cavity. The Raman spectra in Figure 4.29 A shows that the PL/Raman ratio of the WS_2 film inside the cavity is only slightly reduced. The PL signal (Figure 4.29 B) appears slightly broadened, which is attributed to the dispersion of the PL and the measurement set up, which collects light emitted at different angles in a combined spectrum.

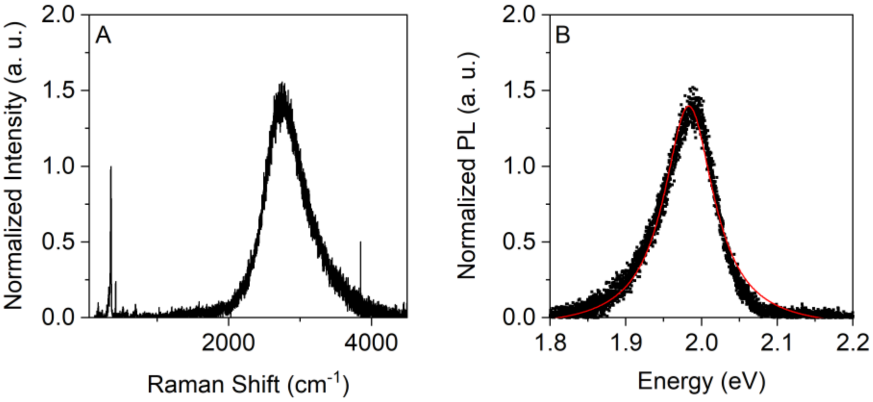

Figure 4.29: Raman (A) and PL spectra (B) of the cavity 10–30k *g* funct, revealing that PL of the WS_2 films remains preserved. The PL signal appears slightly broadened, since the emission wavelength depends on the angle of emission and the PL was collected over different angle.

In conclusion, the formation of exciton-polaritons was only possible with the cavities based on Langmuir films of WS_2. No evidence for strong light-matter coupling and exciton-polaritons could be found in cavities based on the WS_2-PVK composite films. PVK reference cavities were produced in high quality, whereas WS_2 filled cavities suffered from aggregation and bad film quality, reflected in broad cavity modes, abnormal line shapes, and vertical stripes in angle resolved reflectivity spectra. All cavities based on Langmuir films of WS_2 showed a Rabi splitting (~ 120 meV) and evidence for strong coupling, despite unexpected large linewidth of the modes. The PL remains preserved in the cavities filled with functionalized WS_2 but was only detected in sensitive setups such as the Raman microscope. Recording angle resolved PL failed due to the overall weak PL intensity in the cavity.

4.2.5 Summary and Conclusion

In this chapter, WS_2 thin films were prepared in the form of PVK-composite and Langmuir films with the aim of eventually implementing the films in optical microcavities to create exciton-polaritons. This requires a high WS_2 concentration in the films without a loss of film quality, which could only be accomplished for the Langmuir films.

The WS_2-PVK composite films were prepared by spin coating from THF/NMP. The preparation of the spin coating solution included centrifugation of WS_2 in NMP, which resulted in a loss of ML flakes and hence reduction of the dispersion quality. This was partially compensated by long and time-consuming overnight centrifugations. The composite films were spin-coated in different thicknesses and with different WS_2 contents, but sufficient quality was only accomplished for low concentrations of WS_2. In the samples of this thesis, the PL of the films significantly dropped when the optical density at the position of the A-exciton reached 0.024 per 100 nm film thickness. Additionally, aggregation of the nanosheets and local roughness of the film surface increased with the WS_2 content or optical density. In contradiction to the expectations, there is no direct correlation between the optical density of the film and the surface roughness. This is attributed to hills and valleys of polymer that sometimes formed at the surface on or between patches of aggregated nanosheets, strongly increasing the surface roughness independent of the WS_2 content. While the reproducibility of the film preparation was acceptable within one preparation batch, it was poor between different batches.

The Langmuir films were prepared by self-assembly of WS_2 nanosheets at a phase interface of water and hexane, where WS_2 was injected from IPA, and deposited by vertical lifting of a glass substrate. Long drying times were required, since the films were dried under ambient conditions to avoid cracks that can form during heating or drying in vacuum. The deposition method is applicable to all nanosheet sizes tested, and multiple depositions of nanosheet films are possible, where the number of depositions linearly scales with the optical density of the films. After reaching optical densities sufficient for strong light-matter coupling, the films had a thickness between 10 and 25 nm, depending on the size of the nanosheets, allowing to place the films at defined positions in a cavity. However, the PL of the films decreased, and the surface roughness increased with the deposition number. The decrease in the PL was reduced by functionalization of the WS_2 nanosheets with 3,5-dichlorobenzenediazonium tetrafluoroborate. Additionally, the functionalization prevented broadening and preserved the line shape of the PL.

Both PVK composite films and Langmuir films were implemented into microcavities. The composite films were tested with closed and with open cavity architecture. Good quality of the closed cavity was only accomplished for the reference cavities without WS_2 or with relatively low WS_2 content and thick composite film. However, no strong coupling was observed in this case, which is attributed to the low mode volume of higher order cavity modes or the random orientation of the WS_2 flakes in the films, making the excitation less efficient. Closed cavities with higher WS_2 content showed broad cavity modes, abnormal double line shape, and vertical stripes in the angle resolved reflectivity originating from aggregation. The linewidth was reduced in the open cavity design, but the cavity modes still showed an abnormal double line profile. These double line profiles do not seem to originate from strong light-matter interaction, but from artificial splitting that might be caused by very rough surfaces of the WS_2-PVK composite films, forming different cavity modes. The polymer composite films of WS_2 are not promising candidates for polaritonic applications since they can only be produced in high quality when the WS_2 content is kept low. Nevertheless, it is important to keep this approach in mind, since the films might be used in future for applications, where a low WS_2 concentration is sufficient or even desired.

Lastly, the Langmuir films of WS_2 were embedded in the middle of a microcavity, sandwiched between Al_2O_3 and PMMA spacers. The linewidth of the reference cavity is surprisingly high (142 ± 3 meV), but all WS_2 filled cavities showed a Rabi splitting. The splitting is not pronounced and fitting is difficult due to the broad polaritonic modes. The samples were sent to collaborators to remeasure the reflectivity at higher angles, where the difference in the energy position of the lower and upper polariton is larger. The polaritonic modes were fitted, assuming a Rabi splitting about 120 meV, which is in between of the splittings reported for CVD grown ML WS_2 and mechanically-exfoliated FL WS_2. It was not possible to measure the dispersion of the PL, due to weak PL intensity. However, with very sensitive equipment such as the Raman microscope, PL is still measurable, and it was shown, that the PL/Raman ratio is only slightly reduced by the processing required to finish the cavity after deposition of the films.

In conclusion, strong light-matter coupling was only accomplished when Langmuir films of WS_2 were implemented into microcavities. This is attributed to three advantages of the Langmuir films over the polymer composite films: First, thinner film thickness allows to tune the exciton resonance to the ground mode of the cavity. Second, the nanosheets in the Langmuir films are deposited with a parallel orientation with respect to the substrate, resulting in a more efficient excitation. Last, the overall film quality of the Langmuir films is superior to the composite films with better homogeneity and less aggregation. To the author's best knowledge, this is the first time that exciton-polaritons were observed in homogenous and large-scale thin films of WS_2 nanosheets and hence an important step towards polaritonic devices in an industrial environment. In future, it might be worth to deposit heterostructures such WS_2/*h*-BN/WS_2 to realize a spatial separation of the individual WS_2 layers, which might further contribute to the preservation of the PL. The PLQY could further be improved by chemical treatment, for example with TFSI[53] or by using WS_2 nanosheets with improved lateral dimensions, for example by employing other exfoliation methods such as electrochemical exfoliation. Additionally, a larger number of depositions would increase the Rabi splitting and also the number of emitters and hence the PL intensity, assuming that the PLQY does not decrease any further.

4.3 Exploration of New Materials – Germanene Derivatives

4.3.1 Introduction

In the previous chapter, film formation techniques were investigated using WS_2 as a model system, and the thin films were implemented in optical microcavities, resulting in strong light-matter coupling. However, a problematic issue present in the whole chapter was the relatively low PLQY of LPE produced WS_2 monolayers. This chapter aims to explore different materials with stronger photoluminescence which might be suitable candidates for potential applications in optics.

Materials that have recently gained attention are germanene or silicene – the Ge or Si equivalents to the most prominent two-dimensional material graphene.[175] The work on these materials has been hindered by the fact that germanene or silicene do not exist in nature and thus cannot be exfoliated from bulk crystals. Many investigations have been restricted to theoretical methods, but recently it has been predicted that germanene or silicene can be stable in their free-standing form in a low buckling configuration and it was accomplished to engineer silicene on single crystal metal substrates such as Ag(111) substrates[176, 177] or germanene on Pt(111).[178]

While the practical work with these materials remains difficult, it was demonstrated that relatively stable hydrogen-terminated germanene (Ge-H, germanane) can be synthesized from $CaGe_2$ (germanide), forming layered VdW crystals.[179, 180] Additionally, $CaGe_2$ can directly be turned into alkyl derivatized germanenes, which are considered to exhibit even better stability.[181-183] For example, methyl-terminated germanene (Ge-Me) was suggested as an improved version of germanane.[181, 182, 184] In contrast to TMDs, these germanene derivatives exhibit a direct band gap[185] and are fluorescent in bulk structure,[179, 181, 184] which might resolve difficulties experienced in the previous chapters, related to aggregation and PL quenching. The possibilities to functionalize germanene derivatives and tailor their optical properties led to several implementations of germanene derivatives in devices or applications such as field-effect transistors,[186] bio-sensors,[187] or microrobots.[188] Despite the tremendous interest in these materials, processing and characterization is still in its infancy. For example, no size selection has been carried out in previous studies and characterizations were conducted on polydisperse dispersions, neglecting that properties of nanosheets are often size-dependent. Furthermore, the demonstrated applications have been based on single crystals[186] or dispersions,[188] but not on networks of nanosheets.

The aim of this study was to subject germanene derivatives to LPE and LCC, to characterize the fractions of different nanosheet sizes, and to elucidate whether these germanene derivatives are promising materials for the fabrication of light-emitting devices based on homogenous nanosheet thin films. The experiments were carried out with Ge-H and Ge-Me. Parts of this chapter were experimentally supported by Dr. Kevin Synnatschke, Dr. Adam Kelly (SEM images), and Dr. Felix Berger (PLQY measurements). The bulk materials were synthesized by the group of Prof. Dr. Sofer, University of Prague, and provided alongside the basic characterization of the bulk materials.

4.3.2 Bulk Crystals of Germanene Derivatives

As mentioned above, the bulk materials were provided by the Sofer group, including basic characterization by powder XRD, X-ray photoelectron spectroscopy (XPS), Fourier transform infrared (FTIR) spectroscopy, and thermal gravimetric mass spectrometry (TGMS). Additionally, SEM images and Raman spectra were recorded in Heidelberg.

Ge-H and Ge-Me were synthesized from $CaGe_2$ by reaction with HCl or CH_3I (Scheme 4.7), respectively, forming layered crystals with the structure displayed in Figure 4.30.

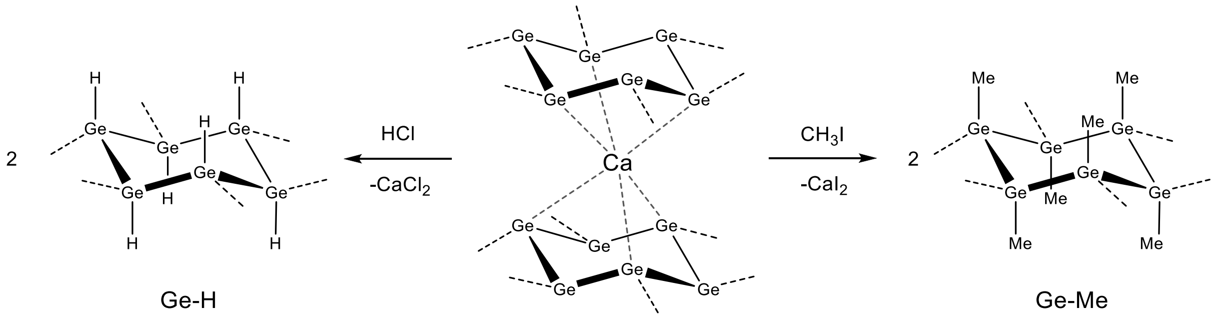

Scheme 4.7: Preparation of germanene derivatives. Ge-H and Ge-Me are synthesized from calcium germanide ($CaGe_2$) by reaction with HCl or CH_3I, respectively.

The structure of the germanene derivative features a hexagonal 2H unit cell and is illustrated in Figure 4.30 A, including a side view (left) and a top view (right). The layered structure is further highlighted by the SEM images of bulk Ge-Me in Figure 4.30 B.

The provided powder XRD spectra are displayed in Figure A 45 (Appendix). The main reflection (002) of Ge-Me at ~ 10.46° (Figure A 45 A) corresponds to the interlayer distance. Additionally, higher order reflections, (004), (100), (006), and (110), are visible at ~ 20.75°, ~ 26.21°, ~ 31.06°, and ~ 45.88°, respectively. The parameters *a* and *c* related to the 2H hexagonal unit cell are 3.92 Å according to the (100) reflection, and 16.90 Å according to the (002) reflection (8.45 Å per layer). In the powder XRD spectrum of Ge-H (Figure A 45 B) only the main reflection (002) and the higher order reflection (004) are visible at ~ 15.62° and ~ 32.11°, respectively. The *c* parameter of the 2H unit cell is 11.34 Å (5.67 Å per layer).

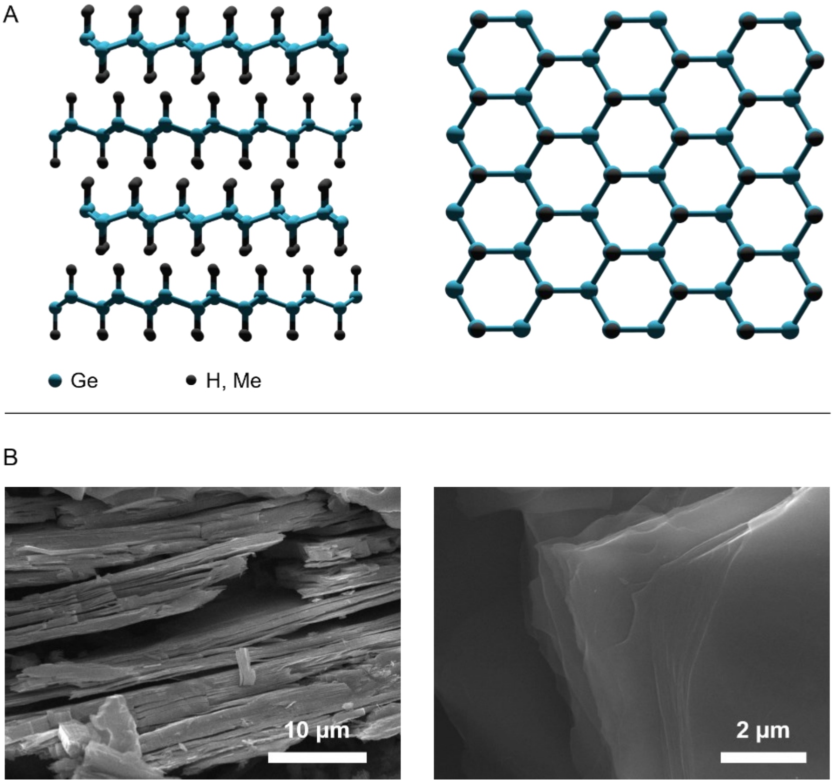

Figure 4.30: A: Structure of germanene derivatives with hexagonal 2H unit cell from side view (left) and top view (right). B: SEM images of bulk Ge-Me, featuring the layered structure of the crystals.

The XPS spectra of the bulk materials are presented in the Appendix in Figure A 46 (Ge-Me) and Figure A 47 (Ge-H). According to the survey spectra, Ge-Me contains 36.9 atomic % germanium, 37.9 atomic % carbon, and 25 atomic % oxygen. According to the respective core level spectra, 85.3 % of the oxygen and 48.3 % of the carbon are linked to contamination occurring during sample preparation and handling. The surface oxidation of Ge-Me is only ~ 0.5 %. 51.7 % of the carbon is due to Ge-C bonds and the ratio Ge/Ge-C is ~ 1.9/1. Minor traces of iodine were found (0.2 atomic %), which might originate from the formation of Ge-I. Ge-H contains 67.1 atomic % germanium, 9.6 atomic % oxygen, and 19.6 atomic % carbon. Oxygen and carbon contamination are mostly adventitious, and the surface oxidation of Ge-H is estimated as 1.8 %. Traces of chlorine were found (3.7 atomic %) due to the formation of Ge-Cl.

The FTIR spectrum of Ge-Me (Appendix, Figure A 48 A) features a C-H stretching mode at ~ 2900 cm^{-1}, C-H bending modes at ~ 1400 cm^{-1} and ~ 1240 cm^{-1}, and a C-H rocking mode at ~ 770 cm^{-1}, corresponding to the methyl group. The Ge-C bond is observed at ~ 570 cm^{-1} together with a weaker mode at ~ 500 cm^{-1}. Additionally, a Ge-H vibration is observed at ~ 1980 cm^{-1}, revealing that some Ge-atoms are bonded to hydrogen instead of methyl. The FTIR spectrum of Ge-H (Appendix, Figure A 48 B) features a Ge-H stretching mode at ~ 2000 cm^{-1}, bending modes at ~ 825 cm^{-1} and ~ 765 cm^{-1}, and waging modes at ~ 575 cm^{-1} and ~ 475 cm^{-1}.

Figure A 49 (Appendix) shows Raman spectra of Ge-Me. Under 532 nm excitation, a Ge-Ge Raman signal is visible at ~ 288 cm^{-1} (E_{2g}) and fluorescence dominates the low energy region of the spectrum, already indicating a relatively strong PL of the material in the bulk form. At an excitation wavelength of 633 nm the Raman signal and PL of Ge-Me overlap and only PL is visible due to the higher intensity. The Raman spectra of Ge-H (Appendix, Figure A 50) feature an intense germanium mode at ~ 301 cm^{-1} (E_{2g}) and weak mode at ~ 226 cm^{-1} (A_{1g}).

Lastly, TGMS spectra (Appendix, Figure A 51) were provided, where the thermal degradation of the sample is observed gravimetrically, and where the decomposition products are identified by mass spectrometry. The major decomposition of Ge-Me is observed between ~ 380 and ~ 600 °C. The Ge-C bond begins to break at ~ 180 °C and methane is detected in the MS trace. Below this temperature only hydrogen is detected from the cleavage of Ge-H bonds (mass loss ~ 0.5 %), which start to evolve around ~ 120 °C. At 360 °C the ion intensity of methane significantly rises and reaches the maximum ion intensity at ~ 460 °C, from where on the ion intensity decreases until ~ 500 °C until most methyl groups are cleaved. In this temperature range, decomposition products with the general formula $GeH_n(CH_3)_{4-n}$ are also detected and cause higher mass loss than the cleavage of methyl groups only. Additionally, water is detected in the TGMS spectrum which is due to adsorbed water. The mass loss of Ge-H (Figure A 51 B) starts at ~ 100 °C, where adsorbed water is detected. Decomposition of the Ge-H bonds follows at ~ 150 °C, where hydrogen is detected in the ion trace. Additionally, traces of GeH_4 are detected from ~ 130 °C, which is even earlier than the breaking of Ge-H bonds, which might be due to terminal GeH_2 that are weaker bonded than GeH_2 in the plane of the material.

The data prove that the provided bulk crystals of the germanene derivatives are intact and suitable for the investigations that will be described below.

4.3.3 LPE, LCC and Langmuir Films of Germanene Derivatives

LPE and LCC of Germanene Derivatives under Inert Gas conditions

The standard exfoliation protocol used in previous chapters for the exfoliation of TMDs was not applicable to the exfoliation of the germanene derivatives due to low stability of the exfoliated nanosheets and oxidation under ambient conditions, as will be demonstrated below. Therefore, inert gas exfoliation and size selection was required. Handling of chemicals or solvents and the preparation of the dispersions was executed under nitrogen atmosphere using a glove box.

Bulk powders of the germanene derivatives were dispersed in dried and degassed NMP in a pear-shaped flask. After sealing the flask, it was removed from the glove box and the exfoliation was conducted by bath sonication for ~ 16 h while an argon flow was bubbled through the dispersion. The exfoliated stock dispersions were brought back into the glove box and distributed across Eppendorf tubes for the size selection. LCC was performed with centrifugation steps at 50 *g*, 100 *g*, 400 *g*, 1k *g*, 5k *g*, and 10k *g*, where the centrifugation was executed in closed Eppendorf tubes outside the glovebox. The decanting steps were carried out inside the glovebox. Eppendorf tubes are not designed for inert gas chemistry and thus not perfectly sealed, but this procedure reduces the impact of oxygen to the feasible minimum. Six sediments were collected in fresh NMP during the size selection cascade and characterized by AFM, UV-Vis and PL spectroscopy.

Preparation of Ge-Me Langmuir Films

Nanosheet films were prepared by the nanosheet self-assembling procedure described in chapter 4.1.2. However, nanosheet film formation was only executed with Ge-Me for the following two reasons: First, Ge-Me nanosheets are larger in their lateral dimensions and thus exhibit a more desirable aspect ratio. Second, the PL of the Ge-H dispersions is not only broader but is also emitted in the blue range of the visible spectrum, which is in contradiction to the literature-known PL spectrum of the bulk material, which indicates that either degradation or a chemical reaction occurred during sonication (the full discussion on the PL data will be presented further below). For the formation of Ge-Me Langmuir films, Ge-Me nanosheets were injected from NMP to a water/toluene phase interface. While NMP was avoided in previous chapters for the formation of TMD films, it is a convenient choice in this particular case since no additional solvent transfer or purification step is required. After nanosheet self-assembly, the toluene layer was removed from the top, and the nanosheet film was deposited by vertical lifting of a glass substrate through the nanosheet film. The deposited film was subsequently dried under ambient conditions. Due to the limited stability of the nanosheets under ambient conditions, film preparation was only possible with nanosheets of large or medium size. Smaller nanosheets degraded during the long drying times, leading to bleached color of the films and quenched PL. The films were characterized by optical microscopy, AFM, SEM, UV-Vis, and PL spectroscopy.

4.3.4 Characterization of the Nanosheet Dispersions and Langmuir Films

Microscopic Characterization

First, the dimensions of the exfoliated nanosheets were investigated by AFM. The nanosheet fractions collected during LCC were transferred to IPA and deposited on cleaned, pre-heated Si-wafer by flash evaporation before the microscopic investigation. Figure 4.31 A–D show example images of Ge-Me nanosheet fractions collected at different centrifugal forces (more AFM images of Ge-Me and Ge-H are available in the Appendix, Figure A 52–Figure A 54). With proceeding centrifugation cascade, the nanosheets become smaller and thinner. To quantify this observation, statistical investigation of the nanosheet length, width, and height was carried out (Appendix, Figure A 55–Figure A 58), where length refers to the longest dimension of the nanosheets and width was measured orthogonal to the nanosheet length. Figure 4.31 E and F show length (E) and height (F) histograms of the Ge-Me fractions 50–100 *g* and 5–10k *g*. While the size distribution in the 50–100 *g* fraction is rather broad with lateral nanosheet dimensions up to ~ 1.5 µm and nanosheet heights from ~ 25 to 100 nm, it is narrowed in the 5–10k *g* fraction with nanosheet lengths between 50 and 250 nm and nanosheet heights from 2 to 15 nm.

Germanane or its alkyl derivatives are generally considered as relatively stable[180, 181, 183] but here, basal plane degradation of the nanosheets was revealed by the AFM investigation. This basal plane degradation most likely occurred after exposition to air and was found in all fractions of the size selection including large nanosheets (Figure 4.31 G). However, it is most dominant in the fraction of the smallest nanosheets (Figure 4.31 H), which explains why film formation was only successful with nanosheets of large or medium size. The AFM analysis of the Ge-H fractions showed similar trends and is summarized in Figure A 52 (Appendix). Further evaluation of the AFM data and a comparison between Ge-H and Ge-Me are presented in Figure 4.32. The average nanosheet height (A) and length (B) of the fractions are plotted against central RCF in Figure 4.32 A and B. As explained in previous chapters, the data follow an empirical power law, resulting in a straight line on the log-log scale. The data points of the Ge-H height are slightly shifted to larger values compared to the Ge-Me data points, which could be because of real differences in the nanosheet dimensions, different levels of oxidation, or due to natural batch to batch variations arising from sample handling such as pipetting after size selection. However, no significant difference in the nanosheet length is discernible between Ge-Me and Ge-H in Figure 4.32 B. Figure 4.32 C and D show the width (C) and height (D) of the individual nanosheets as a function of their length, including data of > 2800 nanosheets. The plot suggests a relation between the width and length or height and length of the nanosheets, respectively, according to the exfoliation model described before[94] and does not reveal differences in the exfoliability of Ge-Me and Ge-H at first glance.

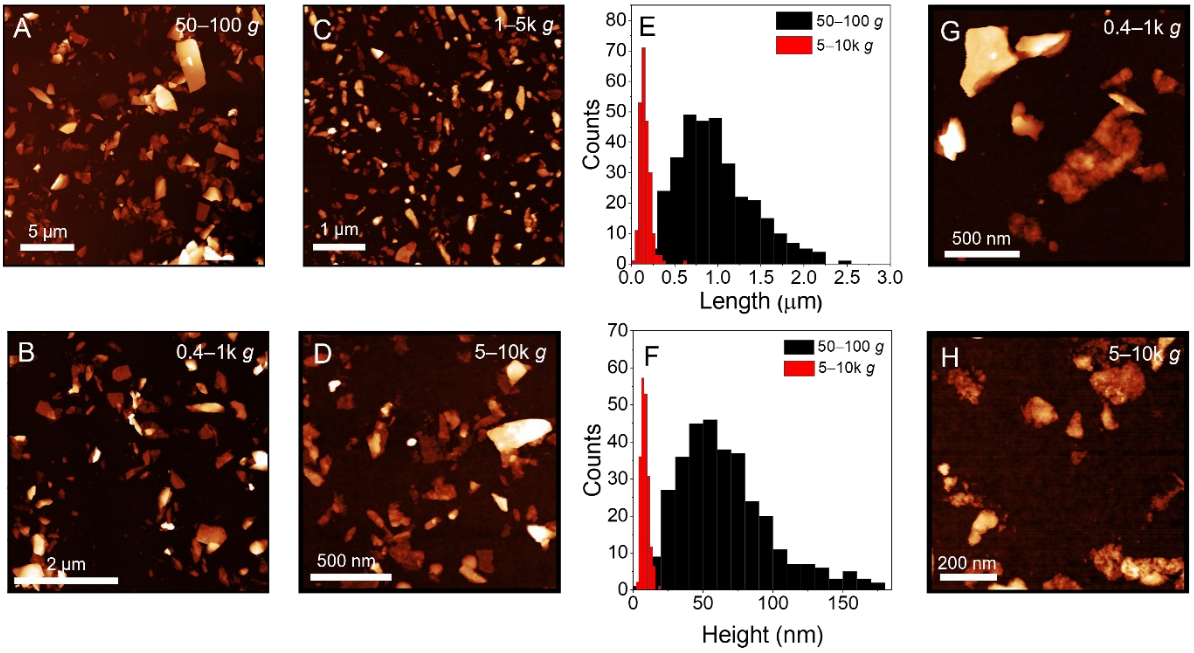

Figure 4.31: Atomic force microscopy on liquid phase exfoliated and size-selected Ge-Me nanosheets, deposited on Si-wafer. A–D: Example AFM images of different nanosheet fractions collected during LCC, showing decreasing nanosheet size with proceeding steps in the centrifugation cascade. E, F: Nanosheet length (E) and height (F) distribution of the nanosheet fractions 50–100 *g* and 5–10k *g*. The nanosheets in the fraction 50–100 *g* exhibit a broad size distribution in length and height. The distribution is narrowed in the fraction 5–10k *g* and the nanosheets are overall smaller and thinner. G, H: AFM images of degraded nanosheets. Nanosheet degradation is observed in all fractions of the size selection including large nanosheets (0.4–1k *g*, G) but is most dominant in fractions containing smaller nanosheets (5–10k *g*, H).

This relation is further explored in Figure 4.32 E and F, where the arithmetic mean aspect ratios of the length to the width (E), $\langle L\rangle/\langle w\rangle$, and length to height (F), $\langle L\rangle/\langle H\rangle$ of the nanosheets in one fraction are plotted against central RCF. The aspect ratio $\langle L\rangle/\langle w\rangle$ increases with central RCF for both Ge-Me and Ge-H. This increase can potentially be attributed to a shape filtering effect during centrifugation as discussed recently in the case of graphene.[189] No significant difference between Ge-Me and Ge-H is discernible.

More interesting than the $\langle L\rangle/\langle w\rangle$ aspect ratio is probably the $\langle L\rangle/\langle H\rangle$ aspect ratio, as this is a measure of the exfoliability of the two compounds. The aspect ratio $\langle L\rangle/\langle H\rangle$ of both germanene derivatives remains constant with central RCF, which is in agreement with theoretical models mentioned before, describing the length to height aspect ratio as a result of intra- and interlayer binding strength.[94] With an aspect ratio of 20.5 ± 1.1 the nanosheets of Ge-Me are significantly larger in lateral dimensions than the Ge-H nanosheets, which exhibit an aspect ratio of 16.5 ± 0.6. This difference can be rationalized by the different sizes of the substituents (-H vs $-CH_3$). The substituents are localized at the basal planes of the layers and a larger substituent might reduce the interlayer binding strength, resulting in better exfoliability and thus larger $\langle L\rangle/\langle H\rangle$ aspect ratio. This is in agreement with the observation, that the length to width aspect ratio is identical for both materials, since the intralayer binding strength should not be significantly altered by the basal plane functionalization.

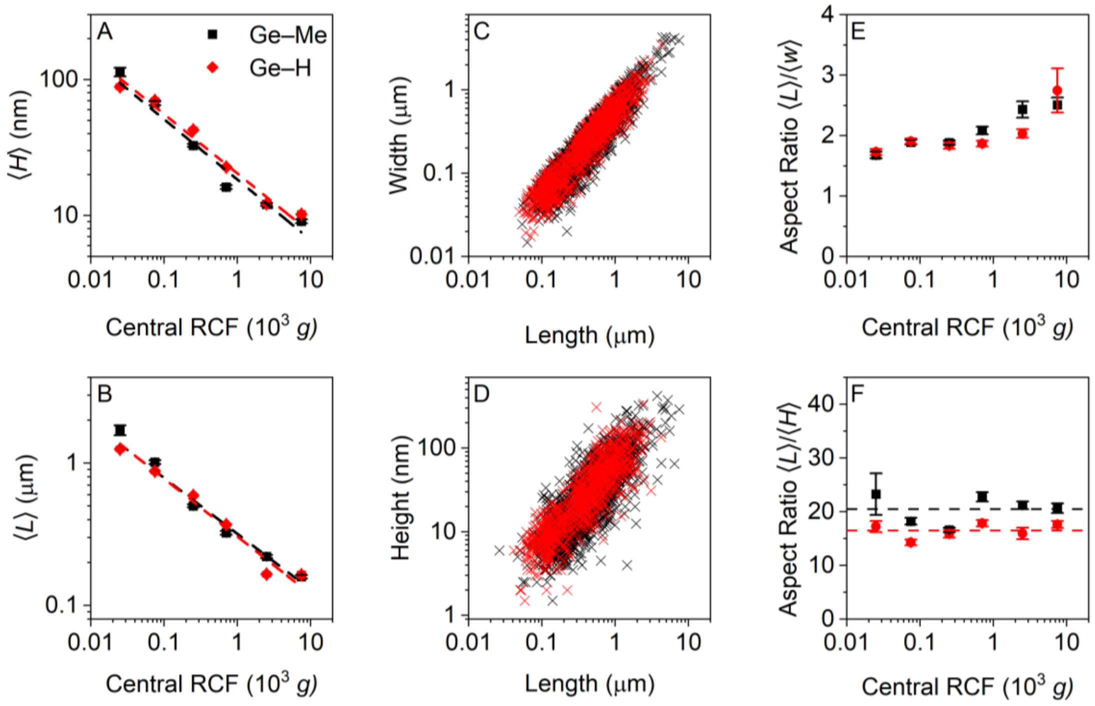

Figure 4.32: Size information about Ge-Me and Ge-H nanosheets, derived from the AFM images shown in Figure A 52 and Figure A 54 in the Appendix. A, B: Average nanosheet height (A) and length (B) of the nanosheets as a function of central RCF. C, D: Width (C) and height (D) of the nanosheets as a function of the nanosheet length. Each data point is an individual nanosheet measured by AFM. E: Arithmetic mean length to width aspect ratio of the nanosheets in one size-selected fraction as a function of central RCF. The aspect ratio increases with proceeding centrifugation cascade for both Ge-Me and Ge-H. F: Arithmetic mean length to height aspect ratio as a function of central RCF. The aspect ratio remains constant with an average aspect ratio (indicated by the dashed line) of 20.5 for Ge-Me and 16.5 for Ge-H.

Figure 4.33 shows the microscopic investigation of the Ge-Me nanosheet films formed by nanosheet self-assembly at the liquid-liquid interface. The films appear mostly homogenous under the optical microscope (A–D) over large areas, but inhomogeneity and polydispersity are visible in the films deposited from the fractions containing the largest nanosheets. These inhomogeneities are further highlighted by the SEM images (E–F), where big differences in the size of deposited flakes as well as incomplete coverage with partial visibility of the underlying substrate is observed. Note that this is not due to the film preparation methodology but reflects the broad size distribution of the dispersions collected during early stages of the size selection cascade. Films deposited from dispersions containing smaller nanosheets are expected to exhibit improved morphologies due to a narrower nanosheet size distribution. However, beginning from the fraction 0.4–1k *g*, the deposition of nanosheet films became problematic due to stability reasons. While the film formation at the water/toluene interface was still possible and led to a visible, closed nanosheet film at the phase interface, the films did not survive the long drying times under ambient conditions which are required for high film quality (see chapter 4.2.3). It was still possible to observe the nanosheets by AFM (Figure 4.33 G and H), but the film appeared colorless and despite the good PL of the germanene derivatives (see characterization below), no PL was detected from the films.

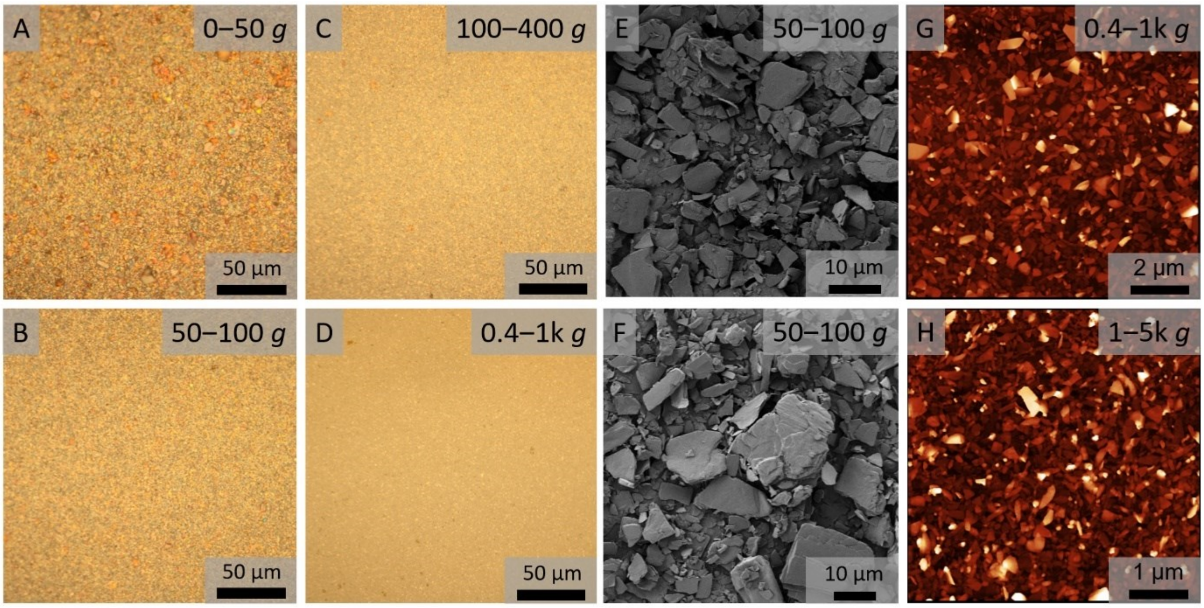

Figure 4.33: Microscopic investigation of Ge-Me nanosheet films, formed by nanosheet self-assembly at a water/toluene phase interface, including optical microscopy (A–D), SEM (E, F), and AFM (G, H). The films appear mostly homogenous under the optical microscope (A–D) over large areas, but inhomogeneity and polydispersity are visible in the films deposited from the fractions containing the largest nanosheets. These inhomogeneities are further highlighted by the SEM images (E–F). Big differences in the size of deposited flakes as well as incomplete coverage with partial visibility of the underlying substrate is observed. Films from the smallest nanosheets could still be observed with the AFM (H), but the color and PL of the films had completely vanished.

Spectroscopic Characterization

The optical properties of the germanene derivatives were investigated by UV-Vis and PL spectroscopy. The full dataset of UV-Vis data acquired for Ge-Me and Ge-H is available in Figure A 59–Figure A 61 (Appendix). In previous publications, diffuse reflectance absorption (DRA) measurements were carried out on Ge-Me and Ge-H crystals, reporting a DRA onset at 1.69 eV for Ge-Me[181] and 1.59 eV for Ge-H,[180] which means that the methyl-derivatization results in a blue-shift of the absorption edge. In the UV-Vis measurements carried out for this study, no significant differences between the spectra recorded from Ge-Me and Ge-H are discernible. This might indicate that the absorbance is dominated by the germanene body with only negligible impact of the derivatization. Since the UV-Vis data of both germanene derivatives are identical, only the spectra of Ge-Me will be explicitly discussed.

A summary of the UV-Vis data of Ge-Me is presented in Figure 4.34, including extinction, absorbance, and scattering as a function of wavelength. The absorbance was measured in the center of an integrating sphere and was subtracted from the extinction to calculate the scattering background. Example spectra of extinction, absorbance, and scattering spectra are shown in Figure 4.34 A and B, recorded for the fractions 100–400 *g* (A) and 5–10k *g*. The size-dependent changes of the extinction and absorbance are further illustrated in Figure 4.34 C and D. These changes are comparable to changes in UV-Vis spectra of TMDs, which have been explained before. In short, the changes of the extinction are the sum of changes in absorbance and scattering background. The scattering background is the major contribution for excitation energies below the absorption edge (> 700 nm). In the high energy region of the spectrum, the extinction is dominated by the absorbance. While the scattering is pronounced in fractions containing large nanosheets (see Figure 4.34 A), it becomes negligible in fractions containing small nanosheets (see Figure 4.34 B).

As reported for other materials, size-dependent changes can be utilized for *in-situ* determination of nanosheet dimensions such as the nanosheet length, taking advantage of the fact that changes in the absorbance are often related to edge effects, where the electronic structure is altered compared to the basal plane. Here, the resonant intensity ratio 600/355 was calculated from the extinction and the absorbance and plotted against the nanosheet length (Figure 4.34 E), determined from AFM. This intensity ratio is comparable for extinction and absorbance, indicating that changes in the extinction are mostly due to changes in the absorbance and thus related to edge effects. As explained in the theory section of the thesis, the intensity ratio of the absorbance at two different wavelength, $Abs(\lambda_1)/Abs(\lambda_2)$, can be described by equation (2.14) (see chapter 2.4). However, the curve progression for the germanene derivatives can also be described by an empirical power law in the form of equation (4.13). After rearrangement of the equation, the mean Ge-Me nanosheet length in a dispersion can be estimated by equation (4.14) (or equation (4.15) in case of Ge-H).

$$\frac{Ext_{600}}{Ext_{355}} = A * \langle L \rangle^{m} \tag{4.13}$$

$$\langle L \rangle_{\mathrm{Ge-Me}}(\mathrm{nm}) = \left[\frac{Ext_{600}}{0.00413 * Ext_{355}}\right]^{1.424} \tag{4.14}$$

$$\langle L \rangle_{\mathrm{Ge-H}}\,(\mathrm{nm}) = \left[\frac{Ext_{600}}{0.00115 * Ext_{355}}\right]^{1.032} \tag{4.15}$$

Figure 4.34 F shows a ratio at a point in the non-resonant region of the spectrum (800 nm) and a wavelength in the resonant regime (355 nm) of the extinction and the absorbance as a function of the nanosheet length. As expected, significant differences are observed between extinction and absorbance, as scattering contributes strongly to the extinction spectra in the non-resonant regime. The intensity ratio determined from the absorbance slightly decreases with increasing nanosheet size, whereas it increases by an order of magnitude in the extinction spectra due to the size dependence of the scattering background.

The nanosheet thickness is commonly reflected in energy-shifts of optical, in particular excitonic transitions. However, in the spectra of the germanene derivatives, no sharp or pronounced transitions are discernible, which makes the *in-situ* determination of the nanosheet thickness impossible, but this is only a minor limitation. In contrast to TMDs, germanene derivatives are also fluorescent in their bulk structure, which reduces the importance of the knowledge about the exact thickness or layer number for future optical applications. In addition, the well-defined scaling of length and thickness which was quantified by AFM above still allows to estimate the thickness of the nanosheets from the length that can be determined from optical extinction spectra.

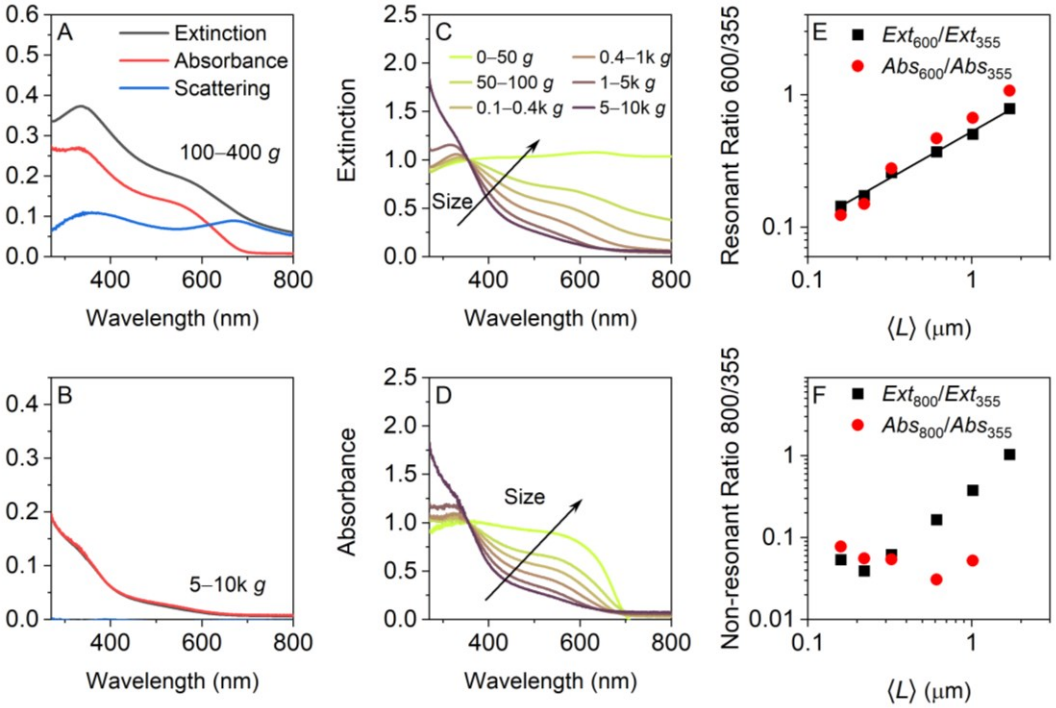

Figure 4.34: UV-Vis spectroscopy on dispersions of exfoliated and size-selected Ge-Me nanosheets. A, B: Extinction, absorbance, and scattering spectra of the nanosheet fractions 100–400 *g* (A) and 5–10k *g*. C, D: Extinction (C) and absorbance (D) spectra of different nanosheet sizes collected during LCC, showing size-dependent changes. E, F: Intensity ratios of the extinction and absorbance as a function of the nanosheet length, including the resonant ratio 600/300 (E) and the non-resonant ratio 800/355 (F).

For investigation of the photoluminescence properties of the germanene derivatives, PLE contour plots were recorded for the different dispersions (Appendix, Figure A 62 and Figure A 63) and the Ge-Me nanosheet films (Appendix, Figure A 64). Figure 4.35 shows a selection of the PLE maps recorded from Ge-Me dispersions and Ge-Me films, containing different nanosheet sizes. Dispersions of large Ge-Me nanosheets exhibit PL with an emission maximum between 670 and 680 nm, which is relatively invariant with respect to the excitation wavelength (0–50 *g*, Figure 4.35 A) with the strongest emission under excitation between 350 and 550 nm. The emission maximum gradually shifts towards lower excitation wavelength with increasing nanosheet size, (100–400 *g*, Figure 4.35 B) and excitation below 350 nm becomes more relevant. The PLE map recorded from the dispersion of the smallest nanosheets (5–10k *g*, Figure 4.35 C) is substantially different and exhibits the strongest PL under ~ 275 nm excitation. Excitation at higher wavelength results in only weak PL.

The PLE maps recorded from the Ge-Me nanosheet films show qualitatively similar trends (Figure 4.35 D–F, Figure A 64). PL Emission of Ge-Me films deposited from dispersions containing large nanosheets is relatively invariant for a wide range of excitation, but the emission maximum successively shifts towards lower excitation wavelength with decreasing nanosheet size. The size-dependent changes in the PLE maps of Ge-Me can be rationalized by the size-dependent changes of the UV-Vis absorbance. The PLE maps were recorded for an excitation range from 250 to 550 nm, which is a wavelength range where the absorbance has a strong size dependence as well. The absorbance of large nanosheets is relatively flat in this range but becomes steeper with decreasing nanosheet size, which correlates with the changes observed in the PLE maps.

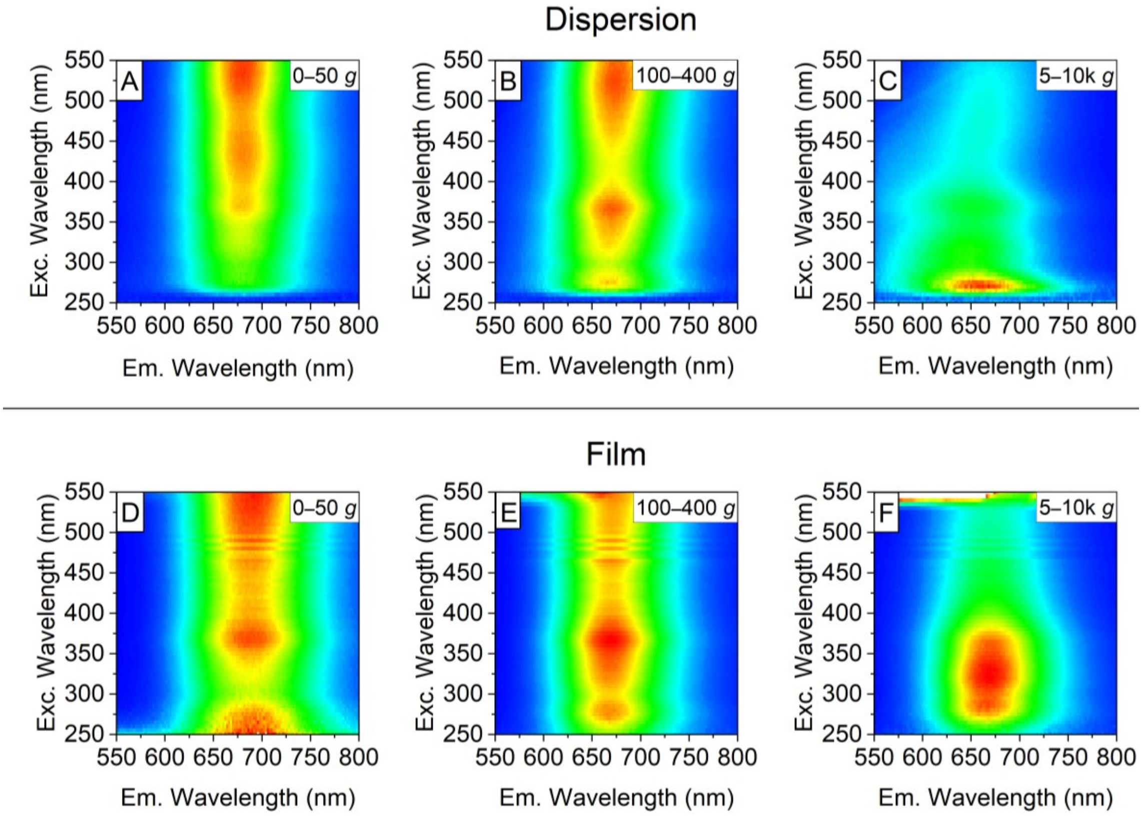

Figure 4.35: PLE contour plots of Ge-Me nanosheet dispersions and films. Top row: Different Ge-Me nanosheet sizes in dispersion. Large nanosheets of Ge-Me show approximately invariant emission at 670–700 nm over a wide range of excitation (A). The emission maximum successively shifts toward lower excitation wavelength with decreasing nanosheet size (B, C,). Bottom row: Different Ge-Me nanosheet sizes in films. Size-dependent trends are qualitatively similar to the PLE maps recorded from dispersion. The emission of large nanosheets is relatively invariant with respect to the excitation wavelength (D) but shifts towards lower excitation wavelength with decreasing nanosheet size (E, F), even though the trend is not as pronounced as it is in dispersion.

Interestingly, the PLE maps acquired from the Ge-H dispersions (Appendix, Figure A 67) show unexpected PL emission. No size-dependent trends are discernible, and all fractions collected during LCC exhibit an emission maximum at ~ 475 nm for an excitation wavelength of ~ 365 nm. In contrast to Ge-Me, strong emission is only detected for a relatively short range of excitation between ~ 350 and ~ 375 nm. As will be discussed below, this PL emission is in an unexpected range in particular because the emission occurs at higher energy than the absorption edge and hints towards an unsuccessful exfoliation of intact Ge-H even though the nanosheets showed a similar morphology as Ge-Me in the AFM.

For a more quantitative evaluation, PL spectra were recorded with an excitation wavelength of 370 (Ge-Me) or 365 nm (Ge-H), respectively, and fitted by Lorentzians (Appendix, Figure A 65–Figure A 67). In case of low nanosheet concentration, a second Lorentzian was added to the fits to account for the weak but non-negligible PL background originating from NMP. PL position, FWHM, and PL intensity were extracted from the fits and are compared in Figure 4.36.

Figure 4.36 A shows the PL positions of the size-selected nanosheet fractions as a function of central RCF. The PL position of Ge-Me and Ge-H averaged over all nanosheet fractions are 1.85 ± 0.01 eV (1.84 ± 0.01 eV in the Ge-Me films) and 2.60 ± 0.00 eV, respectively. A slight blue shift of the PL is observed for the Ge-Me dispersions with decreasing nanosheet size, which is less pronounced in the Ge-Me films. As anticipated from the PLE maps (Appendix, Figure A 63), no significant differences in the PL positions of the Ge-H dispersions are observed. The linewidth of the PL is compared in Figure 4.36 B. Some scatter in the data is observed for both Ge-Me dispersions and Ge-Me films, but no systematic size-dependent trends are discernible. Importantly, no broadening of the Ge-Me PL is observed after nanosheet film formation and deposition, which is promising for potential device fabrication. On average, the FWHM of the PL was determined to 0.31 ± 0.02 eV in the dispersions and 0.30 ± 0.01 eV in the films. With an average FWHM of 0.84 ± 0.00 eV, Ge-H exhibits significantly broader PL. A slight sharpening of the PL is observed for Ge-H with decreasing nanosheet size, but differences are small. Figure 4.36 compares the PL intensities of the dispersions. The PL intensities were divided by the corresponding absorbance at 370 or 365 nm to correct for different but unknown nanosheet concentrations and were subsequently normalized on the highest PL recorded for one material. Note that a direct comparison of the PL intensities is only possible within the same material but not between the two derivatives due to different optical fingerprints.

The strongest PL of Ge-Me was detected for the fraction 0–50 *g*, containing the largest nanosheets. With increasing RCF or decreasing nanosheet size, the relative PL intensity drops to ~ 0.2. The decreasing PL intensity might be attributed to the observed nanosheet degradation, which was most pronounced in the fractions of small nanosheets. However, the same trend is not observed for the Ge-H dispersions, where the data show some strong scatter from relative PL intensities of 0.5 to 1, but no clear size-dependent trend.

As mentioned above, the PL emission of Ge-H nanosheets was observed in the blue range of the visible spectrum, which is in contradiction with the absorbance profile, as well as the PL emission of bulk Ge-H and literature reports. Intact Ge-H emits PL at ~ 1.7 eV or ~ 730 nm, respectively, which is redshifted in comparison to the emission of Ge-Me.[181] Additionally, the PL emission of Ge-H is blue shifted with respect to the absorption edge, which is rather counterintuitive. One might argue that the blue PL emission originates from NMP, which shows PL emission in a comparable range, especially after sonication due to sonochemical degradation.[164] However, this is unlikely for two reasons. First, the samples are strongly diluted with fresh NMP. Second, Ge-Me was exfoliated under identical conditions with the same solvent (from the same bottle), but only weak PL emission related to NMP is observed. This implies that Ge-H either degraded during exfoliation, underwent chemical reactions with NMP (for example 4-fluorphenyl substituted germanene emits in the blue range[188]), or formed charge transfer complexes with NMP. While some of these explanations are more imaginable than others, it is beyond the scope of this work to clarify this issue. Due to the unconventional PL emission and the undesired smaller lateral dimensions of the Ge-H nanosheets, further work (such as film fabrication) was focused on Ge-Me rather than Ge-H.

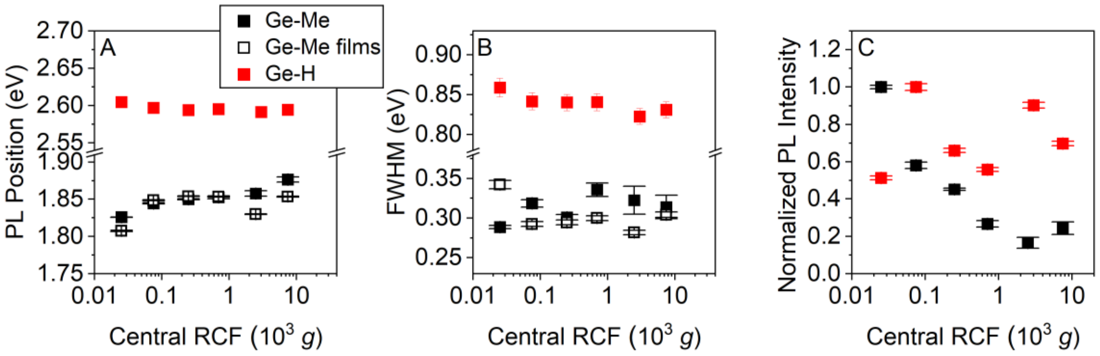

Figure 4.36: Quantitative PL information about Ge-Me and Ge-H nanosheet dispersions, and Ge-Me nanosheet films, derived from the PL spectra shown in Figure A 65–Figure A 67 (Appendix). The PL spectra were recorded at an excitation wavelength of 370 nm (Ge-Me) and 365 nm (Ge-H), respectively. A: PL position as a function of central RCF. A slight blue shift is discernible for the Ge-Me dispersions, which is less pronounced in the films. The PL position of the Ge-H dispersions is mostly invariant with respect to the nanosheet size. B: FWHM as a function of central RCF. Some scatter in the data is observed for the Ge-Me dispersions, but no clear size-dependent trend is discernible. The PL of the Ge-Me films does not show any broadening. The PL of Ge-H shows a minor sharpening with decreasing nanosheet size but is significantly broader than the PL of Ge-Me. C: Normalized PL intensity against central RCF. The PL was divided by the absorbance at 370 or 365 nm, respectively, to correct for different but unknown nanosheet concentrations, and subsequently normalized on the highest PL intensity. The PL intensity of Ge-Me significantly decreases with the nanosheet size. For the Ge-H dispersion, this trend is not discernible but strong scatter in the data points is observed.

To further investigate the PL properties of Ge-Me nanosheet films, PLQY measurements were performed on films with three different nanosheet sizes (0–50 *g*, 50–100 *g*, 100–400 *g*). PLQY measurements were carried out in the center of an integrating sphere at 530 nm excitation, revealing PLQY values between ~ 3 and 12 % (Figure 4.37 A). In this experiment, the PLQY values rise with decreasing nanosheet size, which is the opposite trend expected from PL experiments on the dispersions which showed a relative increase in PL with increasing size. However, multiple reabsorption events of the light can occur during the measurements in the integrating sphere, artificially decreasing the calculated PLQY. This has a stronger impact in case of larger/thicker nanosheets, since the films intrinsically exhibit a higher optical density due to the higher mass of the deposited nanosheets. Figure 4.37 B shows UV-Vis extinction spectra of the Ge-Me films used for the PLQY measurement, revealing strong differences in the optical density that correlate inversely with the determined PLQY, thus pointing toward reabsorption. A PLQY of 12 % can therefore be considered as realistic value for all nanosheet sizes. Note that the films were prepared by a single deposition and that the films cannot be produced with lower optical density to test this hypothesis.

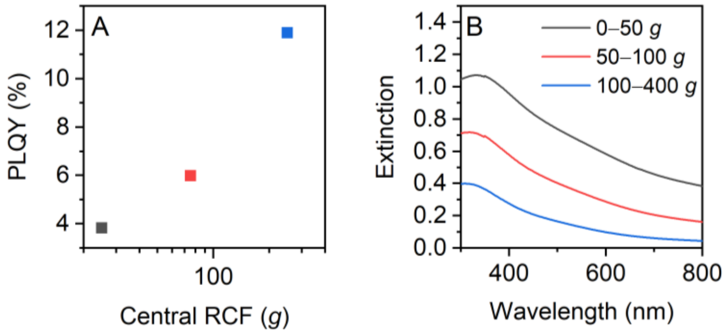

Figure 4.37: PLQY measurements of Ge-Me nanosheet films (A), including three different nanosheet sizes. The PLQY was measured by an absolute method in the center of an integrating sphere. The graph shows a strong increase in the PLQY from 4 to 12 % with decreasing nanosheet size. The relatively low PLQY values of large nanosheets can be attributed to the high optical density of the films (see B), which leads to multiple reabsorption in the integrating sphere and artificially decreases the determined PLQY values.

After characterization of the germanene derivatives and films, the question arises in which way the materials are suitable candidates for potential applications. Since the UV-Vis spectra of the germanene derivatives do not feature any sharp and pronounced excitonic transitions, they are not promising candidates for the implementation in optical microcavities for strong light-matter coupling. However, the relatively strong PL hints towards the usability in light-emitting devices, such as LEDs or light-emitting field effect transistors (LEFETs). A major limitation might be the inaccessibility of nanosheet films consisting of smaller nanosheets, which exhibit a smoother morphology and improved homogeneity compared to nanosheet films deposited from large/thick sheets isolated at low centrifugal accelerations in the size selection. In this work, the implementation of Ge-Me nanosheets into LEFETs was tested with Ge-Me nanosheet films deposited from the fractions 0–50 *g*, 50–100 *g*, and 100–400 *g*. While some current passed through the device (only for the fraction 0–50 *g*), no switching behavior of the transistor was observed. Nanosheet films were sent to collaborators for network conductivity measurements, but a stable electrical current was only detected in the nanosheet networks based on the 50–100 *g* fraction and no reproducibility of the measurements was accomplished. The unsatisfying results of device fabrication are attributed to the polydispersity of the nanosheets in the films, leading to inhomogeneities and poor morphologies. This implies that more promising results might be obtained when films of smaller nanosheets are employed. To achieve this, degradation of the nanosheets needs to be suppressed and within this work, no further attempts were carried out.

4.3.5 Summary and Conclusion

Two different derivatives of germanene, Ge-Me and Ge-H, were subjected to LPE and LCC under inert gas conditions, and Langmuir films of Ge-Me were prepared and deposited. The nanosheet dispersions and films were characterized by AFM, SEM, optical microscopy, UV-VIS, and fluorescence spectroscopy, and metrics were developed for *in-situ* estimation of the average nanosheet size in dispersion by UV-Vis extinction spectroscopy.

After exfoliation, Ge-H exhibits blue PL which is in contradiction to the intrinsic PL of intact Ge-H, implying that Ge-H underwent degradation or chemical reaction with NMP during sonication. Therefore, further experiments were focused on Ge-Me. Ge-Me shows promising properties for the implementation in optoelectronic devices, first of all strong photoluminescence at ~ 1.85 eV or 670 nm, respectively, with a linewidth of ~ 0.31 eV. In case of large or medium sized nanosheets, the PL emission is relatively invariant with respect to the excitation wavelength. No broadening of the PL was observed after deposition of the nanosheets and PLQY values up to 12 % were determined in the Ge-Me nanosheet films. However, a drawback is that nanosheet degradation was observed which was most pronounced for small nanosheets, even though Ge-Me is considered as relatively stable. In consequence, nanosheet film formation was only successful for larger nanosheets of Ge-Me, where the films were relatively inhomogeneous as a result of the broad size distribution of large nanosheets in dispersion. In this work, implementation of Ge-Me nanosheet films in LEFETs was tried without success, which was attributed to the unfavorable morphology of the Ge-Me films.

For future device fabrication, films of smaller nanosheets should be employed which requires the suppression of nanosheet degradation. This could be accomplished by film formation under inert gas conditions or improvement of the stability, for example by derivatization of germanene with different substituents. For example, larger substituents might sterically protect the sheets. Additionally, larger substituents might decrease the interlayer binding strength and result in nanosheets with larger lateral dimensions.

5 Conclusion and Outlook

The first part of this thesis was devoted to the optimization of sonication-assisted LPE and in a first step, the impact of the starting material on the exfoliated nanosheets was investigated. It was demonstrated on the example of MoS_2 that neither purity, nor crystallite size or defectiveness of the bulk starting material has an impact on the dimensions of the exfoliated nanosheets. However, differences were observed in the relative PL intensity of the nanosheet dispersions, which might be attributed to the defectiveness of the starting material. This is supported by the fact that the strongest PL was observed for nanosheets exfoliated from a single crystal of MoS_2, which is expected to carry the fewest number of defects. While this is a hypothesis without experimental evidence, it is further supported by the study on the pretreatment of bulk WS_2, where it was shown that defectiveness of the nanosheets indeed reduces the relative PLQY expressed as PL/Raman signal. The study on the pretreatment of the starting material showed that the exfoliation efficiency can be improved through intercalation of the pretreatment agents and hence lowering of the interlayer binding strength, but significant enhancement of the exfoliation process over scission was only observed when non-ideal low energy sonication was chosen. While only negligible enhancement was observed under established high power sonication conditions, the results of the study provide important information for the understanding of the exfoliation process.

In the next chapter, thin films of WS_2 were produced, characterized, and eventually implemented into optical microcavities. First, WS_2-PVK composite films were prepared. Sufficient film quality was only accomplished when the WS_2 content in the films was kept low. At high WS_2 concentrations, the PL of the nanosheets was almost completely quenched due to strong aggregation, which was further reflected in a high surface roughness of the films. In the set of samples prepared for this thesis, an extinction at the resonance of the A-exciton around 0.024 per 100 nm film thickness marked the turning point, from where on the PL started to vanish. This is disadvantageous since relatively high optical densities are required for strong light-matter coupling experiments. Nevertheless, cavities were produced with the WS_2-PVK composite films, but no evidence for strong light-matter coupling could be observed, which was attributed to the following reasons: First, the overall film quality is too poor, resulting in a bad quality of the cavities. Second, the nanosheets in the films are embedded with random orientation, making the excitation inefficient. Lastly, the polymer films were relatively thick, which implies that higher order cavity modes were tuned to the exciton resonance, which is accompanied by lower mode volumes of the photonic modes. While the nanosheet polymer composite films do not appear to be promising candidates for polaritonic research, they might still find applications in other fields, where low nanosheet concentrations are required in the polymer matrix.

Next, Langmuir films of WS_2 were prepared at liquid-liquid phase interfaces. The deposition of these films results in homogenous nanosheet networks, and multiple depositions are possible with a linear scaling of the optical density with the number of deposited layers. The PL of the films decreases with the number of layers but can be preserved by functionalization of the WS_2 sheets with diazonium salts prior to film formation. After five depositions, optical densities are accomplished that are sufficient for the implementation in optical microcavities. At this stage, the relative PLQY expressed as PL/Raman ratio is substantially higher than the PLQY of the WS_2-polymer composite films. Additionally, the thickness of the Langmuir films is in the range of ~ 10–20 nm, allowing to design cavities with desired thickness and to place the films at a defined position in a cavity. Therefore, Langmuir films of WS_2 were implemented into microcavities. A Rabi splitting was observed in all cases, proving strong light-matter coupling and the formation of exciton-polaritons. However, despite all the accomplishments that have been made, it was not possible to measure the dispersion of the PL, due to low intensity and limited sensitivity of the setup for angle resolved measurements. With sensitive instruments such as the Raman microscope, PL was still measurable, showing that the PL/Raman ratio is only slightly reduced during the processes required to finish the cavity. In future experiments, it might be required to increase the number of emitters in the cavity by depositing a greater number of WS_2 layers, resulting in stronger PL. However, each additional layer might lead to unfavorable PL quenching and it might be necessary to spatially separate the layers more efficiently, which can be accomplished by alternating deposition of WS_2 and a spacer such as *h*-BN or PMMA. While the preparation of the cavities would be very time consuming, the approach would also be very promising and worth the effort. Alternatively, other means to increase the PLQY should be explored which have been successful in the case of micromechanically-exfoliated or CVD-grown TMDs, for example treatment with TFSI.[53]

Since weak PL in the WS_2 films was a recurrent challenge over the course of this work, the last chapter aimed for the exploration of less known materials, such as germanene derivatives, which exhibit strong PL also in bulk structure. Therefore, hydrogen and methyl derivatized germanene were subjected to LPE and LCC. In case of Ge-H, the photoluminescence properties were not preserved after sonication, even though the exfoliation and size selection were carried out under inert gas conditions. The characterization of the exfoliated Ge-Me nanosheets revealed promising properties. Since Ge-Me does not exhibit sharp optical transitions, it cannot be used in optical microcavities, but strong PL at ~ 670 nm could potentially be exploited in light-emitting devices such as LEDs or LEFETs. After preparation of Langmuir films of Ge-Me nanosheets, the PL was preserved. PLQY values up to 12 % were observed without a significant broadening of the emission. However, even though Ge-Me is considered as relatively stable, basal plane degradation of the nanosheets under ambient conditions was observed in AFM images, that was most dominant in fractions containing smaller nanosheets. As a consequence, preparation of the

Langmuir films was only possible for larger sheets, resulting in rather inhomogeneous films with an undesired morphology. This is not due to the film preparation methodology but reflects the broad size distribution in fractions isolated at low centrifugal acceleration of the size selection cascade. The implementation of Ge-Me films in LEFETs failed, which was attributed to the inhomogeneities in the nanosheet networks. Nevertheless, nanosheet degradation might be suppressed in future when inert gas film preparation protocols are developed, allowing to create devices based on homogeneous thin films of the smaller Ge-Me fractions. Additionally, derivatization with different substituents might result in greater stability as well as improved aspect ratios of the nanosheets, and eventually in working light-emitting devices.

Last but not least, it should be noted that the fundamental insights and learnings from this thesis should be readily applicable to a whole host of other layered materials that can be exfoliated by LPE and size-selected with LCC. To date, thousands of layered crystals are predicted and the current investigations only focus on a few materials that just represent the tip of the iceberg. With more detailed knowledge on little explored structures, it might be possible to select more suitable candidates and turn the learnings from this thesis into the basis for applications.

6 Experimental Section

6.1 Chemicals

The MoS_2 bulk materials were purchased from Sigma-Aldrich with 6 µm particle size (SA6, 69860), with 2 µm particle size (SA2, 99 %, 234842), and with 90 nm particle size (SAnp, 99 %, 804169), from Tribotecc (Tribo), from Alfa Aesar (AA, 98 %, 12213) or from SPI Supplies (Crystal, 429MS-AB). WS_2 (243639), sodium cholate hydrate (C1254), PMMA (M_W ~ 350,000, 445746), and PVK (M_n ~ 25000–50000, 368350) were purchased from Sigma-Aldrich. Germanene derivatives were provided by the group of Prof. Dr. Sofer, University of Chemistry and Technology, Prague.

6.2 Preparation of Nanosheet Dispersions

MoS_2 Dispersions (Chapter 4.1.3)

600 mg (120 mg in case of the sample Crystal) of bulk MoS_2 powder was dispersed in 80 mL aqueous SC-solution (8 g/L) and the dispersion was tip sonicated for 1 h (60 % amplitude, pulse 8 s on and 2 s off, 5 °C) and subsequently centrifuged for 90 min at 3820 *g*. The supernatant was discarded, and the sediment redispersed in fresh SC-solution (2 g/L) and sonicated again for 5 h (60 % amplitude, pulse 6 s on and 2 s off, 5 °C). The exfoliated stock dispersion was subjected to LCC, starting with centrifugation at 100 *g* (0.1k *g*) for 2 h. The sediment of this centrifugation step was discarded, and the supernatant was successively centrifuged again at 0.4k *g*, 0.8k *g*, 2k *g*, 5k *g*, 10k *g*, and 30k *g*. The sediments of these centrifugation steps were collected and redispersed in a defined volume of fresh SC-solution (0.1 g/L). The supernatant of the last centrifugation step was discarded. Centrifugations were carried out in a Hettich MIKRO 220R centrifuge equipped with a fixed angle rotor 1016 (from 0.1k to 2k *g*, in 20 mL aliquots filled into 50 mL conical bottom centrifuge tubes, VWR high performance) or 1195-A (5k *g* to 30k *g*, in 1.5 mL aliquots filled into 1.5 mL Eppendorf tubes).

WS_2 Dispersions (Chapter 4.1.4)

Bulk WS_2 powders were subjected to the following pretreatments prior to exfoliation:

NaCl stir: 2.4 g of WS_2 were dispersed in aqueous NaCl solution (80 mL, 1 M) and stirred for eight days under ambient conditions. The dispersion was filtered by vacuum filtration (MF^{TM}-membrane from Merck Millipore LTD., 0.025 µm pore size, 47 mm diameter), thoroughly washed with water, dried under vacuum, and weighed.

NMP stir: 2.4 g of WS_2 were dispersed in NMP (80 mL) and stirred for seven days under ambient conditions. The dispersion was filtered, dried under vacuum, and weighed, as described above.

BuLi stir: 2.4 g of WS_2 were dispersed in dry *n*-hexane (20 mL), and *n*-BuLi in *n*-hexane (0.6 mL, 2 M) was added. The solution was stirred overnight at 60 °C and quenched with water (100 mL). The aqueous phase was washed with *n*-hexane and subsequently filtered, dried under vacuum, and weighed, as described before.

H_2O bath: 2.4 g of WS_2 were dispersed in water (80 mL) and bath sonicated for 7 h (Bransonic® CPXH 2800-E from Branson Ultrasonics Corporation). The filling height of the sonication bath was adjusted in such a way that hot spots were formed, and the WS_2 dispersion was placed in the middle of the hot spot. Ice was added during sonication for cooling, requiring re-adjustment of the filling height. After finished sonication, the dispersion was filtered, dried under vacuum, and weighed, as described before.

LiCl bath: 2.4 g of WS_2 were dispersed in a solution of LiCl in *n*-hexane solution (20 mL, 21 g/L) and bath sonicated for 4 h with adjustment of the filling height and ice cooling, as described above. After finished sonication, the dispersion was filtered, thoroughly washed with water, dried in vacuum, and weighed.

The WS_2 powders obtained after the pretreatments were dispersed in aqueous SC-solution (80 mL, 2 g/L) and tip sonicated for 5 h (30 % or 60 % amplitude, respectively, pulse: 6 s on, 4 s off, 5 °C). The exfoliated stock dispersions were subjected to LCC with centrifugation steps at 0.1k *g*, 0.4k *g*, 2k *g*, 5k *g*, 10k *g*, and 30k *g*. The sediments were collected and redispersed in a defined volume of fresh SC-solution (0.1 g/L), except for the sediment of the first centrifugation step which was discarded, as well as the supernatant of the last centrifugation step. Centrifugations were carried out in the Hettich MIKRO 220R centrifuge equipped with a fixed angle rotor 1016 (from 0.1k to 2k *g*, in 20 mL aliquots filled into 50 mL conical bottom centrifuge tubes, VWR high performance,) or 1195-A (5k *g* to 30k *g*, in 1.5 mL aliquots filled into 1.5 mL Eppendorf tubes).

WS_2 Dispersions for Thin Film preparation (Chapter 4.2)

2.4 g of WS_2 was dispersed in aqueous SC-solution (80 mL, 8 g/L), tip sonicated for 1 h (60 % amplitude, pulse: 8 s on, 2 s off, 5 °C), and centrifuged at 7.8k *g*. The supernatant of this centrifugation step was discarded, and the sediment redispersed in fresh SC-solution (80 mL, 2 g/L). The redispersed WS_2 was sonicated for typically 5 to 7 h (60 % amplitude, pulse: 6 s on and 4 s off) and subsequently subjected to LCC with typical centrifugation steps at 0.4k *g*, 1k *g*, 5k *g*, 10k *g*, and 30k *g*. The sediment of the first centrifugation step was discarded and the sediments of the following steps collected in fresh SC-solution (0.1 g/L).

Dispersions of Germanene Derivatives (Chapter 4.3)

Ge-Me or Ge-H were dispersed in dried, distilled, and degassed NMP under nitrogen atmosphere in a pear-shaped flask, resulting in a concentration of ~ 1 g/L. The flask was sealed, removed from the glovebox and the dispersion was bath sonicated for ~ 16 h. The filling height was adjusted in such a way that hot spots were formed and the dispersion of the germanene derivatives was placed in the center of a hot spot. The sonication bath was cooled by successively adding ice to the bath and following re-adjustment of the filling height. After sonication, the flask was brought back into the glovebox and the dispersion distributed across 1.5 mL Eppendorf tubes. The dispersions were subjected to LCC with centrifugation steps at 50 *g*, 100 *g*, 400 *g*, 1k *g*, 5k *g*, and 10k *g*. The centrifugation was carried out in closed Eppendorf tubes outside the glovebox, using the Hettich MIKRO 220R centrifuge equipped with a fixed angle rotor 1195-A. After each centrifugation step, the tubes were transferred back into the glovebox to decant the dispersions under nitrogen atmosphere. The sediments were collected in fresh NMP, and the supernatant of the last centrifugation step was discarded.

6.3 Preparation of Nanosheet Thin Films

WS_2-PVK Composite Films (Chapter 4.2.2)

The WS_2 fractions 5–10k *g* or 10–30k *g* collected during LCC were centrifuged at 31k *g* for 2 h (Hettich MIKRO 220R equipped with fixed angle rotor 1195-A) and the sediment was redispersed in fresh water. The centrifugation was repeated, but the sediment of the second centrifugation was redispersed in NMP, and the NMP dispersion subjected to a third, overnight centrifugation at 23k *g*. After finished centrifugation, the supernatant was discarded, and the sediment collected without any further dilution and labelled as WS_2 concentrate. The WS_2 concentrate was mixed to PVK in THF (30 g/L) in a ratio 1:2 and the combined solution centrifuged for 30 min at 100 *g*, to remove potentially formed aggregates in the solution. The supernatant of this centrifugation step was used as spin coating solution within the next 30 min.

Spin coating was carried out in a glovebox under inert gas atmosphere. 175 µL of the spin coating solution was dynamically dispensed on a glass substrate (AF32®eco from Schott, 25×20×0.5 mm) and spun at relatively low speed ω_1 for the time *t*. After the expired time *t*, the spin coating speed was increased to ω_2 within ~ 1 s and the substrate was spun for additional 60 s. After finished spin coating, the WS_2-PVK composite film was left at 80 °C for 1 h. The spin coating parameters are listed in Table 6.1.

WS_2 Langmuir Films (Chapter 4.2.3)

The WS_2 fractions obtained during LCC were centrifuged at 31k *g* for 2 h (Hettich MIKRO 220R equipped with fixed angle rotor 1195-A). The sediment was redispersed in fresh water and subsequently centrifuged again at 31k *g* for 2 h. The new sediment was redispersed in IPA and diluted to optical densities with extinction values between ~ 0.3 and ~ 0.8. Dispersions of functionalized WS_2 were already provided in IPA in desired concentration. Glass substrates (AF32®eco from Schott, 25×20×0.5 mm) were cleaned by bath sonication in THF, IPA, and water for 10 minutes each. The glass substrates were horizontally placed in a beaker, using a homemade substrate holder, and the beaker was filled with water until the glass substrate was a couple of millimeters below the water surface. A thin layer of *n*-hexane was added to the beaker, forming a two-phase system. The WS_2/IPA dispersion (100–300 µL, volume was adapted to the WS_2 concentration in such a way, that a closed film formed without overloading the surface) was injected to the water/*n*-hexane interface, resulting in nanosheet self-assembly at the phase interface. The *n*-hexane layer was removed from the top and residues of the solvent were allowed to evaporate, before the glass substrate was lifted through the nanosheet film, keeping a horizontal orientation. The film was dried by leaving it under ambient conditions overnight and subsequently heating it to 50 °C for 1 h under vacuum.

Table 6.1: Spin coating parameters used for the preparation of the WS_2-PVK composite films in chapter 4.2. 175 µL of the spin coating solution was dynamically dispensed on the substrate and spun at relatively low speed ω_1 for the time t. After the expired time t, the spin coating speed was increased to ω_2 within ~ 1 s and the substrate was spun for additional 60 s. After finished spin coating, the WS_2-PVK composite film was left at 80 °C for 1 h.

Sample	**ω_1 (rpm)**	**t (min)**	**ω_2 (rpm)**
Batch 1 Film I	1000	15	1000
Batch 1 Film II	100	15	1000
Batch 1 Film III	120	15	1000
Batch 1 Film IV	100	15	1500
Batch 2 Film I	80	15	500
Batch 2 Film II	80	15	1000
Batch 2 Film III	100	40	1000
Batch 3 Film I	100	15	1000
Batch 3 Film II	120	15	1000
Batch 3 Film III	100	5	1000
Batch 3 Film IV	100	30	1000
Batch 4 Film I	80	15	750
Batch 4 Film II	100	15	1000
Batch 4 Film III	80	15	1000
Batch 4 Film IV	80	15	1000
Batch 5 Film I	80	15	1000
Batch 5 Film II	100	15	1000
Batch 5 Film III	60	15	1000
Batch 5 Film IV	80	15	750

Ge-Me Langmuir Films (Chapter 4.3.3)

NMP dispersions of Ge-Me collected during LCC were diluted with fresh NMP until optical densities with extinction values between ~ 0.3 and ~ 0.8 were achieved. Glass substrates (AF32®eco from Schott, 25×20×0.5 mm) were cleaned as described above and horizontally placed in a beaker, using a homemade substrate holder. The beaker was filled with water until the glass substrate was a couple of millimeters below the water surface and a thin layer of toluene was added to the beaker. The Ge-Me dispersion was injected to the water/toluene interface, forming the nanosheet film. The organic layer was removed from the top and residues of toluene were allowed to evaporate, before the glass substrate was lifted through the nanosheet film, keeping a horizontal orientation. The film was dried by the procedure described above.

6.4 Preparation of Optical Microcavities

Cavity Architecture I: An adhesive layer of 2 nm chromium followed by 100 nm Ag were deposited on glass substrates (AF32®eco from Schott, 25×20×0.5 mm) by electron beam evaporation. WS_2-PVK composite films were spin-coated on the bottom mirror according to Table 6.2, and the cavity was finished by growing a thin layer of Al_2O_3 by atomic layer deposition (ALD, 2 nm) on the film, spin coating a thin layer of PMMA (6 g/L in *n*-butyl acetate, 4000 rpm, 60 s), and deposition of a 30 nm thick Ag top mirror by thermal evaporation.

Architecture II (open cavity): An adhesive layer of 2 nm chromium followed by 30 nm Ag were deposited on glass substrates (AF32®eco from Schott, 25×20×0.5 mm) by electron beam evaporation. WS_2-PVK composite films were spin-coated on the mirror according to Table 6.2, and a silver coated lens (100 nm Ag) was approached to the mirror, using a home build sample holder.

Architecture III: An adhesive layer of 2 nm chromium followed by 100 nm Ag were deposited on glass substrates (AF32®eco from Schott, 25×20×0.5 mm) by electron beam evaporation. 75 nm of Al_2O_3 was grown on the mirror and up to five layers of WS_2 Langmuir films were deposited on the Al_2O_3. The cavities were finished by spin coating of PMMA from *n*-butyl acetate (ButOAc, 7.5 g/L, 4000 rpm, 60 s) on the WS_2 film and deposition of 30 nm of silver by thermal evaporation.

Table 6.2: Spin coating parameters for the preparation of the WS_2-PVK composite films in the optical microcavities. 175 µL of the spin coating solution was dynamically dispensed on the substrate and spun at relatively low speed ω_1 for the time *t*. After the expired time *t*, the spin coating speed was increased to ω_2 within ~ 1 s and the substrate was spun for additional 60 s. After finished spin coating, the WS_2-PVK composite film was left at 80 °C for 1 h.

Sample	**ω_1 (rpm)**	***t* (min)**	**ω_2 (rpm)**
Ref (Thermal Evap)	100	1	1000
Ref (Ebeam)	100	1	1000
Cav CF1	100	10	1000
Cav CF2	100	15	1000
Cav CF3	100	15	1000
Cav CF4	100	5	1000
Cav CF5	100	15	1000
Cav CF Open	100	15	1000

6.5 Sample Characterization

SEM/EDX: The SEM images were recorded on a JEOL JSM-7610F field emission scanning electron microscope (FE-SEM), using an In-lens Schottky field emission electron gun with 5 kV acceleration voltage at 2.5×10^{-9} mbar. The microscope was equipped with a dual (upper and lower) detector system consisting of collector, scintillator, light guide, and photomultiplier units for secondary electron imaging.

EDX measurements were carried out at 15 kV in 28.5° detection angle with 9 mm working distance.

Powder XRD: Powder XRD spectra were recorded on a SmartLab X-ray diffractometer from Rigaku equipped with a HyPix-3000 detector. The measurements were carried out in glass capillaries with 0.6 mm diameter in Debye-Scherrer geometry using monochromatic Cu K α1 radiation (λ = 1.54059 Å). The baseline was corrected by measuring an empty capillary and the samples were measured by a 1D scan with a rotation speed of 60 rpm.

Sonication: Tip sonication was carried out with a Sonics VCX 500 from Sonics & Materials, equipped with a horn tip (1.27 cm diameter) for 500 W ultrasonic processor from Sigma-Aldrich and an external cooling system. Bath sonication was carried out with a Bransonic® CPXH 2800-E bath sonicator from Branson Ultrasonics.

Centrifugation: Centrifugations were carried out on an Avanti J26XP centrifuge from Beckman Coulter or a MIKRO 220R centrifuge from Andreas Hettich GmbH. The Avanti J26XP centrifuge was equipped with the fixed angle rotors JA-25.50 or JA-25.15 and the MIKRO 220R centrifuge with the fixed angle rotors 1016 or 1195-A.

UV-Vis spectroscopy: UV-VIS-NIR extinction spectra of nanosheet dispersions were recorded on a Varian Cary 6000i UV-Vis-NIR or Varian Cary 60 UV-Vis spectrometer from Agilent in SUPRASIL® quartz cuvettes with 4 mm beam path from Hellma GmbH & Co. KG. The absorbance spectra were carried out on the Varian Cary 6000i UV-Vis-NIR spectrometer in the center of an integrating sphere (external DRA-1800). Extinction spectra of thin films were measured on the Varian Cary 6000i using the UV-Vis-NIR solid sample holder from Agilent.

Raman spectroscopy: The Raman spectra were recorded on a Renishaw InVIA confocal Raman microscope equipped with 50× long working distance objective (Olympus, N.A. 0.5) and 532 nm or 633 nm excitation laser. The Raman emission was collected in streamline mode and dispersed by a 2400 l/mm or 1200 l/mm grating. For the measurements in dispersion, a droplet was placed on aluminum foil and the focus was set to the surface of the droplet. 5–10 spots were measured in the edge region of the droplets under ambient conditions with ~ 1 % of the laser power and averaged.

Fluorescence spectroscopy: Fluorescence measurements were recorded on a Horiba Fluorolog-3 Fluorescence spectrometer equipped with a Syncerity PMT detector, a 450 W xenon lamp for excitation, and monochromators for both excitation and emission (1200 l/mm grating blazed at 330 for excitation, and 1200 l/mm blazed at 500 nm or 600 l/mm blazed at 1000 nm for emission). Bandwidths between 2 and 8 nm were used on both excitation and emission side with acquisition times between 0.1 and 0.3 s. The excitation light was cut off by long pass filters, absorbing below 400, 495, or 550 nm. Dispersions were measured in SUPRASIL® quartz cuvettes with right angle geometry between excitation source and detector. The films were measured on glass substrates or aluminum foil and the position and angle were adjusted to maximize the signal.

AFM: The acquisition of the AFM images was carried out under ambient conditions on an ICON scanning probe microscope from Bruker equipped with an aluminum coated silicon nitride (ScanAsyst Air) or silicon (OLTESPA-R3) cantilever. The images were recorded in the mode "ScanAsyst in Air" with image size range from 3×3 to 40×40 µm, typical scan rates of 0.5–1 Hz and 1024 lines per image. The WS_2-polymer composite films were scanned as produced using the ScanAsyst Air cantilever. For the measurement of Ge-Me or Ge-H nanosheets, Si/SiO_2-wafer with on oxide layer of 300 nm were cleaned by bath sonicating in THF, IPA, and H_2O for 10 min each. The NMP dispersions of the germanene derivatives were diluted with an excess of IPA and flash-evaporated on the pre-heated Si-wafer (150 °C). The wafers were thoroughly rinsed with water and IPA, subsequently dried under nitrogen flow, and scanned using the OLTESPA-R3 cantilever.

Reflectivity measurements: Angle resolved reflectivity measurements (at angles up to 40°) were recorded with a Fourier imaging setup. The basic principle is illustrated in Figure 6.1. Reflected light was collected by an 50× objective (Olympus LCPLFLN50xLCD, *f* = 45 mm, N.A. = 0.7) and directed to a 1340×400 Si CCD camera (Princeton Instruments, PIXIS:400) through a Fourier lens (achromatic doublet, *f* = 200 mm) and a tube lens (achromatic doublet, *f* = 300 mm). The sample was illuminated by a collimated white light source that was directed into the objective by a broadband beam splitter (Thorlabs BSW29R, 50:50 split ratio).

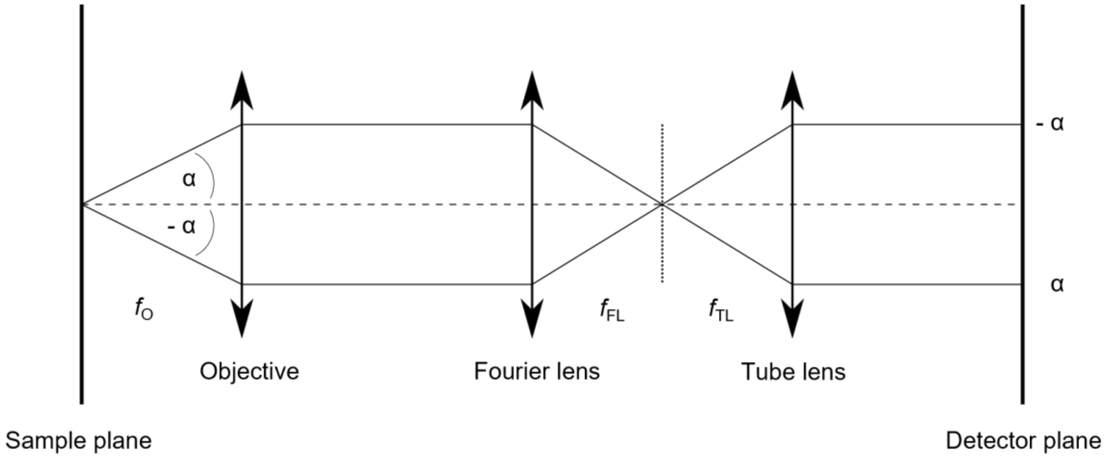

Figure 6.1: Illustration of the Fourier imaging setup employed to record angle resolved reflectivity measurements.

At higher angles, the angle-resolved reflectivity was recorded by collaborators (Dr. Andreas Mischok, Group of Prof. Dr. Gather, University of Cologne) with a variable-angle spectroscopic ellipsometer (VASE, M2000, J.A. Woollam). The polariton dispersions were modelled by a coupled oscillator Hamiltonian[166], assuming an exciton energy of 1.99 eV and an effective refractive index of 1.85, yielding a coupling strength of 0.12 eV.

PLQY measurements: PLQY measurements were carried out in the center of an integrating sphere by an absolute method. A spectrally filtered output of a supercontinuum laser source (Fianium WhiteLase SC400, bandpass tuned to 530 nm) was used as excitation source and the PL was out-coupled via optical fiber, dispersed by a grating spectrograph (Acton SpectraPro SP2358, 150 l/mm grating), and detected by a liquid nitrogen cooled InGaAs line camera (Princeton Instruments OMA V:1024-1.7 LN). Excitation light was cut off by a long pass filter absorbing below 590 nm. The absorbance of the sample was determined by comparing the scattered laser intensities with and without samples inside the integrating sphere.

7 Appendix

7.1 Appendix Chapter 4.1

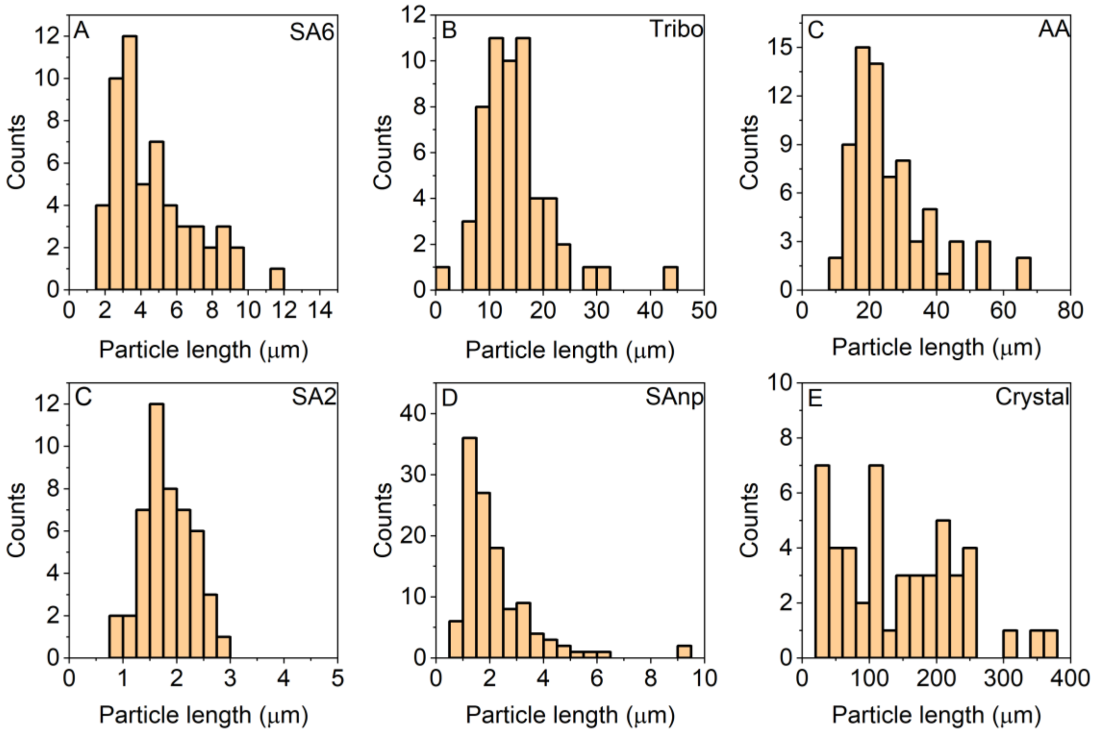

Figure A 1: Particle length distribution of MoS_2 bulk materials. Particle length refers to the longest dimension of the particle and was derived from the SEM images shown in Figure 4.1. A: Sigma Aldrich, 6 µm particle size, B: Tribotecc, C: Alfa Aesar, D: Sigma Aldrich, 2 µm particle size, E: Sigma Aldrich, nanopowder, F: Ground MoS_2 crystal from SPI Supplies.

Table A 1: Elemental analysis of SA6 by EDX

Element	Weight %	Atom %
C	0.51 ± 0.24	2.21 ± 1.02
O	0.72 ± 0.14	2.36 ± 0.44
F	0.09 ± 0.14	0.25 ± 0.38
Al	0.10 ± 0.05	0.20 ± 0.09
S	35.83 ± 1.45	58.95 ± 2.36
Sc	0.38 ± 0.85	0.44 ± 0.99
Ti	0.28 ± 0.63	0.31 ± 0.69
Cr	0.65 ± 0.71	0.65 ± 0.71
Fe	0.54 ± 0.54	0.50 ± 0.50
Ni	0.22 ± 0.21	0.20 ± 0.19
Cu	1.70 ± 0.22	1.41 ± 0.20
Zn	0.84 ± 0.05	0.68 ± 0.04
Y	0.57 ± 0.09	0.34 ± 0.05
Mo	54.15 ± 2.67	29.78 ± 1.69
Pb	1.57 ± 1.76	0.40 ± 0.45

Table A 2: Elemental analysis of Tribo by EDX

Element	Weight %	Atom %
B	0.06 ± 0.13	0.27 ± 0.60
C	0.80 ± 0.28	3.50 ± 1.04
O	0.70 ± 0.27	2.30 ± 0.91
F	0.38 ± 0.53	1.00 ± 1.41
Na	0.08 ± 0.09	0.20 ± 0.23
Al	0.16 ± 0.13	0.29 ± 0.24
S	33.51 ± 5.11	54.76 ± 6.17
Fe	0.87 ± 1.70	0.85 ± 1.67
Ni	0.60 ± 0.62	0.54 ± 0.55
Cu	1.50 ± 0.44	1.23 ± 0.34
Zn	0.78 ± 0.42	0.62 ± 0.32
Mo	56.07 ± 2.70	30.79 ± 2.24
Pb	1.09 ± 1.18	0.29 ± 0.314
Sc	0.97 ± 2.18	1.19 ± 2.66
Mn	0.56 ± 1.25	0.56 ± 1.24

Table A 3: Elemental analysis of AA by EDX

Element	Weight %	Atom %
C	1.43 ± 0.90	5.95 ± 3.40
O	1.46 ± 0.57	4.64 ± 1.56
S	32.29 ± 2.66	51.73 ± 1.69
Sc	2.03 ± 4.54	2.27 ± 5.08
Cr	0.63 ± 0.94	0.63 ± 0.92
Fe	0.54 ± 0.53	0.49 ± 0.47
Cu	2.19 ± 0.43	1.76 ± 0.28
Zn	1.15 ± 0.26	0.90 ± 0.18
Y	0.44 ± 0.27	0.25 ± 0.15
Mo	54.13 ± 7.68	29.29 ± 5.96
Pb	1.07 ± 1.49	0.25 ± 0.36
Co	0.26 ± 0.15	0.23 ± 0.14

Table A 4: Elemental analysis of SA2 by EDX

Element	Weight %	Atom %
B	0.07 ± 0.09	0.33 ± 0.45
C	0.56 ± 0.18	2.48 ± 0.78
O	0.91 ± 0.22	3.00 ± 0.63
S	33.87 ± 1.69	55.74 ± 1.74
Cr	0.92 ± 0.50	0.94 ± 0.53
Cu	1.89 ± 0.44	1.57 ± 0.41
Zn	1.00 ± 0.22	0.81 ± 0.21
Mo	52.66 ± 1.67	28.98 ± 0.84
Pb	3.29 ± 3.20	0.86 ± 0.85
Sc	3.63 ± 2.14	4.23 ± 2.49
Nd	0.44 ± 0.99	0.17 ± 0.38

Table A 5: Elemental analysis of SAnp by EDX

Element	Weight %	Atom %
B	0.41 ± 0.61	1.79 ± 2.62
C	2.01 ± 1.36	8.05 ± 5.41
O	1.18 ± 0.88	3.58 ± 2.72
S	35.80 ± 2.12	54.07 ± 3.31
Sc	1.52 ± 2.94	1.68 ± 3.29
Cu	3.36 ± 0.97	2.54 ± 0.69
Zn	1.58 ± 0.61	1.17 ± 0.44
Y	0.44 ± 0.33	0.24 ± 0.18
Mo	50.73 ± 2.68	25.61 ± 1.51
Pb	1.26 ± 2.42	0.30 ± 0.58

Table A 6: Elemental analysis of Crystal by EDX

Element	Weight %	Atom %
C	0.22 ± 0.37	0.92 ± 1.58
O	1.84 ± 1.47	5.66 ± 4.14
F	0.14 ± 0.15	0.35 ± 0.38
S	37.74 ± 2.94	59.67 ± 2.52
Cr	0.32 ± 0.45	0.33 ± 0.45
Cu	2.45 ± 0.14	1.96 ± 0.11
Mo	51.87 ± 3.75	27.58 ± 3.54
Ru	0.92 ± 0.72	0.47 ± 0.38
N	0.11 ± 0.17	0.39 ± 0.60
Y	0.34 ± 0.34	0.20 ± 0.20

Table A 7: Mo:S ratios of the MoS_2 bulk starting materials, derived from the elemental analysis shown in Table A 1–Table A 6

Starting material	Mo:S ratio		
	Mo	:	S
SA6	1	:	1.98 ± 0.03
Tribo	1	:	1.78 ± 0.07
AA	1	:	1.77 ± 0.30
SA2	1	:	1.92 ± 0.00
SAnp	1	:	2.11 ± 0.00
Crystal	1	:	2.16 ± 0.19

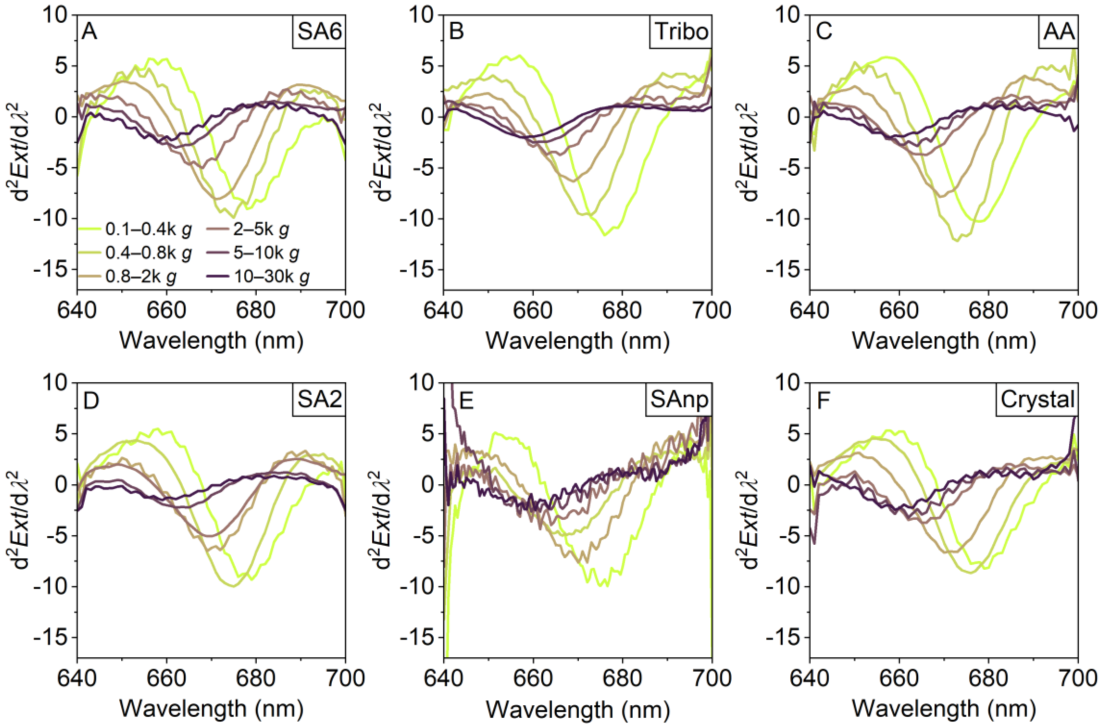

Figure A 2: Second derivative, d²*Ext*/d*λ*², of the A-exciton region of the extinction spectra shown in Figure 4.3. The shift of the A-exciton originates from decreasing layer number of the nanosheets and changing band gap. A: Sigma Aldrich, 6 µm particle size, B: Tribotecc, C: Alfa Aesar, D: Sigma Aldrich, 2 µm particle size, E: Sigma Aldrich, nanopowder, F: Ground MoS_2 crystal from SPI Supplies.

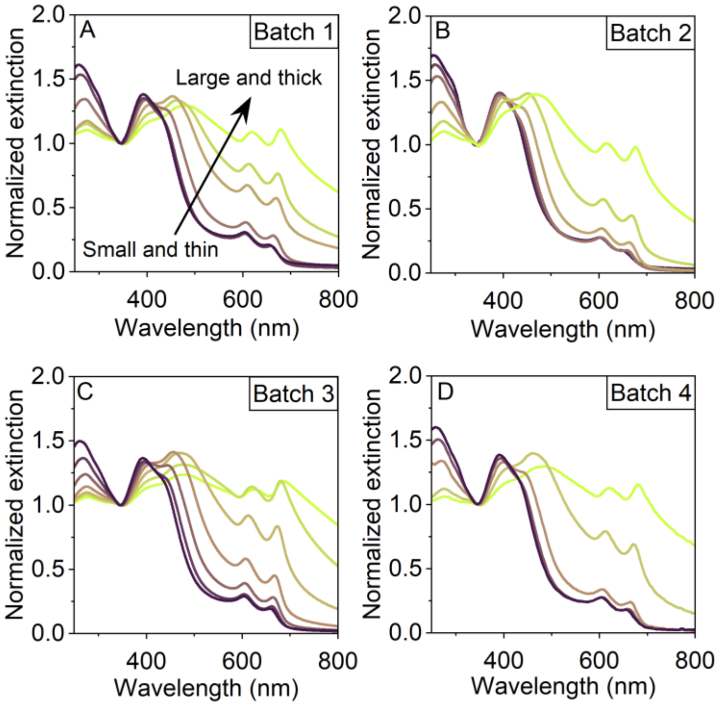

Figure A 3: UV-Vis extinction spectra of MoS_2 nanosheet dispersions. Four different batches were produced from the starting material SA6 by LPE and LCC to assess natural batch to batch variations in LPE. A: Batch 1, B: Batch 2, C: Batch 3, D: Batch 4.

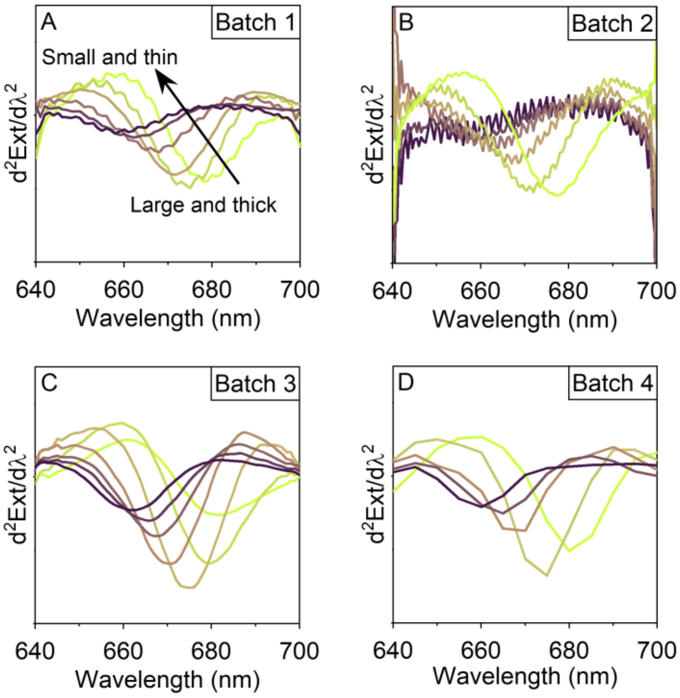

Figure A 4: Second derivative of the A-exciton region of the UV-Vis extinction spectra shown in Figure A 3. The spectra were used to determine the position of the A-exciton and calculate the mean layer number ⟨*N*⟩ of the nanosheets in the dispersions. A: Batch 1, B: Batch 2, C: Batch 3, D: Batch 4.

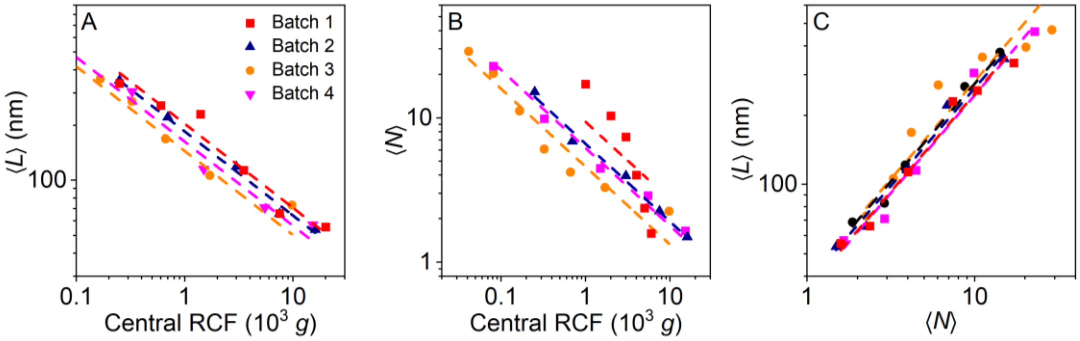

Figure A 5: Size information extracted from the UV-Vis extinction spectra shown in Figure A 3 and Figure A 4. A: Mean nanosheet length ⟨*L*⟩ as a function of central RCF. B: Mean layer number ⟨*N*⟩ as a function of central RCF. C: ⟨*L*⟩ as a function of ⟨*N*⟩. The data were fitted by power law functions according to equation (4.3) and (4.4).

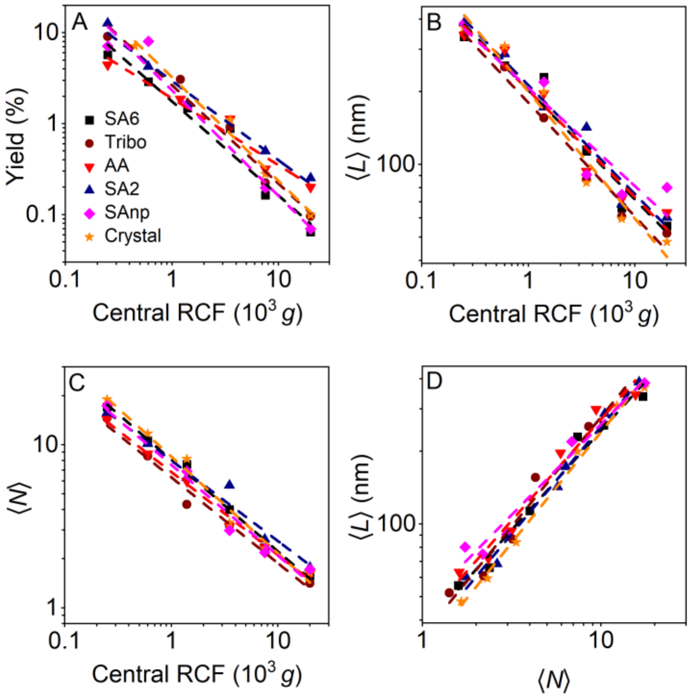

Figure A 6: Yield and size information derived from the optical extinction spectra shown in Figure 4.3. The data were fitted by power laws according to equation (4.3) and (4.4). A–C: Yield (A), ⟨*L*⟩ (B) and ⟨*N*⟩ (C) as a function of central RCF. D: ⟨*L*⟩ as a function of ⟨*N*⟩.

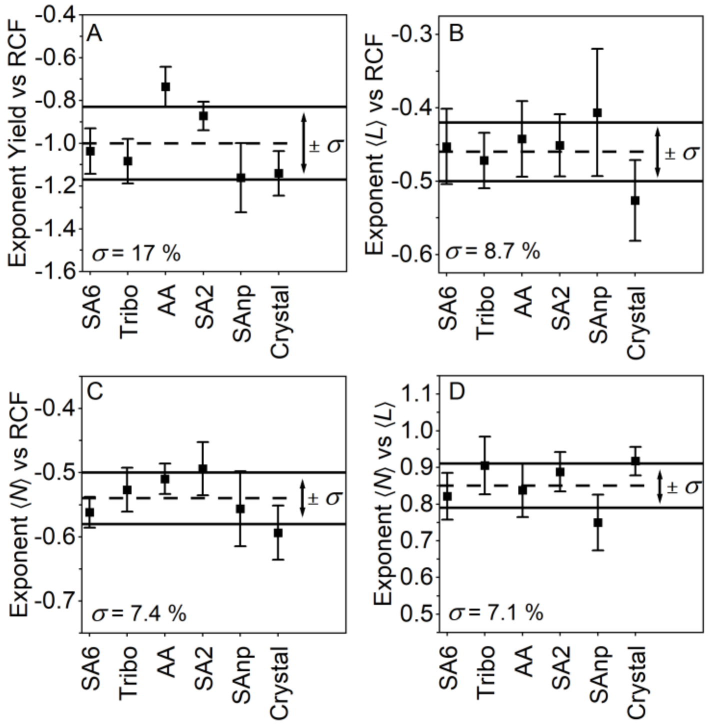

Figure A 7: Exponents extracted from the fits shown in Figure A 6. Only minor variations of the exponents are discernible. The dashed lines represent the mean value of the extracted exponents, and the solid lines represent the range of standard deviation found between the different batches. A: Exponent yield vs RCF. B: Exponent ⟨*L*⟩ vs RCF. C: Exponent ⟨*N*⟩ vs RCF. D: Exponent ⟨*N*⟩ vs ⟨*L*⟩.

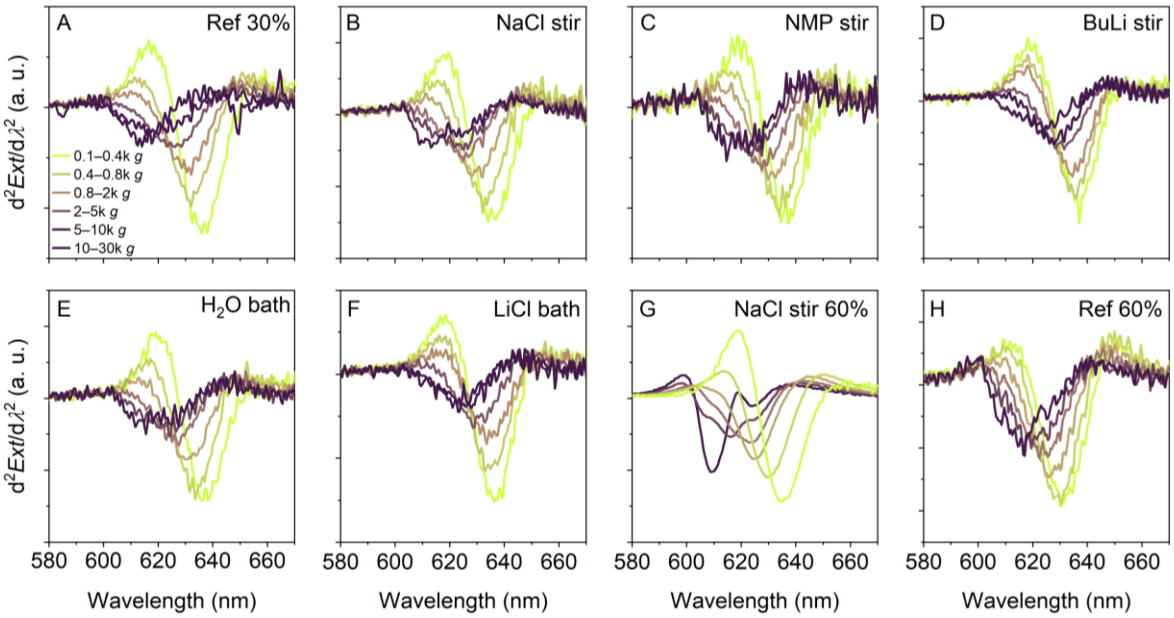

Figure A 8: Second derivative of the UV-Vis extinction spectra shown in Figure 4.12. The spectra were used to determine the position of the A-exciton and to calculate the mean layer number ⟨*N*⟩ of the WS_2 nanosheets in dispersion. A: Ref 30 %, B: NaCl stir, C: NMP stir, D: BuLi stir, E: H_2O bath, F: LiCl bath, G: NaCl stir 60 %, H: Ref 60 %.

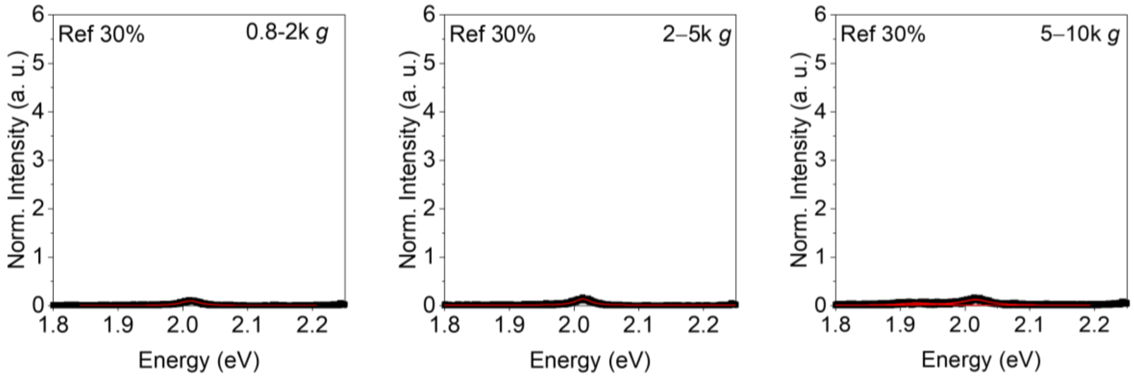

Figure A 9: Photoluminescence spectra (λ_{exc} = 532 nm) of WS_2 nanosheet dispersions produced by sonication-assisted LPE (tip sonication with 30 % amplitude) and LCC. Spectra were derived from the Raman spectra shown in Figure 4.13. The PL was fitted by Lorentzians for quantitative analysis. Spectra of LCC fractions that did not show any PL are excluded.

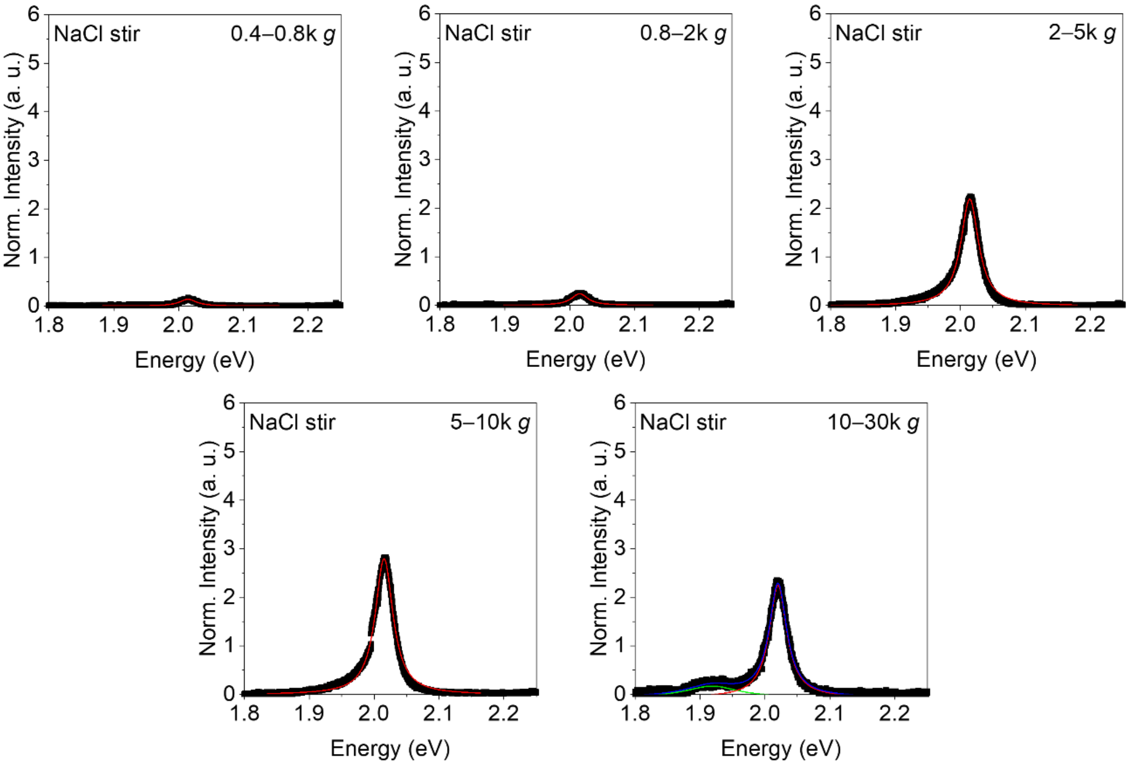

Figure A 10: Photoluminescence spectra (λ_{exc} = 532 nm) of WS_2 nanosheet dispersions produced by sonication-assisted LPE (tip sonication with 30 % amplitude) and LCC. The powder of bulk WS_2 was stirred in aqueous NaCl solution prior to exfoliation. Spectra were derived from the Raman spectra shown in Figure 4.13. The PL was fitted by Lorentzians for quantitative analysis. Spectra of LCC fractions that did not show any PL are excluded.

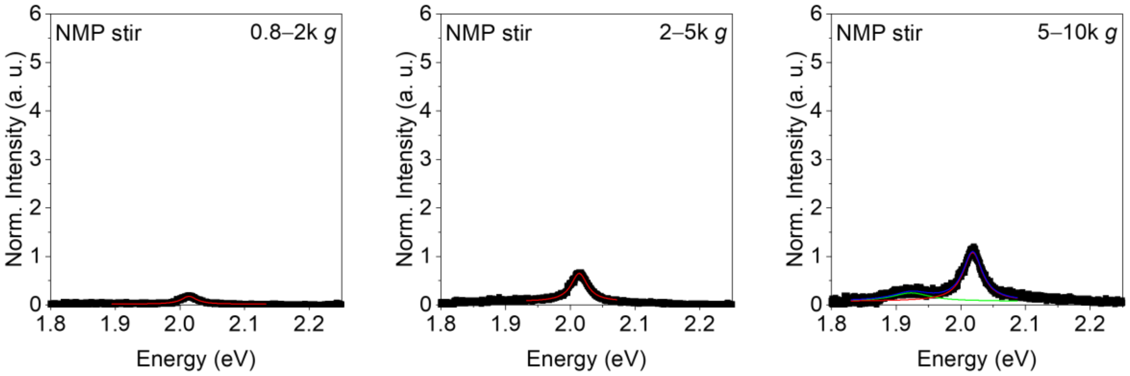

Figure A 11: Photoluminescence spectra (λ_{exc} = 532 nm) of WS_2 nanosheet dispersions produced by sonication-assisted LPE (tip sonication with 30 % amplitude) and LCC. The powder of bulk WS_2 was stirred in NMP prior to exfoliation. Spectra were derived from the Raman spectra shown in Figure 4.13. The PL was fitted by Lorentzians for quantitative analysis. Spectra of LCC fractions that did not show any PL are excluded.

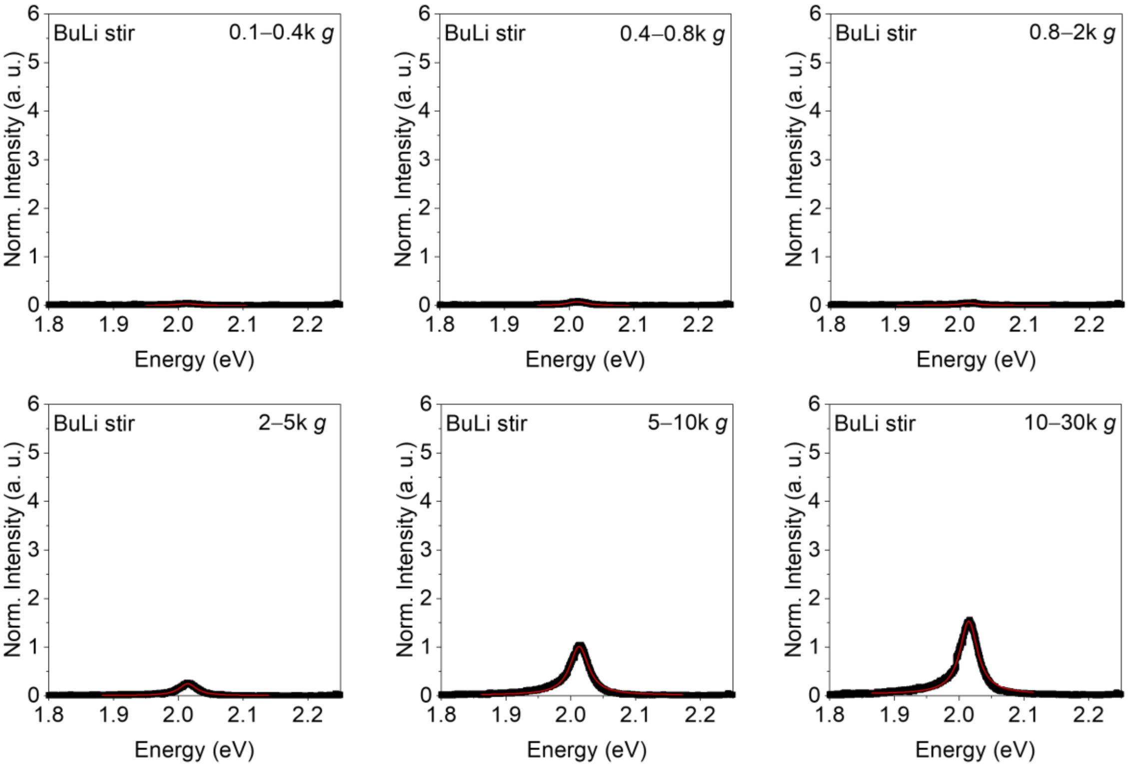

Figure A 12: Photoluminescence spectra (λ_{exc} = 532 nm) of WS_2 nanosheet dispersions produced by sonication-assisted LPE (tip sonication with 30 % amplitude) and LCC. The powder of bulk WS_2 was stirred in *n*-BuLi/*n*-hexane prior to exfoliation. Spectra were derived from the Raman spectra shown in Figure 4.13. The PL was fitted by Lorentzians for quantitative analysis.

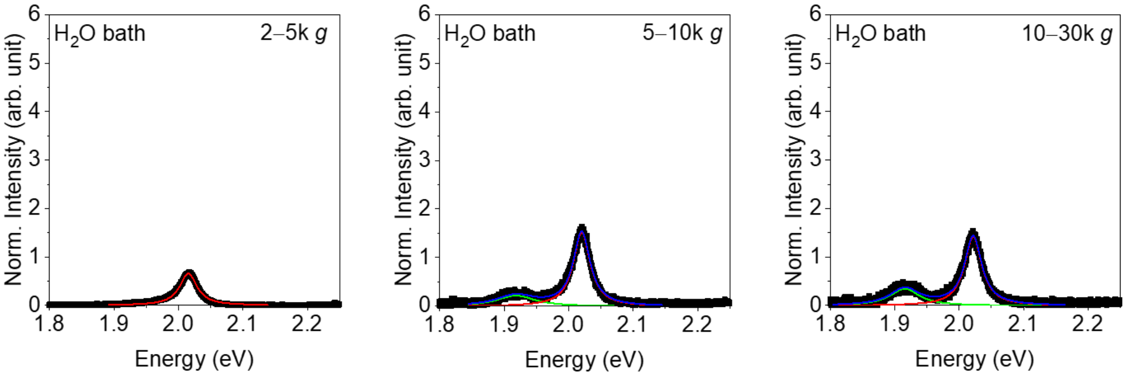

Figure A 13: Photoluminescence spectra (λ_{exc} = 532 nm) of WS_2 nanosheet dispersions produced by sonication-assisted LPE (tip sonication with 30 % amplitude) and LCC. The powder of bulk WS_2 was bath sonicated in water prior to exfoliation. Spectra were derived from the Raman spectra shown in Figure 4.13. The PL was fitted by Lorentzians for quantitative analysis. Spectra of LCC fractions that did not show any PL are excluded.

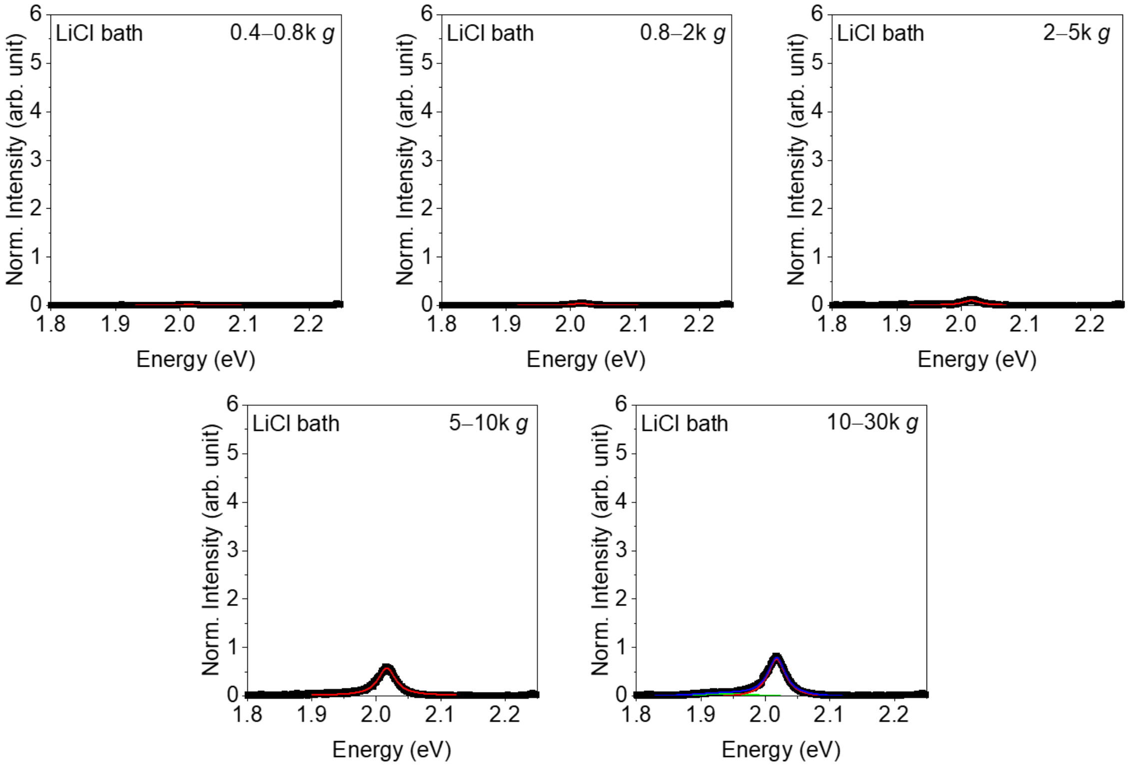

Figure A 14: Photoluminescence spectra (λ_{exc} = 532 nm) of WS$_2$ nanosheet dispersions produced by sonication-assisted LPE (tip sonication with 30 % amplitude) and LCC. The powder of bulk WS$_2$ was bath sonicated in aqueous LiCl solution prior to exfoliation. Spectra were derived from the Raman spectra shown in Figure 4.13. The PL was fitted by Lorentzians for quantitative analysis. Spectra of LCC fractions that did not show any PL are excluded.

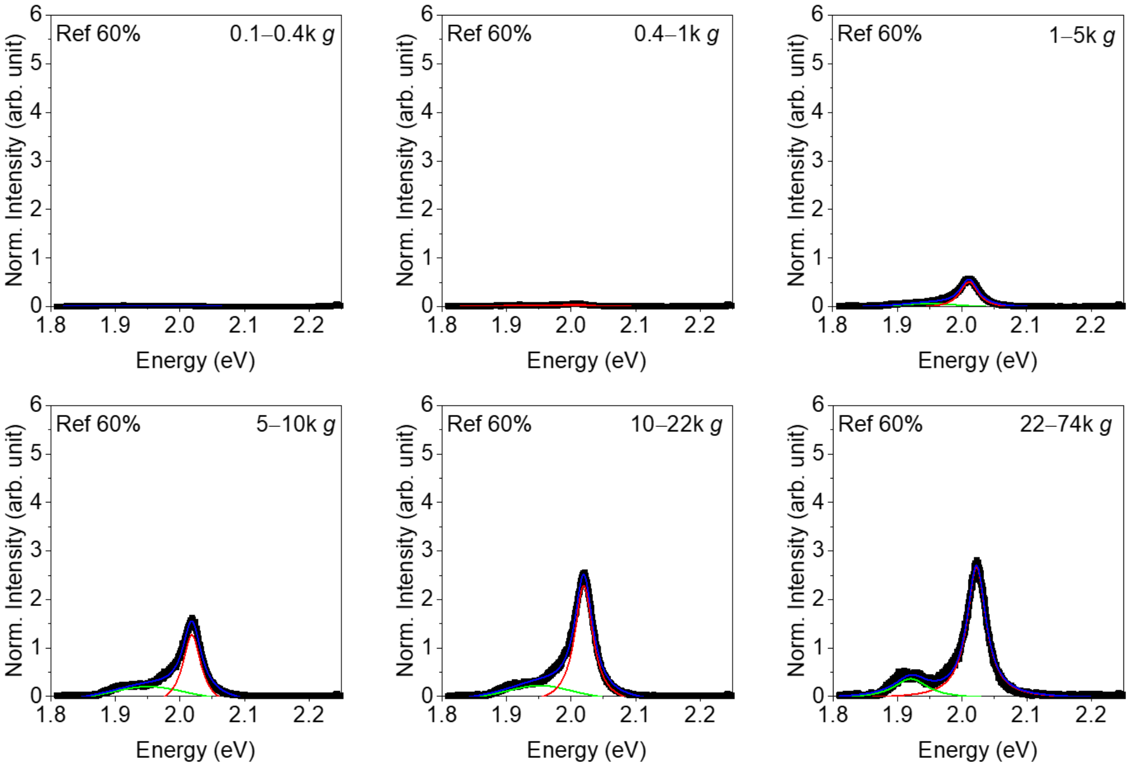

Figure A 15: Photoluminescence spectra (λ_{exc} = 532 nm) of WS$_2$ nanosheet dispersions produced by sonication-assisted LPE (tip sonication with 60 % amplitude) and LCC. Spectra were derived from the Raman spectra shown in Figure 4.13. The PL was fitted by Lorentzians for quantitative analysis.

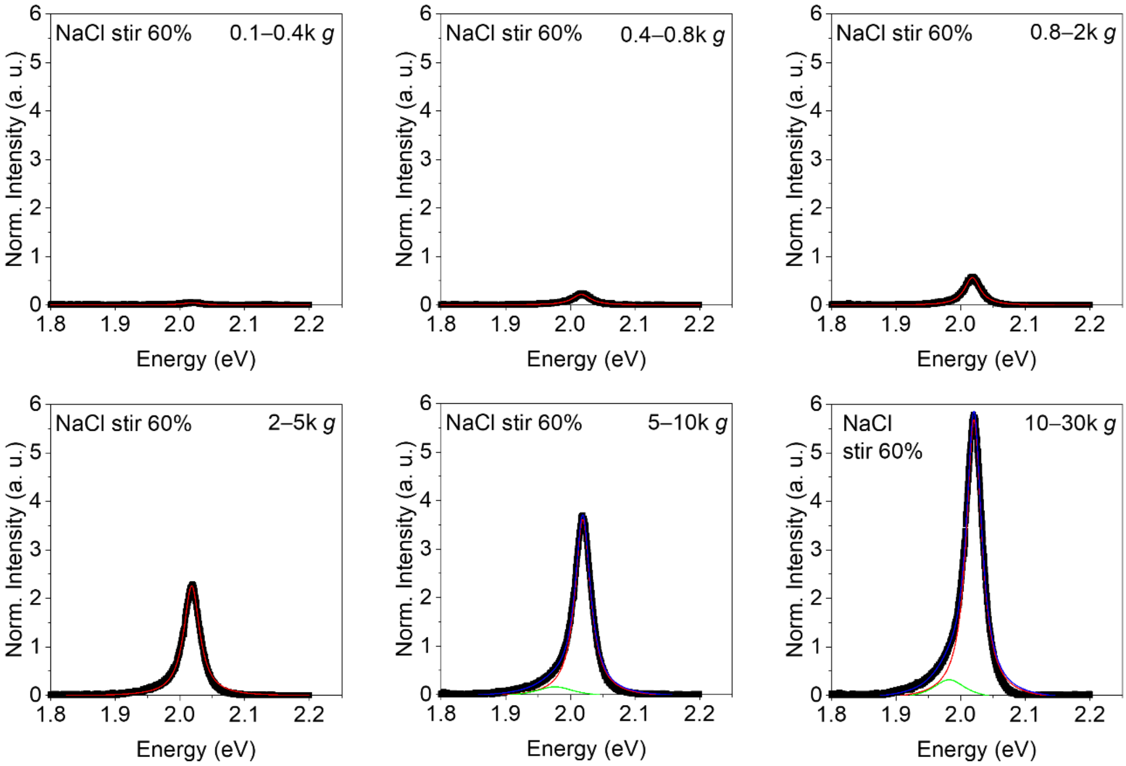

Figure A 16: Photoluminescence spectra (λ_{exc} = 532 nm) of WS_2 nanosheet dispersions produced by sonication-assisted LPE (tip sonication with 60 % amplitude) and LCC. The powder of bulk WS_2 was stirred in aqueous NaCl solution prior to exfoliation. Spectra were derived from the Raman spectra shown in Figure 4.13. The PL was fitted by Lorentzians for quantitative analysis.

7.2 Appendix Chapter 4.2

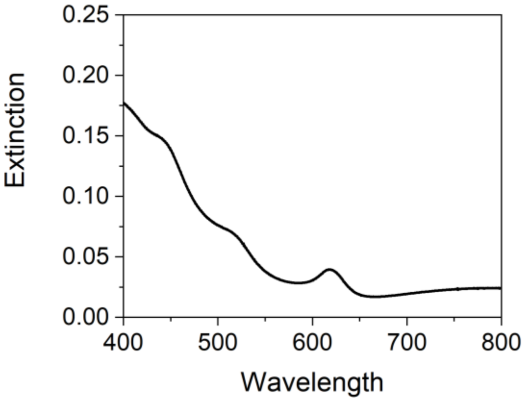

Figure A 17: UV-Vis extinction spectrum of a WS_2-PVK composite film, spin-coated from NMP:THF = 1:2 at 500 rpm for 60 s. The resulting optical density of the film is too low for the implementation in optical microcavities.

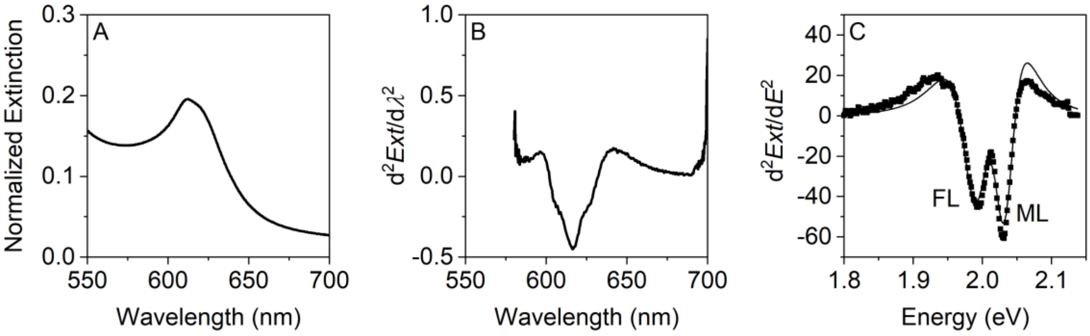

Figure A 18: Different methods of spectral processing. A: Region of the A-exciton in a UV-Vis extinction spectra of a WS_2 nanosheet dispersions. B, C: Second derivatives of the spectrum shown in A. The spectrum in B was differentiated twice and subsequently smoothed by adjacent averaging. The spectrum in C was smoothed by the Lowess method prior to the differentiation and fitted by the second derivative of Lorentzians. While the fine structure in B is lost, it is preserved in C, and the optical transition from both FL and ML nanosheets are discernible, allowing to extract the ML volume fraction of the nanosheets in the dispersion.

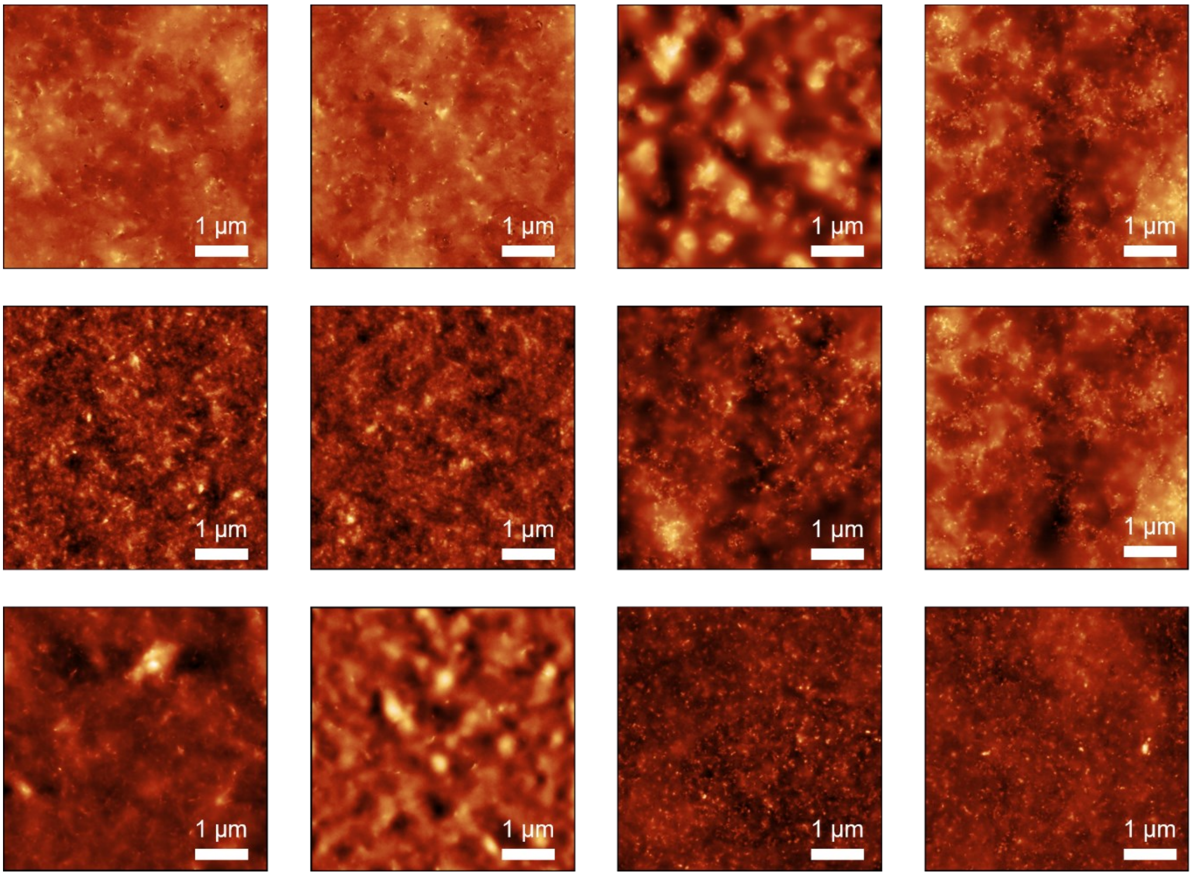

Figure A 19: AFM images of WS_2-PVK composite films, revealing different morphologies of the films. RMS roughness of the films was extracted for the comparison in Figure 4.20. The films were prepared according to the spin-coating protocol presented in Scheme 4.3.

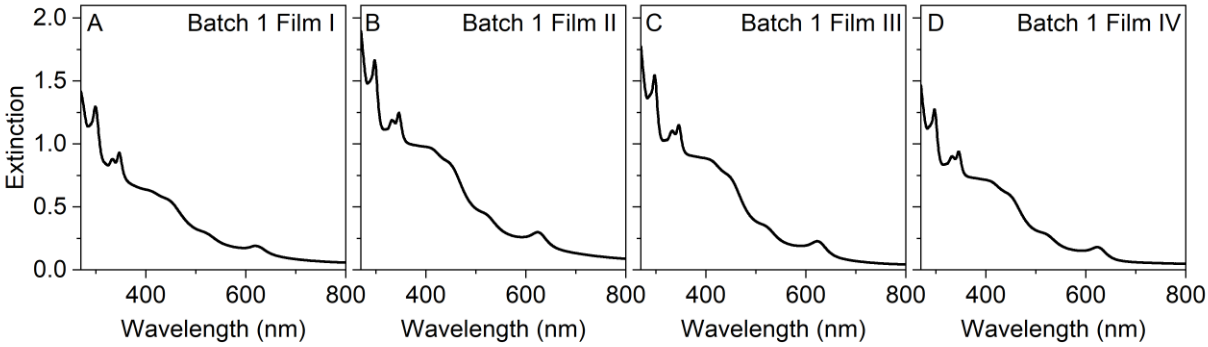

Figure A 20: UV-Vis extinction spectra of WS_2-PVK composite films (batch 1). The optical density at the position of the A-exciton was extracted from the spectra for the comparison in Figure 4.20.

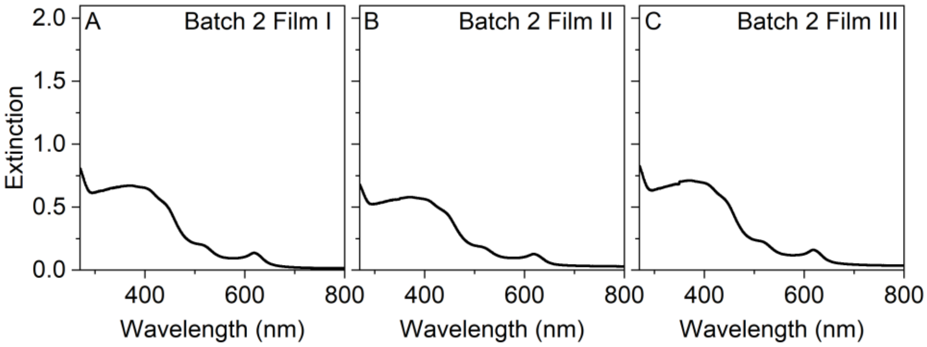

Figure A 21: UV-Vis extinction spectra of WS_2-PVK composite films (batch 2). The optical density at the position of the A-exciton was extracted from the spectra for the comparison in Figure 4.20.

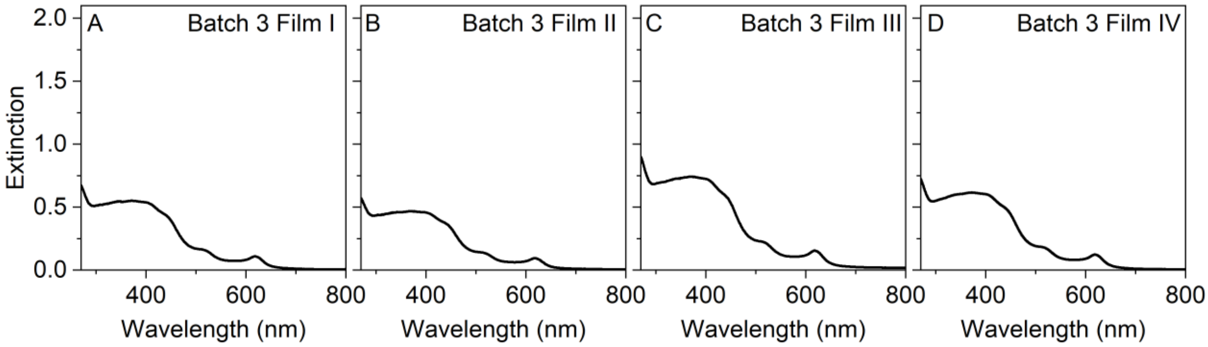

Figure A 22: UV-Vis extinction spectra of WS_2-PVK composite films (batch 3). The optical density at the position of the A-exciton was extracted from the spectra for the comparison in Figure 4.20.

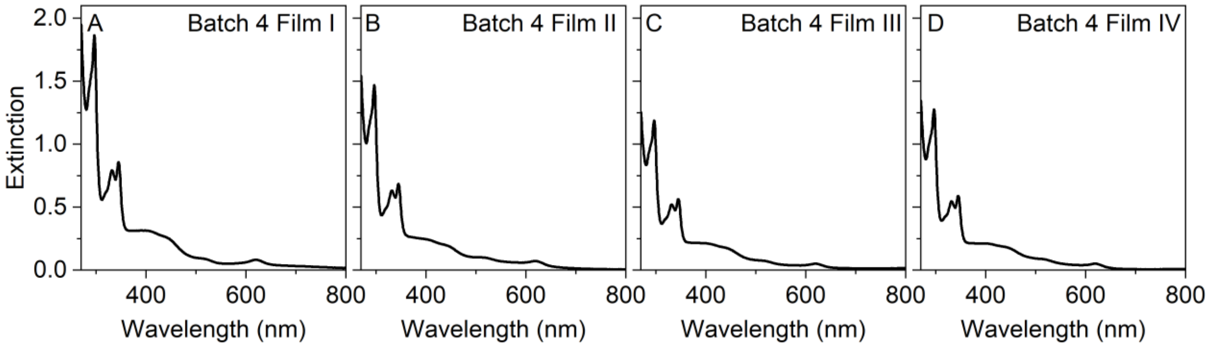

Figure A 23: UV-Vis extinction spectra of WS_2-PVK composite films (batch 4). The optical density at the position of the A-exciton was extracted from the spectra for the comparison in Figure 4.20.

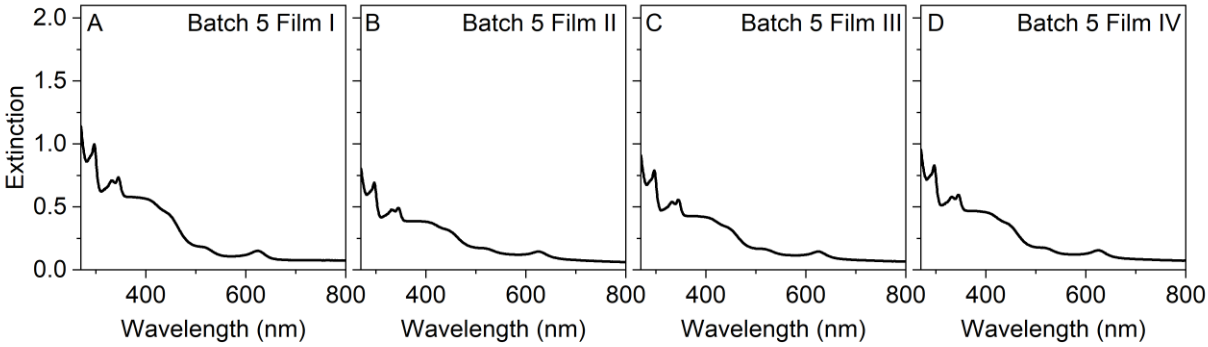

Figure A 24: UV-Vis extinction spectra of WS_2-PVK composite films (batch 5). The optical density at the position of the A-exciton was extracted from the spectra for the comparison in Figure 4.20.

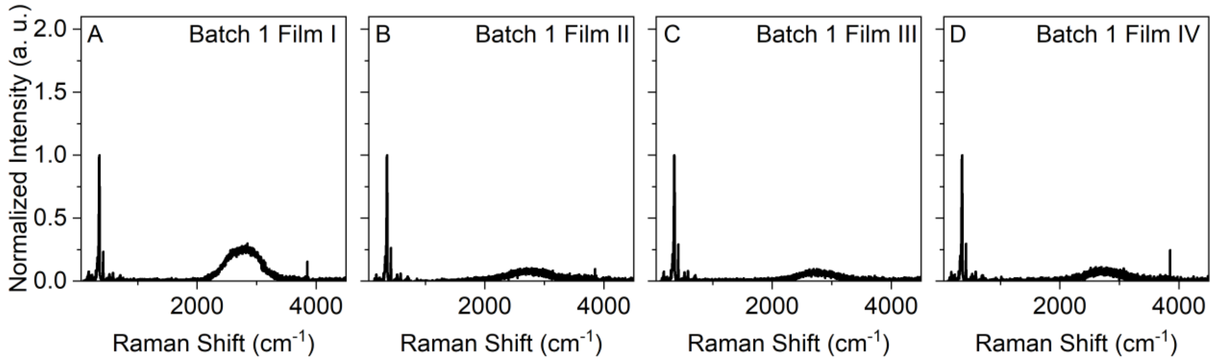

Figure A 25: Raman spectra of WS_2-PVK composite films (batch 1). The PL/Raman ratio was extracted from the spectra for the comparison in Figure 4.20.

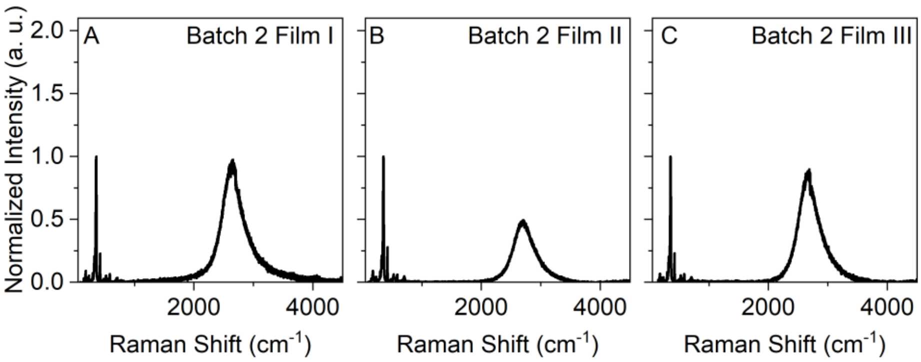

Figure A 26: Raman spectra of WS_2-PVK composite films (batch 2). The PL/Raman ratio was extracted from the spectra for the comparison in Figure 4.20.

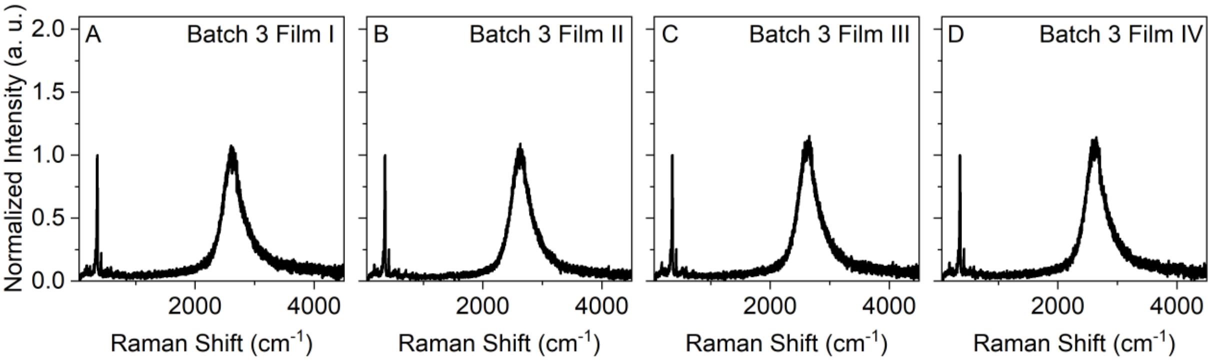

Figure A 27: Raman spectra of WS_2-PVK composite films (batch 3). The PL/Raman ratio was extracted from the spectra for the comparison in Figure 4.20.

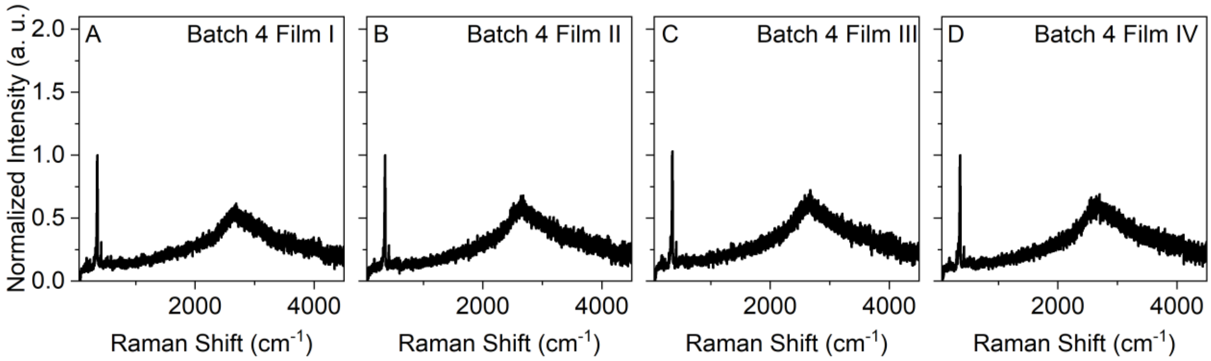

Figure A 28: Raman spectra of WS_2-PVK composite films (batch 4). The PL/Raman ratio was extracted from the spectra for the comparison in Figure 4.20.

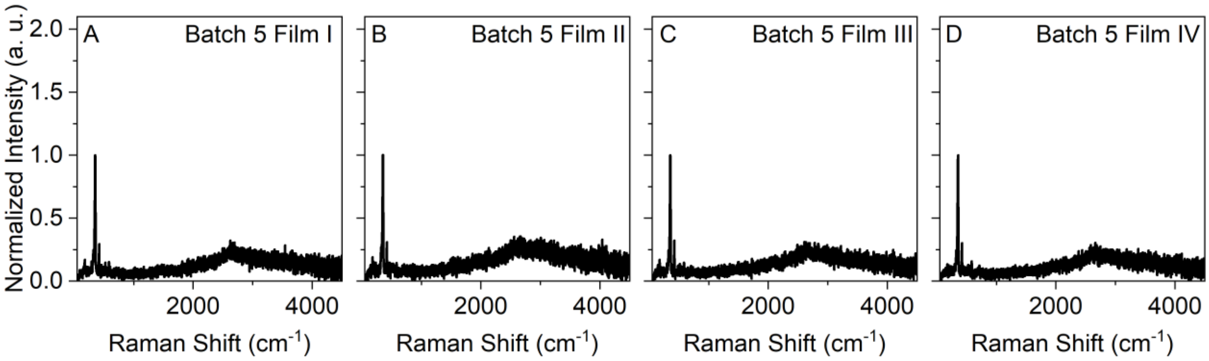

Figure A 29: Raman spectra of WS_2-PVK composite films (batch 5). The PL/Raman ratio was extracted from the spectra for the comparison in Figure 4.20.

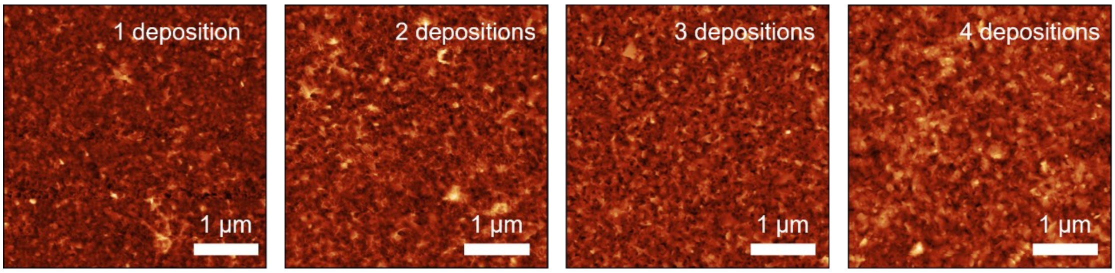

Figure A 30: AFM images of WS_2 films prepared by nanosheet self-assembly at a liquid-liquid phase interface and deposited on glass, according to Scheme 4.4. The nanosheets were produced from the size selection fraction 1–5k *g*. Four nanosheet depositions were executed, as indicated in the upper right corner of the images.

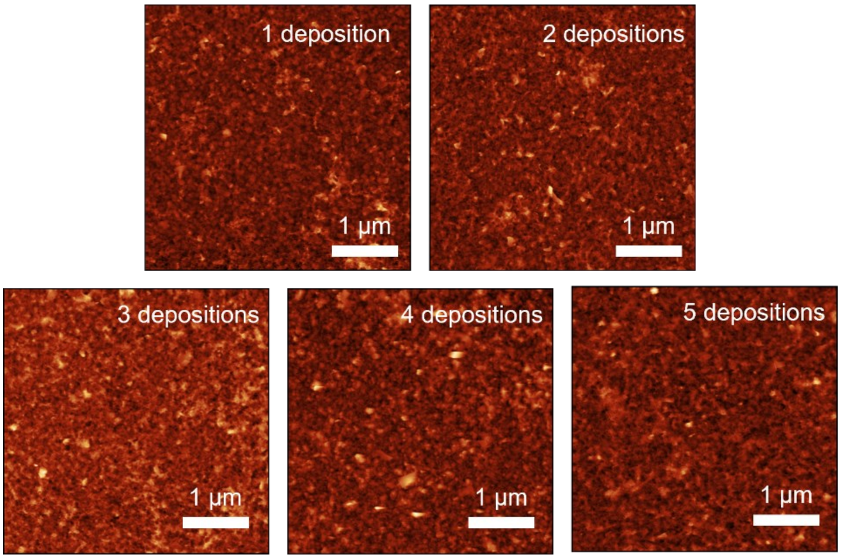

Figure A 31: AFM images of WS_2 films prepared by nanosheet self-assembly at a liquid-liquid phase interface and deposited on glass, according to Scheme 4.4. The nanosheets were produced from the size selection fraction 5–10k *g*. Five nanosheet depositions were executed, as indicated in the upper right corner of the images.

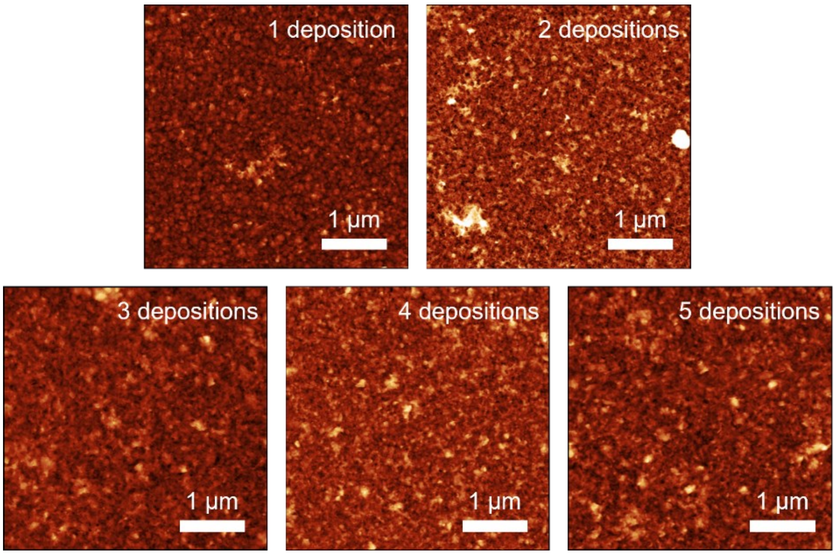

Figure A 32: AFM images of WS_2 films prepared by nanosheet self-assembly at a liquid-liquid phase interface and deposited on glass, according to Scheme 4.4. The nanosheets were produced from the size selection fraction 10–30k *g*. Five nanosheet depositions were executed, as indicated in the upper right corner of the images.

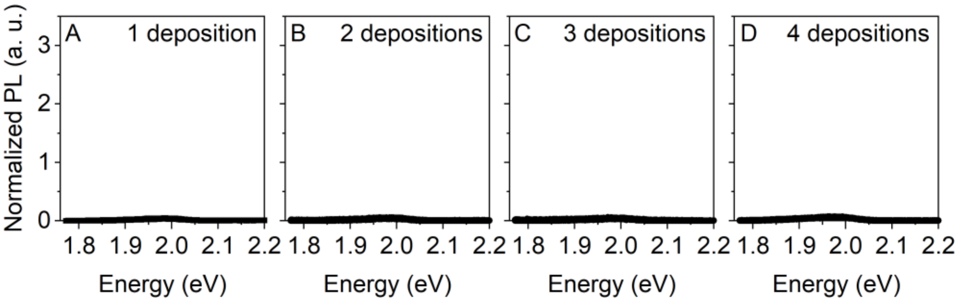

Figure A 33: PL spectra (λ_{exc} = 532 nm) of WS_2 films produced by nanosheet self-assembly at a liquid-liquid phase interface. The nanosheets were deposited from the fraction 1–5k *g* of the size selection. A: 1 deposition, B: 2 depositions, C: 3 depositions, D: 4 depositions.

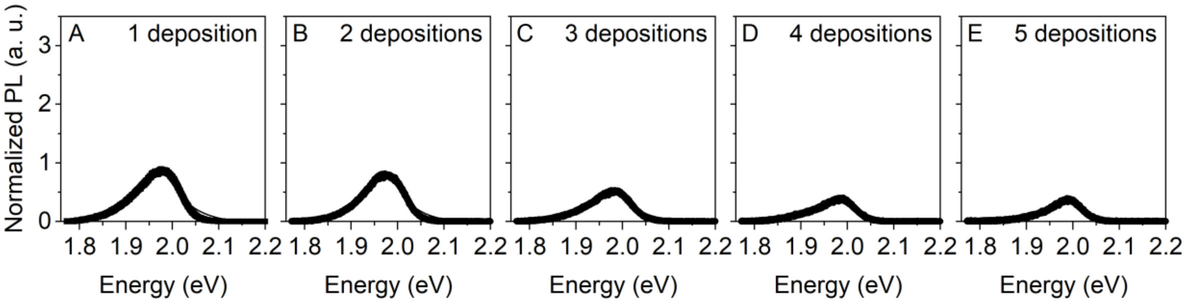

Figure A 34: PL spectra (λ_{exc} = 532 nm) of WS_2 films produced by nanosheet self-assembly at a liquid-liquid phase interface. The nanosheets were deposited from the fraction 5–10k *g* of the size selection. A: 1 deposition, B: 2 depositions, C: 3 depositions, D: 4 depositions, E: 5 depositions.

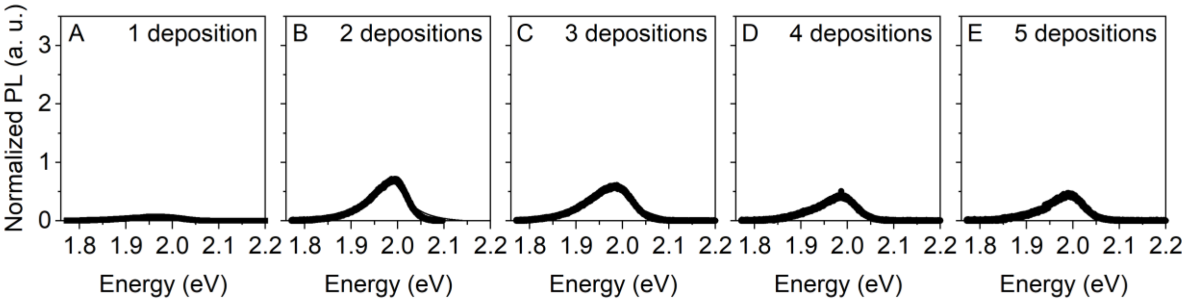

Figure A 35: PL spectra (λ_{exc} = 532 nm) of WS_2 films produced by nanosheet self-assembly at a liquid-liquid phase interface. The nanosheets were deposited from the fraction 10–30k *g* of the size selection. A: 1 deposition, B: 2 depositions, C: 3 depositions, D: 4 depositions, E: 5 depositions.

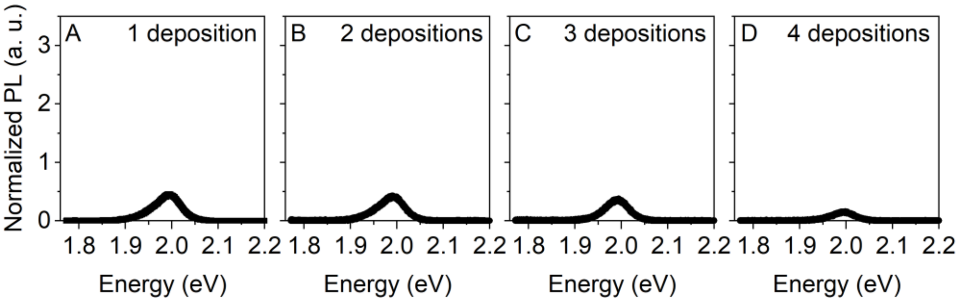

Figure A 36: PL spectra (λ_{exc} = 532 nm) of WS_2 films produced by nanosheet self-assembly at a liquid-liquid phase interface. The nanosheets were deposited from the fraction 1–5k *g* of the size selection and functionalized with 3,5-dichlorobenzenediazonium tetrafluoroborate prior to deposition. A: 1 deposition, B: 2 depositions, C: 3 depositions, D: 4 depositions.

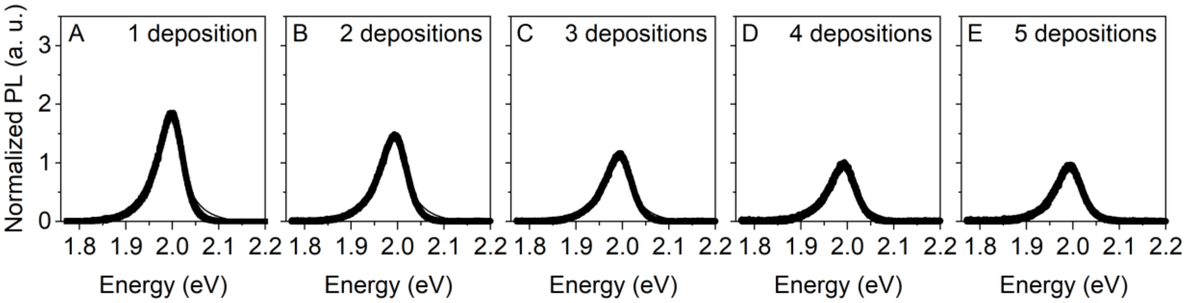

Figure A 37: PL spectra (λ_{exc} = 532 nm) of WS_2 films produced by nanosheet self-assembly at a liquid-liquid phase interface. The nanosheets were deposited from the fraction 5–10k *g* of the size selection and functionalized with 3,5-dichlorobenzenediazonium tetrafluoroborate prior to deposition. A: 1 deposition, B: 2 depositions, C: 3 depositions, D: 4 depositions, E: 5 depositions.

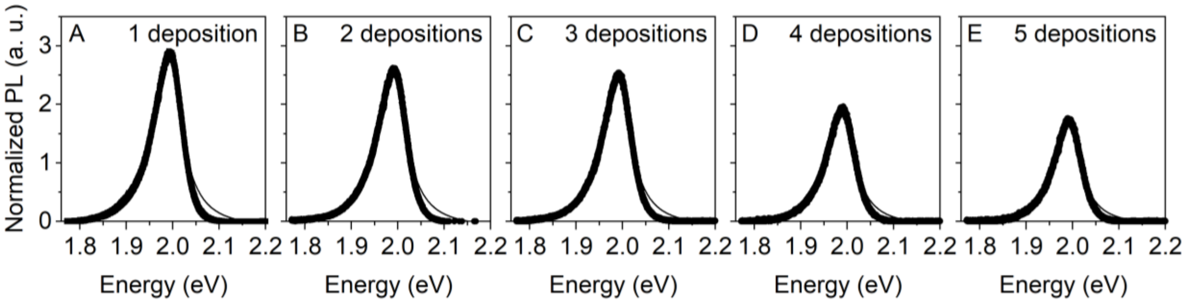

Figure A 38: PL spectra (λ_{exc} = 532 nm) of WS_2 films produced by nanosheet self-assembly at a liquid-liquid phase interface. The nanosheets were deposited from the fraction 10–30k *g* of the size selection and functionalized with 3,5-dichlorobenzenediazonium tetrafluoroborate prior to deposition. A: 1 deposition, B: 2 depositions, C: 3 depositions, D: 4 depositions, E: 5 depositions.

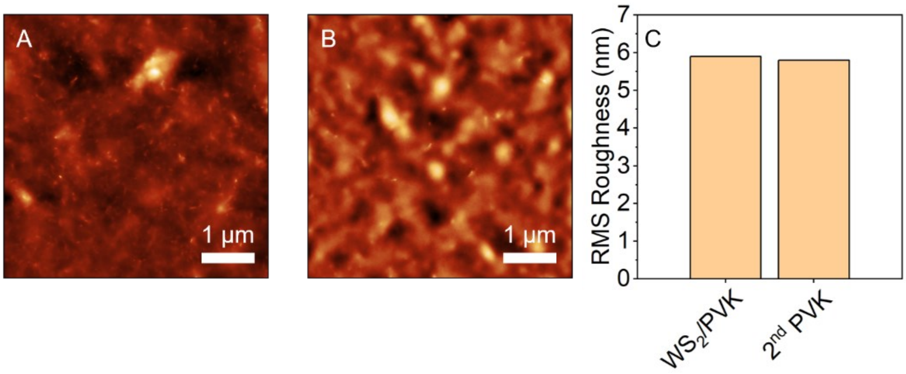

Figure A 39: Surface comparison of WS_2-PVK composite films. A: AFM image of a WS_2-PVK composite film. B: AFM image of the WS_2-PVK film shown in A, after spin coating a second layer of pure PVK on top of the film. C: RMS roughness of the films shown in A and B. The roughness was determined to 5.9 and 5.8 nm, respectively, without any significant smoothening effect of the second spin coating step.

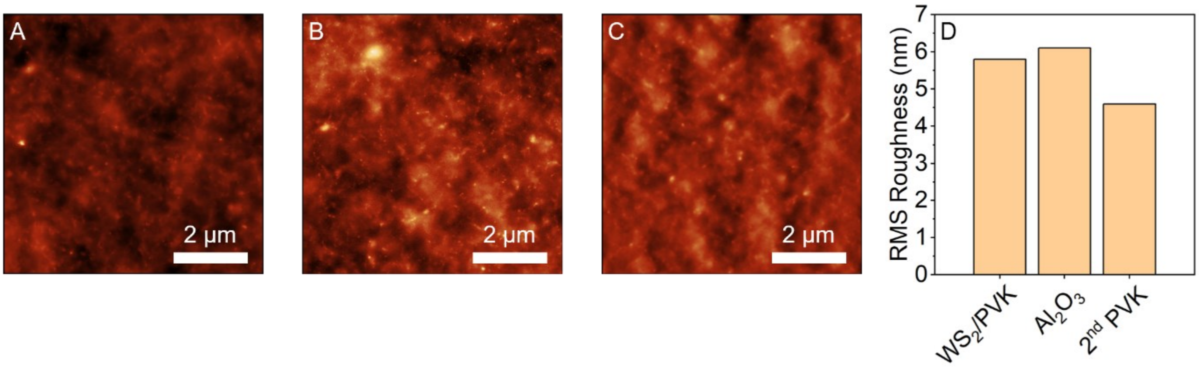

Figure A 40: Surface comparison of WS_2-PVK composite films. A: AFM image of a WS_2-PVK composite film. B, C: AFM image of the WS_2-PVK film shown in A, after growing a thin layer of Al_2O_3 (B) and spin coating a thin layer of PMMA (C) on the composite film. D: RMS roughness determined from the AFM images shown in A–C, showing a smoothening of the surface from 5.8 to 4.6 nm.

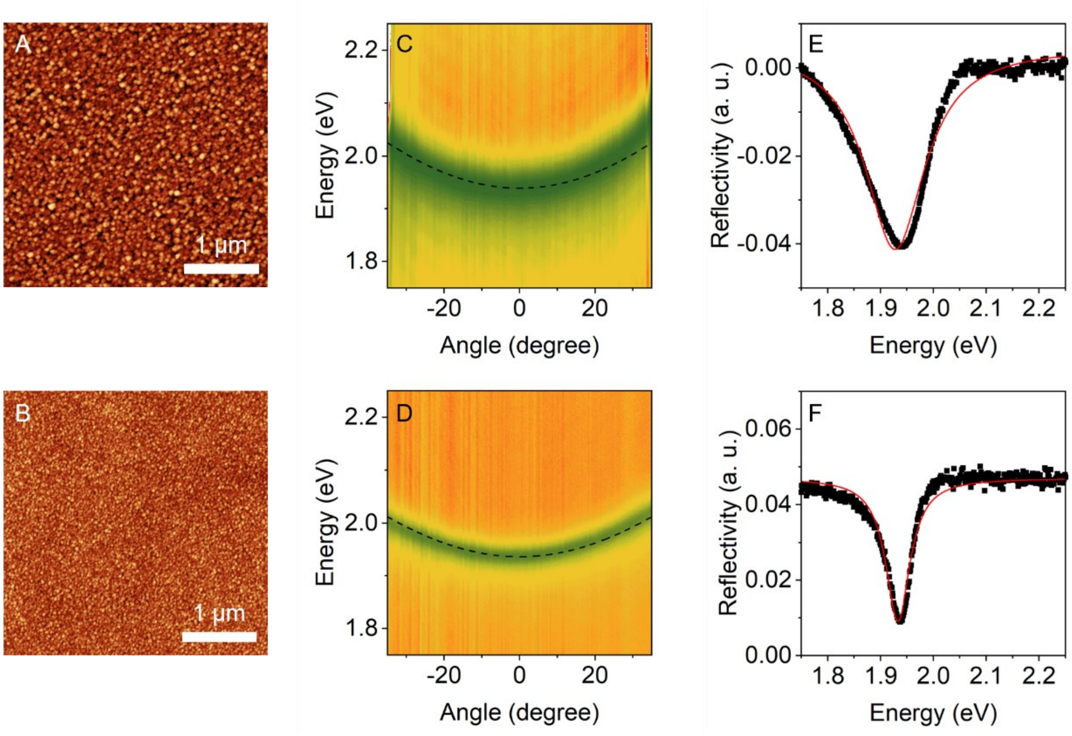

Figure A 41: Characterization of PVK reference cavities in the design presented in Scheme 4.6 A, where the bottom Ag mirror was deposited by thermal evaporation (top row) or e-beam evaporation (bottom row). A, B: AFM images of the bottom silver mirror, deposited by thermal evaporation (A) and e-beam evaporation (B). C, D: Angle resolved reflectivity spectra of the cavities, showing different linewidths of the cavity mode. E, F: Line profiles of the cavity modes shown in C and D, featuring FWHM values of 56 and 137 meV, corresponding to quality factors of 34.5 and 14.0, respectively.

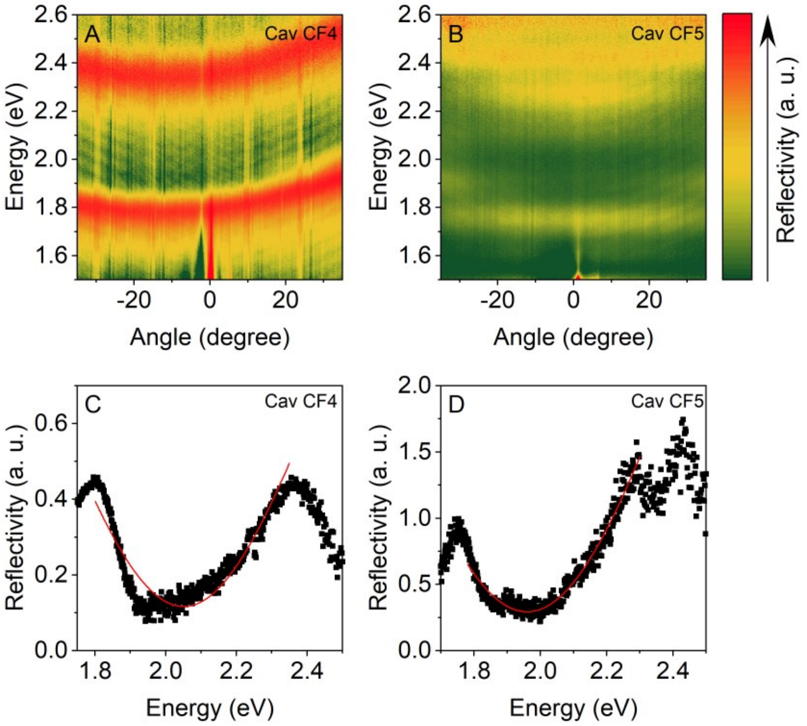

Figure A 42: A, B: Angle resolved reflectivity of optical microcavities based on WS_2-PVK composite films, showing very broad and asymmetric cavity modes. The cavities were produced without deposition of Al_2O_3 and PMMA on the WS_2-PVK composite film, which would have smoothed the surface. C, D: Line profiles of the cavity modes at an angle of observation of zero degree, extracted from the contour maps shown in A and B.

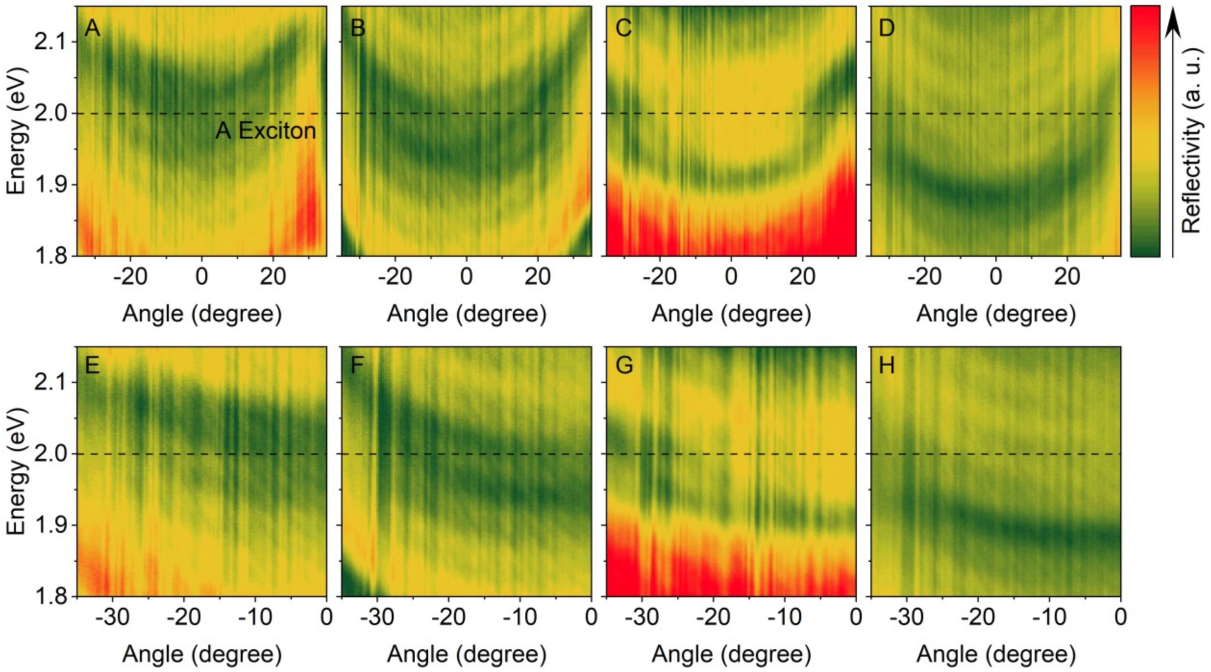

Figure A 43: Angle resolved reflectivity with variations in the detuning of the cavity Cav CF2 (from left to right) shown in Figure 4.26 C. The graphs in the bottom row show a section of the graphs shown in the top row. Different detunings were accomplished by the measurement of different spots, taking advantage of natural thickness variations that develop during spin coating.

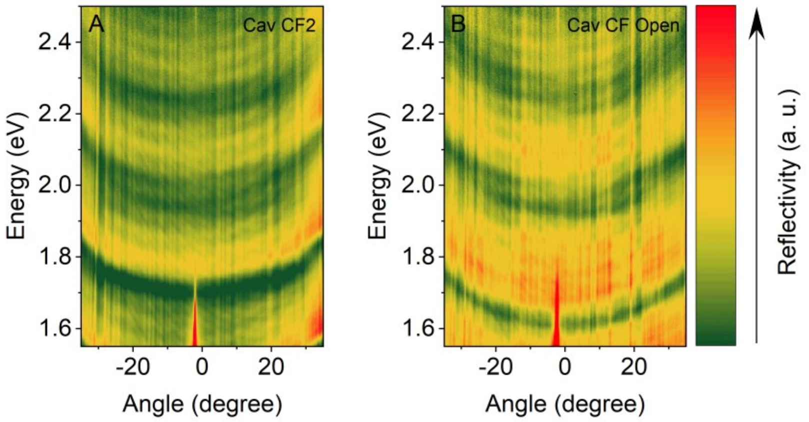

Figure A 44: Angle resolved reflectivity spectra with extended energy range of the closed (A) and open cavity (B) shown in Figure 4.26 C and D. The extended energy range shows that also higher order cavity modes show abnormal line profiles.

.

7.3 Appendix Chapter 4.3

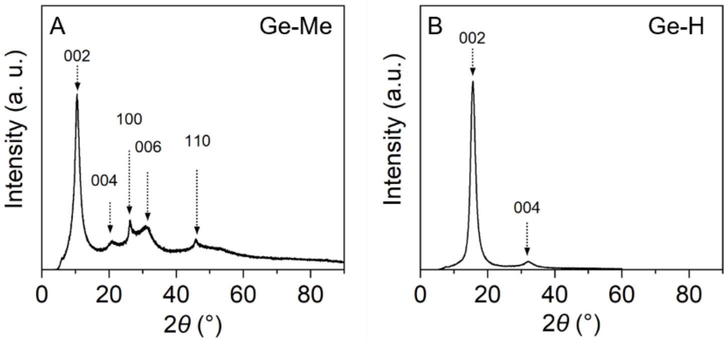

Figure A 45: XRD spectra of bulk Ge-Me (A) and Ge-H (B). The spectrum of Ge-Me (A) features a main reflection (002) at ~ 10.46°, corresponding to the interlayer distance, and higher order reflections (004), (100), (006), and (110) are visible at ~ 20.75°, ~ 26.21°, ~ 31.06°, and ~ 45.88°, respectively. The parameter *a* and *c* related to the 2H hexagonal unit cell are 3.92 Å according to the (100) reflection and 16.90 Å according to the (002) reflection (8.45 per layer Å). The spectrum of Ge-H (B) features the main reflection (002) and the higher order reflection (004) at ~ 15.62° and ~ 32.11°, respectively. The *c* parameter of the 2H unit cell is 11.34 Å (5.67 Å per layer).

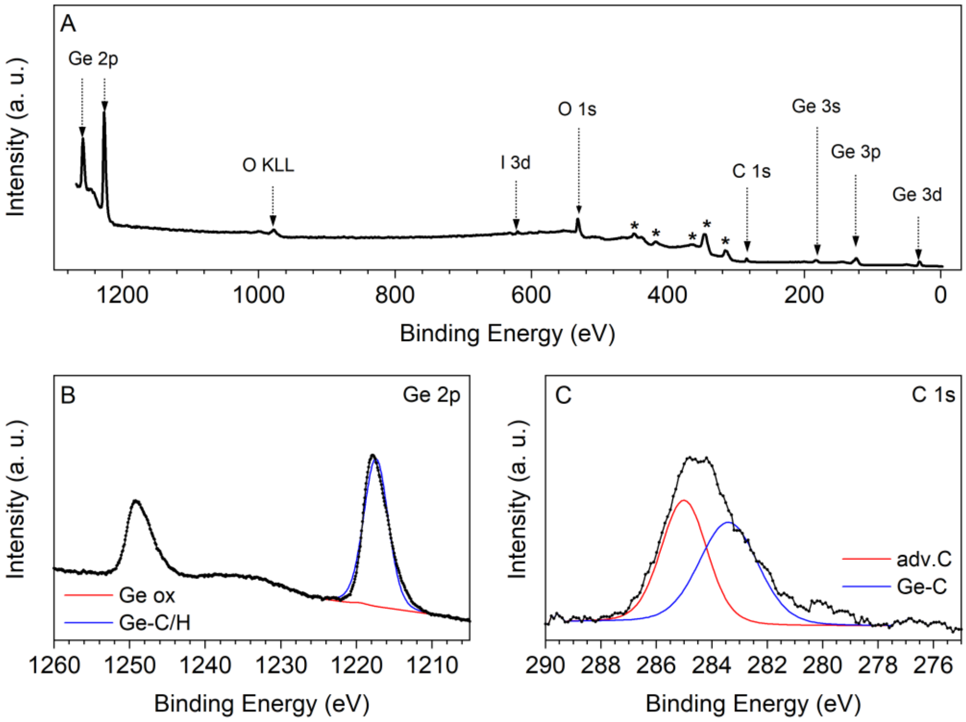

Figure A 46: XPS spectra of bulk Ge-Me. A: Survey spectrum. B, C: High resolution Ge 2p (B) and C 1s (C) spectra. Ge-Me contains 36.9 atomic % germanium, 37.9 atomic % carbon, and 25 atomic % oxygen. 85.3 % of the oxygen and 48.3 % of the carbon is due to adventitious contamination. The surface oxidation of Ge-Me is only ~ 0.5 %. 51.7 % of the carbon is due to Ge-C bond and the ratio Ge/Ge-C is ~ 1.9/1. Minor traces of iodine were found (0.2 atomic %), which might originate from the formation of Ge-I.

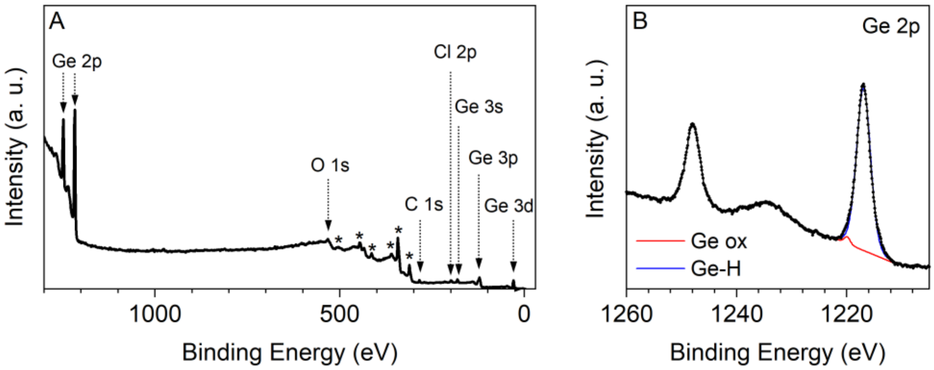

Figure A 47: XPS spectra of bulk Ge-H. A: Survey spectrum. B: High resolution Ge 2p spectrum. Ge-H contains 67.1 atomic % germanium, 9.6 atomic % oxygen, and 19.6 atomic % carbon. Oxygen and carbon contamination are mostly adventitious, and the surface oxidation of Ge-H is 1.8 %. Traces of chlorine were found (3.7 atomic %) due to the formation of Ge-Cl.

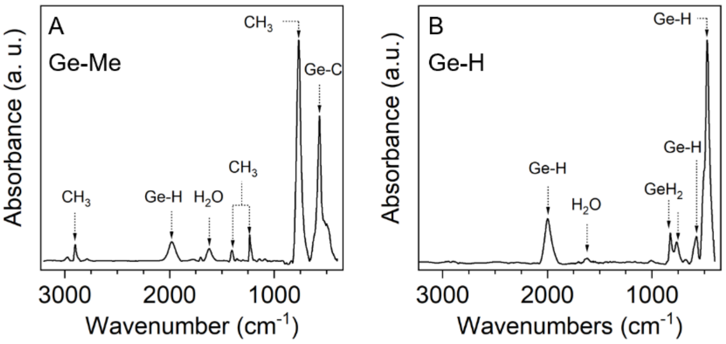

Figure A 48: FTIR spectra of bulk Ge-Me (A) und Ge-H (B). The FTIR spectrum of Ge-Me features a C-H stretching mode at ~ 2900 cm^{-1}, C-H bending modes at ~ 1400 cm^{-1} and ~ 1240 cm^{-1}, a C-H rocking mode at ~ 770 cm^{-1}, Ge-C stretching modes at ~ 570 cm^{-1} and weaker at ~ 500 cm^{-1}, and a Ge-H mode at ~ 1980 cm^{-1}. The FTIR spectrum of Ge-H features a Ge-H stretching mode at ~ 2000 cm^{-1}, Ge-H bending modes at ~ 825 cm^{-1} and ~ 765 cm^{-1}, and Ge-H modes at ~ 575 cm^{-1} and ~ 475 cm^{-1}.

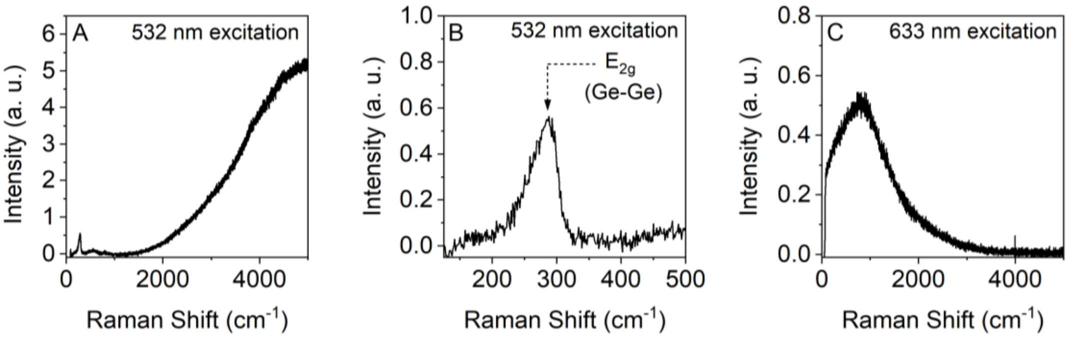

Figure A 49: Raman spectra of Ge-Me bulk crystals. A: Raman spectrum under 532 nm excitation, featuring Raman signals attributed to germanium at ~ 288 cm^{-1} (E_{2g}) and strong PL in the low energy region of the spectrum. B: Section of the Raman spectrum in A. C: Raman spectrum under 633 nm excitation. Under this excitation wavelength, the Raman signal and PL overlap and only the PL is visible due to higher intensity.

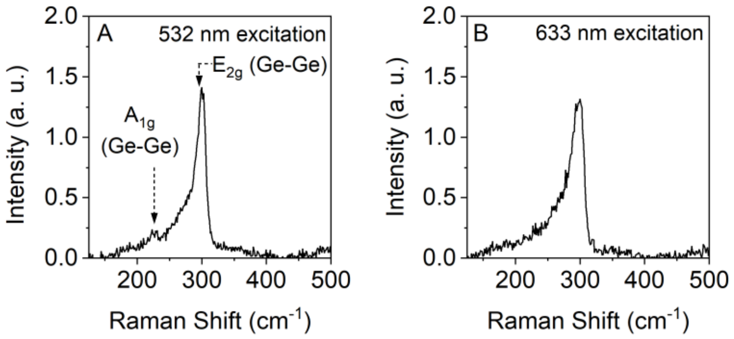

Figure A 50: Raman spectra of Ge-H bulk crystals under 532 (A) and 633 nm (B) excitation, featuring a pronounced Raman signal attributed to germanium at ~ 301 cm^{-1} (E_{2g}) and a weaker signal at 226 cm^{-1} (A_{1g}).

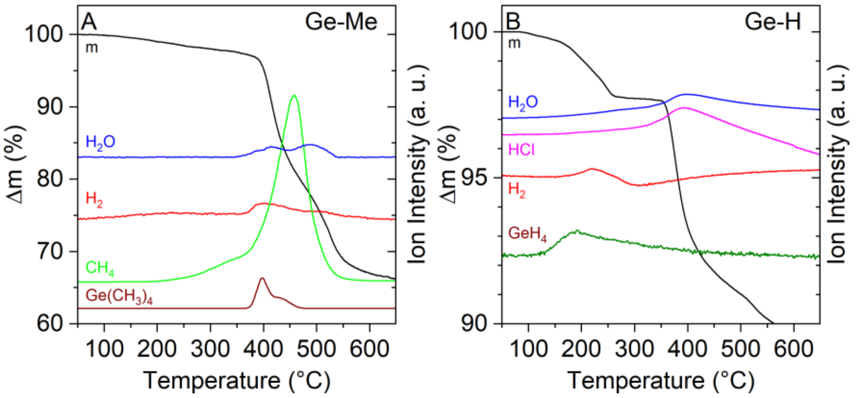

Figure A 51: TGMS spectra of bulk Ge-Me (A) and Ge-H (B). Major decomposition of Ge-Me is observed between ~ 380 and 600 °C. Detected decomposition products are hydrogen, methane, and products with the general formula $GeH_n(CH_3)_{4-n}$, originating from cleavage of Ge-H bonds, Ge-C bonds, and Ge-Ge bonds, respectively. Major decomposition of Ge-H is observed between ~ 100 and 450 °C. Detected decomposition products are hydrochloride, hydrogen and GeH_4, originating from cleavage of Ge-Cl bonds (which indicates partial derivatization with chlorine), Ge-H, and Ge-Ge bonds, respectively. The absolute values of the ion intensity are not comparable between different decomposition products since the intensities are not corrected for detector sensitivity.

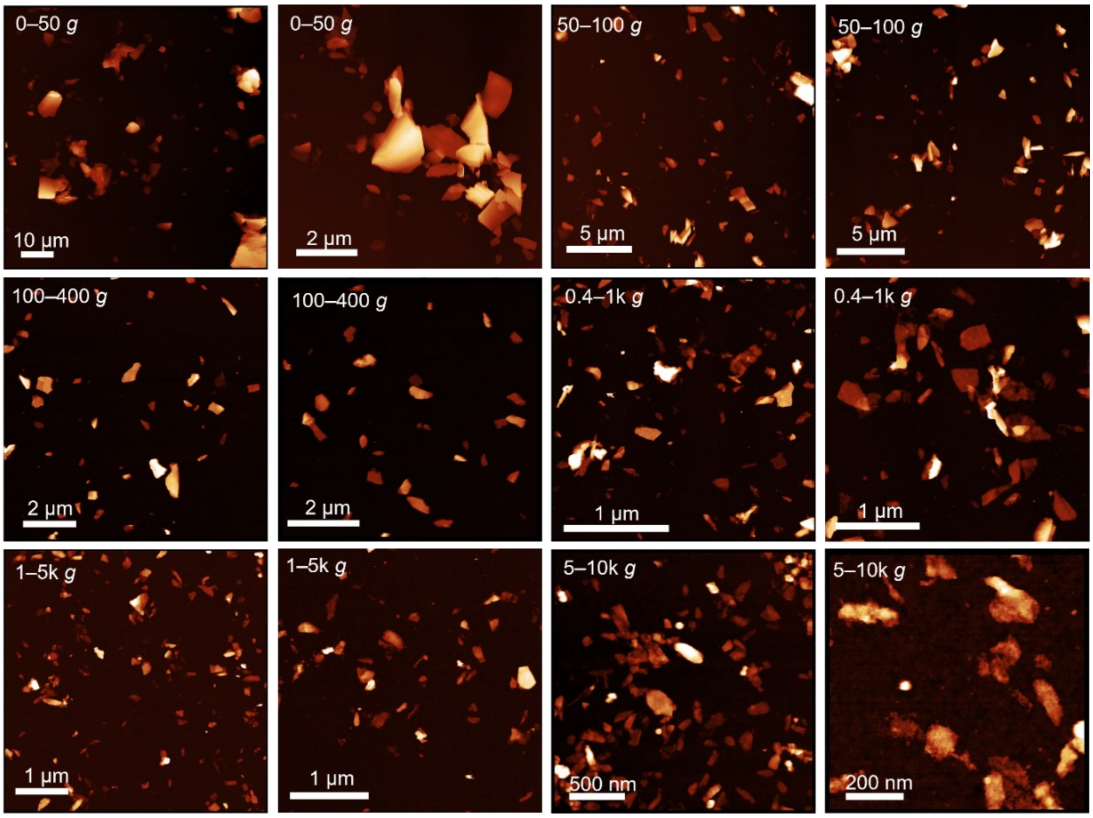

Figure A 52: Selected AFM images of liquid phase exfoliated and size-selected Ge-Me nanosheets, containing images of all fractions of the size selection. The nanosheets were transferred to IPA and deposited on cleaned Si-wafer by flash evaporation prior to measurements.

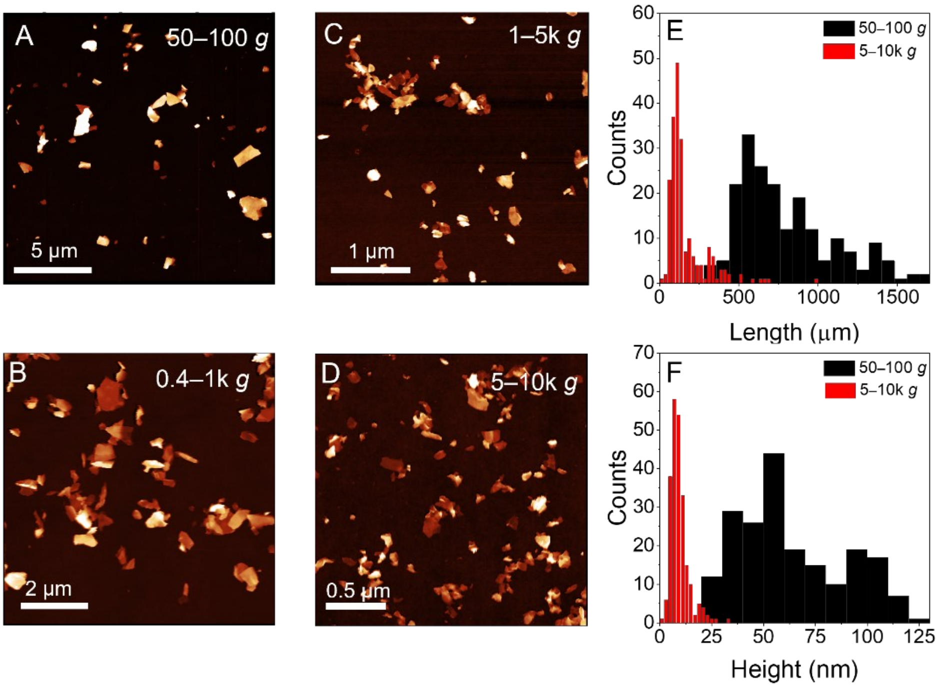

Figure A 53: Summary of the AFM analysis of exfoliated Ge-H nanosheets. A–D: AFM images of deposited nanosheets, collected at different fractions of the size selection, including 50–100 *g* (A), 0.4–1k *g* (B), 1–5k *g* (C), 5–10k *g* (D). E, F: Size distribution of the nanosheet length (E) and nanosheet height (F) of the fractions 50–100 *g* and 5–10k *g*.

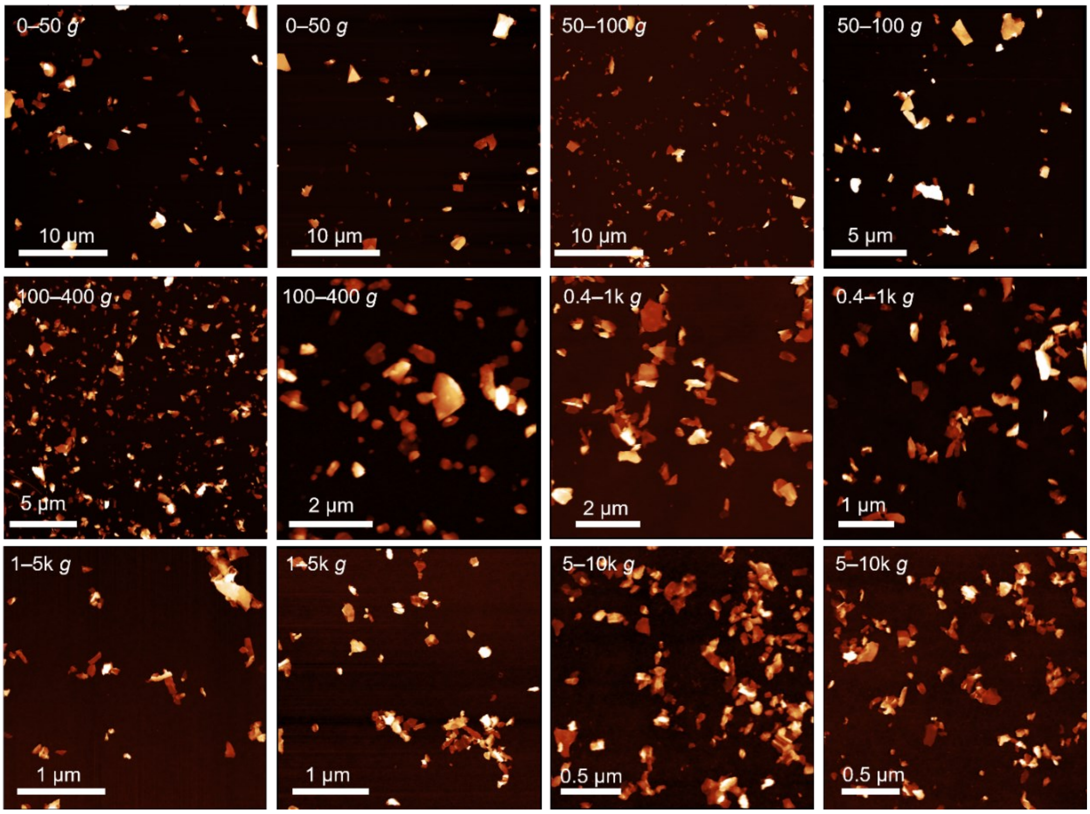

Figure A 54: Selected AFM images of liquid phase exfoliated and size-selected Ge-H nanosheets, containing images of all fractions of the size selection. The nanosheets were transferred to IPA and deposited on cleaned Si-wafer by flash evaporation prior to measurements.

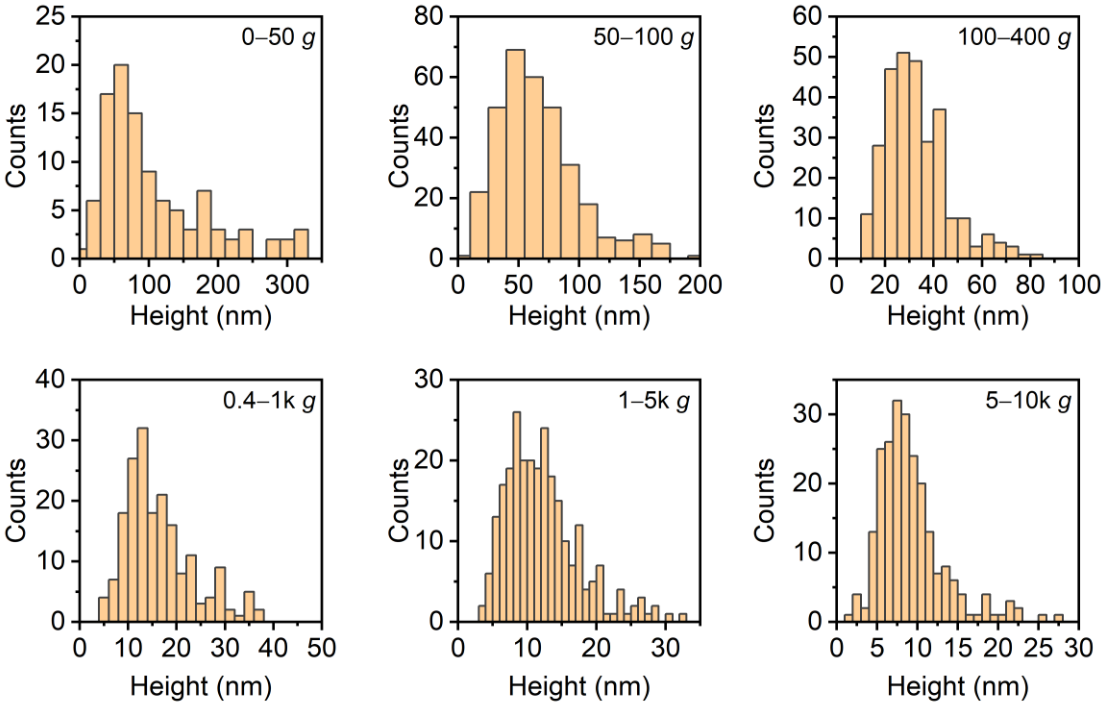

Figure A 55: Height distribution of Ge-Me nanosheets obtained by LPE and collected during LCC, derived from the AFM images shown in Figure A 52. With proceeding size selection cascade, the nanosheet height decreases and the distribution becomes narrower.

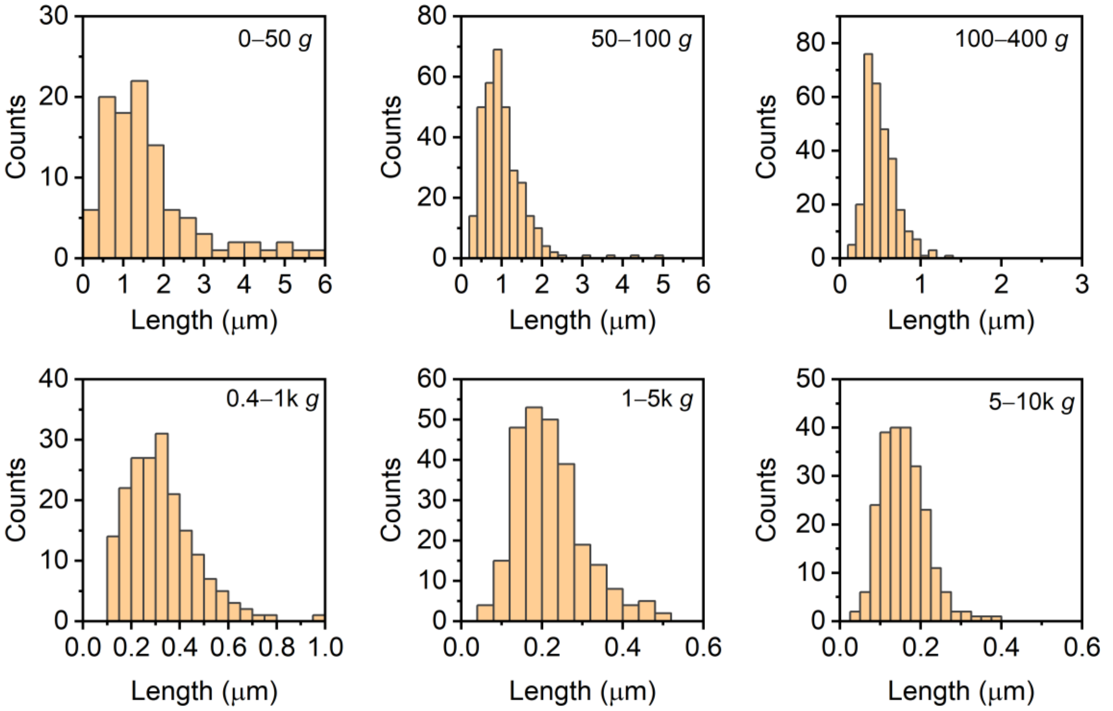

Figure A 56: Length distribution of Ge-Me nanosheets obtained by LPE and collected during LCC, derived from the AFM images shown in Figure A 52. With proceeding size selection cascade, the nanosheet length decreases and the distribution becomes narrower.

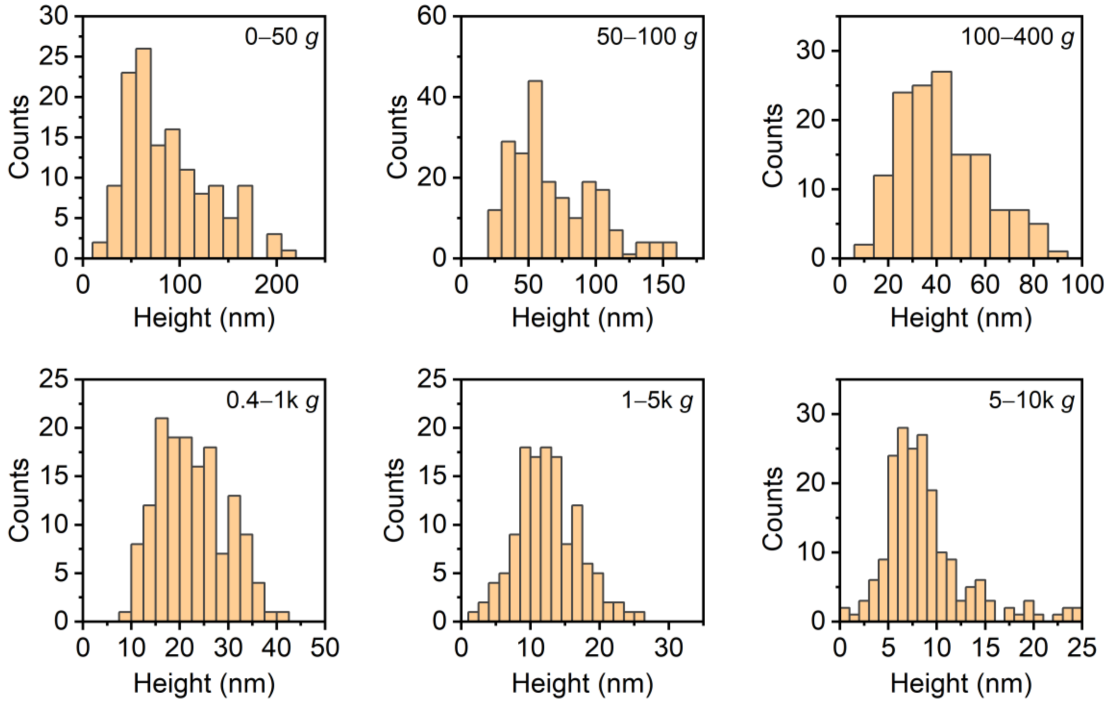

Figure A 57: Height distribution of Ge-H nanosheets obtained by LPE and collected during LCC, derived from the AFM images shown in Figure A 54. With proceeding size selection cascade, the nanosheet height decreases and the distribution becomes narrower.

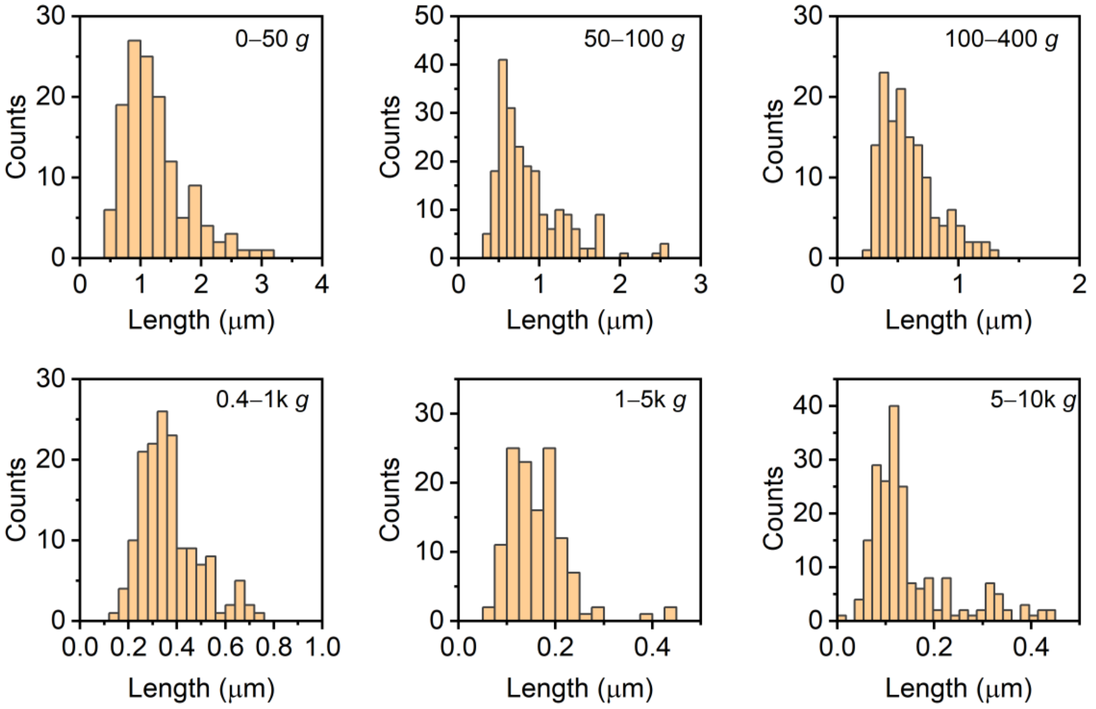

Figure A 58: Length distribution of Ge-H nanosheets obtained by LPE and collected during LCC, derived from the AFM images shown in Figure A 54. With proceeding size selection cascade, the nanosheet length decreases and the distribution becomes narrower.

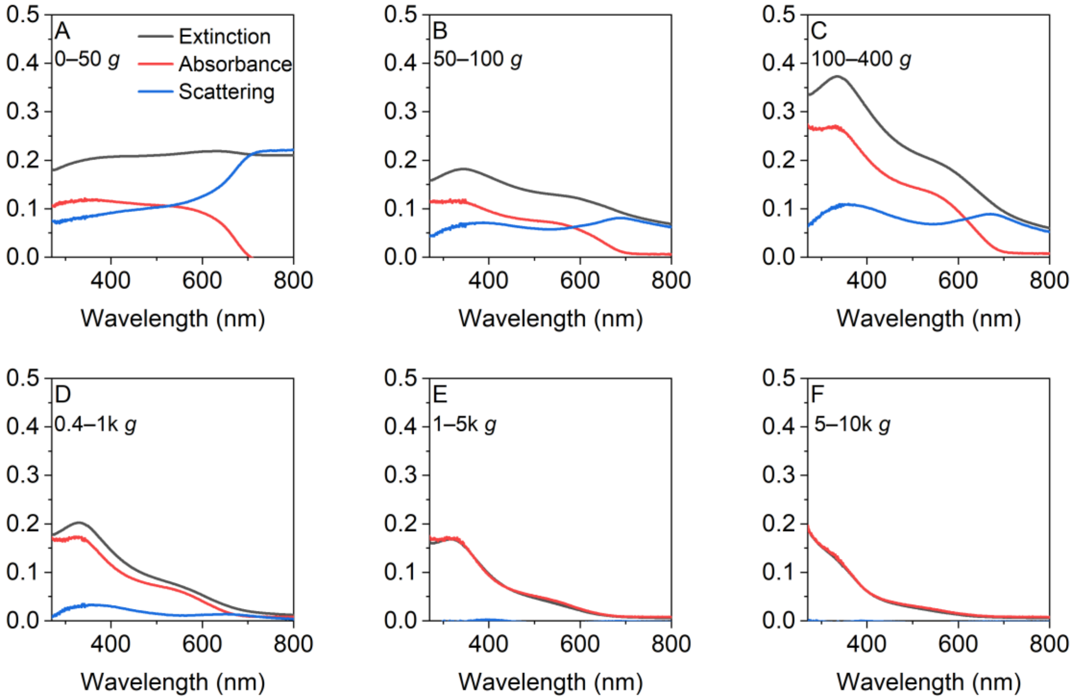

Figure A 59: UV-Vis spectra of exfoliated and size-selected Ge-Me nanosheets, including extinction, absorbance, and scattering background. The absorbance was measured in an integrating sphere and subtracted from the extinction to calculate the scattering. A: 0–50 *g*; B: 50–100 *g*; C: 100–400 *g*; D: 0.4–1k *g*; E: 1–5k *g*, F: 5–10k *g*.

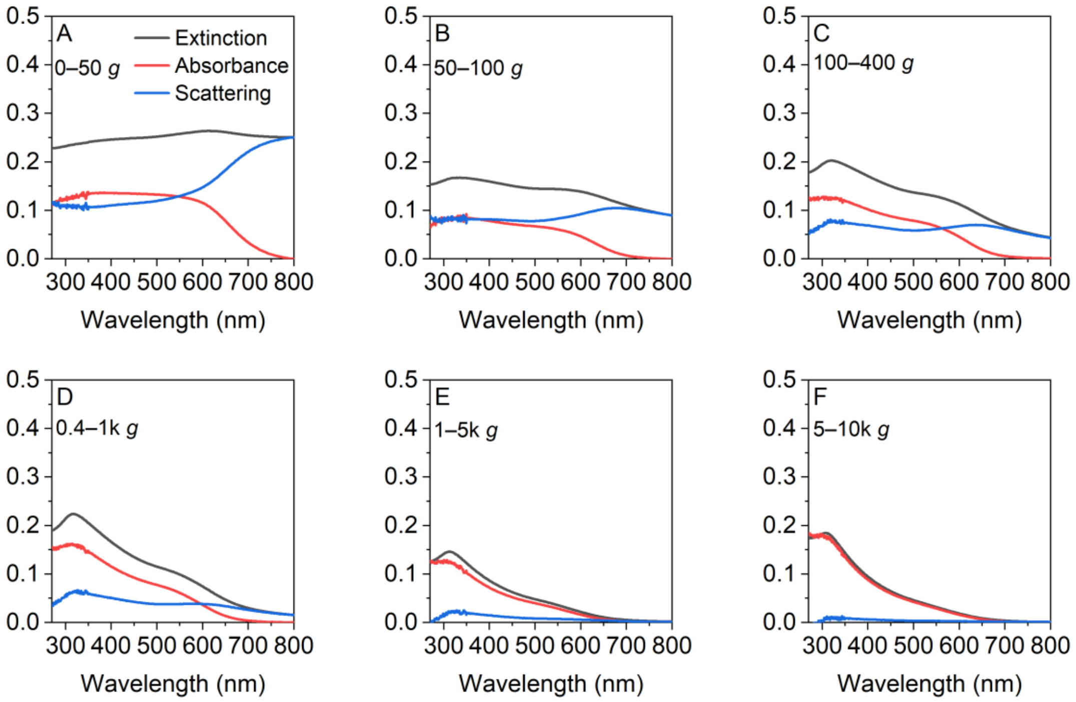

Figure A 60: UV-Vis spectra of exfoliated and size-selected Ge-H nanosheets, including extinction, absorbance and scattering background. The absorbance was measured in an integrating sphere and subtracted from the extinction to calculate the scattering. A: 0–50 *g*; B: 50–100 *g*; C: 100–400 *g*; D: 0.4–1k *g*; E: 1–5k *g*, F: 5–10k *g*.

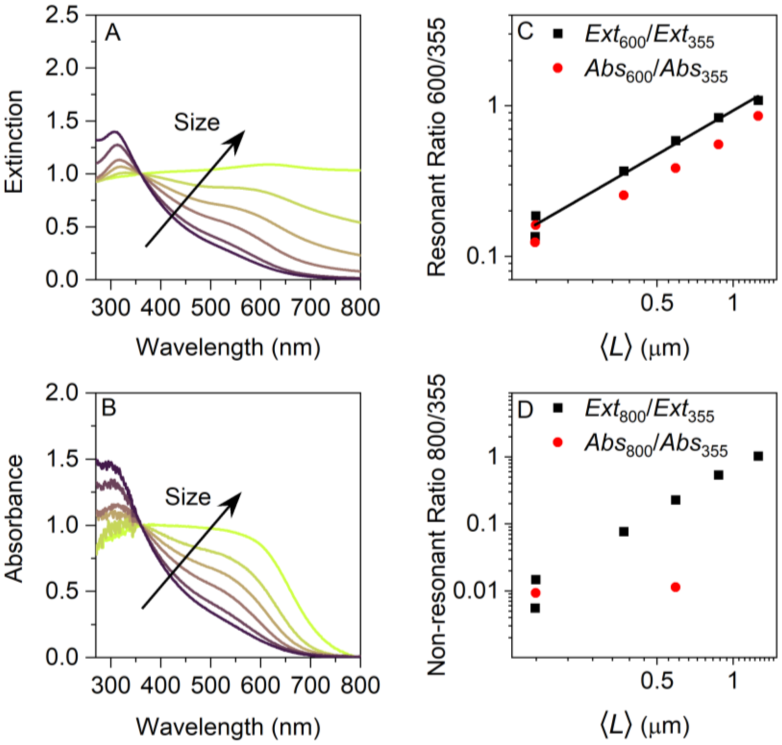

Figure A 61: UV-Vis summary of the Ge-H UV-Vis data shown in Figure A 60, showing the size-dependent changes in the extinction (A) and absorbance (B), and the resonant ratio 600/355 (C) as well as the non-resonant ratio 800/355 (D) as a function of the nanosheet length.

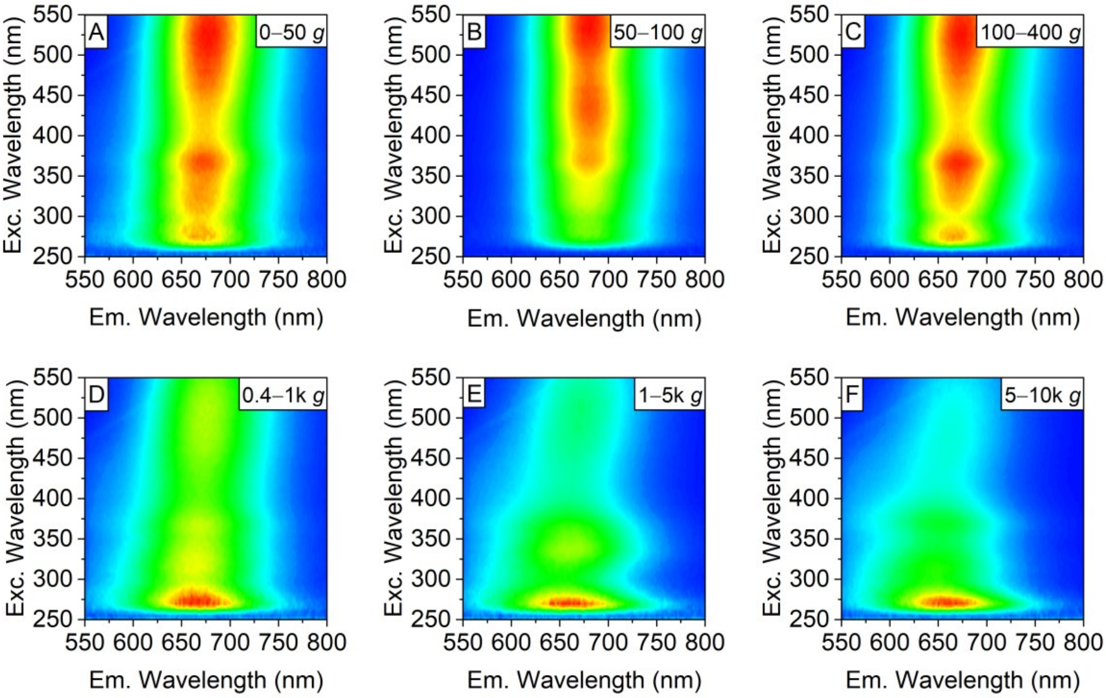

Figure A 62: PLE contour plots of dispersions containing exfoliated and size-selected Ge-Me nanosheets. Dispersions of large nanosheets feature a PL emission at ~ 670 nm that is relatively invariant with respect to the excitation wavelength. With decreasing nanosheet size, the emission maximum successively shifts towards smaller excitation wavelength. A: 0–50 *g*; B: 50–100 *g*; C: 100–400 *g*; D: 0.4–1k *g*; E: 1–5k *g*, F: 5–10k *g*.

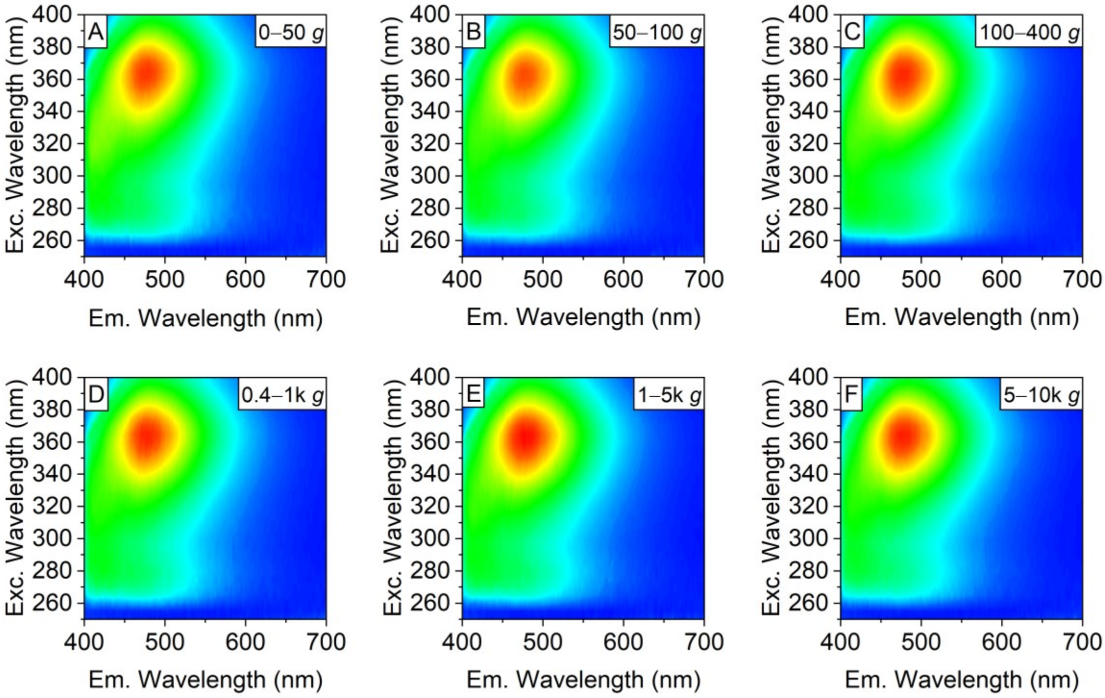

Figure A 63: PLE contour plots of dispersions containing exfoliated and size-selected Ge-H nanosheets. In contrast to the Ge-Me dispersions, no size-dependent trend is discernible. The maximum PL is detected at ~ 475 nm at an excitation wavelength of ~ 365 nm, which is in contradiction to the literature known PL emission of Ge-H. A: 0–50 *g*; B: 50–100 *g*; C: 100–400 *g*; D: 0.4–1k *g*; E: 1–5k *g*, F: 5–10k *g*.

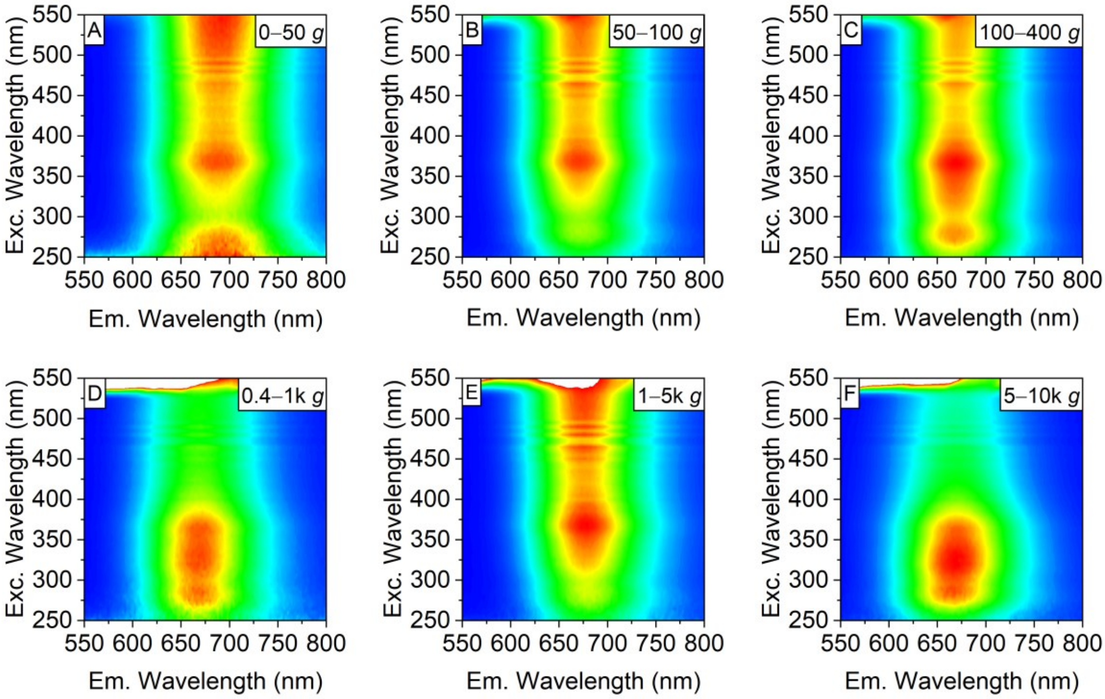

Figure A 64: PLE contour plots of Ge-Me nanosheet films, formed by nanosheet self-assembly at a water-toluene phase interface and deposited on glass. The PL is comparable to the PL recorded in dispersion, but size-dependent trends are less pronounced. A: 0–50 *g*; B: 50–100 *g*; C: 100–400 *g*; D: 0.4–1k *g*; E: 1–5k *g*, F: 5–10k *g*.

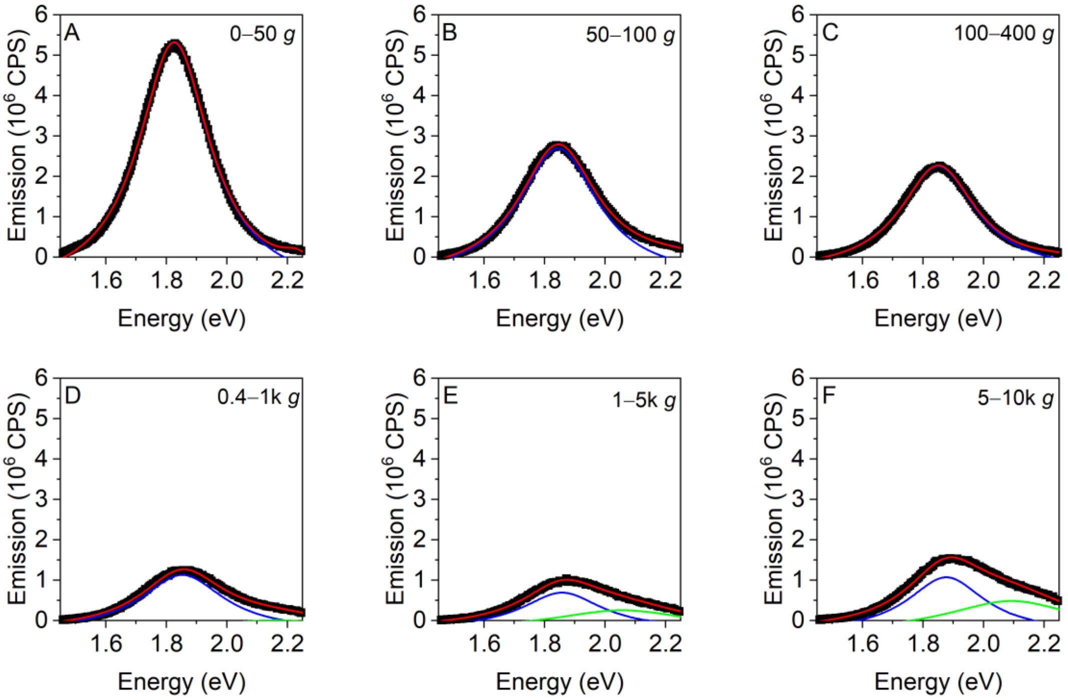

Figure A 65: PL spectra (λ_{exc} = 370 nm) of dispersions containing exfoliated and size-selected Ge-Me nanosheets, fitted by Lorentzians to extract quantitative information about PL position, linewidth, and intensity. The PL intensity of the spectra was divided through the absorbance at 370 nm to correct for different but unknown nanosheet concentrations. A: 0–50 *g*; B: 50–100 *g*; C: 100–400 *g*; D: 0.4–1k *g*; E: 1–5k *g*, F: 5–10k *g*.

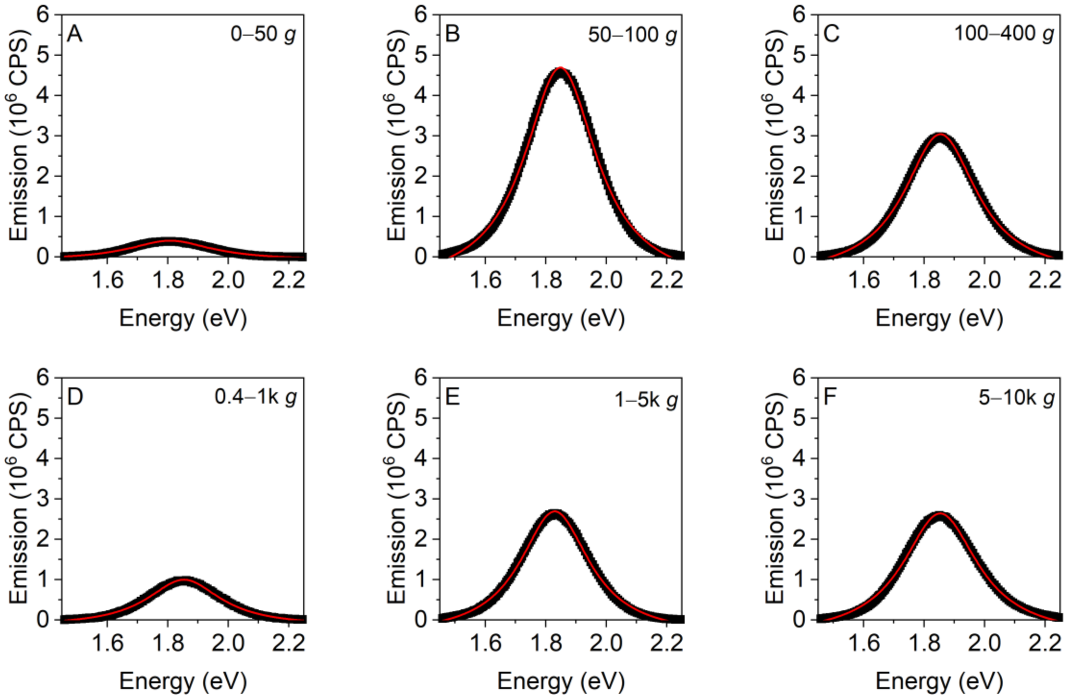

Figure A 66: PL spectra (λ_{exc} = 370 nm) of Ge-Me nanosheet films, formed by nanosheet self-assembly at a water-toluene phase interface and deposited on glass. The PL spectra were fitted by Lorentzians to extract quantitative information about PL position and linewidth. A: 0–50 *g*; B: 50–100 *g*; C: 100–400 *g*; D: 0.4–1k *g*; E: 1–5k *g*, F: 5–10k *g*.

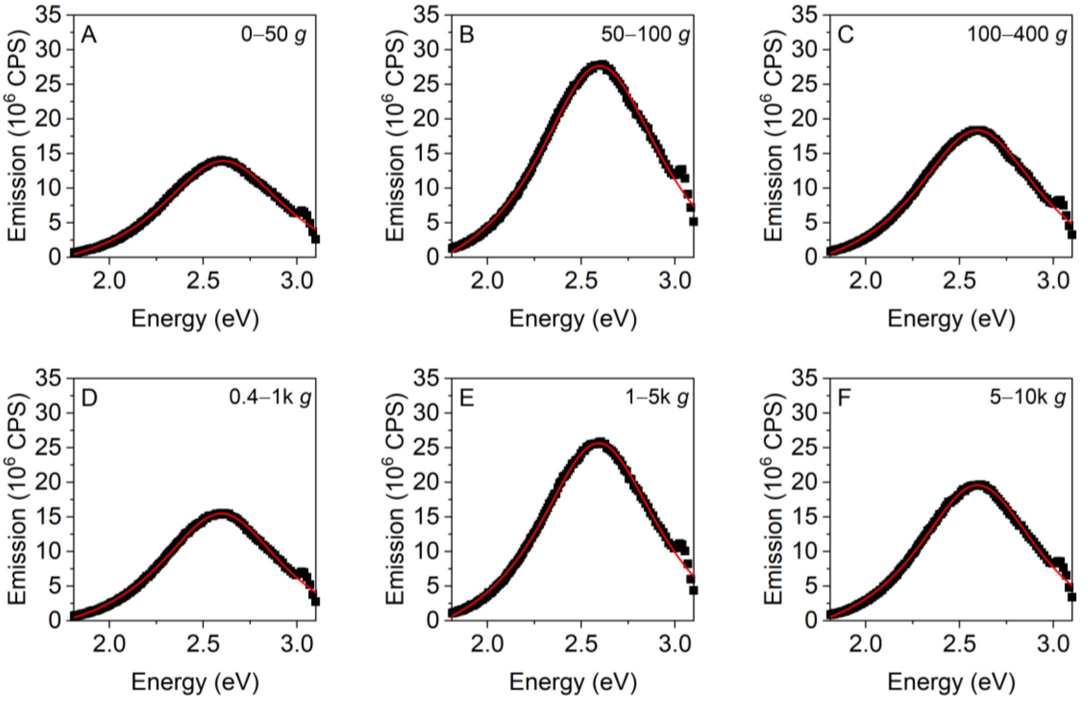

Figure A 67: PL spectra (λ_{exc} = 365 nm) of dispersions containing exfoliated and size-selected Ge-H nanosheets, fitted by Lorentzians to extract quantitative information about PL position, linewidth, and intensity. The PL intensity of the spectra was divided through the absorbance at 365 nm to correct for different but unknown nanosheet concentrations. A: 0–50 *g*; B: 50–100 *g*; C: 100–400 *g*; D: 0.4–1k *g*; E: 1–5k *g*, F: 5–10k *g*.

References

1. Chambouleyron, I.; Martinez, J. M., Chapter 12 - Optical properties of dielectric and semiconductor thin films. In *Handbook of Thin Films*, Singh Nalwa, H., Ed. Academic Press: Burlington, **2002**; pp 593-622.
2. Kebede, M. A.; Imae, T., Chapter 1.1 - Low-Dimensional Nanomaterials. In *Advanced Supramolecular Nanoarchitectonics*, Ariga, K.; Aono, M., Eds. William Andrew Publishing, **2019**; pp 3-16.
3. Novoselov, K. S.; Geim, A. K.; Morozov, S. V.; Jiang, D.; Zhang, Y.; Dubonos, S. V.; Grigorieva, I. V.; Firsov, A. A., Electric Field Effect in Atomically Thin Carbon Films. *Science* **2004,** *306* (5696), 666-669.
4. Berger, C.; Song, Z.; Li, T.; Li, X.; Ogbazghi, A. Y.; Feng, R.; Dai, Z.; Marchenkov, A. N.; Conrad, E. H.; First, P. N.; de Heer, W. A., Ultrathin Epitaxial Graphite: 2D Electron Gas Properties and a Route toward Graphene-based Nanoelectronics. *The Journal of Physical Chemistry B* **2004,** *108* (52), 19912-19916.
5. Lee, C.; Wei, X.; Kysar, J. W.; Hone, J., Measurement of the Elastic Properties and Intrinsic Strength of Monolayer Graphene. *Science* **2008,** *321* (5887), 385-388.
6. Zhu, Y.; Murali, S.; Cai, W.; Li, X.; Suk, J. W.; Potts, J. R.; Ruoff, R. S., Graphene and Graphene Oxide: Synthesis, Properties, and Applications. *Advanced Materials* **2010,** *22* (35), 3906-3924.
7. Wang, G.; Chernikov, A.; Glazov, M. M.; Heinz, T. F.; Marie, X.; Amand, T.; Urbaszek, B., Colloquium: Excitons in atomically thin transition metal dichalcogenides. *Reviews of Modern Physics* **2018,** *90* (2), 021001.
8. He, K.; Kumar, N.; Zhao, L.; Wang, Z.; Mak, K. F.; Zhao, H.; Shan, J., Tightly Bound Excitons in Monolayer WSe_2. *Physical Review Letters* **2014,** *113* (2), 026803.
9. Chernikov, A.; Berkelbach, T. C.; Hill, H. M.; Rigosi, A.; Li, Y.; Aslan, O. B.; Reichman, D. R.; Hybertsen, M. S.; Heinz, T. F., Exciton Binding Energy and Nonhydrogenic Rydberg Series in Monolayer WS_2. *Physical Review Letters* **2014,** *113* (7), 076802.
10. Schneider, C.; Glazov, M. M.; Korn, T.; Höfling, S.; Urbaszek, B., Two-dimensional semiconductors in the regime of strong light-matter coupling. *Nature Communications* **2018,** *9* (1), 2695.
11. Podzorov, V.; Gershenson, M. E.; Kloc, C.; Zeis, R.; Bucher, E., High-mobility field-effect transistors based on transition metal dichalcogenides. *Applied Physics Letters* **2004,** *84* (17), 3301-3303.
12. Radisavljevic, B.; Radenovic, A.; Brivio, J.; Giacometti, V.; Kis, A., Single-layer MoS2 transistors. *Nature Nanotechnology* **2011,** *6* (3), 147-150.
13. Higgins, T. M.; Finn, S.; Matthiesen, M.; Grieger, S.; Synnatschke, K.; Brohmann, M.; Rother, M.; Backes, C.; Zaumseil, J., Electrolyte-Gated n-Type Transistors Produced from Aqueous Inks of WS2 Nanosheets. *Advanced Functional Materials* **2019,** *29* (4), 1804387.
14. Daus, A.; Vaziri, S.; Chen, V.; Köroğlu, Ç.; Grady, R. W.; Bailey, C. S.; Lee, H. R.; Schauble, K.; Brenner, K.; Pop, E., High-performance flexible nanoscale transistors based on transition metal dichalcogenides. *Nature Electronics* **2021,** *4* (7), 495-501.
15. Kang, D.-H.; Kim, M.-S.; Shim, J.; Jeon, J.; Park, H.-Y.; Jung, W.-S.; Yu, H.-Y.; Pang, C.-H.; Lee, S.; Park, J.-H., High-Performance Transition Metal Dichalcogenide Photodetectors Enhanced by Self-Assembled Monolayer Doping. *Advanced Functional Materials* **2015,** *25* (27), 4219-4227.
16. Kang, D.-H.; Pae, S. R.; Shim, J.; Yoo, G.; Jeon, J.; Leem, J. W.; Yu, J. S.; Lee, S.; Shin, B.; Park, J.-H., An Ultrahigh-Performance Photodetector based on a Perovskite–Transition-Metal-Dichalcogenide Hybrid Structure. *Advanced Materials* **2016,** *28* (35), 7799-7806.
17. Mawlong, L. P. L.; Ahn, J.-H., 3D-Structured Photodetectors Based on 2D Transition-Metal Dichalcogenide. *Small Structures* **2022,** *3* (1), 2100149.
18. Chen, B.; Chao, D.; Liu, E.; Jaroniec, M.; Zhao, N.; Qiao, S.-Z., Transition metal dichalcogenides for alkali metal ion batteries: engineering strategies at the atomic level. *Energy & Environmental Science* **2020,** *13* (4), 1096-1131.
19. Zhang, Z.; Yang, M.; Zhao, N.; Wang, L.; Li, Y., Two-dimensional transition metal dichalcogenides as promising anodes for potassium ion batteries from first-principles prediction. *Physical Chemistry Chemical Physics* **2019,** *21* (42), 23441-23446.

20. Lee, W. S. V.; Xiong, T.; Wang, X.; Xue, J., Unraveling MoS2 and Transition Metal Dichalcogenides as Functional Zinc-Ion Battery Cathode: A Perspective. *Small Methods* **2021,** *5* (1), 2000815.

21. Wang, C.; Yang, F.; Gao, Y., The highly-efficient light-emitting diodes based on transition metal dichalcogenides: from architecture to performance. *Nanoscale Advances* **2020,** *2* (10), 4323-4340.

22. Ou, H.; Matsuoka, H.; Tempia, J.; Yamada, T.; Takahashi, T.; Oi, K.; Takaguchi, Y.; Endo, T.; Miyata, Y.; Chen, C.-H.; Li, L.-J.; Pu, J.; Takenobu, T., Spatial Control of Dynamic p–i–n Junctions in Transition Metal Dichalcogenide Light-Emitting Devices. *ACS Nano* **2021,** *15* (8), 12911-12921.

23. Sanvitto, D.; Kéna-Cohen, S., The road towards polaritonic devices. *Nature Materials* **2016,** *15*, 1061.

24. Bajoni, D., Polariton lasers. Hybrid light–matter lasers without inversion. *Journal of Physics D: Applied Physics* **2012,** *45* (31), 313001.

25. Gu, J.; Chakraborty, B.; Khatoniar, M.; Menon, V. M., A room-temperature polariton light-emitting diode based on monolayer WS2. *Nature Nanotechnology* **2019**.

26. Ballarini, D.; De Giorgi, M.; Cancellieri, E.; Houdré, R.; Giacobino, E.; Cingolani, R.; Bramati, A.; Gigli, G.; Sanvitto, D., All-optical polariton transistor. *Nature Communications* **2013,** *4* (1), 1778.

27. Zasedatelev, A. V.; Baranikov, A. V.; Urbonas, D.; Scafirimuto, F.; Scherf, U.; Stöferle, T.; Mahrt, R. F.; Lagoudakis, P. G., A room-temperature organic polariton transistor. *Nature Photonics* **2019,** *13* (6), 378-383.

28. Szydłowska, B. M.; Graf, A.; Kelly, A.; Blau, W. J.; Gather, M. C.; Zaumseil, J.; Backes, C., Preparation of WS2–PMMA composite films for optical applications. *Journal of Materials Chemistry C* **2020,** *8* (31), 10805-10815.

29. Yu, X.; Prévot, M. S.; Guijarro, N.; Sivula, K., Self-assembled 2D WSe2 thin films for photoelectrochemical hydrogen production. *Nature Communications* **2015,** *6* (1), 7596.

30. Neilson, J.; Avery, M. P.; Derby, B., Tiled Monolayer Films of 2D Molybdenum Disulfide Nanoflakes Assembled at Liquid/Liquid Interfaces. *ACS Applied Materials & Interfaces* **2020,** *12* (22), 25125-25134.

31. Kalosi, A.; Demydenko, M.; Bodik, M.; Hagara, J.; Kotlar, M.; Kostiuk, D.; Halahovets, Y.; Vegso, K.; Marin Roldan, A.; Maurya, G. S.; Angus, M.; Veis, P.; Jergel, M.; Majkova, E.; Siffalovic, P., Tailored Langmuir–Schaefer Deposition of Few-Layer MoS2 Nanosheet Films for Electronic Applications. *Langmuir* **2019,** *35* (30), 9802-9808.

32. Han, S. A.; Bhatia, R.; Kim, S.-W., Synthesis, properties and potential applications of two-dimensional transition metal dichalcogenides. *Nano Convergence* **2015,** *2* (1), 17.

33. Saito, R.; Tatsumi, Y.; Huang, S.; Ling, X.; Dresselhaus, M. S., Raman spectroscopy of transition metal dichalcogenides. *Journal of Physics: Condensed Matter* **2016,** *28* (35), 353002.

34. Polcar, T.; Cavaleiro, A., Self-adaptive low friction coatings based on transition metal dichalcogenides. *Thin Solid Films* **2011,** *519* (12), 4037-4044.

35. Polcar, T.; Cavaleiro, A., Review on self-lubricant transition metal dichalcogenide nanocomposite coatings alloyed with carbon. *Surface and Coatings Technology* **2011,** *206* (4), 686-695.

36. Irving, B. J.; Nicolini, P.; Polcar, T., On the lubricity of transition metal dichalcogenides: an ab initio study. *Nanoscale* **2017,** *9* (17), 5597-5607.

37. Scharf, T. W.; Prasad, S. V., Solid lubricants: a review. *Journal of Materials Science* **2013,** *48* (2), 511-531.

38. Berman, D.; Erdemir, A.; Sumant, A. V., Graphene: a new emerging lubricant. *Materials Today* **2014,** *17* (1), 31-42.

39. Manzeli, S.; Ovchinnikov, D.; Pasquier, D.; Yazyev, O. V.; Kis, A., 2D transition metal dichalcogenides. *Nature Reviews Materials* **2017,** *2* (8), 17033.

40. Wang, Q. H.; Kalantar-Zadeh, K.; Kis, A.; Coleman, J. N.; Strano, M. S., Electronics and optoelectronics of two-dimensional transition metal dichalcogenides. *Nature Nanotechnology* **2012,** *7* (11), 699-712.

41. Ayari, A.; Cobas, E.; Ogundadegbe, O.; Fuhrer, M. S., Realization and electrical characterization of ultrathin crystals of layered transition-metal dichalcogenides. *Journal of Applied Physics* **2007,** *101* (1), 014507.

42. Frey, G. L.; Reynolds, K. J.; Friend, R. H.; Cohen, H.; Feldman, Y., Solution-Processed Anodes from Layer-Structure Materials for High-Efficiency Polymer Light-Emitting Diodes. *Journal of the American Chemical Society* **2003,** *125* (19), 5998-6007.

43. Reynolds, K. J.; Barker, J. A.; Greenham, N. C.; Friend, R. H.; Frey, G. L., Inorganic solution-processed hole-injecting and electron-blocking layers in polymer light-emitting diodes. *Journal of Applied Physics* **2002,** *92* (12), 7556-7563.

44. Voiry, D.; Salehi, M.; Silva, R.; Fujita, T.; Chen, M.; Asefa, T.; Shenoy, V. B.; Eda, G.; Chhowalla, M., Conducting MoS2 Nanosheets as Catalysts for Hydrogen Evolution Reaction. *Nano Letters* **2013,** *13* (12), 6222-6227.

45. Voiry, D.; Yamaguchi, H.; Li, J.; Silva, R.; Alves, D. C. B.; Fujita, T.; Chen, M.; Asefa, T.; Shenoy, V. B.; Eda, G.; Chhowalla, M., Enhanced catalytic activity in strained chemically exfoliated WS2 nanosheets for hydrogen evolution. *Nature Materials* **2013,** *12* (9), 850-855.

46. Zhou, M.; Wang, W.; Lu, J.; Ni, Z., How defects influence the photoluminescence of TMDCs. *Nano Research* **2021,** *14* (1), 29-39.

47. Zhou, W.; Zou, X.; Najmaei, S.; Liu, Z.; Shi, Y.; Kong, J.; Lou, J.; Ajayan, P. M.; Yakobson, B. I.; Idrobo, J.-C., Intrinsic Structural Defects in Monolayer Molybdenum Disulfide. *Nano Letters* **2013,** *13* (6), 2615-2622.

48. Neupane, G. P.; Tran, M. D.; Yun, S. J.; Kim, H.; Seo, C.; Lee, J.; Han, G. H.; Sood, A. K.; Kim, J., Simple Chemical Treatment to n-Dope Transition-Metal Dichalcogenides and Enhance the Optical and Electrical Characteristics. *ACS Applied Materials & Interfaces* **2017,** *9* (13), 11950-11958.

49. Lien, D.-H.; Uddin, S. Z.; Yeh, M.; Amani, M.; Kim, H.; Ager, J. W.; Yablonovitch, E.; Javey, A., Electrical suppression of all nonradiative recombination pathways in monolayer semiconductors. *Science* **2019,** *364* (6439), 468-471.

50. Tongay, S.; Suh, J.; Ataca, C.; Fan, W.; Luce, A.; Kang, J. S.; Liu, J.; Ko, C.; Raghunathanan, R.; Zhou, J.; Ogletree, F.; Li, J.; Grossman, J. C.; Wu, J., Defects activated photoluminescence in two-dimensional semiconductors: interplay between bound, charged and free excitons. *Scientific Reports* **2013,** *3* (1), 2657.

51. Chow, P. K.; Jacobs-Gedrim, R. B.; Gao, J.; Lu, T.-M.; Yu, B.; Terrones, H.; Koratkar, N., Defect-Induced Photoluminescence in Monolayer Semiconducting Transition Metal Dichalcogenides. *ACS Nano* **2015,** *9* (2), 1520-1527.

52. Tao, Y.; Yu, X.; Li, J.; Liang, H.; Zhang, Y.; Huang, W.; Wang, Q. J., Bright monolayer tungsten disulfide via exciton and trion chemical modulations. *Nanoscale* **2018,** *10* (14), 6294-6299.

53. Amani, M.; Lien, D.-H.; Kiriya, D.; Xiao, J.; Azcatl, A.; Noh, J.; Madhvapathy, S. R.; Addou, R.; KC, S.; Dubey, M.; Cho, K.; Wallace, R. M.; Lee, S.-C.; He, J.-H.; Ager, J. W.; Zhang, X.; Yablonovitch, E.; Javey, A., Near-unity photoluminescence quantum yield in MoS_2. *Science* **2015,** *350* (6264), 1065-1068.

54. Yuan, L.; Huang, L., Exciton dynamics and annihilation in WS2 2D semiconductors. *Nanoscale* **2015,** *7* (16), 7402-7408.

55. Yu, Y.; Yu, Y.; Xu, C.; Barrette, A.; Gundogdu, K.; Cao, L., Fundamental limits of exciton-exciton annihilation for light emission in transition metal dichalcogenide monolayers. *Physical Review B* **2016,** *93* (20), 201111.

56. Lee, Y.; Ghimire, G.; Roy, S.; Kim, Y.; Seo, C.; Sood, A. K.; Jang, J. I.; Kim, J., Impeding Exciton–Exciton Annihilation in Monolayer WS2 by Laser Irradiation. *ACS Photonics* **2018,** *5* (7), 2904-2911.

57. Wang, H.; Zhang, C.; Rana, F., Ultrafast Dynamics of Defect-Assisted Electron–Hole Recombination in Monolayer MoS2. *Nano Letters* **2015,** *15* (1), 339-345.

58. Wang, H.; Strait, J. H.; Zhang, C.; Chan, W.; Manolatou, C.; Tiwari, S.; Rana, F., Fast exciton annihilation by capture of electrons or holes by defects via Auger scattering in monolayer metal dichalcogenides. *Physical Review B* **2015,** *91* (16), 165411.

59. Gutiérrez, M.; Henglein, A., Preparation of colloidal semiconductor solutions of MoS2 and WSe2 via sonication. *Ultrasonics* **1989,** *27* (5), 259-261.

60. Bunch, J. S.; Yaish, Y.; Brink, M.; Bolotin, K.; McEuen, P. L., Coulomb Oscillations and Hall Effect in Quasi-2D Graphite Quantum Dots. *Nano Letters* **2005,** *5* (2), 287-290.

61. Hernandez, Y.; Nicolosi, V.; Lotya, M.; Blighe, F. M.; Sun, Z.; De, S.; McGovern, I. T.; Holland, B.; Byrne, M.; Gun'Ko, Y. K.; Boland, J. J.; Niraj, P.; Duesberg, G.; Krishnamurthy, S.; Goodhue, R.; Hutchison,

J.; Scardaci, V.; Ferrari, A. C.; Coleman, J. N., High-yield production of graphene by liquid-phase exfoliation of graphite. *Nature Nanotechnology* **2008,** *3* (9), 563-568.

62. Coleman, J. N.; Lotya, M.; O'Neill, A.; Bergin, S. D.; King, P. J.; Khan, U.; Young, K.; Gaucher, A.; De, S.; Smith, R. J.; Shvets, I. V.; Arora, S. K.; Stanton, G.; Kim, H.-Y.; Lee, K.; Kim, G. T.; Duesberg, G. S.; Hallam, T.; Boland, J. J.; Wang, J. J.; Donegan, J. F.; Grunlan, J. C.; Moriarty, G.; Shmeliov, A.; Nicholls, R. J.; Perkins, J. M.; Grieveson, E. M.; Theuwissen, K.; McComb, D. W.; Nellist, P. D.; Nicolosi, V., Two-Dimensional Nanosheets Produced by Liquid Exfoliation of Layered Materials. *Science* **2011,** *331* (6017), 568-571.

63. Smith, R. J.; King, P. J.; Lotya, M.; Wirtz, C.; Khan, U.; De, S.; O'Neill, A.; Duesberg, G. S.; Grunlan, J. C.; Moriarty, G.; Chen, J.; Wang, J.; Minett, A. I.; Nicolosi, V.; Coleman, J. N., Large-Scale Exfoliation of Inorganic Layered Compounds in Aqueous Surfactant Solutions. *Advanced Materials* **2011,** *23* (34), 3944-3948.

64. Griffin, A.; Harvey, A.; Cunningham, B.; Scullion, D.; Tian, T.; Shih, C.-J.; Gruening, M.; Donegan, J. F.; Santos, E. J. G.; Backes, C.; Coleman, J. N., Spectroscopic Size and Thickness Metrics for Liquid-Exfoliated h-BN. *Chemistry of Materials* **2018,** *30* (6), 1998-2005.

65. Synnatschke, K.; Cieslik, P. A.; Harvey, A.; Castellanos-Gomez, A.; Tian, T.; Shih, C.-J.; Chernikov, A.; Santos, E. J. G.; Coleman, J. N.; Backes, C., Length- and Thickness-Dependent Optical Response of Liquid-Exfoliated Transition Metal Dichalcogenides. *Chemistry of Materials* **2019,** *31* (24), 10049-10062.

66. Zhu, X.; Chen, S.; Zhang, M.; Chen, L.; Wu, Q.; Zhao, J.; Jiang, Q.; Zheng, Z.; Zhang, H., TiS2-based saturable absorber for ultrafast fiber lasers. *Photon. Res.* **2018,** *6* (10), C44-C48.

67. Vega-Mayoral, V.; Tian, R.; Kelly, A. G.; Griffin, A.; Harvey, A.; Borrelli, M.; Nisi, K.; Backes, C.; Coleman, J. N., Solvent exfoliation stabilizes TiS2 nanosheets against oxidation, facilitating lithium storage applications. *Nanoscale* **2019,** *11* (13), 6206-6216.

68. Liu, Y.; Ji, X.; Liu, J.; Tong, W. W. L.; Askhatova, D.; Shi, J., Tantalum Sulfide Nanosheets as a Theranostic Nanoplatform for Computed Tomography Imaging-Guided Combinatorial Chemo-Photothermal Therapy. **2017,** *27* (39), 1703261.

69. Kang, J.; Sangwan, V. K.; Wood, J. D.; Liu, X.; Balla, I.; Lam, D.; Hersam, M. C., Layer-by-Layer Sorting of Rhenium Disulfide via High-Density Isopycnic Density Gradient Ultracentrifugation. *Nano Letters* **2016,** *16* (11), 7216-7223.

70. Harvey, A.; Backes, C.; Gholamvand, Z.; Hanlon, D.; McAteer, D.; Nerl, H. C.; McGuire, E.; Seral-Ascaso, A.; Ramasse, Q. M.; McEvoy, N.; Winters, S.; Berner, N. C.; McCloskey, D.; Donegan, J. F.; Duesberg, G. S.; Nicolosi, V.; Coleman, J. N., Preparation of Gallium Sulfide Nanosheets by Liquid Exfoliation and Their Application As Hydrogen Evolution Catalysts. *Chemistry of Materials* **2015,** *27* (9), 3483-3493.

71. Petroni, E.; Lago, E.; Bellani, S.; Boukhvalov, D. W.; Politano, A.; Gürbulak, B.; Duman, S.; Prato, M.; Gentiluomo, S.; Oropesa-Nuñez, R.; Panda, J.-K.; Toth, P. S.; Del Rio Castillo, A. E.; Pellegrini, V.; Bonaccorso, F., Liquid-Phase Exfoliated Indium–Selenide Flakes and Their Application in Hydrogen Evolution Reaction. **2018,** *14* (26), 1800749.

72. Brent, J. R.; Lewis, D. J.; Lorenz, T.; Lewis, E. A.; Savjani, N.; Haigh, S. J.; Seifert, G.; Derby, B.; O'Brien, P., Tin(II) Sulfide (SnS) Nanosheets by Liquid-Phase Exfoliation of Herzenbergite: IV–VI Main Group Two-Dimensional Atomic Crystals. *Journal of the American Chemical Society* **2015,** *137* (39), 12689-12696.

73. Zhang, P.; Zhao, F.; Long, P.; Wang, Y.; Yue, Y.; Liu, X.; Feng, Y.; Li, R.; Hu, W.; Li, Y.; Feng, W., Sonication-assisted liquid-phase exfoliated α-GeTe: a two-dimensional material with high Fe3+ sensitivity. *Nanoscale* **2018,** *10* (34), 15989-15997.

74. Hanlon, D.; Backes, C.; Higgins, T. M.; Hughes, M.; O'Neill, A.; King, P.; McEvoy, N.; Duesberg, G. S.; Mendoza Sanchez, B.; Pettersson, H.; Nicolosi, V.; Coleman, J. N., Production of Molybdenum Trioxide Nanosheets by Liquid Exfoliation and Their Application in High-Performance Supercapacitors. *Chemistry of Materials* **2014,** *26* (4), 1751-1763.

75. Boland, J. B.; Harvey, A.; Tian, R.; Hanlon, D.; Vega-Mayoral, V.; Szydlowska, B.; Griffin, A.; Stimpel-Lindner, T.; Jaskaniec, S.; Nicolosi, V.; Duesberg, G.; Coleman, Jonathan N., Liquid phase exfoliation of MoO2 nanosheets for lithium ion battery applications. *Nanoscale Advances* **2019,** *1* (4), 1560-1570.

76. Hanlon, D.; Backes, C.; Doherty, E.; Cucinotta, C. S.; Berner, N. C.; Boland, C.; Lee, K.; Harvey, A.; Lynch, P.; Gholamvand, Z.; Zhang, S.; Wang, K.; Moynihan, G.; Pokle, A.; Ramasse, Q. M.; McEvoy, N.; Blau, W. J.; Wang, J.; Abellan, G.; Hauke, F.; Hirsch, A.; Sanvito, S.; O'Regan, D. D.; Duesberg, G. S.; Nicolosi, V.; Coleman, J. N., Liquid exfoliation of solvent-stabilized few-layer black phosphorus for applications beyond electronics. *Nature Communications* **2015,** *6* (1), 8563.

77. Lin, S.; Chui, Y.; Li, Y.; Lau, S. P., Liquid-phase exfoliation of black phosphorus and its applications. *FlatChem* **2017,** *2*, 15-37.

78. Brent, J. R.; Savjani, N.; Lewis, E. A.; Haigh, S. J.; Lewis, D. J.; O'Brien, P., Production of few-layer phosphorene by liquid exfoliation of black phosphorus. *Chemical Communications* **2014,** *50* (87), 13338-13341.

79. Gu, J.; Du, Z.; Zhang, C.; Ma, J.; Li, B.; Yang, S., Liquid-Phase Exfoliated Metallic Antimony Nanosheets toward High Volumetric Sodium Storage. **2017,** *7* (17), 1700447.

80. Gibaja, C.; Rodriguez-San-Miguel, D.; Ares, P.; Gómez-Herrero, J.; Varela, M.; Gillen, R.; Maultzsch, J.; Hauke, F.; Hirsch, A.; Abellán, G.; Zamora, F., Few-Layer Antimonene by Liquid-Phase Exfoliation. **2016,** *55* (46), 14345-14349.

81. Synnatschke, K.; Shao, S.; van Dinter, J.; Hofstetter, Y. J.; Kelly, D. J.; Grieger, S.; Haigh, S. J.; Vaynzof, Y.; Bensch, W.; Backes, C., Liquid Exfoliation of Ni2P2S6: Structural Characterization, Size-Dependent Properties, and Degradation. *Chemistry of Materials* **2019,** *31* (21), 9127-9139.

82. Dangol, R.; Dai, Z.; Chaturvedi, A.; Zheng, Y.; Zhang, Y.; Dinh, K. N.; Li, B.; Zong, Y.; Yan, Q., Few-layer NiPS3 nanosheets as bifunctional materials for Li-ion storage and oxygen evolution reaction. *Nanoscale* **2018,** *10* (10), 4890-4896.

83. Harvey, A.; Boland, J. B.; Godwin, I.; Kelly, A. G.; Szydłowska, B. M.; Murtaza, G.; Thomas, A.; Lewis, D. J.; O'Brien, P.; Coleman, J. N., Exploring the versatility of liquid phase exfoliation: producing 2D nanosheets from talcum powder, cat litter and beach sand. *2D Materials* **2017,** *4* (2), 025054.

84. Harvey, A.; He, X.; Godwin, I. J.; Backes, C.; McAteer, D.; Berner, N. C.; McEvoy, N.; Ferguson, A.; Shmeliov, A.; Lyons, M. E. G.; Nicolosi, V.; Duesberg, G. S.; Donegan, J. F.; Coleman, J. N., Production of Ni(OH)2 nanosheets by liquid phase exfoliation: from optical properties to electrochemical applications. *Journal of Materials Chemistry A* **2016,** *4* (28), 11046-11059.

85. McAteer, D.; Godwin, I. J.; Ling, Z.; Harvey, A.; He, L.; Boland, C. S.; Vega-Mayoral, V.; Szydłowska, B.; Rovetta, A. A.; Backes, C.; Boland, J. B.; Chen, X.; Lyons, M. E. G.; Coleman, J. N., Liquid Exfoliated Co(OH)2 Nanosheets as Low-Cost, Yet High-Performance, Catalysts for the Oxygen Evolution Reaction. **2018,** *8* (15), 1702965.

86. Ayán-Varela, M.; Villar-Rodil, S.; Paredes, J. I.; Munuera, J. M.; Pagán, A.; Lozano-Pérez, A. A.; Cenis, J. L.; Martínez-Alonso, A.; Tascón, J. M. D., Investigating the Dispersion Behavior in Solvents, Biocompatibility, and Use as Support for Highly Efficient Metal Catalysts of Exfoliated Graphitic Carbon Nitride. *ACS Applied Materials & Interfaces* **2015,** *7* (43), 24032-24045.

87. Lange, R. Z.; Synnatschke, K.; Qi, H.; Huber, N.; Hofer, G.; Liang, B.; Huck, C.; Pucci, A.; Kaiser, U.; Backes, C.; Schlüter, A. D., Enriching and Quantifying Porous Single Layer 2D Polymers by Exfoliation of Chemically Modified van der Waals Crystals. **2020,** *59* (14), 5683-5695.

88. Molina-Mendoza, A. J.; Giovanelli, E.; Paz, W. S.; Niño, M. A.; Island, J. O.; Evangeli, C.; Aballe, L.; Foerster, M.; van der Zant, H. S. J.; Rubio-Bollinger, G.; Agraït, N.; Palacios, J. J.; Pérez, E. M.; Castellanos-Gomez, A., Franckeite as a naturally occurring van der Waals heterostructure. *Nature Communications* **2017,** *8* (1), 14409.

89. Niu, Y.; Villalva, J.; Frisenda, R.; Sanchez-Santolino, G.; Ruiz-González, L.; Pérez, E. M.; García-Hernández, M.; Burzurí, E.; Castellanos-Gomez, A., Mechanical and liquid phase exfoliation of cylindrite: a natural van der Waals superlattice with intrinsic magnetic interactions. *2D Materials* **2019,** *6* (3), 035023.

90. Griffin, A.; Nisi, K.; Pepper, J.; Harvey, A.; Szydłowska, B. M.; Coleman, J. N.; Backes, C., Effect of Surfactant Choice and Concentration on the Dimensions and Yield of Liquid-Phase-Exfoliated Nanosheets. *Chemistry of Materials* **2020,** *32* (7), 2852-2862.

91. Cai, X.; Jiang, Z.; Zhang, X.; Zhang, X., Effects of Tip Sonication Parameters on Liquid Phase Exfoliation of Graphite into Graphene Nanoplatelets. *Nanoscale Research Letters* **2018,** *13* (1), 241.

92. Baig, Z.; Mamat, O.; Mustapha, M.; Mumtaz, A.; Munir, K. S.; Sarfraz, M., Investigation of tip sonication effects on structural quality of graphene nanoplatelets (GNPs) for superior solvent dispersion. *Ultrasonics Sonochemistry* **2018,** *45*, 133-149.

93. Karger, L.; Synnatschke, K.; Settele, S.; Hofstetter, Y. J.; Nowack, T.; Zaumseil, J.; Vaynzof, Y.; Backes, C., The Role of Additives in Suppressing the Degradation of Liquid-Exfoliated WS2 Monolayers. *Advanced Materials* **2021,** *33* (42), 2102883.

94. Backes, C.; Campi, D.; Szydlowska, B. M.; Synnatschke, K.; Ojala, E.; Rashvand, F.; Harvey, A.; Griffin, A.; Sofer, Z.; Marzari, N.; Coleman, J. N.; O'Regan, D. D., Equipartition of Energy Defines the Size–Thickness Relationship in Liquid-Exfoliated Nanosheets. *ACS Nano* **2019,** *13* (6), 7050-7061.

95. Neppiras, E. A., Acoustic cavitation. *Physics Reports* **1980,** *61* (3), 159-251.

96. Yi, M.; Shen, Z., A review on mechanical exfoliation for the scalable production of graphene. *Journal of Materials Chemistry A* **2015,** *3* (22), 11700-11715.

97. Zhou, G.; Rajak, P.; Susarla, S.; Ajayan, P. M.; Kalia, R. K.; Nakano, A.; Vashishta, P., Molecular Simulation of MoS2 Exfoliation. *Scientific Reports* **2018,** *8* (1), 16761.

98. Turner, P.; Hodnett, M.; Dorey, R.; Carey, J. D., Controlled Sonication as a Route to in-situ Graphene Flake Size Control. *Scientific Reports* **2019,** *9* (1), 8710.

99. Yi, M.; Shen, Z.; Zhang, X.; Ma, S., Vessel diameter and liquid height dependent sonication-assisted production of few-layer graphene. *Journal of Materials Science* **2012,** *47* (23), 8234-8244.

100. Li, Z.; Young, R. J.; Backes, C.; Zhao, W.; Zhang, X.; Zhukov, A. A.; Tillotson, E.; Conlan, A. P.; Ding, F.; Haigh, S. J.; Novoselov, K. S.; Coleman, J. N., Mechanisms of Liquid-Phase Exfoliation for the Production of Graphene. *ACS Nano* **2020,** *14* (9), 10976-10985.

101. Rooney, A. P.; Li, Z.; Zhao, W.; Gholinia, A.; Kozikov, A.; Auton, G.; Ding, F.; Gorbachev, R. V.; Young, R. J.; Haigh, S. J., Anomalous twin boundaries in two dimensional materials. *Nature Communications* **2018,** *9* (1), 3597.

102. Hess, P., Surface Acoustic Waves in Materials Science. *Physics Today* **2002,** *55* (3), 42-47.

103. Kosynkin, D. V.; Higginbotham, A. L.; Sinitskii, A.; Lomeda, J. R.; Dimiev, A.; Price, B. K.; Tour, J. M., Longitudinal unzipping of carbon nanotubes to form graphene nanoribbons. *Nature* **2009,** *458* (7240), 872-876.

104. Ma, L.; Wang, J.; Ding, F., Strain-Induced Orientation-Selective Cutting of Graphene into Graphene Nanoribbons on Oxidation. *Angewandte Chemie International Edition* **2012,** *51* (5), 1161-1164.

105. Jawaid, A.; Nepal, D.; Park, K.; Jespersen, M.; Qualley, A.; Mirau, P.; Drummy, L. F.; Vaia, R. A., Mechanism for Liquid Phase Exfoliation of MoS2. *Chemistry of Materials* **2016,** *28* (1), 337-348.

106. Backes, C., 12 - Production of graphene and other two-dimensional nanosheets by liquid phase exfoliation. In *Graphene (Second Edition)*, Skakalova, V.; Kaiser, A. B., Eds. Woodhead Publishing: 2021; pp 251-314.

107. Coleman, J. N., Liquid-Phase Exfoliation of Nanotubes and Graphene. *Advanced Functional Materials* **2009,** *19* (23), 3680-3695.

108. Backes, C.; Szydłowska, B. M.; Harvey, A.; Yuan, S.; Vega-Mayoral, V.; Davies, B. R.; Zhao, P.-l.; Hanlon, D.; Santos, E. J. G.; Katsnelson, M. I.; Blau, W. J.; Gadermaier, C.; Coleman, J. N., Production of Highly Monolayer Enriched Dispersions of Liquid-Exfoliated Nanosheets by Liquid Cascade Centrifugation. *ACS Nano* **2016,** *10* (1), 1589-1601.

109. Ogilvie, S.; Large, M.; O'Mara, M.; Lynch, P.; Lee, C.; King, A.; Backes, C.; Dalton, A., Size selection of liquid-exfoliated 2D nanosheets. *2D Materials* **2019,** *6*.

110. Backes, C.; Smith, R. J.; McEvoy, N.; Berner, N. C.; McCloskey, D.; Nerl, H. C.; O'Neill, A.; King, P. J.; Higgins, T.; Hanlon, D.; Scheuschner, N.; Maultzsch, J.; Houben, L.; Duesberg, G. S.; Donegan, J. F.; Nicolosi, V.; Coleman, J. N., Edge and confinement effects allow in situ measurement of size and thickness of liquid-exfoliated nanosheets. *Nature Communications* **2014,** *5*, 4576.

111. Green, A. A.; Hersam, M. C., Solution Phase Production of Graphene with Controlled Thickness via Density Differentiation. *Nano Letters* **2009,** *9* (12), 4031-4036.

112. Zhu, J.; Kang, J.; Kang, J.; Jariwala, D.; Wood, J. D.; Seo, J.-W. T.; Chen, K.-S.; Marks, T. J.; Hersam, M. C., Solution-Processed Dielectrics Based on Thickness-Sorted Two-Dimensional Hexagonal Boron Nitride Nanosheets. *Nano Letters* **2015,** *15* (10), 7029-7036.

113. Benameur, M. M.; Radisavljevic, B.; Héron, J. S.; Sahoo, S.; Berger, H.; Kis, A., Visibility of dichalcogenide nanolayers. *Nanotechnology* **2011,** *22* (12), 125706.

114. Lotya, M.; Rakovich, A.; Donegan, J. F.; Coleman, J. N., Measuring the lateral size of liquid-exfoliated nanosheets with dynamic light scattering. *Nanotechnology* **2013,** *24* (26), 265703.

115. Harvey, A.; Backes, C.; Boland, J. B.; He, X.; Griffin, A.; Szydlowska, B.; Gabbett, C.; Donegan, J. F.; Coleman, J. N., Non-resonant light scattering in dispersions of 2D nanosheets. *Nature Communications* **2018,** *9* (1), 4553.

116. Backes, C.; Paton, K. R.; Hanlon, D.; Yuan, S.; Katsnelson, M. I.; Houston, J.; Smith, R. J.; McCloskey, D.; Donegan, J. F.; Coleman, J. N., Spectroscopic metrics allow in situ measurement of mean size and thickness of liquid-exfoliated few-layer graphene nanosheets. *Nanoscale* **2016,** *8* (7), 4311-4323.

117. Ueberricke, L.; Coleman, J. N.; Backes, C., Robustness of Size Selection and Spectroscopic Size, Thickness and Monolayer Metrics of Liquid-Exfoliated WS2. *physica status solidi (b)* **2017,** *254* (11), 1700443.

118. Backes, C.; Higgins, T. M.; Kelly, A.; Boland, C.; Harvey, A.; Hanlon, D.; Coleman, J. N., Guidelines for Exfoliation, Characterization and Processing of Layered Materials Produced by Liquid Exfoliation. *Chemistry of Materials* **2017,** *29* (1), 243-255.

119. Ott, S.; Wolff, N.; Rashvand, F.; Rao, V. J.; Zaumseil, J.; Backes, C., Impact of the MoS2 Starting Material on the Dispersion Quality and Quantity after Liquid Phase Exfoliation. *Chemistry of Materials* **2019,** *31* (20), 8424-8431.

120. Ott, S.; Lakmann, M.; Backes, C., Impact of Pretreatment of the Bulk Starting Material on the Efficiency of Liquid Phase Exfoliation of WS2. *Nanomaterials* **2021,** *11* (5), 1072.

121. Zhang, X.; Qiao, X.-F.; Shi, W.; Wu, J.-B.; Jiang, D.-S.; Tan, P.-H., Phonon and Raman scattering of two-dimensional transition metal dichalcogenides from monolayer, multilayer to bulk material. *Chemical Society Reviews* **2015,** *44* (9), 2757-2785.

122. Lee, C.; Yan, H.; Brus, L. E.; Heinz, T. F.; Hone, J.; Ryu, S., Anomalous Lattice Vibrations of Single- and Few-Layer MoS2. *ACS Nano* **2010,** *4* (5), 2695-2700.

123. O'Brien, M.; McEvoy, N.; Hanlon, D.; Hallam, T.; Coleman, J. N.; Duesberg, G. S., Mapping of Low-Frequency Raman Modes in CVD-Grown Transition Metal Dichalcogenides: Layer Number, Stacking Orientation and Resonant Effects. *Scientific Reports* **2016,** *6* (1), 19476.

124. Terrones, H.; Corro, E. D.; Feng, S.; Poumirol, J. M.; Rhodes, D.; Smirnov, D.; Pradhan, N. R.; Lin, Z.; Nguyen, M. A. T.; Elías, A. L.; Mallouk, T. E.; Balicas, L.; Pimenta, M. A.; Terrones, M., New First Order Raman-active Modes in Few Layered Transition Metal Dichalcogenides. *Scientific Reports* **2014,** *4* (1), 4215.

125. McCreary, A.; Berkdemir, A.; Wang, J.; Nguyen, M. A.; Elías, A. L.; Perea-López, N.; Fujisawa, K.; Kabius, B.; Carozo, V.; Cullen, D. A.; Mallouk, T. E.; Zhu, J.; Terrones, M., Distinct photoluminescence and Raman spectroscopy signatures for identifying highly crystalline WS2 monolayers produced by different growth methods. *Journal of Materials Research* **2016,** *31* (7), 931-944.

126. Tuschel, D., Photoluminescence spectroscopy using a Raman spectrometer. *Spectroscopy* **2016,** *31* (9), 14-21.

127. Kalt, H.; Klingshirn, C. F., The Polariton Concept. In *Semiconductor Optics 1: Linear Optical Properties of Semiconductors*, Springer International Publishing: Cham, **2019**; pp 101-132.

128. Rahimi-Iman, A., Fundamentals of Polariton Physics. In *Polariton Physics: From Dynamic Bose–Einstein Condensates in Strongly-Coupled Light–Matter Systems to Polariton Lasers*, Springer International Publishing: Cham, **2020**; pp 33-64.

129. Coleman, J. N., Liquid Exfoliation of Defect-Free Graphene. *Accounts of Chemical Research* **2013,** *46* (1), 14-22.

130. Ciesielski, A.; Samorì, P., Graphene via sonication assisted liquid-phase exfoliation. *Chemical Society Reviews* **2014,** *43* (1), 381-398.

131. Bracamonte, M. V.; Lacconi, G. I.; Urreta, S. E.; Foa Torres, L. E. F., On the Nature of Defects in Liquid-Phase Exfoliated Graphene. *The Journal of Physical Chemistry C* **2014,** *118* (28), 15455-15459.

132. Skaltsas, T.; Ke, X.; Bittencourt, C.; Tagmatarchis, N., Ultrasonication Induces Oxygenated Species and Defects onto Exfoliated Graphene. *The Journal of Physical Chemistry C* **2013,** *117* (44), 23272-23278.

133. Polyakova, E. Y.; Rim, K. T.; Eom, D.; Douglass, K.; Opila, R. L.; Heinz, T. F.; Teplyakov, A. V.; Flynn, G. W., Scanning Tunneling Microscopy and X-ray Photoelectron Spectroscopy Studies of Graphene Films Prepared by Sonication-Assisted Dispersion. *ACS Nano* **2011,** *5* (8), 6102-6108.

134. Kozhemyakina, N. V.; Eigler, S.; Dinnebier, R. E.; Inayat, A.; Schwieger, W.; Hirsch, A., Effect of the Structure and Morphology of Natural, Synthetic and Post-processed Graphites on Their Dispersibility and Electronic Properties. *Fullerenes, Nanotubes and Carbon Nanostructures* **2013,** *21* (9), 804-823.

135. Çelik, Y.; Flahaut, E.; Suvacı, E., A comparative study on few-layer graphene production by exfoliation of different starting materials in a low boiling point solvent. *FlatChem* **2017,** *1*, 74-88.

136. Botas, C.; Pérez-Mas, A. M.; Álvarez, P.; Santamaría, R.; Granda, M.; Blanco, C.; Menéndez, R., Optimization of the size and yield of graphene oxide sheets in the exfoliation step. *Carbon* **2013,** *63*, 576-578.

137. Savjani, N.; Lewis, E. A.; Pattrick, R. A. D.; Haigh, S. J.; O'Brien, P., MoS2 nanosheet production by the direct exfoliation of molybdenite minerals from several type-localities. *RSC Advances* **2014,** *4* (67), 35609-35613.

138. An, X.; Simmons, T.; Shah, R.; Wolfe, C.; Lewis, K. M.; Washington, M.; Nayak, S. K.; Talapatra, S.; Kar, S., Stable Aqueous Dispersions of Noncovalently Functionalized Graphene from Graphite and their Multifunctional High-Performance Applications. *Nano Letters* **2010,** *10* (11), 4295-4301.

139. Read, O.; Shin, Y.; Hu, C.-x.; Zarattini, M.; Boyes, M.; Just-Baringo, X.; Panigrahi, A.; Larrosa, I.; Casiraghi, C., Insights into the exfoliation mechanism of pyrene-assisted liquid phase exfoliation of graphene from lateral size-thickness characterisation. *Carbon* **2022,** *186*, 550-559.

140. Abdelkader, A. M.; Cooper, A. J.; Dryfe, R. A. W.; Kinloch, I. A., How to get between the sheets: a review of recent works on the electrochemical exfoliation of graphene materials from bulk graphite. *Nanoscale* **2015,** *7* (16), 6944-6956.

141. Xia, Z. Y.; Pezzini, S.; Treossi, E.; Giambastiani, G.; Corticelli, F.; Morandi, V.; Zanelli, A.; Bellani, V.; Palermo, V., The Exfoliation of Graphene in Liquids by Electrochemical, Chemical, and Sonication-Assisted Techniques: A Nanoscale Study. **2013,** *23* (37), 4684-4693.

142. Eda, G.; Yamaguchi, H.; Voiry, D.; Fujita, T.; Chen, M.; Chhowalla, M., Photoluminescence from Chemically Exfoliated MoS2. *Nano Letters* **2011,** *11* (12), 5111-5116.

143. Hong, J.; Hu, Z.; Probert, M.; Li, K.; Lv, D.; Yang, X.; Gu, L.; Mao, N.; Feng, Q.; Xie, L.; Zhang, J.; Wu, D.; Zhang, Z.; Jin, C.; Ji, W.; Zhang, X.; Yuan, J.; Zhang, Z., Exploring atomic defects in molybdenum disulphide monolayers. *Nature Communications* **2015,** *6* (1), 6293.

144. Kunstmann, J.; Wendumu, T. B.; Seifert, G., Localized defect states in MoS2 monolayers: Electronic and optical properties. *physica status solidi (b)* **2017,** *254* (4), 1600645.

145. Djamil, J.; Hansen, A.-L.; Backes, C.; Bensch, W.; Schürmann, U.; Kienle, L.; Düvel, A.; Heitjans, P., Using light, X-rays and electrons for evaluation of the nanostructure of layered materials. *Nanoscale* **2018,** *10* (45), 21142-21150.

146. Liang, K. S.; Chianelli, R. R.; Chien, F. Z.; Moss, S. C., Structure of poorly crystalline MoS2 — A modeling study. *Journal of Non-Crystalline Solids* **1986,** *79* (3), 251-273.

147. Chianelli, R. R.; Prestridge, E. B.; Pecoraro, T. A.; Deneufville, J. P., Molybdenum Disulfide in the Poorly Crystalline "Rag" Structure. *Science* **1979,** *203* (4385), 1105-1107.

148. Wilson, J. A.; Yoffe, A. D., The transition metal dichalcogenides discussion and interpretation of the observed optical, electrical and structural properties. *Advances in Physics* **1969,** *18* (73), 193-335.

149. Splendiani, A.; Sun, L.; Zhang, Y.; Li, T.; Kim, J.; Chim, C.-Y.; Galli, G.; Wang, F., Emerging Photoluminescence in Monolayer MoS2. *Nano Letters* **2010,** *10* (4), 1271-1275.

150. Mak, K. F.; Lee, C.; Hone, J.; Shan, J.; Heinz, T. F., Atomically Thin MoS_2: A New Direct-Gap Semiconductor. *Physical Review Letters* **2010,** *105* (13), 136805.

151. Neumann, A.; Lindlau, J.; Nutz, M.; Mohite, A. D.; Yamaguchi, H.; Högele, A., Signatures of defect-localized charged excitons in the photoluminescence of monolayer molybdenum disulfide. *Physical Review Materials* **2018,** *2* (12), 124003.

152. Goodman, A. J.; Willard, A. P.; Tisdale, W. A., Exciton trapping is responsible for the long apparent lifetime in acid-treated MoS_2. *Physical Review B* **2017,** *96* (12), 121404.

153. Berger, F. J.; Lüttgens, J.; Nowack, T.; Kutsch, T.; Lindenthal, S.; Kistner, L.; Müller, C. C.; Bongartz, L. M.; Lumsargis, V. A.; Zakharko, Y.; Zaumseil, J., Brightening of Long, Polymer-Wrapped Carbon Nanotubes by sp3 Functionalization in Organic Solvents. *ACS Nano* **2019,** *13* (8), 9259-9269.

154. Piao, Y.; Meany, B.; Powell, L. R.; Valley, N.; Kwon, H.; Schatz, G. C.; Wang, Y., Brightening of carbon nanotube photoluminescence through the incorporation of sp3 defects. *Nature Chemistry* **2013,** *5* (10), 840-845.

155. Kang, N.; Paudel, H. P.; Leuenberger, M. N.; Tetard, L.; Khondaker, S. I., Photoluminescence Quenching in Single-Layer MoS2 via Oxygen Plasma Treatment. *The Journal of Physical Chemistry C* **2014,** *118* (36), 21258-21263.

156. Liu, X.; Galfsky, T.; Sun, Z.; Xia, F.; Lin, E.-c.; Lee, Y.-H.; Kéna-Cohen, S.; Menon, V. M., Strong light–matter coupling in two-dimensional atomic crystals. *Nature Photonics* **2015,** *9* (1), 30-34.

157. Flatten, L. C.; He, Z.; Coles, D. M.; Trichet, A. A. P.; Powell, A. W.; Taylor, R. A.; Warner, J. H.; Smith, J. M., Room-temperature exciton-polaritons with two-dimensional WS2. *Scientific Reports* **2016,** *6*, 33134.

158. Latini, S.; Ronca, E.; De Giovannini, U.; Hübener, H.; Rubio, A., Cavity Control of Excitons in Two-Dimensional Materials. *Nano Letters* **2019,** *19* (6), 3473-3479.

159. Bhatt, P.; Dutta, J.; George, J., Electromagnetic Field Dependence of Strong Coupling in WS2 Monolayers. *Physica status solidi RRL* **2021,** 15, 2000580.

160. Wang, Q.; Sun, L.; Zhang, B.; Chen, C.; Shen, X.; Lu, W., Direct observation of strong light-exciton coupling in thin WS2 flakes. *Opt. Express* **2016,** *24* (7), 7151-7157.

161. Wang, S.; Li, S.; Chervy, T.; Shalabney, A.; Azzini, S.; Orgiu, E.; Hutchison, J. A.; Genet, C.; Samorì, P.; Ebbesen, T. W., Coherent Coupling of WS2 Monolayers with Metallic Photonic Nanostructures at Room Temperature. *Nano Letters* **2016,** *16* (7), 4368-4374.

162. Shao, J.-J.; Lv, W.; Yang, Q.-H., Self-Assembly of Graphene Oxide at Interfaces. **2014,** *26* (32), 5586-5612.

163. Wells, R. A.; Johnson, H.; Lhermitte, C. R.; Kinge, S.; Sivula, K., Roll-to-Roll Deposition of Semiconducting 2D Nanoflake Films of Transition Metal Dichalcogenides for Optoelectronic Applications. *ACS Applied Nano Materials* **2019,** *2* (12), 7705-7712.

164. Ogilvie, S. P.; Large, M. J.; Fratta, G.; Meloni, M.; Canton-Vitoria, R.; Tagmatarchis, N.; Massuyeau, F.; Ewels, C. P.; King, A. A. K.; Dalton, A. B., Considerations for spectroscopy of liquid-exfoliated 2D materials: emerging photoluminescence of N-methyl-2-pyrrolidone. *Scientific Reports* **2017,** *7* (1), 16706.

165. Babgohari, M. Z.; Ghorashi, S. M. B.; Mirjalili, G., Optical and structural properties of PVK/CA/PVK thin films fabricated by spin coating method. *Optik* **2017,** *131*, 862-868.

166. Tropf, L.; Gather, M. C., Investigating the Onset of the Strong Coupling Regime by Fine-Tuning the Rabi Splitting in Multilayer Organic Microcavities. *Advanced Optical Materials* **2018,** *6* (17), 1800203.

167. Chu, X. S.; Yousaf, A.; Li, D. O.; Tang, A. A.; Debnath, A.; Ma, D.; Green, A. A.; Santos, E. J. G.; Wang, Q. H., Direct Covalent Chemical Functionalization of Unmodified Two-Dimensional Molybdenum Disulfide. *Chemistry of Materials* **2018,** *30* (6), 2112-2128.

168. Nowack, T. Covalent functionalization of transition metal dichalcogenides in the liquid phase. *Master Thesis* **2020**, University of Heidelberg.

169. Hertzog, M.; Wang, M.; Mony, J.; Börjesson, K., Strong light–matter interactions: a new direction within chemistry. *Chemical Society Reviews* **2019,** *48* (3), 937-961.

170. Barachati, F.; Fieramosca, A.; Hafezian, S.; Gu, J.; Chakraborty, B.; Ballarini, D.; Martinu, L.; Menon, V.; Sanvitto, D.; Kéna-Cohen, S., Interacting polariton fluids in a monolayer of tungsten disulfide. *Nature Nanotechnology* **2018,** *13* (10), 906-909.

171. Liu, X.; Bao, W.; Li, Q.; Ropp, C.; Wang, Y.; Zhang, X., Control of Coherently Coupled Exciton Polaritons in Monolayer Tungsten Disulphide. *Physical Review Letters* **2017,** *119*.

172. Houdré, R.; Stanley, R. P.; Ilegems, M., Vacuum-field Rabi splitting in the presence of inhomogeneous broadening: Resolution of a homogeneous linewidth in an inhomogeneously broadened system. *Physical Review A* **1996,** *53* (4), 2711-2715.

173. Rice, P. R.; Brecha, R. J., Cavity induced transparency. *Optics Communications* **1996,** *126* (4), 230-235.

174. Coles, D. M.; Somaschi, N.; Michetti, P.; Clark, C.; Lagoudakis, P. G.; Savvidis, P. G.; Lidzey, D. G., Polariton-mediated energy transfer between organic dyes in a strongly coupled optical microcavity. *Nature Materials* **2014,** *13* (7), 712-719.
175. Dimoulas, A., Silicene and germanene: Silicon and germanium in the “flatland”. *Microelectronic Engineering* **2015,** *131*, 68-78.
176. Lin, C.-L.; Arafune, R.; Kawahara, K.; Tsukahara, N.; Minamitani, E.; Kim, Y.; Takagi, N.; Kawai, M., Structure of Silicene Grown on Ag(111). *Applied Physics Express* **2012,** *5* (4), 045802.
177. Feng, B.; Ding, Z.; Meng, S.; Yao, Y.; He, X.; Cheng, P.; Chen, L.; Wu, K., Evidence of Silicene in Honeycomb Structures of Silicon on Ag(111). *Nano Letters* **2012,** *12* (7), 3507-3511.
178. Li, L.; Lu, S.-z.; Pan, J.; Qin, Z.; Wang, Y.-q.; Wang, Y.; Cao, G.-y.; Du, S.; Gao, H.-J., Buckled Germanene Formation on Pt(111). *Advanced Materials* **2014,** *26* (28), 4820-4824.
179. Vogg, G.; Brandt, M. S.; Stutzmann, M., Polygermyne—A Prototype System for Layered Germanium Polymers. **2000,** *12* (17), 1278-1281.
180. Bianco, E.; Butler, S.; Jiang, S.; Restrepo, O. D.; Windl, W.; Goldberger, J. E., Stability and Exfoliation of Germanane: A Germanium Graphane Analogue. *ACS Nano* **2013,** *7* (5), 4414-4421.
181. Jiang, S.; Butler, S.; Bianco, E.; Restrepo, O. D.; Windl, W.; Goldberger, J. E., Improving the stability and optical properties of germanane via one-step covalent methyl-termination. *Nature Communications* **2014,** *5* (1), 3389.
182. Liu, Z.; Wang, Z.; Sun, Q.; Dai, Y.; Huang, B., Methyl-terminated germanane GeCH3 synthesized by solvothermal method with improved photocatalytic properties. *Applied Surface Science* **2019,** *467-468*, 881-888.
183. Knapp, D.; Brunschwig, B. S.; Lewis, N. S., Chemical, Electronic, and Electrical Properties of Alkylated Ge(111) Surfaces. *The Journal of Physical Chemistry C* **2010,** *114* (28), 12300-12307.
184. Livache, C.; Ryan, B. J.; Ramesh, U.; Steinmetz, V.; Gréboval, C.; Chu, A.; Brule, T.; Ithurria, S.; Prévot, G.; Barisien, T.; Ouerghi, A.; Panthani, M. G.; Lhuillier, E., Optoelectronic properties of methyl-terminated germanane. **2019,** *115* (5), 052106.
185. Shu, H.; Li, Y.; Wang, S.; Wang, J., Thickness-Dependent Electronic and Optical Properties of Bernal-Stacked Few-Layer Germanane. *The Journal of Physical Chemistry C* **2015,** *119* (27), 15526-15531.
186. Madhushankar, B. N.; Kaverzin, A.; Giousis, T.; Potsi, G.; Gournis, D.; Rudolf, P.; Blake, G. R.; van der Wal, C. H.; van Wees, B. J., Electronic properties of germanane field-effect transistors. *2D Materials* **2017,** *4* (2), 021009.
187. Song, Z.; Ang, W. L.; Sturala, J.; Mazanek, V.; Marvan, P.; Sofer, Z.; Ambrosi, A.; Ding, C.; Luo, X.; Bonanni, A., Functionalized Germanene-Based Nanomaterials for the Detection of Single Nucleotide Polymorphism. *ACS Applied Nano Materials* **2021,** *4* (5), 5164-5175.
188. Maric, T.; Beladi-Mousavi, S. M.; Khezri, B.; Sturala, J.; Nasir, M. Z. M.; Webster, R. D.; Sofer, Z. k.; Pumera, M., Functional 2D Germanene Fluorescent Coating of Microrobots for Micromachines Multiplexing. **2020,** *16* (27), 1902365.
189. Chacham, H.; Santos, J. C. C.; Pacheco, F. G.; Silva, D. L.; Martins, R. M.; Del’Boccio, J. P.; Soares, E. M.; Altoé, R.; Furtado, C. A.; Plentz, F.; Neves, B. R. A.; Cançado, L. G., Controlling the Morphology of Nanoflakes Obtained by Liquid-Phase Exfoliation: Implications for the Mass Production of 2D Materials. *ACS Applied Nano Materials* **2020,** *3* (12), 12095-12105.